NANYANG TECHNOLOGICAL UNIVERSITY

DYNAMICS OF WATER WAVES OVER FRINGING CORAL REEFS

YAO YU

SCHOOL OF CIVIL AND ENVIRONMENTAL ENGINEERING

2012

DYNAMICS OF WATER WAVES OVER FRINGING CORAL REEFS

YAO YU

2012

Dynamics of Water Waves over Fringing Coral Reefs

Yao Yu

School of Civil and Environmental Engineering

A thesis submitted to the Nanyang Technological University
in fulfillment of the requirement for the degree of
Doctor of Philosophy

2012

ACKNOWLEDGEMENT

The work presented in this thesis is done under the collaborative supervision of Asst. Prof. Zhenhua Huang at Nanyang Technological University (NTU) and Prof. Stephen G. Monismith at Stanford University under Singapore Stanford Partnership (SSP) Program. During the last four years, Prof. Huang and Prof. Monismith have guided me with utmost patience and I was deeply inspired with their original ideas and profound insights. The research challenges posed by them have been endless in that it aroused my industrious work in pursing for progress as well as my elevating the quality of this thesis. Herewith, the author expresses the greatest gratitude to them.

My thanks also go to Asso. Prof. Edmond, Lo. and Dr. Sivadas whose earlier laboratory work acts as a key reference of experimental settings in this thesis. Meanwhile, I feel grateful to Dr. Chunrong Liu, Dr. Zikun Xing, Dr. Hongtao Nie, Mr. Zhida Yuan and Mr. Sim Yisheng Shawn for their guidance and assistance during the laboratory or numerical experiments at NTU. As for technician supports that from NTU Hydraulic Modeling Laboratory staffs of Mr. Fok Yew Seng, Mr. Lim Kok Hin and Mr. Foo Shiang Kim, appreciation is also expressed. Special thanks are due to Prof. Lynett, P., who made the original numerical code available for this research. Last but not the least, I owe my sincere gratitude to the students, faculty, staff of the Environmental Fluid Mechanics Lab at Stanford University for their helpful discussions and suggestions.

Although my teammates and friends may not have their interests rooted in this area, their support in many ways is most appreciated. In particular, I would like to acknowledge Mr. Conghao Xu and Mrs. Yao Yao for their proofreading this thesis. Finally, I am greatly indebted with my parents, my relatives and all the dear persons for their constant love, understanding and support to my Ph.D candidature.

TABLE OF CONTENTS

SUMMARY

This thesis reported a comprehensive study of the wave dynamics over fringing reefs with and without a ridge, including laboratory experiments, numerical modeling and theoretical analyses.

Laboratory experiments were first performed in a wave flume to measure the main aspects of breaking-wave characteristics over an idealized submerged fringing reef. Results were reported for different monochromatic waves, reef-flat submergences and fore-reef slopes. Dimensionless analysis showed that the relative submergence on the reef flat is a dominant factor affecting the breaking-wave characteristics. Results comparisons with other coastal profiles were conducted and some empirical equations were proposed. A laboratory study of wave-induced setup over an idealized fringing reef in the absence/presence of a steep reef crest (ridge) was then conducted. Experimental results were reported for a range of reef-crest submergences under both monochromatic and spectral waves. The behaviors of the wave transformation and wave setup in the presence of the ridge were compared with those in the absence of the ridge. Additional high-resolution wave measurements were conducted to analyze the cross-shore evolution of harmonic waves and momentum flux. The undertow measurements were also supplemented to study the vertical flow structures across the reef.

A numerical study based on the one-dimensional (1D), fully nonlinear and weakly dispersive Boussinesq equations is presented in this thesis. An empirical eddy viscosity model was adopted to account for wave breaking and a shock-capturing Finite Volume-based solver was employed with a delicate treatment of boundary conditions. The numerical results were validated with several scenarios from the aforementioned wave setup experiments, representing various combinations of reef profiles, reef-crest submergences and wave conditions. The model was then applied to study the effects of fore-reef slopes and profile shapes on the wave transformation and setup over the fringing reefs.

To gain more physical insights into wave setup generation on fringing reefs, the analytical modeling approaches were attempted. Several existing one-dimensional horizontal (1DH) models were evaluated and proven to be insufficient to reproduce our laboratory data. To seek a proper description of wave-induced setup under very steep reef crest (ridge), two theoretical models were presented in this thesis: a kinematic model based on the cross-shore mass balance and some hydraulics, and a dynamic model based on 1D momentum balance and the radiation stress concept. Both models were validated against the laboratory data involving a variety of reef profiles and reef-crest submergences under both monochromatic and spectral waves. The 1DH dynamic model was also applied to some field reefs. The two-dimensional horizontal (2DH) formulation of the dynamics model was then derived and validated by a field case study. Both models have the empirical parameter related only to reef morphology.

The main contributions of this thesis are: (1) a systematic experimental study of breaking-wave characteristics for fringing reefs; (2) a comprehensive understanding of the role of a ridge structure located on the reef edge in determining the wave-induced setup over fringing reefs; (3) analytical models for 1DH non-emergent fringing reef (with/without a ridge).

LIST OF TABLES

LIST OF FIGURES

LIST OF SYMBOLS

a wave amplitude

B cross-shore reef-crest (ridge) width

B_c cross-shore crest width of low-crested structure

b alongshore reef-crest (ridge) length

b_0 cross-shore fore-reef width

C_d bottom drag coefficient

C_d^g bottom drag coefficient for channel

C_d^r bottom drag coefficient for reef

C_r Courant number

c wave celerity/phase speed

c_g group velocity

c_0^g deep-water (offshore) group velocity

c_i^g group velocity of incident waves

c_t^g group velocity of transmitted waves

d reef crest (ridge) height

D total instantaneous water depth, $D = h + \eta$

D_c critical flow depth above reef crest

$\overline{D}$ total mean water depth, $\overline{D} = h + \overline{\eta}$

$\overline{D}_r$ mean water depth on reef flat, $\overline{D}_r = h + \overline{\eta}_r$

E wave energy density

E_0 deep-water (offshore) wave energy density

E_c specific energy of open channel flow

E_i energy density of incident waves

E_r energy density of reflected waves

E_t energy density of transmitted waves

E_{fb} energy flux dissipated due to bottom friction before wave breaking

F freeboard of low-crested structure

F_{co} nonlinearity parameter in Gourlay (1994)

f friction coefficient

f_p peak wave frequency

g gravitational acceleration

H local wave height

H_0 deep-water (offshore) wave height

H_b breaker wave height

H_b^G breaker wave height measured from wave gauge

H_b^I breaker wave height measured from recorded image

H_i incident wave height

H_r reflected wave height

H_t transmitted wave height

H_s significant wave height

H_{s0} deep-water (offshore) significant wave height

H_{rms} root-mean-square wave height

H_{rms0} deep-water (offshore) root-mean-square wave height

h still water depth

h_0 still water depth in the deep section of the flume

h_b breaker water depth

h_c still water depth on the reef crest (reef-crest submergence)

h_g still water depth in channel

h_p representative water depth for surf zone

h_r still water depth on the reef flat (reef-flat submergence)

h_s still water depth at endpoint of surf zone

K wave-crest asymmetry factor in Gourlay (1996a)

K_d energy loss coefficient

K_p reef-crest shape factor in Gourlay and Colleter (2005)

K_r reflection coefficient

K_r^p reflection coefficient predicted by model

K_r^m reflection coefficient measured in the experiments

K_t transmission coefficient

k wave number

L local wave length

L_0 deep-water (offshore) wave length

L_e distance between breaking point and reef edge

L_g cross-shore channel width

L_l cross-shore lagoon width

L_r cross-shore reef-flat width

L_s total surfzone width

L_r^e effective cross-shore reef-flat width

N grid number per incident wave length

n_M Manning coefficient

P normalized cross-shore radiation stress

Q_B total backward volumetric flux during the backwash phase of wave breaking

Q_F total forward volumetric flux during the up-rush phase of wave breaking

Q_{F0} offshore total forward volumetric flux during the forward phase of wave motion

q mean flow rate per unit width

q_c critical flow rate for open channel flow

R_b ad-hoc dissipative term accounting for wave breaking in the numerical model

R_f ad-hoc dissipative term accounting for bottom friction in the numerical model

S deep-water (offshore) wave steepness, $S = H_0 / gT^2$

S_{ij} radiation stress tensor

S_{xx} cross-shore radiation stress

S_{xx}^{b} cross-shore radiation stress at breaking point

S_{xx}^{s} cross-shore radiation stress at the endpoint of surf zone

s fore-reef slope

s_a averaged slope for composite fore-reef

s_e equivalent slope for fore-reef including reef crest (ridge) effect

T wave period

T_p peak wave period

T_s significant wave period

T_{02} mean zero-upcrossing period

T^* duration of breaking event in the numerical breaking model

t_0 the time at which breaking event starts in the numerical breaking model

U cross-shore depth-averaged mean velocity

U_b cross-shore depth-averaged mean velocity at breaking point

U_g cross-shore depth-averaged mean velocity in channel

U_r cross-shore depth-averaged mean velocity on reef flat

u cross-shore time-mean velocity

u_{ref} cross-shore time-mean velocity at a reference water depth

$u(t)$ cross-shore instantaneous velocity

u_b cross-shore instantaneous bottom velocity

u_α cross-shore instantaneous velocity at the water depth z_α

u_w cross-shore wave orbital velocity

W sponge layer width in numerical model

W_g alongshore channel length

W_r alongshore reef-flat length

W_s relative surfzone width

w_w vertical wave orbital velocity

$w(t)$ vertical instantaneous velocity

x_b coordinate of breaking point

x_c coordinate of reef crest

x_e coordinate of reef edge

x_r coordinate of leeside edge of the ridge

x_s coordinate of endpoint of surf zone

α scaling factor for energy dissipation due to bottom friction

α_1, α_2, α_3 empirical coefficients in the numerical breaking model

β empirical parameter in the proposed kinematic model

β_0 empirical parameter in the proposed dynamic model

γ breaker depth index;

γ_1 breaker depth index for fore-reef

γ_2 breaker depth index for reef flat

γ_m breaker depth index for plane beaches

δ empirical coefficient related to turbulence intensity in numerical breaking model

ε_b energy dissipation rate due to wave breaking

ε_f energy dissipation rate due to bottom friction

η free water surface elevation

$\overline{\eta}$ deviation of mean water level from still water level (wave-induced setup/setdown)

$\overline{\eta}_a$ averaged wave-induced setup over reef-flat width

$\overline{\eta}_b$ wave-induced setdown at breaking point

$\overline{\eta}_L$ wave-induced setup in lagoon

$\overline{\eta}_r$ maximum wave-induced setup on reef flat

$\overline{\eta}_r^o$ maximum wave-induced setup observed in the experiments

$\overline{\eta}_r^p$ maximum wave-induced setup predicted by the model

$\overline{\eta}_r^{ave}$ maximum wave-induced setup averaged for a dataset

$\overline{\eta}_{r0}^{ave}$ reference maximum wave-induced setup averaged for a dataset

$\eta_t^{(F)}$ saturated value for breaking cessation in the numerical breaking model

$\eta_t^{(I)}$ threshold value for breaking inception in the numerical breaking model

θ fore-reef slope angle

θ' equivalent fore-reef slope angle

κ energy reduction coefficient

ρ water density

μ wave length scaling parameter defined by $\mu = h / L$

ν empirical eddy viscosity in the numerical breaking model

τ_x^b cross-shore bottom shear stress

ω angular frequency

ξ_0 surf-similarity parameter in terms of deep-water wave height

ξ_b surf-similarity parameter in terms of breaker wave height

ξ_i surf-similarity parameter in terms of incident wave height

Ω breaker height index

Δx grid size

Δt time step

CHAPTER 1 INTRODUCTION

1.1 Significance of Wave Dynamics over Coral Reefs

Coral reefs are abundant in shallow tropical and subtropical coastal regions, where significant amounts of surface wave energy can be dissipated through wave breaking and bottom friction processes. Coral reefs provide a wide and varied habitat that supports some of the most diverse assemblages of living organisms found anywhere on Earth (Darwin, 1842). It has been well known over decades that reefs represent islands of enormous productivity because they are efficient at trapping nutrients, zooplankton, and possibly phytoplankton from the surrounding waters.

Coral reefs exist under a wide range of physical environments. Flow on reefs can be driven by waves, tides, wind, and buoyancy. The dominant driving mechanism varies among different reefs and is a combination of geomorphologic, meteorological and oceanographic forcing condition at a specific site. Although winds, tides and buoyancy forcing could individually dominate the hydrodynamic characteristics of some reefs at certain times, wave action is being increasingly recognized as a significant agent in determining the reef-flat environment, island formation as well as many aspects of reef area ecology. To date, this has been the primary focus of nearshore hydrodynamic studies.

There are sound ecological, environmental, geomorphic as well as engineering implications for research on wave dynamics over coral reefs. For example, the wave-induced setup can drive mean currents and build up a circulation in a lagoon, which are crucial to the production, dispersal as well as retention of larval fish, corals and other invertebrates (Hench et al., 2008). Meanwhile, flow-mediated mass transfer may also facilitate reef zonation and segregation, and prevent coral bleaching, this highlights the primary connection between reef health and hydrodynamic processes (Monismith, 2007). Moreover, water movement associated with waves is essential for sediment transport in the reef area, which ultimately

contributes to reef organism distribution, geomorphic development of reef systems and island shoreline stability (Kench and Brander, 2006). Additionally, coral reefs and reef-top islands are becoming increasingly significant to coastal engineering works in tropical region, where waves propagate over the reef crest and water turbulence associated with wave breaking imposes forces on the various types of structures, such as tourist facilities and infrastructure on coral cays, maritime activities in reef waters as well as the locations for navigation aids and weather stations (Gourlay and Colleter, 2005). Last but not the least, coral reefs shelter many tropical islands from the flood hazards associated with tsunamis, hurricanes, and high surf events (Roeber et al., 2010), an improved understanding of the physics of wave-induced inundation over reef systems is required to develop predictive models for hurricane/typhoon emergency planning purposes and to assess the hurricane/typhoon-induced erosion (Demirbilek and Nwogu, 2007).

1.2 Wave Dynamics over Coral Reefs at the Reef Scale

The hydrodynamics of coral reefs under wave effects entails a wide range of scales of fluid motions: the largest scale as regional circulation and lagoon flushing, smaller depth scale turbulent flow evoked by reef morphology, and finally the smallest scale of flow in the benthic organisms, i.e., coral colonies (Monismith, 2007). At a reef-scale of 100 to 1000 m, the interaction between the wave processes and the reef profile is of increasing interest for researchers and engineers. Several studies have examined the interaction of waves with reef structures for the purpose of engineering design. Results showed that coral reefs act much like submerged breakwaters, bars, or depth-limited coastlines which lead to dramatic transformations in wave characteristics and rapid attenuation of wave energy (Kench and Brander, 2006). It is the wave energy leaking onto coral reef flats that is of critical importance in determining the transport of sediment around reef systems and controlling the flow and exchange of oceanic water throughout reef systems, this ultimately contributes to island morphology and reef productivity.

The physical structure of coral reefs is notably different from that of normal coastal beaches. The geomorphology of a typical "barrier" (platform) reef is divided into four main regions (Fig. 1.1): (1) a sloping fore-reef; (2) a steep reef crest (a ridge or similar configuration); (3) a reef flat (reef-top) where the bottom slope is minimal, and (4) a deep open lagoon. If the lagoon is closed or there is no lagoon, i.e., the reef is backed by a coastline, it is called a "fringing" reef. Depending crucially upon the amount of light received from the sun as well as on the consumption of nutrients and larvae, coral reefs commonly grow to about mean low tide level and their mature form of a planar reef is essentially horizontal. Hence tidal modulation usually comes into play. At low tide, waves will break on the fore-reef, dissipating most energy through turbulence over a limited spatial area, thus no significant wave energy will propagate across the reef flat; at high tide, depth-limited waves are able to propagate across the reef flat, either as transformed incident waves, reformed waves, or wave bores. Meanwhile, unlike beaches, which typically have mild slopes and relatively smooth bottoms, coral reefs often form a steep transition from relatively deep to shallow water and generate a very rough bottom surface. Moreover, coral reef organisms are known to form some of the roughest surfaces in the coastal ocean, thus frictional dissipation rates can be expected to be higher than sandy or even rocky reef sites located along the continental shelf.

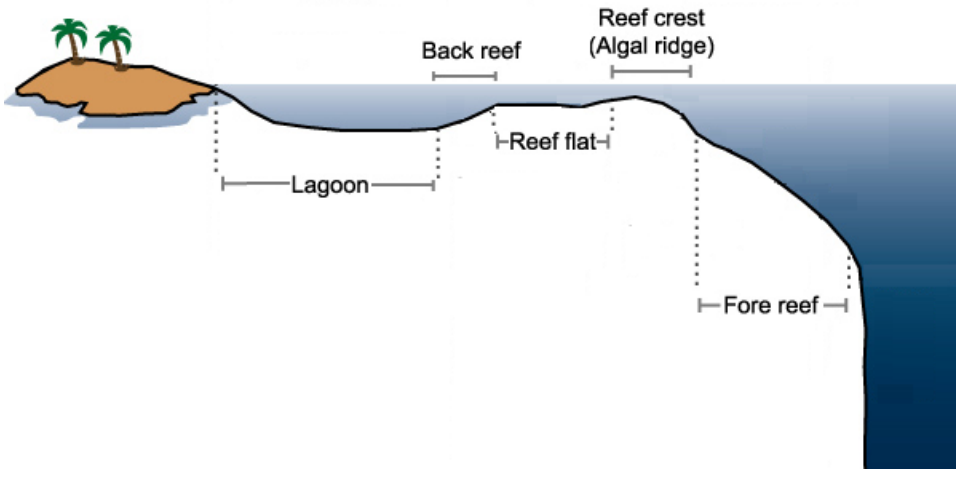

Fig. 1.1 A typical coral reef profile (adapted from http://oceanexplorer.noaa.gov /explorations/ 07twilightzone/background/plan/media/reef_diagram.html).

The precise character of wave modification and spatial extent of energy dissipation are controlled by the morphology of the reef structure (elevation, reef slope, and reef flat width) and relative water depth at the reef crest (Kench and Brander, 2006). As waves shoal and break on the fore-reef slope, the location of the initial breaker zone on the seaward edge of the reef creates a wide surf zone in which wave-induced setup and wave-driven flow are significant in determining both the mean water levels and mass transport on the reef flat. The whole process can be divided into two subjects (shown below), of which much literature is concerned with one or both. As for the energy balance, the turbulence energy dissipation on reefs arises from both the effect of cross-reef current and the loss of energy from breaking of surface gravity waves.

1.2.1 Wave transformation and breaking

A wave transformation process can involve up to five sub-processes, namely wave shoaling, wave refraction, wave diffraction, wave bed friction damping, and energy dissipation due to wave breaking (Nelson, 1996). In view of wave energy dissipation, wave attenuation is involved during the whole process. As waves propagate over the reef, they undergo several cross-shore transformations (see Fig. 1.2 for an illustration). Waves first begin to interact with the fore-reef when their wavelength becomes comparable to the local water depth. As they move further shoreward and shoal, the waves increase in height while dissipate some of their energy due to bottom friction. Eventually their heights become some critical fraction of the water depth and the waves become unstable and break. At a given cross-reef location, a maximum allowable wave height is controlled by the local water depth according to the depth-limited condition

$$H_b = \gamma h \tag{1.1}$$

where H_b is the breaker wave height and γ is a empirical breaker index ,which is smaller on the reef flat than that often used in engineering practice ($\gamma = 0.78$); h is the local still water depth. The waves may break at fore-reef slope (plunging) or on the outer reef flat (spilling), depending on local water depth and offshore wave conditions. For wave motion through surf zone, the transformation of wave

continues as they break, resulting in a moving bore. The surf zone always extends over a finite distance on the reef flat, starting from the incipient breaking point to the location where energy dissipation by wave breaking ceases, bore disappears and oscillatory waves over the reef flat reform. The reformed waves continue to propagate towards the shoreline, while dissipating some of their energy to bottom friction. Unlike beaches where the water depth approaches zero toward shore, the water depth over the reef flat is nonzero and relatively constant. Waves with height smaller than the critical breaking height determined by Eq. (1.1) are then free to pass onto the reef flat. The reef thus serves as a low-pass wave height filter by filtering out waves with heights larger than the depth-limited maximum. For spectral waves, wave breaking and accompanying energy transfer to both high and low frequency waves may cause a flattening and broadening of the wave spectrum after the waves pass over the reef flat (e.g., Hardy and Young 1996; Jago et al., 2007; Péquignet et al., 2011). Low-frequency motions may also be generated due to the so-called surf beat or reef-flat resonance (e.g., Demirbilek et al., 2007; Péquignet et al., 2009).

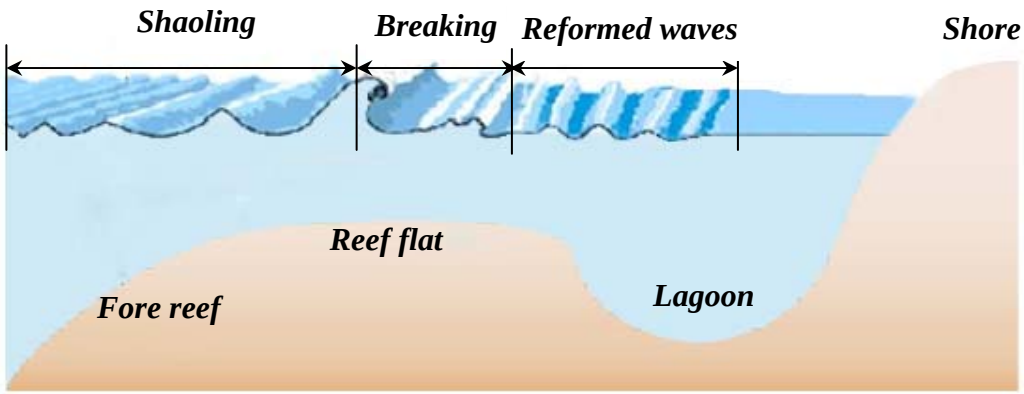

Fig. 1.2 Wave transformation over coral reef (adapted from Monismith, 2007).

1.2.2 Wave-induced setup and wave-driven flow

Wave-induced setup and wave-driven flows have probably received the most attention. Reefs often surround lagoons and low atolls and provide protection from incident waves by dissipating the wave energy through the surf zone on the seaward side of the reef. Wave-induced setup and currents due to wave breaking over the

reef could therefore have a significant impact on the circulation and flushing of the lagoon. Most researchers analyzed two-dimensional (2D) reef profiles with a seaward sloping fore-reef and a horizontal reef flat (see Fig. 1.3). The waves break on the sloping fore-reef, dissipating their energy and generating a rise of mean sea level. In regard to wave energy, this means that not all energy lost from the wave field is converted to heat and turbulence, some energy is used to maintain a sea surface slope known as wave setup. The maximum setup occurs at or near the reef edge, i.e., at the seaward side of the horizontal reef flat, because over the reef flat, where the depth is constant, there is no forcing due to wave breaking. Consequently, a cross-reef flow driven by the barotropic pressure gradient resulting from the maximum setup in the surf zone arises since the water level at the downstream side of the reef is always assumed to be the same as that seaward of the surf zone (sea level). Then the bottom friction dissipates the energy associated with the cross-reef flow, which in turn affects the wave setup and current across the reef flat and throughout the lagoon. For a reef with an open lagoon (barrier reef), the current eventually exits the lagoon via gaps or channels between the lagoon and open sea and a regional circulation always forms in analogy to the “rip current” around barred beaches or detached breakwaters. For a reef with a closed lagoon or without lagoon (fringing reef), the cross-shore wave setup on the reef flat is more or less constant thus the wave-generated flow is relatively weak. Water may also form closed gyres or eddies on the reef flat because the wave setup can vary laterally along the line of the reef crest. Water also flows laterally along the fore reef. The extent of this lateral flow is controlled by the lateral bathymetry and friction (Hearn, 2011).

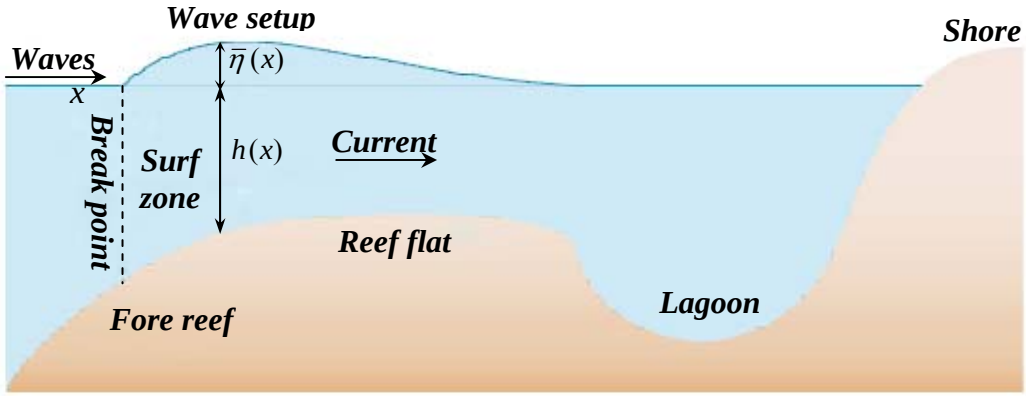

Fig. 1.3 Wave-induced setup and wave-driven flow (adapted from Monismith, 2007)

1.2.3 Theoretical background

Owing to the varied reef profiles as well as large roughness of the reef flats, coral reef hydrodynamics at reef scale presents considerable difficulties for both experimental and numerical modeling. Therefore, experimental and numerical studies on wave interaction with coral reefs are limited. However, field measurements of wave transformation and related topics (wave-induced setup and wave-driven flow) can be found in a large sum of published papers. Detailed literature reviews on the concerned topics will be given in subsequent chapters. In the following paragraphs, a theoretical illustration of coral reef hydrodynamics is introduced first, which functions as the fundamental physical laws of the present study.

The basic idea is that incident waves break on the fore-reef slope of the reef and push water onto the reef flat and then into the lagoon (if it exists) by wave setup. The theoretical explanation of this process is firstly advanced by Longuet-Higgins and Stewart (1962) who showed that spatial gradient in wave radiation stress, i.e., the depth-integrated momentum flux term associated with propagating waves, appears as a body force acting on the mean flow. The reference frame with x-axis orthogonal to the shore and y-axis parallel to the shore is considered here. The

depth-integrated wave-averaged momentum equation governing the horizontal flow can be written as (e.g., Mei et al., 2005)

$$\frac{\partial U_j}{\partial t} + U_i \frac{\partial U_j}{\partial x_i} = -g \frac{\partial \overline{\eta}}{\partial x_j} - \frac{1}{\rho(\overline{\eta} + h)} \frac{\partial S_{ij}}{\partial x_i} - \frac{\tau_j^b}{\rho(\overline{\eta} + h)} \tag{1.2}$$

where $U_i = U_i^E + U_i^s$ is the *ith* component of the Lagrangian mean velocity, written here as the sum of the depth-averaged Eulerian mean (wave-averaged) velocity (U_i^E) and depth-averaged Stokes drift velocity (U_i^s) (Monismith, 2007), $\overline{\eta}$ is the deviation of the mean water level (MWL) from still water level (SWL), h is the local still water depth, S_{ij} is the radiation stress tensor and τ_j^b is the bottom shear stress. For waves propagating in the x direction (normal to shore), Eq. (1.2) reduces to the following horizontally one-dimensional (1DH) form in steady state

$$g(h + \overline{\eta}) \frac{\partial \overline{\eta}}{\partial x} + \frac{1}{\rho} \frac{dS_{xx}}{dx} + \frac{d}{\partial x}\left(\frac{q^2}{h + \overline{\eta}} \right) + \frac{\tau_x^b}{\rho} = 0 \tag{1.3}$$

The corresponding continuity equation gives

$$\frac{\partial q}{\partial x} = 0 \tag{1.4}$$

where $q = U(h + \overline{\eta})$ is the cross-shore mean flow rate per unit width, U is the cross-shore depth-averaged mean velocity, S_{xx} is the cross-shore radiation stress and can be estimated using linear wave theory, τ_x^b is the cross-shore bottom shear stress.

In the surf zone, the decrease in wave height due to frictional dissipation is generally very slow compared with the rapid decrease due to breaking. Even for a spilling breaker that has a wider surf zone than a plunging breaker, existing literature (e.g., Thornton and Guza, 1983) has shown that the ratio of friction dissipation rate to breaking dissipation rate is very small (e.g., less than 3%). Thus comparing with wave breaking, the wave decay associated with frictional dissipation is negligible and it contributes little to the variation of S_{xx} and the wave

setup. The decay of roller indeed contributes to wave-induced setup as found in the existing literature (e.g., Apotsos et al., 2007), but this is essentially a contribution from nonlinear breaking waves (spilling breakers). As it will be discussed in section 3.4.4, this is the primary reason why using S_{xx} based on linear-shallow wave approximation in surf zones does not agree with the laboratory observations. There are some empirical models in the literature to explicitly account for this as additional contribution to the radiation stress calculated by using linear wave theory, see e.g., Svendsen (1984a).

For a barrier reef with an open lagoon, previous investigations (e.g., Lowe et al., 2009a) found that there was a net ($q > 0$) wave-induced mass transport (Mean Eulerian flow plus Stokes drift) from the reef flat to the lagoon and that the Stokes drift may contribute to the wave-induced setup as shown in Eq. (1.3). However, there is no net wave-induced mass transport in a closed flume or for a fringing reef, and the Stokes drift is not important for fringing reefs.

1.3 Objectives and Scope

1.3.1 Objectives

The objective of this study is to investigate experimentally, numerically, and theoretically the wave dynamics (wave transformation, wave-induced setup and wave-driven flow) over idealized fringing reefs. Of particular importance is to evaluate the maximum wave-induced setup on the reef flat. Both monochromatic and spectral waves are considered. Special attention is given to the cross-shore interaction between breaking waves and reef-crests (ridges).

1.3.2 Scope

The scope of experimental, numerical and theoretical investigations is listed below:

Laboratory experiments:

Two sets of laboratory experiments are conducted in a wave flume. Both experiments are concerned with 1DH reef profiles. The first set of experiments is a

direct measurement of the main aspects of breaking-wave characteristics over an idealized fringing reef model, including the breaker type and location, the breaker indices, surfzone width, wave transmission, reflection and energy dissipation. Different combinations of water depths and fore-reef slopes are examined with a series of monochromatic wave conditions. The primary focus of the second set of experiments is given to the comparison of wave-induced setup in the presence/absence of a rectangular ridge located at the reef crest subjected to both monochromatic and spectral waves. As supplements to the second set of experiments, a spatially high-resolution wave measurement is conducted with monochromatic waves, followed by flow undertow measurements at different cross-shore locations. The effects of reef-flat surface roughness on the wave transformation and setup are also investigated experimentally.

Numerical experiments:

Among the available nearshore modeling techniques and tools, a Boussinesq-type model is calibrated and validated. The numerical experiments are compared with four representative scenarios from the second set of experiments above. Special attention is given to the cross-shore variations of wave height and setup. A review of the published numerical works on similar topic is also conducted. The model is then applied to study the effects of both fore-reef slope and fore-reef shape on the cross-shore wave transformation and setup. Only 1DH wave modeling is performed; simulations on wave-induced current or in the presence of ambient current are not discussed.

Analytical models:

Data from the first set of experiments above are used to validate the applicability of available empirical formulae for other coastal profiles into the fringing reefs. Some empirical expressions for the idealized fringing reefs are also proposed. For the second set of experiments above, the performance of existing analytical models is evaluated and their limitations to reproduce the experimental data are discussed. Two analytical models are then developed in this thesis to interpret the generation of wave setup: a kinematic theory based on mass balance, and a dynamic theory

based on momentum and energy balance. While the kinematic model is only employed to account for the data in the 1DH laboratory experiments, the dynamic model is applied to both laboratory and field studies. A 2DH formulation for the dynamic model is also derived. Both models are derived with some simplifications.

1.4 Outline

This chapter has introduced several general aspects of coral reef hydrodynamics at reef scale and provides the theoretical background as well as the objectives and scope of the present study. Chapter 2 reports an experimental study on the influences of varying relative reef-flat submergence and fore-reef slopes on the properties of breaking waves over an idealized fringing reef. Chapter 3 primarily deals with laboratory experiments on the effect of a ridge structure located at a reef edge on the wave transformation, setup and flow on the reef flat. A numerical model based on the depth-integrated, fully nonlinear Boussinesq-type equations is validated in Chapter 4 to reproduce some data obtained in Chapter 3 as well as to conduct new numerical experiments. Subsequently in Chapter 5, some existing 1DH analytical models are tested against the wave setup data obtained in Chapter 3. In Chapter 6, an analytical model for wave setup is presented based on the mass balance and hydraulic theories, and validated by a series of laboratory datasets. In Chapter 7, an alternative analytical model is formulated using momentum and energy balances, and validated by the same laboratory datasets investigated in Chapter 6 as well as some field datasets. The 2DH formulation and its application to field data are also discussed. Chapter 8 summarizes the major conclusions of the present study and suggests several avenues for future work. Some original laboratory data in Chapters 2 and 3, supplemental experiments on the effects of reef-flat roughness as well as some equation derivations for numerical and analytical models can be found in the Appendices.

CHAPTER 2 BREAKING WAVE CHARACTERISTICS FOR LABORATORY FRINGING REEFS

2.1 Literature Review

As introduced in Chapter 1, wave transformation over a coral reef is similar to the wave transformation over shallow shelves. The ocean waves first shoal on the fore-reef and then break either on the fore-reef or the reef flat. The surfzone width is normally defined as the horizontal distance between the location where waves start breaking and the location where wave breaking ceases. A significant amount of wave energy can be dissipated during wave breaking. Wave breaking over coral reefs is responsible for many nearshore processes, and thus knowledge of wave breaking is an essential part of coral reef hydrodynamics. For example, the breaking-induced setup and near-shore currents have a significant impact on the circulation and flushing of lagoons, and thus the transport of organisms, nutrient, sediments (e.g., Hearn, 1999; Callaghan et al., 2006). Breaking waves may also affect mass transfer rates for flow through and over corals and biological tolerance of benthic substrates (e.g., Madin et al., 2006; Monismith, 2007). The breaking-wave force imposing on artificial reefs is a preliminary design consideration for shoreline protection (e.g., Ahrens, 1987; Shirlal et al., 2007; Carmo et al., 2011).

The hydrodynamics of wave breaking over coral reefs is controlled mainly by the morphology of the reef profiles (fore-reef slope, reef-flat bathymetry and reef-flat width) and the characteristics of the incident waves. A major difference between a submerged fringing reef and an emerged plane beach is that fringing reef usually has a reef flat where the water depth is a more or less constant. The presence of the reef flat may: (1) delay wave breaking and move the incipient breaking point shoreward (Gourlay, 1994; Demirbilek et al., 2007); (2) make the wave breaking and the resulting near-shore currents different from those for a plane beach (Gouraly and Colleter, 2005); (3) function like a semi-infinite broad weir which may impose a hydraulic control on the amount of water leaving the reef flat if the water above it is very shallow (Gourlay, 1996a). In contrast to beaches which

typically have mild slopes, coral reefs often have a steep transition from relatively deep to shallow waters. Recently, there is also an increasing interest in using artificial reefs as the breakwaters while serving other purposes (e.g., promote marine life, control erosion or improve surfing). Artificial reefs are relatively short-crested compared to natural reefs which have a typical reef-flat width of several hundreds to thousands meters.

Over the past decades, numerous theoretical, experimental and numerical studies have been done on various aspects of wave breaking process for different natural and man-made coastal structures such as beaches (planar or barrier) and low-crested structures (LCS) (e.g., the low-crested breakwater). However, the mechanics of wave breaking is still not fully understood. The majority of current knowledge about the characteristics of breaking waves (e.g., the breaker type, breaker depth index and breaker height index) has been obtained merely from experimental measurements of waves breaking on emergent, planar slopes in two-dimensional laboratory wave flumes. Representative studies are the earlier work by Iversen (1952), Galvin (1969), Goda (1970), Weggel (1972), Svendsen (1984a), Nelson (1994) and the recent work by Tsai et al. (2005), She and Canning (2007), Camnenen and Larson (2007) and Goda (2010). The empirical relationships obtained from these studies have been used in coastal engineering designs. For LCS, similar studies can be found in e.g., Johnson (2006); Van der Meer et al. (2005).

Not much research has been done on the characteristics of wave breaking over coral reefs. Smith and Kraus (1991) pioneered the study of wave breaking over reef-like submerged structures; they carried out a comprehensive laboratory study of wave interaction with submerged bars and artificial reefs with various geometries. Their results demonstrated that waves with identical deep-water characteristics broke differently on plane beaches and bars/reefs. Significant differences were found in properties such as breaker type, breaker height index, breaker depth index, plunge distance and splash distance. In particular, it was found that the transition values of the surf-similarity parameter (discussed later) used to classify the breaker types for plane slopes were invalid for barred/reef profiles. Gourlay (1994) examined the

transformation of monochromatic waves on a fringing reef with a steep seaward face and a gradually sloping reef flat. His results demonstrated that breaking conditions could be described using a nonlinearity parameter denoted in his paper by F_{co}, which contains both offshore wave and local bathymetry information: waves with identical deep-water steepness (0.048) broke in a plunging manner when $F_{co} > 150$ and in a spilling manner when $F_{co} < 100$. More recently, Blenkinsopp and Chaplin (2008) performed an experimental study of the effects of relative reef-crest submergence on wave breaking over a submerged, truncated 1/10 slope (i.e., the plane slope is truncated at a certain level below the water surface and there is no horizontal part to mimic the reef flat in their model). They found that the reef-crest submergence was a dominant factor affecting wave breaking as well as the transmission and reflection characteristics.

A sketch of the coastal profiles reviewed in this section is given in Fig. 2.1. Even though the above mentioned researchers have carried out some measurements of wave breaking over submerged reef-like structures, each of them used a specific reef profile with a single fore-reef slope during the experiments, and consequently the potential effects of fore-reef slope on breaking waves were not examined. Since it is well known that the characteristics of wave breaking on plane beaches depend crucially on the so-called surf-similarity parameter which represents the relative steepness of beach slope and wave slope, there is a need to answer the following questions: whether or not the same criteria used for plane beaches can still be used for fringing reefs; if not, what are the main differences between wave breaking on these two different conditions. The answers to these questions are important in the study of wave-induced setup over fringing reefs as wave breaking is the main driving force.

The present chapter describes a series of laboratory experiments designed to investigate the influences of both the reef-flat submergence and the fore-reef slope on the characteristics of the breaking of monochromatic waves over submerged fringing reefs. The remainder of this chapter is organized as follows: the laboratory setting, instruments and experimental procedures are introduced in section 2.2; The

direct measurements of breaking properties are described in section 2.3, and the dimensionless data analysis are performed in section 2.4, where the main aspects of breaking-wave characteristics for reefs, including the breaker type and location, the breaker indices, surfzone width, wave transmission, reflection and energy dissipation, are reported; The main results are summarized and key conclusions are drawn in section 2.5.

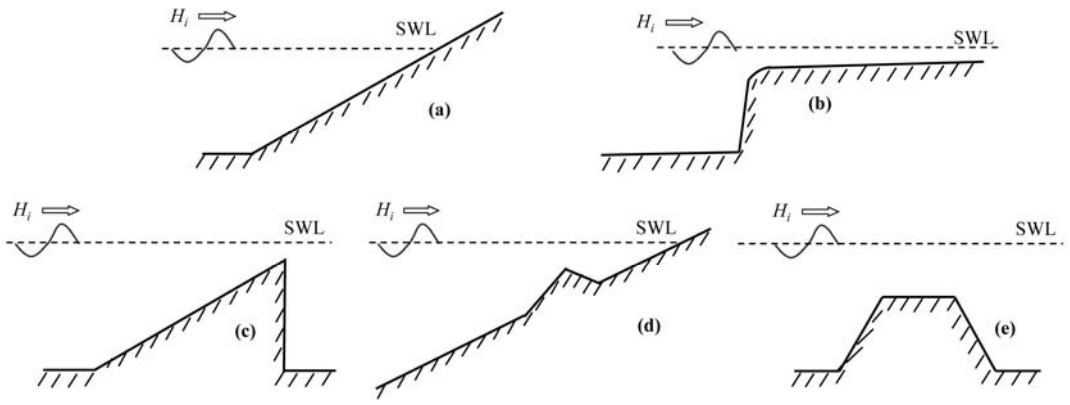

Fig. 2.1 Reviewed coastal profiles: (a) emerged plane slope (e.g., Goda, 2010); (b) submerged fringing reef (e.g., Gourlay, 1994); (c) submerged plane slope (e.g., Blenkinsopp and Chaplin, 2008); (d) submerged barred beach (e.g., Smith and Kraus, 1991); (e) submerged low-crested breakwater (e.g., Van der Meer et al., 2005); H_i - incident wave height; SWL - still water level.

2.2 Experimental Setup

2.2.1 Facilities, reef model and instrumentation

Referring to Fig. 2.2, the laboratory experiments were carried out in a glass-walled wave flume (36 m long, 0.55 m wide and 0.60 m deep) in the Hydraulics Modeling Laboratory at the Nanyang Technological University, Singapore. A servo-controlled piston type wavemaker was placed at one end of the flume to generate the designed waves. At the other end, a beach with a gentle slope of 1:8 started at approximately 32 m from the wavemaker; the slope was covered with porous mats of 10 cm thick to reduce wave reflection. Pilot tests conducted without the reef model showed that

the porous mats on the final beach could effectively dissipate the incident waves and the reflection coefficient of the beach was less than 5% for the tested regular waves, i.e., only 0.25% of the energy in the incident waves could be reflected. When the reef model is present, most energy in the incident waves has been dissipated by wave breaking and the transmitted waves propagate to the final beach is much smaller than the incident waves. As a result, the wave energy reflected from the final beach must be much smaller than 0.25% of the incident wave energy and the effects of wave reflection from the beach on wave breaking can be safely ignored.

There are a variety of reef profiles that have been studied in the literatures (see Gourlay, 1996b); the present study focuses on the one-dimensional horizontal (1DH) reef profile that has a plane sloping fore-reef and an idealized horizontal reef flat. This type of fringing reef model has been the focus of several analytical studies (e.g., Tait, 1972; Gourlay, 1996a; Symonds et al., 1995; Hearn, 1999; Gourlay and Colleter, 2005). The use of the idealized reef profile is intended to provide a reasonable first approximation of fringing reef configurations and to make reference to similar studies of wave interactions with plane beaches/submerged low-crested structures. To construct the idealized fringing-reef model, a 1:6 plane slope joins a horizontal platform at 18.35 m from the wavemaker. The horizontal platform was 6m wide and its length was the same as the inner width of the flume. Both the slope and the horizontal platform were made with PVC plates, and the entire model was firmly held at 0.35 m above the flume bottom by several stainless steel rods attaching to the two walls of the flume.

In this experimental study, the reef model was constructed in accordance with Froude similarity using a representative geometric scale factor of 1:25. Given the reef flat of 6 m in width at the laboratory scale, the corresponding reef-flat width at the prototype scale is 150 m, which is generally less than the typical natural reef flat (several hundred to thousand meters). Since the focus of these experiments is on wave breaking over fringing reefs, the effect of flat width should be small as long as the laboratory reef flat is sufficiently long for waves to complete the surfzone

process. Since the reduced off-reef water depth in the model did not affect wave transformation on the reef flat significantly (Gourlay, 1994), the water depth is designed according to the allowable water depth of the wave flume rather than the geometric scale factor.

Indeed, most natural coral reefs are composed of hard calcium carbonate skeletal material and covered by a wide variety of benthic organisms, and the coral community on the reef flat is more like a layer of porous material. In the Appendix C, results from a set of experiments are reported for a reef flat being covered with a layer of porous mat. The porous mat was used to model the surface roughness and porosity of coral community. The results showed that the effects of porosity and surface roughness were minor since both the waves and the mean currents on the reef flat were weak. The dominant physical process in this study is wave breaking, which occurs in a narrow region on either the fore-reef slope or the reef flat. Therefore, the impermeable material (PVC) was used to construct the reef models (with smooth surfaces) in this study.

To measure the cross-reef wave transformation, 8 resistance-type wave gauges (HR Wallingford Ltd.) were used and their arrangement is shown in Fig. 2.2: G1 and G2 were placed approximately 4.0 m seaward of the toe of the fore-reef slope to separate the incident waves from the reflected waves; G3 was placed on the slope to measure the shoaling waves; G5 - G7 were put in the vicinity of the reef edge to measure the waves in the surf zone; G8 was located around the middle of the reef flat to capture the reformed waves; G4 was used to validate the measurement of breaker wave height from video visualization and its location was adjusted based on a pilot run for each tested condition.

Four USB cameras (C1 - C4, Logitec Ltd.) with a resolution of 640 × 480 pixels were employed to visualize the waves in the surf zone; three of them were aligned perpendicular to the wave flume by adjusting their locations both horizontally and vertically according to the variation of water level and breaker positions (see Fig. 2.2). The field of view (FOV) of each camera was 1.0 m × 0.8 m, hence a maximum

global view size of 3.0 m × 0.8 m was achieved, which is sufficient to capture the major wave transformation processes such as shoaling, breaking, bore propagation and the reformed waves on the reef flat. The last camera was located above the flume and moved along the flume to determine the shoreward ending locations of the surf zones. Transparent grid sheets with a grid size of 1.0 cm × 1.0 cm were attached to the front glass wall as a reference scale for determination of the wave breaker height, incipient breaking location and surfzone width. The wave gauges and cameras were synchronized through a data acquisition system (DeweSoft Ltd.). The sampling rate of all wave gauges was 50Hz and the frame rate of all cameras was 25 Hz.

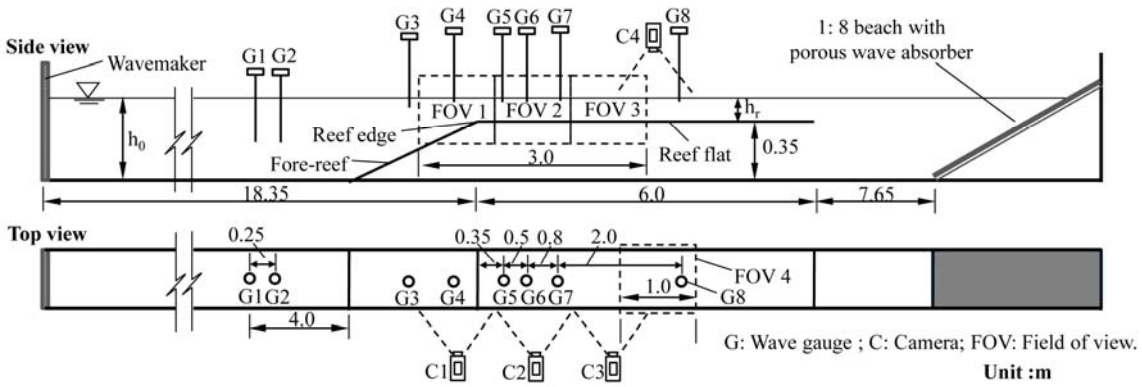

Fig. 2.2 Experimental setup.

2.2.2 Wave conditions and test program

Three wave periods (T =1.0 s, 1.25 s and 1.67 s) were examined in the experiments. For each wave period, the target incident wave height ranged from 0.01 m to 0.13 m. The target wave heights were slightly different from those measured in the experiments. The actual incident wave heights were determined by separating the incident waves from the reflected waves using the waves measured at G1 and G2. The measured incident wave heights were converted to those in deep water for subsequent analysis, see H_0 in Table 2.1.

Referring to Table 2.1, four water depths (h_0 = 38 cm, 40 cm, 42 cm and 45 cm) were examined: where the water depths were measured from the flume bottom; this

gives the following reef-flat submergences (the water depths above the reef flat): h_r = 3 cm, 5 cm, 7 cm and 10 cm, respectively. To examine the effects of fore-reef slope, in addition to the initial slope of 1/6, three other fore-reef slopes (1/3, 1/9 and 1/12) were also examined for the reef-flat submergence of 5 cm. These slopes were chosen because they fall in the representative range of the fore-reef slopes (see e.g., Gourlay, 1996b for a review of different reef profiles in the literature). Based on Froude similarity, for a geometric scale factor of 1:25, the period scale factor is 1:5, thus the equivalent prototype values of the parameters in Table 2.1 are 0.8 m - 2.5 m for h_r, 0.25 m - 3.50 m for H_0 and 5.0 s - 8.4 s for T, which are in agreement with the typical values observed in field conditions (Bonneton et al., 2007; Hench et al., 2008; Lowe et al., 2009a; Vetter et al., 2010).

Waves of large steepness broke before reaching the toe of the fore-reef slope and thus have been excluded from the dataset reported in this study. Waves that were small and passed over the reef flat without breaking were not analyzed. They are categorized as "non-breaking waves" in section 2.4.1. The remaining 230 wave conditions have deep-water wave steepness ranging from 0.003 to 0.088 and relative reef-flat submergence (the ratio of the water depth above the horizontal reef flat to the deep-water wave height) ranging from 0.32 to 3.53.

Table 2.1 Test conditions at laboratory scale

Type	Range
Reef-crest submergence: h_r (m)	0.03, 0.05,0.07, 0.10
Deep-water monochromic wave height: H_0 (m)	0.01-0.14
Monochromic wave period : T (s)	1.0,1.25,1.67
Fore-reef slope: $s = \tan\theta$	1/3,1/6,1/9,1/12

In the experiments, surface elevations were collected for 300 s, starting immediately after the start of the wavemaker. From the pilot tests, it was found that waves in the

flume can reach a relatively steady state about 150 s after starting the wavemaker. Thus only the last 100 wave cycles in the wave records were used to calculate the wave characteristics (i.e., transmitted wave height, wave-induced setup). The cameras were triggered at 250 s after starting the wavemaker and the recording duration was 15 s for all four cameras to ensure that at least ten waves could be extracted from the recorded videos. Between two subsequent tests, several minutes were allowed to elapse so that the water surface could become calm and the effects of residual currents were minimal.

2.3 Results

2.3.1 Qualitative description of breaking waves

The incipient breaking point, the surfzone endpoint, the breaker wave height (H_b) and the breaker water depth (h_b), were determined by analyzing the video images for each test run. The incipient breaking point for plunging breaker is defined as the point where a large portion of the front face of a wave becomes nearly vertical (see Fig. 2.3(a)). This definition is consistent with the majority of the studies of breaking-waves (Iversen, 1952; She et al., 1994; Blenkinsopp and Chaplin, 2008; etc.). For a spilling breaker, the incipient breaking point is defined as the point where the whitewater begins to roll down the front face of a wave. The breaker height is defined as the vertical distance between the wave crest at the incipient breaking point and the trough immediately in front of the incipient breaking point within one wave length. The breaker depth is defined as the vertical distance between the still water level (SWL) and seabed at the incipient breaking point. The total surfzone width (L_s) is defined as the horizontal distance between the incipient breaking point and the endpoint of wave breaking (propagating bores disappear and organized waves reform). It is stressed here that the identification of the endpoint of wave breaking takes some experience.

Wave breaking is a highly nonlinear process, which can be sensitive to variations in bottom geometry, incident wave characteristics, and the presence of current and

reflected waves. In principle, all measured mean quantities should be obtained by averaging an infinite long wave record. However, there is a limitation of the RAM size used to store the high-resolution (1 M per image at a frame rate of 25 Hz) video data from the four cameras, and a finite number of waves are used in practice. The minimum number of waves required to obtain stable mean values was tested using the waves measured at the gauge G4 for a representative wave condition ($h_0 = 0.40\ m$, $H_0 = 0.074\ m$, $T = 1.25\ s$ and $s = 1.6$); the results are listed in Table 2.2. It shows that there is no significant change in both the mean value and the standard derivation when the total number of waves used in the analysis is larger than 10, thus, to minimize the random errors in the measured values of H_b, h_b and L_s determined from the video images, these quantities are averaged over at least 10 waves for each test run.

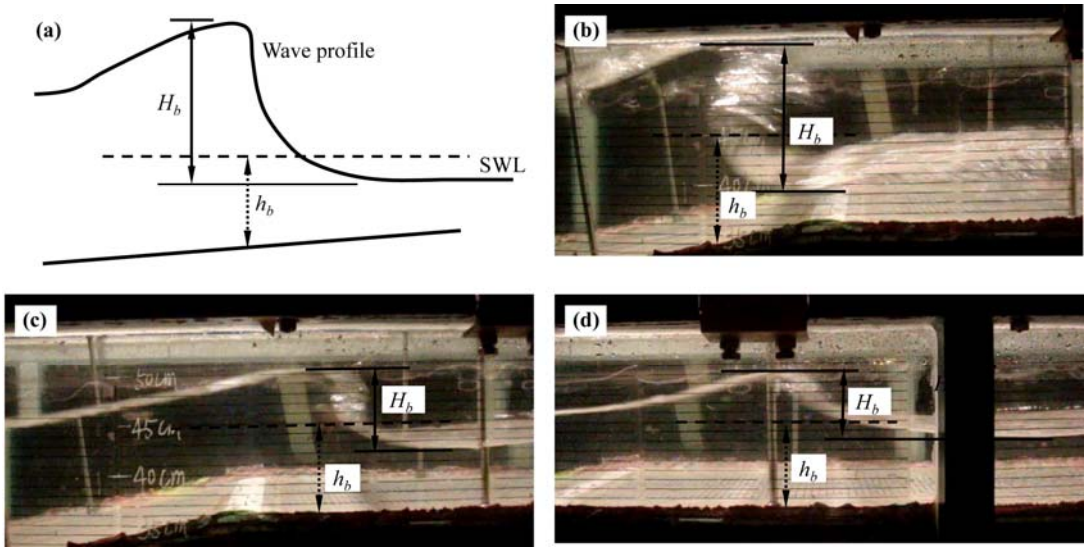

Fig. 2.3 Definitions of breaking wave characteristics and snapshots of different breaker types: (a) definitions; (b) plunging breaker on the fore-reef; (c) plunging breaker on the reef edge; (d) spilling breaker on the reef flat.

Table 2.2 Mean value and standard derivation (std) of breaker wave height (H_b) obtained from N successive waves measured by G4 for a representative wave condition ($h_0 = 0.40\,m$, $H_0 = 0.074\,m$, $T = 1.25\,s$ and $s = 1/6$)

N=10		N=20		N=30		N=40	
mean	std	mean	std	mean	std	mean	std
0.096	0.004	0.094	0.005	0.095	0.005	0.096	0.005

Table 2.3 Measured breaker wave height (H_b^G and H_b^I), breaker depth (h_b) and surfzone width (L_s) of 10 successive waves for a representative wave condition ($h_0 = 0.40\,m$, $H_0 = 0.074\,m$, $T = 1.25\,s$ and $s = 1/6$)

Item[a]	1	2	3	4	5	6	7	8	9	10	Mean	Std
H_b^G (m)	0.094	0.102	0.099	0.087	0.094	0.098	0.099	0.095	0.097	0.096	**0.096**	**0.004**
H_b^I (m)	0.100	0.098	0.105	0.090	0.094	0.108	0.103	0.098	0.105	0.097	**0.100**	**0.006**
h_b (m)	0.090	0.087	0.085	0.084	0.086	0.087	0.089	0.086	0.088	0.086	**0.087**	**0.002**
L_s (m)	1.93	1.95	2.00	1.90	1.97	2.00	1.99	1.97	1.93	1.98	**1.96**	**0.03**

[a] H_b^G is measured at the location of G4, H_b^I, h_b and L_s are determined from the recorded video images.

To validate the breaker wave heights determined from the video images, analysis of the recorded breaking waves was also tried using the wave gauge G4, which was moved to the breaking location determined from the pilot run done for each test condition. The discrepancy between the values of H_b determined by these two approaches is within ±5% for all test runs. For example, Table 2.3 shows the measured breaker wave heights from G4 (H_b^G) as well as from the recorded image (H_b^I) of 10 successive waves for the above representative wave condition. It can be seen that $(H_b^G - H_b^I)/H_b^I = 0.04$ and the standard deviations for both

measurements are small. Table 2.3 also listed the measured H_b, h_b and L_s obtained from 10 successive waves, and their standard deviations are also very small, expect for those of L_s due possibly to the difficulty in judging the endpoint of a surf zone. Therefore, in the following analysis, the values of H_b, h_b and L_s determined from the video images are used since the surface elevation recorded by wave gauge might be affected by the air bubbles entrained in water due to wave breaking.

To test the repeatability of the experiments, the above case was run for three times. Table 2.4 lists the measured breaker wave heights from the video images for 10 successive waves. The discrepancy in the mean values between any two runs in Table 2.4 is within 7% and the standard derivation for each run is also small. Other measured quantities such as h_b and L_s have similar degree of uncertainty (not shown). The possible sources of error in the repeatability tests may come mainly from the wavemaker and reading error.

Therefore, based on the above error analysis, the estimated error for each measured quantity in this study is believed to be less than 10%.

Table 2.4 Measured breaker wave heights of 10 successive waves in three different runs for a representative wave condition ($h_0 = 0.40\,m$, $H_0 = 0.074\,m$, $T = 1.25\,s$ and $s = 1/6$)

Item	1	2	3	4	5	6	7	8	9	10	Mean	Std
Run 1	0.100	0.098	0.105	0.090	0.094	0.108	0.103	0.098	0.105	0.097	**0. 100**	**0.006**
Run 2	0.090	0.093	0.098	0.097	0.100	0.098	0.095	0.094	0.098	0.095	**0.096**	**0.003**
Run 3	0.100	0.098	0.105	0.090	0.094	0.108	0.103	0.098	0.105	0.097	**0.102**	**0.003**

There are several ways to classify the breaker types for plane beaches, and it is generally accepted that waves break in one of the following four forms: spilling,

plunging, collapsing, and surging (Galvin, 1968). However, for the present fringing reef profile with relatively steep fore-reef slopes, it is found that plunging breaker always occurred on the fore-reef for larger waves. As the incident waves became smaller, the breaking point would shift to a location above the reef flat and the plunging breakers could evolve into spilling breakers. As the incident wave height was further reduced, wave breaking would cease and the incident waves could freely pass over the reef flat. Therefore, the breakers in this study are either plunging breakers or spilling breakers, and wave breaking can occur either on the fore-reef or above the reef flat. Illustrations of the breaker types and the breaking locations, as well as the determination of H_b and h_b are shown in Fig. 2.3 (b) - (d).

2.3.2 Determination of wave transmission and reflection coefficients

Wave transmission and reflection characteristics for submerged structures such as low-crested breakwaters are usually quantified by the transmission coefficient, K_t and the reflection coefficient, K_r, which are defined by

$$K_t = H_t / H_i, \quad K_r = H_r / H_i \tag{2.1}$$

where H_i, H_r, H_t, are the incident, reflected and transmitted wave heights, respectively. Strictly speaking, the above definitions are for linear monochromatic waves. According to the conservation of wave energy, an energy loss coefficient, defined as the ratio of wave energy lost through dissipation to the total incident wave energy, can be calculated by

$$K_d = 1 - K_t^2 - K_r^2 \tag{2.2}$$

The wavemaker used in the experiments does not have the active wave absorption function. Therefore, of the incident waves generated in the flume will inevitably be contaminated by the multiple re-reflected waves between the models (both from fore-reef and from final beach) and the wavemaker paddle, leading to a situation where stable partial standing waves may be formed after running the wavemaker for several minutes. The reflection coefficient seaward of fore-reef could be calculated

by making use of this partial standing-wave pattern. In this study, the two-point wave separation method proposed by Goda (2000) is adopted, in which the wave pattern in the flume is treated as the superposition of the right-going incident waves and the left-going reflected waves. The Fourier coefficients (which can be determined by either data fitting or FFT) of the harmonics from the two wave records (i.e., using the wave records at G1 and G2) are needed to calculate H_i and H_r. Those coefficients includes the contributions from both the incident waves and the multiple reflective waves, thus this method inherently considers the effect of multiple reflections. A maximum 10% error was reported for this method (see Goda, 2000).

Note that the energy associated with higher harmonic waves is not considered in Eq. (2.2). However, for highly nonlinear transmitted waves on the reef flat, the contribution from higher harmonic waves should be considered when calculating the energy loss coefficient. In this study, the group velocity is different in front of the fore-reef from that on the reef flat; the conservation of wave power gives the following definition of the transmission coefficient

$$K_t = \sqrt{\frac{E_t c_t^g}{E_i c_i^g}} \tag{2.3}$$

where c_i^g and c_t^g are wave group velocities in the waters in front of the fore-reef and on reef flat, respectively. The incident wave energy flux ($E_i c_i^g$) can be evaluated by the deep-water wave energy flux ($E_0 c_0^g$) based on energy conservation. Using the linear wave approximation, the deep-water energy density is $E_0 = \rho g H_0^2 / 8$, where H_0 is the deep-water wave height converted from the incident wave height (H_i), and the deep-water group velocity is $c_0^g = gT / 4\pi$. However, for the transmitted wave energy, E_t, a detailed analysis of wave records at G8 is required. Fig. 2.4 is an example of the transmitted waves for the case of $h_0 = 0.40\ m$, $H_0 = 0.074\ m$, $T = 1.25\ s$ and fore-reef slope = 1/6. Fig. 2.4(a) shows that there are observable secondary peaks in the wave profiles. For this case, the

ratio of the maximum wave-induced setup on the reef-flat ($\overline{\eta}_r$) to the reef-flat submergence (h_r) is $1/5$, indicating that $\overline{\eta}_r$ should be considered when computing c_t^g for transmitted waves. The generation of both higher and low frequency components are shown in Fig. 2.4(b), where up to the 5th harmonics can be identified. Fig. 2.4(c) demonstrates that the energy contained in the second harmonic is on the same order of magnitude as that in the fundamental harmonic waves. Therefore, E_r is calculated by integrating the energy spectrum obtained at G8 in this study. c_t^g is estimated with $\sqrt{g(h_r+\overline{\eta}_r)}$ by invoking shallow water approximation on the reef flat in view that kh_r ranges from 0.21 to 0.68 for the present data.

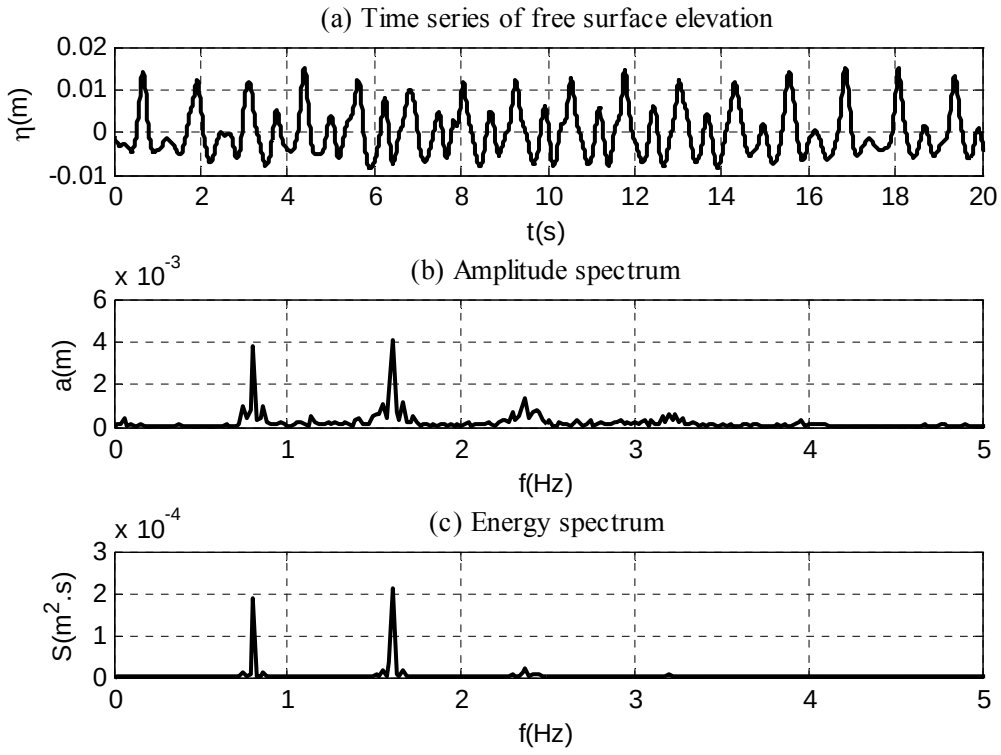

Fig. 2.4 Wave analysis for transmitted waves (from G8) on the reef flat ($h_0 = 0.40\,m$, $H_0 = 0.074\,m$, $T = 1.25\,s$ and $s = 1/6$)

2.3.3 Measured breaking-wave properties

In this section, the following measured properties are discussed: breaker type, breaker location, breaker height (H_b), breaker depth (h_b), total surfzone width (L_s), the wave-induced setup ($\overline{\eta}_r$), transmission coefficient (K_t) and reflection coefficient (K_r). The original data are given in Appendix A.

Firstly, the measured properties for the dataset with a constant fore-reef slope of 1/6 are plotted in Fig. 2.5 as a function of deep-water wave height (H_0). Also shown in the figure are the effects of wave period (T) (indicated by different marker colors) and reef-flat submergence (h_r) (indicated by different marker types).

Figs. 2.5(a) and 2.5(b) show that for both breaker type and breaking location, the trends agree well with the observations described in section 2.3.1. For example, plunging breakers appear more frequently under larger H_0. As for breaking location, breaking on the reef flat is most likely to occur under smaller H_0. However, as shown in Fig. 2.5(b), H_0 alone is not a proper parameter to describe the breaking location due to the overlap of different breaking locations within a wide range of H_0. The effects of wave period on both breaker type and breaking location are not obvious in Figs. 2.5(a) and 2.5(b). Fig. 2.5(c) shows a monotonic increase of H_b with the increase of H_0, and H_b has a weak dependence on T. The effect of h_r is not visible in Fig. 2.5(c). Fig. 2.5(d) shows that h_b has a strong correlation with H_0 and weak correlation with T, but for smaller H_0, h_b becomes almost constant and is only related to h_r due to the waves breaking on the horizontal reef flat. For L_s shown in Fig. 2.5(e), strong dependence on both H_0 and T can be identified, and the dependence on h_r seems to be insignificant. $\overline{\eta}_r$ in Fig 2.5(f) increases with the increase of H_0 but decreases with the increase of h_r, and vice versa for K_t shown in Fig. 2.5(g). The influence of T is negligible for both $\overline{\eta}_r$ and K_t. Lastly, as shown in Fig. 2.5(h), there is no dependence of K_r on H_0, T or h_r.

The measured properties for the dataset with the constant reef-flat submergence of 0.05 m are plotted in Fig. 2.6 as a function of deep-water wave height (H_0). Also shown in the figure are the effects of wave period (T) (indicated by different marker colors) and fore-reef slope (s) (indicated by different marker types).

Without the effect of reef-flat submergence, it can be observed in Fig. 2.6 that overall, the breaker type, breaking location, H_b, h_b, L_s, $\overline{\eta}_r$ and K_t can be described by H_0 alone, except that some scatter due to the effects of T. Again, as shown in Fig. 2.6(e), there is noticeable dependence of L_s on T. The reflection coefficient is also insensitive to either H_0 or T as shown in Fig. 2.6(h). After carefully examining all plots in Fig. 2.6, it is found that the dependence of each measured property on fore-reef slope is found to be weak for this dataset.

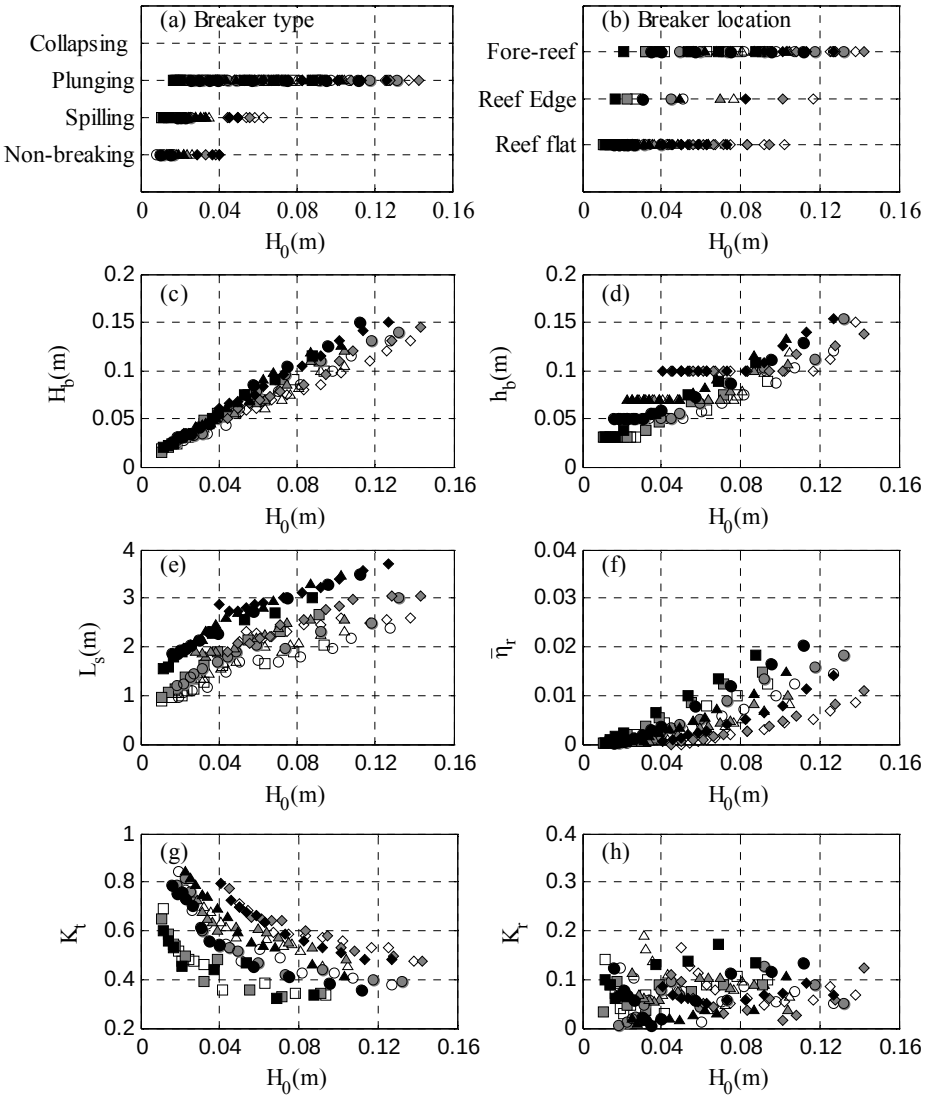

Fig. 2.5 Measured quantities as a function of deep-water wave height (H_0) with fore-reef slope of $s = 1/6$ at different wave periods (T) and reef-flat submergences (h_r): (a) Breaker type; (b) Breaking location; (c) Breaker height (H_b); (d) Breaker depth (h_b); (e) Total surfzone width (L_s); (f) Wave-induced setup ($\bar{\eta}_r$); (g): Transmission coefficient (K_t); (h) Reflection coefficients (K_r). Solid black markers: $T = 1.0\,s$; Solid grey markers: $T = 1.25\,s$; Open markers: $T = 1.67\,s$. Squares: $h_r = 0.03\,m$; Circles: $h_r = 0.05\,m$; Triangles: $h_r = 0.07\,m$; Diamonds: $h_r = 0.10\,m$.

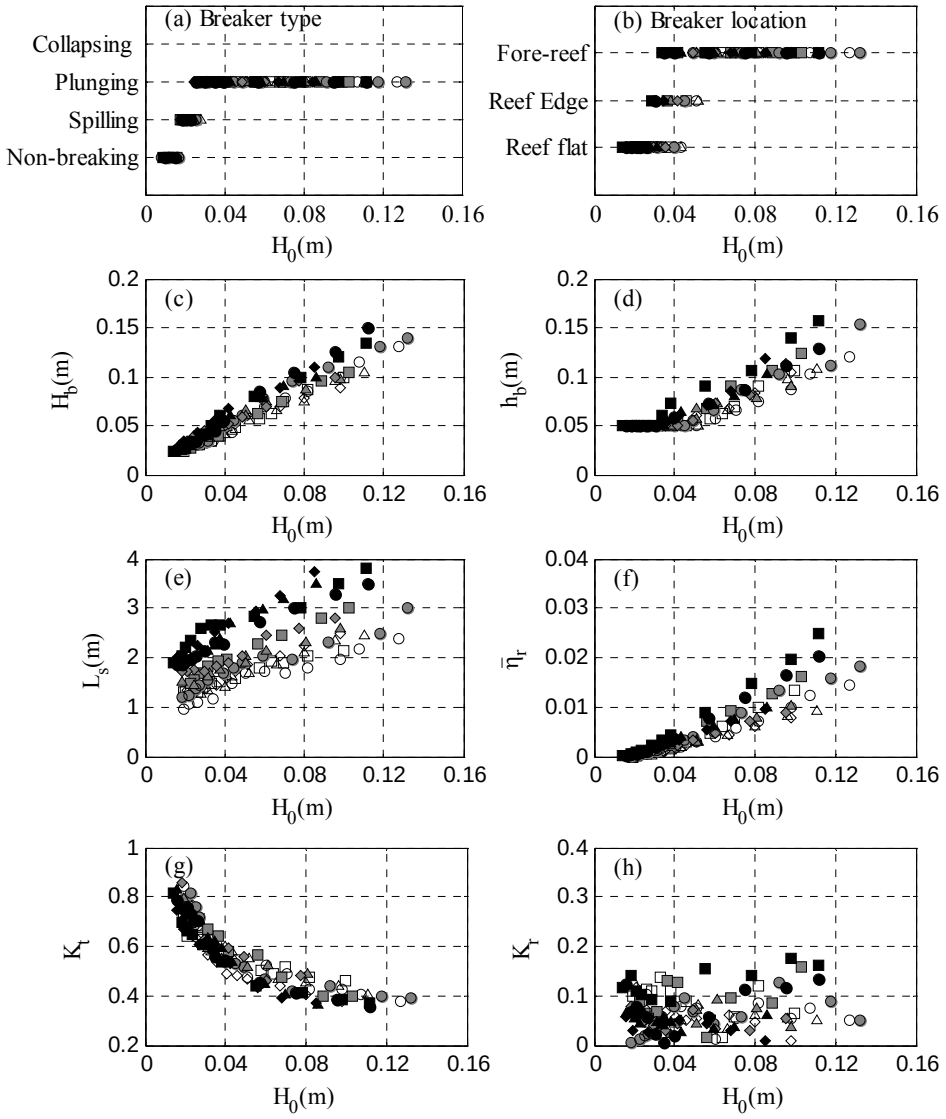

Fig. 2.6 Measured quantities as a function of deep-water wave height (H_0) with reef-flat submergence of $h_r = 0.05\,m$ at different wave periods (T) and fore-reef slopes (s): (a) Breaker type; (b) Breaking location; (c) Breaker height (H_b); (d) Breaker depth (h_b); (e) Total surfzone width (L_s); (f) Wave-induced setup ($\overline{\eta}_r$); (g): Transmission coefficient (K_t); (h) Reflection coefficients (K_r). Solid black markers: $T = 1.0\,s$; Solid grey markers: $T = 1.25\,s$; Open markers: $T = 1.67\,s$. Squares: $s = 1/3$; Circles: $s = 1/6$; Triangles: $s = 1/9$; Diamonds: $s = 1/12$.

A more systematic data analysis will be reported in the following section, where dimensionless parameters are introduced and discussed. The wave-induced setup is

not the focus of this chapter and is used only to estimate the reef-flat mean water level as discussed in section 2.3.2.

2.4 Data Analysis and Discussion

The analysis in section 2.3 has shown that the properties of breaking waves depend primarily on deep-water wave height as well as reef-flat submergence, secondarily on wave period, and least on fore-reef slope. The results in section 2.3 are dimensional and not conclusive due to the multiple dependences. In this section, the two aforementioned datasets are combined and a dimensionless analysis is conducted.

Grouping for the above variables in analogy to those commonly used to characterize breaking waves over beaches and submerged breakwaters yields the following three dimensionless parameters: the deep-water wave steepness, H_0 / L_0 (where $L_0 = gT^2 / 2\pi$, g is the gravity acceleration), the relative reef-flat submergence, h_r / H_0, and the fore-reef slope, s (where $s = \tan\theta$, θ is the fore-reef slope angle). The reef-flat roughness and porosity might not be important if most of wave energy is lost through wave breaking in the surf zone adjacent to the reef edge.

2.4.1 Classification of measured breaking waves

Breaker type

Battjes (1974) used the following surf-similarity parameter

$$\xi_0 = \frac{s}{\sqrt{H_0 / L_o}} \tag{2.4}$$

to describe breaker types for uniform plane slopes. This surf-similarity parameter represents the relative steepness of the incident waves and the seabed slope. Battjes (1974) determined the following transitional values of the surf-similarity parameter based on the experiments of Galvin (1968)

$$\text{Surging or Collapsing if } \xi_0 > 3.3 \tag{2.5a}$$

$$\text{Plunging if } \ 0.5 \le \xi_0 \le 3.3 \tag{2.5b}$$

$$\text{Spilling if } \ \xi_0 < 0.5 \tag{2.5c}$$

Firstly, the breaker type observed in the present experiments are plotted in Fig. 2.7(a) against ξ_0, where the transitions values for plane beaches, i.e., Eq. (2.5) are also shown. It can be observed that most of the plunging-type breakers for the present fringing reef fall correctly in the plunging region as specified by Eq. (2.5). However, spilling breakers for the fringing reef have values of ξ_0 larger than that for the plane slope and no clear transition values of ξ_0 can be identified between plunging and spilling breakers or between spilling breaker and non-breaking waves. Therefore, the surf-similarity parameter is not an appropriate parameter to classify the wave breakers for fringing reefs.

The breaker types classified by the relative reef-flat submergence (h_r / H_0) is given in Fig. 2.7(b), which shows that the influence of the relative reef-crest submergence is dominant. This is somewhat expected: when waves break in most of experiments, they break on the horizontal reef flat, thus, it should be the water depth above the reef flat rather than the fore-reef that controls wave breaking. From these experiments, the transition values estimated for the present fringing reef profile are

$$\text{Plunging if} \quad h_r / H_0 < 1.8 \tag{2.6a}$$

$$\text{Spilling if} \quad 1.8 < h_r / H_0 < 2.7 \tag{2.6b}$$

$$\text{Non-breaking if} \quad h_r / H_0 > 2.7 \tag{2.6c}$$

The overlap around transition values might be due primarily to the subjectivity in determining the breaker types. The above transition values are consistent with those found by Gourlay (1994), although his reef model was not the same as the present. The reason that the breaking conditions for fringing reefs are different from those for plane beaches might be due to the strong seaward return flows over the reef edge during the backwash phase (Smith and Kraus, 1991; Blenkinsopp and Chaplin, 2008).

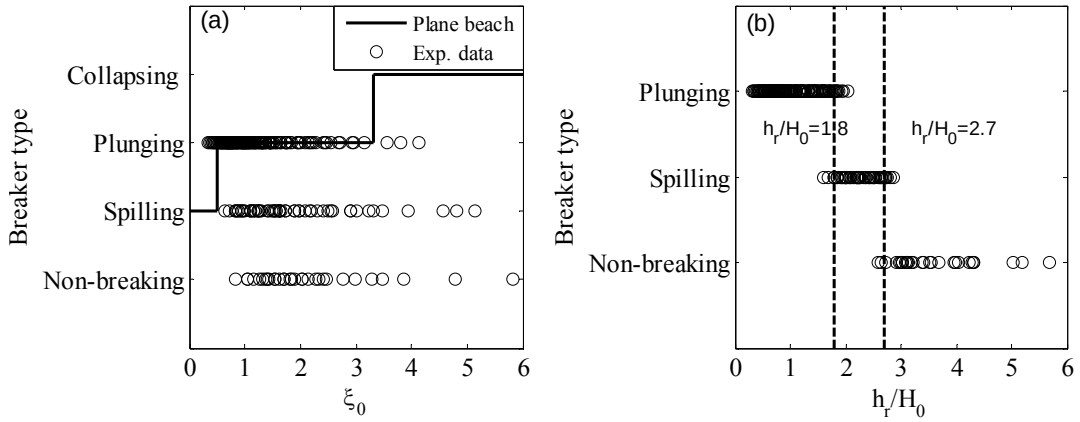

Fig. 2.7 Breaker type as a function of: (a) surf-similarity parameter (ξ_0); (b) relative reef-flat submergence (h_r / H_0).

Breaking location

The observed breaking locations against h_r / H_0 are plotted in Fig. 2.8(a), where a new category "reef-edge breaking" is proposed, since waves in this category can be considered as breaking either on the reef flat or on the fore-reef. The substantial overlap between the "reef-flat breaking" and the "fore-reef breaking" in Fig. 2.8(a) suggests that the reef-flat submergence (h_r) when scaled by the deep-water wave height (H_0), is not an appropriate parameter for classifying breaking locations. Re-scaling h_r using the local breaker wave height (H_b) is then considered. Fig. 2.8(b) shows the breaking locations as a function of the modified relative reef-flat submergences (h_r / H_b); it can be seen that the overlap is significantly reduced. The transition values of h_r / H_b for breaking location can be estimated by

$$\text{Breaking on fore-reef if } \frac{h_r}{H_b} < 1.0 \tag{2.7a}$$

$$\text{Breaking on reef flat if } \frac{h_r}{H_b} \geq 1.0 \tag{2.7b}$$

Again, the remaining overlap in the figure may come mainly from the difficulty in measuring H_b and determining the exact location of a breaker event.

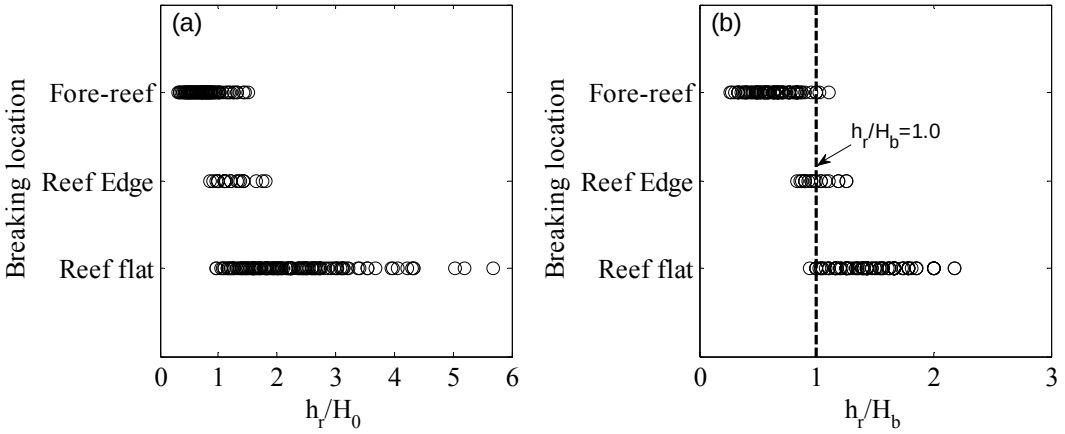

Fig. 2.8 Breaking location as a function of: (a) relative reef-flat submergence (h_r / H_0); (b) modified relative reef-flat submergence (h_r / H_b).

Relating the breaking locations to the breaker wave height (H_b) is reasonable since H_b is directly related to the surfzone dynamics. For example, instead of Eq. (2.4), breaker types for plane beaches are also commonly classified using a surf-similarity parameter (ξ_b) defined by the breaker wave height (H_b)

$$\xi_b = \frac{s}{\sqrt{H_b / L_o}}. \tag{2.8}$$

However, using H_0 to define the surf-similarity parameter is easier to use in practice since the breaker wave height is difficult to measure. There are well-documented empirical equations to transform H_b into H_0 for plane slopes. Since there is no such equation available for the reef profile, this topic will be addressed in the next section.

It is remarked here that the parameter $F_{co} = g^{1.25} H_0^{0.5} T^{2.5} / h_r^{1.75}$ as suggested by Gourlay (1994) for characterization of the breaker types and locations was also

examined; but this parameter does not seem to work for the present experimental setting which involved a variety of wave steepness and fore-reef slopes.

2.4.2. Breaker indices

The breaker wave height and breaker water depth are of considerable interest for coastal engineers, oceanographers and sedimentologists. The breaker water depth is usually required to compute the breaker wave height, and vice versa. Existing methods use the breaker height index and/or the breaker depth index to calculate them. Numerous empirical expressions for wave breaker indices have been proposed in the literature for plane beaches and other coastal profiles; however, only a few of them relevant to the present study will be discussed below. This section will investigate the key parameters used to describe the breaker indices for fringing reefs and the suitability of applying empirical expressions for plane slopes and other coastal profiles (the barred beach or submerged slope) to fringing reefs.

Breaker height index

The breaker height index, Ω, is normally defined as

$$\Omega = \frac{H_b}{H_0} \tag{2.9}$$

Previous studies on plane beaches show that the breaker height index is dependent on both the deep-water wave steepness and the seabed slope（e.g., Komar and Gaughan, 1973; Sakai and Battjes, 1980; Sunamura, 1980), and this index follows a power law of the form

$$\Omega = m(s)\left(\frac{H_0}{L_0}\right)^{-n(s)} \tag{2.10}$$

where the empirical coefficients $m(s)$ and $n(s)$ are determined by fitting to laboratory or field data. For example, the formula proposed by Komar and Gaughan (1973) for plane beaches, as recommended by the Coastal Engineering Manual (USACE 2003), uses $m = 0.56$ and $n = 0.2$. Smith and Kraus (1991) suggested that $m(s) = 0.28 + 2.17s - 6.00s^2$ and $n(s) = 0.36 - 1.59s + 4.85s^2$ for their submerged

bar profile under $0.07 < H_0 / L_0 < 0.92$ and $1/50 < s < 1/10$. For the submerged, truncated slope, Blenkinsopp and Chaplin (2008) suggested that $m = 0.5$ and $n = 0.2$ for $0.008 < H_0 / L_0 < 0.068$. The breaker height indices for the fringing reef models are shown in Fig. 2.9 as a function of deep-water wave steepness; also shown in Fig. 2.9 are the four empirical expressions discussed above. The present experimental data show that Smith and Kraus (1991)'s model is not very sensitive to the fore-reef slope when $s < 1/5$, thus only $s = 1/6$ is plotted in Fig. 2.9 for comparison.

The present data show that the breaker height index (Ω) increases with decreasing deep-water wave steepness (H_0 / L_0). This feature is typical of waves breaking on a plane slope due to the shoaling effect experienced by longer waves before breaking. Data for different fore-reef slopes show similar trends (see Table 2.5 for the fitting parameters corresponds to different fore-reef slopes, their slope dependences are not obvious), implying that the effect of the fore-reef slope on Ω is insignificant. A least-square fitting of all present data to the power law gives

$$\Omega = 0.64 \left(\frac{H_0}{L_0} \right)^{-0.16} \tag{2.11}$$

with $R^2 = 0.72$. Comparisons among the curves in Fig. 2.9 indicate that the values of $m = 0.56$ and $n = 0.2$ suggested by the USACE 2003 for plane beaches are generally sufficient to estimate H_b for these coastal profiles. For completeness, relating Ω to h_r / H_0 is also tried and results are shown in Fig. 2.10. It is found that a weak linear dependence of Ω on relative reef-flat submergence might be identified (with certain degree of scatter) due to the strong linear dependence of H_b on H_0 (shown in section 2.3.3).

Table 2.5 Values of m and n obtained by least-square fitting using Eq. (2.10); the uncertainties for m and n are 95% confidence interval

s	m	n
1/3	0.64±0.11	-0.15±0.04
1/6	0.69±0.04	-0.15±0.01
1/9	0.55±0.09	-0.19±0.04
1/12	0.50±0.06	-0.23±0.03

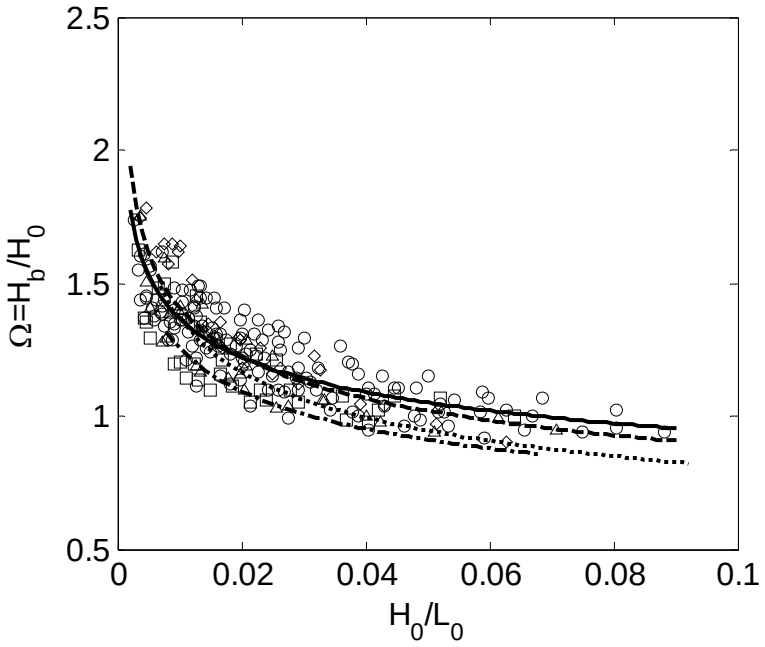

Fig. 2.9 Breaker height index (Ω) as a function of deep-water wave steepness (H_0 / L_0). Squares: Exp., s=1/3; Circles: Exp., s=1/6; Triangles: Exp., s=1/9; Diamonds: Exp., s=1/12. Dashed line: Pred. by Komar and Gaughan (1973); Dotted line: Pred. by Smith and Kraus (1991) with s=1/6; Dash-dot line: Pred. by Blenkinsopp and Chaplin (2008); Solid line: Least-square fitting of Exp. data with power law.

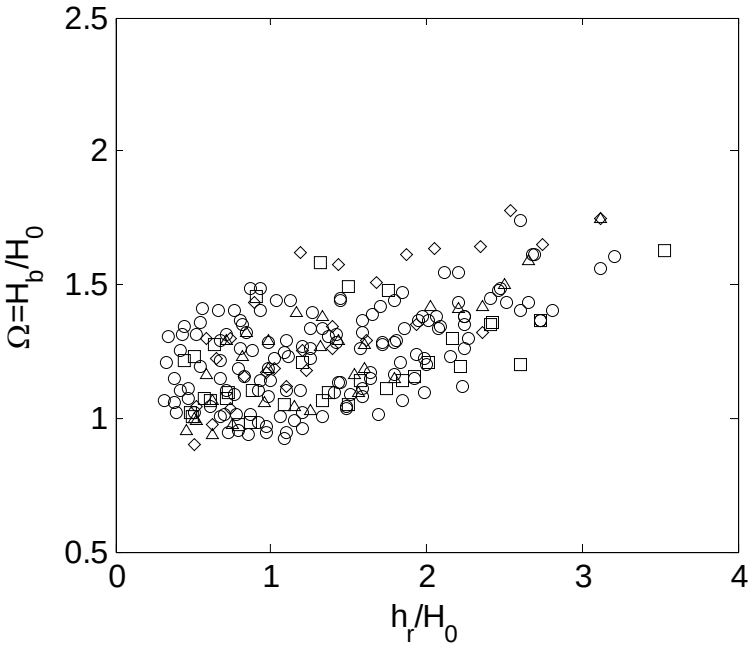

Fig. 2.10 Breaker height index (Ω) as a function of relative reef-flat submergence (h_r / H_0). Squares: Exp., s=1/3; Circles: Exp., s=1/6; Triangles: Exp., s=1/9; Diamonds: Exp., s=1/12.

Breaker depth index

For shallow water waves, the breaker depth index, γ is usually defined as

$$\gamma = \frac{H_b}{h_b} \tag{2.12}$$

which says that the breaker wave height is controlled by the local water depth alone. This breaker water depth has been widely used in the studies of coral reef hydrodynamics (see Lowe et al., 2005; 2009a and Vetter et al., 2010 for field observations; Gourlay, 1994 and Carmo et al., 2011 for laboratory experiments; and Trait, 1972, Hearn, 1999 and Low et al., 2009 for analytical or numerical modeling). Thus, it is worth analyzing the present data using the existing empirical expressions for breaker water depth.

Comparison with the emerged plane slopes

Based on a theoretical analysis, Miche (1944) first proposed a theoretical breaking limit for deep-water waves as $(H_0 / L_0)_b = 0.142$. Quite a few empirical breaking criteria have also been proposed for shallow water waves in the literature. For waves in water of constant depth, McCowan (1894) suggested from his experiments a constant $\gamma = H_b / h = 0.78$, which is still widely used in engineering practice. For waves propagating on sloping sea beds, the dependence of γ on the seabed slope and the incident wave characteristics were recognized. Subsequent formulae for a plane beach of slope s generally fall into three categories: (1) $\gamma = f(s)$, such as Collins (1970), Nelson (1987); (2) $\gamma = f(H_b / L_0 \text{ or } H_b / L_b)$, such as Weggel (1972), Komar (1998); (3) $\gamma = f(s, h_b / L_0 \text{ or } h_b / L_b)$, such as Svendsen (1987), Goda (2010). Most marine designs adopted Eqs. (2.13) or (2.14), which were originally proposed by Weggel (1972) and Goda (1974) (see also USACE, 2003; Goda, 2010). Weggel's expressions read

$$\gamma = \frac{H_b}{h_b} = b - a\frac{H_b}{gT^2} \qquad H_0 / L_0 \le 0.06, s \le 0.1 \tag{2.13}$$

where $a = 43.8(1 - e^{-19s})$ and $b = 15.6/(1 + e^{-19.5s})$. Goda's formula is given by

$$\gamma = \frac{H_b}{h_b} = \frac{A}{h_b / L_0}\left\{1 - \exp\left[-1.5\pi\frac{h_b}{L_0}(1 + 11s^{4/3})\right]\right\} \tag{2.14}$$

where A is a fitting parameter and $A = 0.17$ was suggested for plane slopes. Eq. (2.14) can yield better predictions for mild slopes than for steep slopes (Goda, 2010). Both Wiggle's and Goda's formulae indicate that the value of γ decreases as the seabed slope decreases.

Figs. 2.11 and 2.12 provide the breaker depth indices of the present data as a function of H_b / gT^2 and h_b / L_0, respectively, for different fore-reef slopes and breaking locations (indicated by different subplots). Predictions from Eqs. (2.13) and (2.14) are also shown in the two figures for comparison.

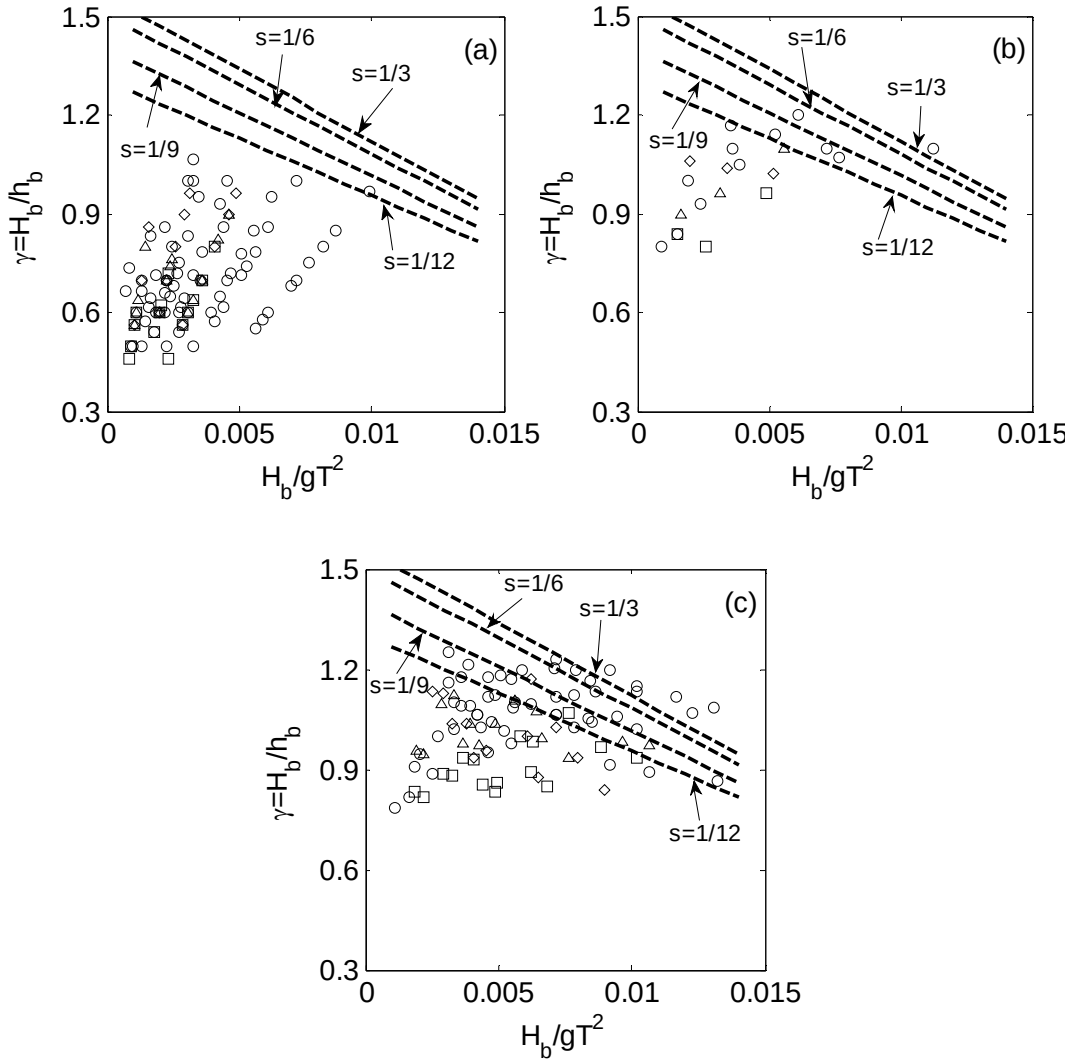

Fig. 2.11 Breaker depth index (γ) as a function of H_b / gT^2. (a): Wave breaking on the reef flat; (b): Wave breaking on the reef edge; (c): Wave breaking on the fore-reef. Squares: Exp., s=1/3; Circles: Exp., s=1/6; Triangles: Exp., s=1/9; Diamonds: Exp., s=1/12. Dashed lines: Pred. by Weggel (1972).

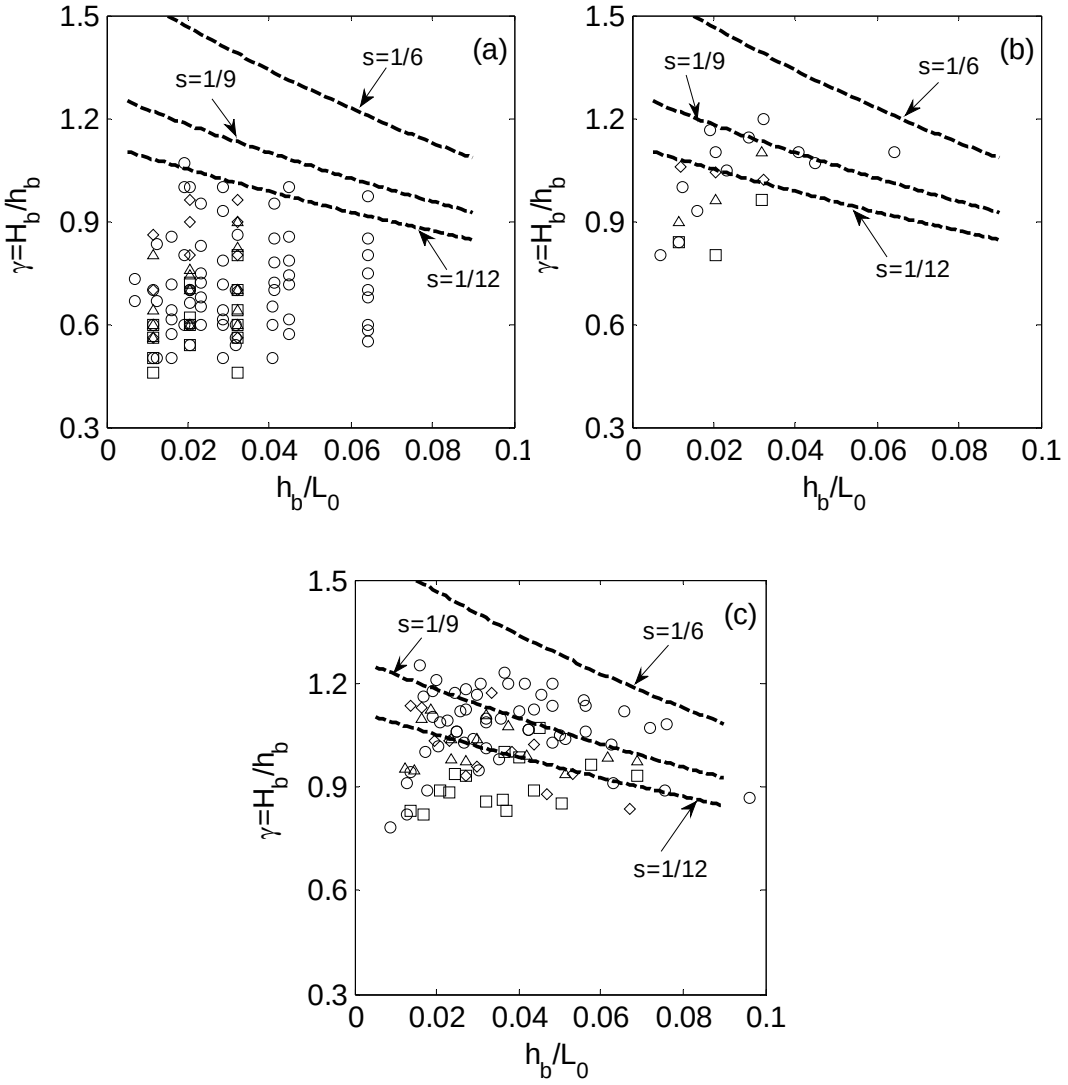

Fig. 2.12 Breaker depth index (γ) as a function of h_b / L_0. (a): Wave breaking on the reef flat; (b): Wave breaking on the reef edge; (c): Wave breaking on the fore-reef. Squares: Exp., s=1/3; Circles: Exp., s=1/6; Triangles: Exp., s=1/9; Diamonds: Exp., s=1/12. Dashed lines: Pred. by Goda (2010).

The source of scatter in both Figs. 2.11 and 2.12 is substantial, and the dependence of γ on H_b / gT^2 or h_b / L_0 is weak, implying that neither of these two parameters are appropriate to describe γ for the present problem. Meanwhile, both Wiggle's and Goda's formulae over-predict γ for the majority of present data, for which wave breaking was found mostly on the reef flat. For waves breaking on the fore-

reef slopes, the predictions are in a reasonable agreement with the present data; slight over-prediction is believed to be attributed partly to the unsuitability of Eqs. (2.13) and (2.14) for steep slopes since they were originally proposed for mild slopes ($s < 1/10$). Physically, wave breaking on a fore-reef is very similar to wave breaking on a plane beach, thus there is always a better agreement between the experiments and predictions when waves break on fore-reefs.

Comparison with submerged profiles

Smith and Kraus (1991) found a linear relationship between γ and the surf-similarity parameter for waves breaking over a bar profile

$$\gamma = \frac{H_b}{h_b} = 0.41 + 0.98\xi_0 \qquad 0.3 \le \xi_0 \le 0.85 \tag{2.15}$$

or in terms of H_0 / L_0 as

$$\gamma = \frac{H_b}{h_b} = 0.41 + 0.98\frac{s}{\sqrt{H_0 / L_0}} \qquad \frac{1.4}{s} \le H_0 / L_0 \le \frac{11.1}{s} \tag{2.16}$$

Note that the maximum value of γ never exceeds 0.55 for a horizontal bottom (Nelson, 1994). Gourlay (1994) proposed the following empirical relation for steep fringing reefs

$$\gamma = \frac{H_b}{h_b} = 0.55 + 0.87\frac{s}{\sqrt{H_0 / L_0}} \qquad \frac{1.4}{s} \le H_0 / L_0 \le \frac{11.1}{s} \tag{2.17}$$

More recent work on submerged slopes (Blenkinsopp and Chaplin, 2008) found

$$\gamma = \frac{H_b}{h_b} = 0.85 \qquad 0.008 \le H_0 / L_0 \le 0.068, 0.76 \le h_r / H_o \le 2.0 \tag{2.18}$$

The breaker depth indices of the present data are plotted in Fig. 2.13 as a function of the deep-water wave steepness for different fore-reef slopes and breaking locations (indicated by different subplots). The predictions based on Eqs. (2.16) - (2.18) are also shown for comparison.

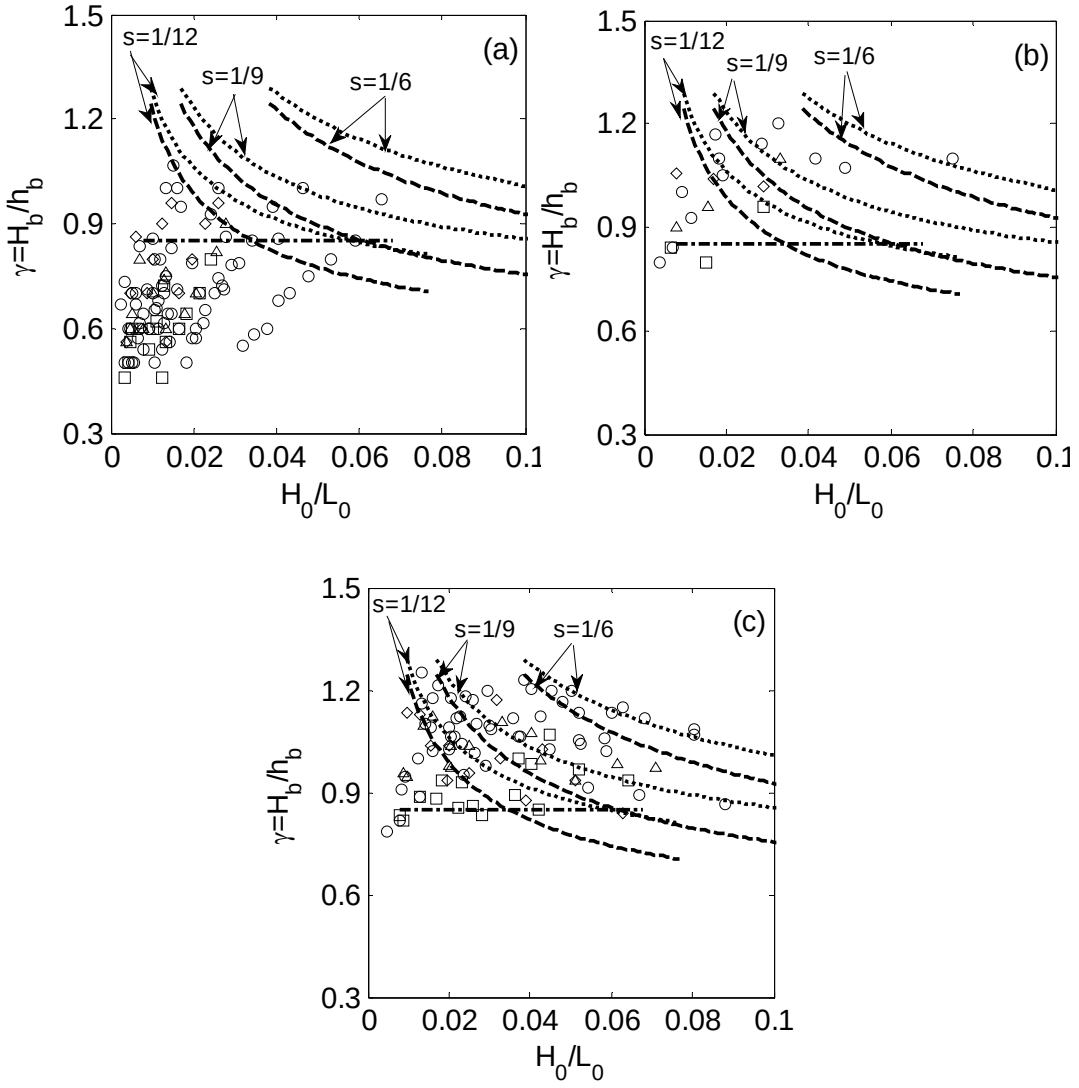

Fig. 2.13 Breaker depth index (γ) as a function of deep-water wave steepness (H_0 / L_0). (a): Wave breaking on the reef flat; (b): Wave breaking on the reef edge; (c): Wave breaking on the fore-reef. Squares: Exp., s=1/3; Circles: Exp., s=1/6; Triangles: Exp., s=1/9; Diamonds: Exp., s=1/12. Dashed lines: Pred. by Smith and Kraus (1991); Dotted lines: Pred. by Gourlay (1994); Dash-dot line: Pred. by Blenkinsopp and Chaplin (2008).

It can be seen from Fig. 2.13 that there is no noticeable dependence of γ on H_0 / L_0 or reef-flat slope for the present data. However, the present data compare favorably with the trend of Blenkinsopp and Chaplin (2008), although the scatter is still considerable. This may be due to their slope (1/10), which falls in the slope range of

the present dataset. Both Eqs. (2.16) and (2.17) reveal a trend of γ decreasing with increasing H_0 / L_0. The overall agreements with the present data are similar to those for plane beaches discussed above: the empirical equations only give reasonable results for the waves with larger γ, i.e., those that break on the fore-reef. For waves with smaller steepness (waves that break on the reef flat), again both equations overestimate the values of γ.

Johnson (2006) conducted a series of laboratory experiments on submerged breakwaters and found that the freeboard (in analogy to the reef-flat submergence for the present fringing reef) controls the depth-limited wave breaking on the breakwaters. The empirical expression proposed by Johnson (2006) is

$$\gamma = \frac{H_b}{h_b} = \begin{cases} 1.55 & h_r / H_0 \le 0.50 \\ 1.91 - 0.72 \dfrac{h_r}{H_o} & 0.50 < h_r / H_0 < 1.50 \\ 0.8 & h_r / H_0 \ge 1.50 \end{cases} \tag{2.19}$$

Breaker depth indices for the present data are plotted in Fig. 2.14 as a function of relative reef-flat submergence under different fore-reef slopes and breaking locations. Also shown in Fig. 2.14 are the predictions of Johnson (2006) and Blenkinsopp and Chaplin (2008).

Although there is scatter at smaller relative submergence, a linear trend similar to that of Eq. (2.19) can be observed: γ is approximately constant for both small and large h_r / H_o and a sloping transition exists in between. Least-square fitting of the present data to linear functions yields

$$\gamma = \frac{H_b}{h_b} = \begin{cases} 1.04 \pm 0.02 & h_r / H_0 \le 0.95 \\ (1.42 \pm 0.07) - (0.39 \pm 0.05) \dfrac{h_r}{H_o} & 0.5 < h_r / H_0 < 2.15 \\ 0.58 \pm 0.02 & h_r / H_0 \ge 2.15 \end{cases} \tag{2.20}$$

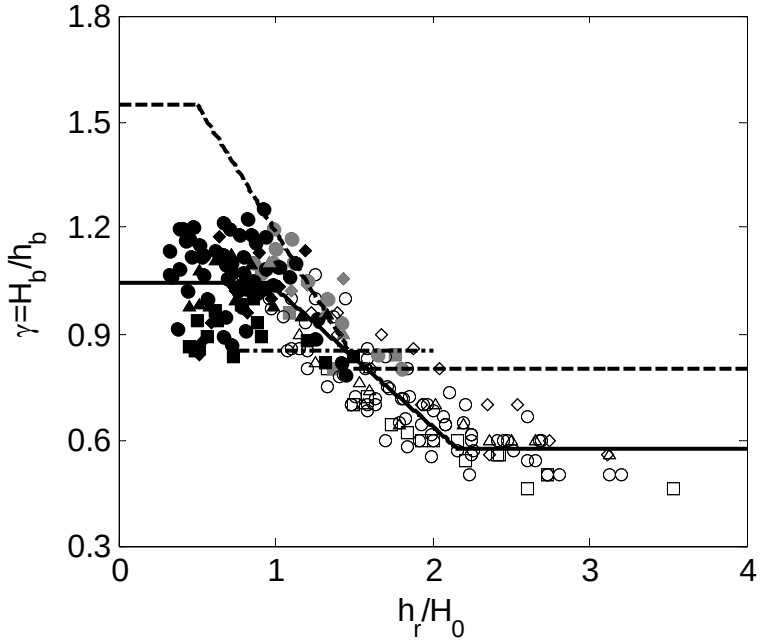

Fig. 2.14 Breaker depth index (γ) as a function of relative reef-flat submergence (h_r / H_0). Squares: Exp., s=1/3; Circles: Exp., s=1/6; Triangles: Exp., s=1/9; Diamonds: Exp., s=1/12. Dashed lines: Pred. by Johnson (2006); Dash-dot line: Pred. by Blenkinsopp and Chaplin (2008); Solid lines: Least-square fitting of Exp. data with linear relationship. Solid black markers: Wave breaking on the fore-reef; Solid grey markers: Wave breaking on the reef edge; Open markers: Wave breaking on the reef flat.

A closer examination of the present data reveals that when $h_r / H_0 \le 0.95$, waves broke on the fore-reef, and when $h_r / H_o \ge 2.15$, waves broke on the reef flat. This is consistent with the observation for plane beaches that γ is slope-dependent and decreases with the decrease of seabed slope. The scatter in present data for those fore-reef breaking cases (small h_r / H_o) may be due to the dependence of γ on H_b / L_0 or H_0 / L_0 as shown in Figs. 2.11 or 2.12, which is not included in the present data regression analysis. However, this trend is not apparent within the present slope range. The lower limit of γ (0.58) is close to the value of 0.55 as found by Nelson (1994) for horizontal bottom. Johnson's results show a consistent higher γ than the present results, which is possibly because of the very steep

seaside slope (1/2) of his breakwater model. The data of Blenkinsopp and Chaplin (2008) appear to be insensitive to h_r / H_o; this may be caused by the narrow range of h_r / H_o (0.76 - 2.0) conducted in his experiments.

2.4.3 Surfzone width

The spatial and temporal scales of the surf zone over coral reefs have received considerable attention in field investigations (e.g., Madin et al., 2006). For plane beaches, the surf zone is traditionally defined as the region extending from the seaward boundary of wave breaking to the limit of wave uprush. In this section, the surfzone width of breaking waves over fringing reefs is investigated, the width is measured from the incipient breaking point to the point where waves cease to break on the horizontal reef flat. The information of surfzone width is valuable to calibrate empirical energy dissipation models in numeral simulations. For example, the eddy-viscosity model as proposed by Kennndy et al. (2000).

Following Gourlay (1994), the measured surfzone width, L_s is scaled by the shallow water wave length ($T\sqrt{g(h_r+\overline{\eta}_r)}$). The relative surfzone width, $W_s = L_s / T\sqrt{g(h_r+\overline{\eta}_r)}$ as a function of deep-water wave steepness is shown in Fig. 2.15 for different fore-reef slopes. It can be observed that W_s is generally within the range of $1.3 < W_s < 3.3$ for the present data. The lower threshold of H_0 / L_0 for waves to break is the critical condition under which waves are small enough to pass through the reef flat without breaking. An approximate parabolic relationship between W_s and H_0 / L_0 can be observed in Fig. 2.15. Also no definite dependence of W_s on fore-reef slopes can be found.

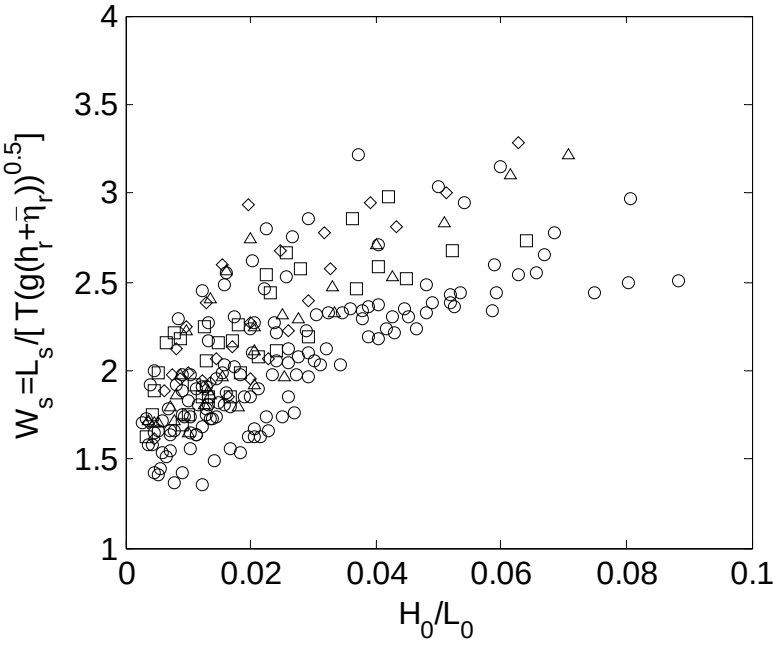

Fig. 2.15 Relative surfzone width (W_s) as a function of deep-water wave steepness (H_0 / L_0). Squares: Exp., s=1/3; Circles: Exp., s=1/6; Triangles: Exp., s=1/9; Diamonds: Exp., s=1/12.

Fig. 2.16 shows W_s as a function of the inverse of the relative reef-flat submergence, h_r / H_o. A least-square fitting of the present data yields

$$W_s = (1.41 \pm 0.05) + (0.84 \pm 0.04)\left(\frac{h_r}{H_o}\right)^{-1} \tag{2.21}$$

Also shown in Fig. 2.16 is the linear relationship proposed by Gourlay (1994), which reads

$$W_s = 2.0 + 1.1\left(\frac{h_r}{H_o}\right)^{-1} \tag{2.22}$$

Eqs. (2.21) and (2.22) reveal that W_s can be described solely by the relative reef-flat submergence. Again, there is no consistent correlation of W_s with fore-reef slope. The surfzone widths for the present idealized fringing reefs are generally smaller than those predicted by Eq. (2.22), obtained from a fringing reef with a sloping reef

flat. This is expected since Eq. (2.22) was developed by Gourlay (1994) for the upper limit of surfzone width. The lower threshold of relative submergence for non-breaking waves indicates $H_0 / h_r = 0.38$, which generally agrees with the value of $H_0 / h_r = 0.40$ as found by Gourlay (1994).

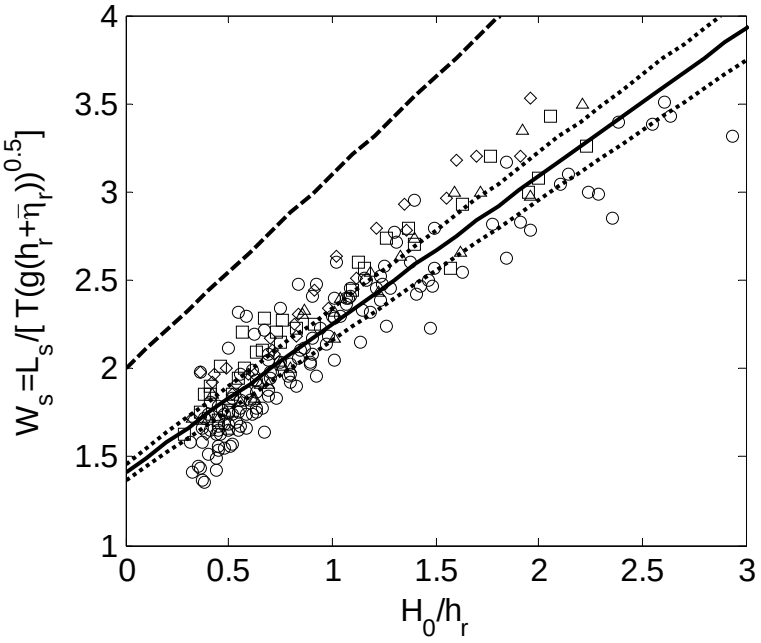

Fig. 2.16 Relative surfzone width (W_s) as a function of the inverse of relative reef-flat submergence (H_0 / h_r). Squares: Exp., s=1/3; Circles: Exp., s=1/6; Triangles: Exp., s=1/9; Diamonds: Exp., s=1/12. Dashed line: Pred. by Gourlay (1994); Solid line: Least-square fitting of Exp. data with linear relationship. Dotted lines represent the 95% confidence limits of the best fitting line.

2.4.4 Wave transmission, reflection and energy dissipation

When waves interact with fringing reefs, a large portion of the energy will be dissipated by wave breaking and bottom friction; the remaining wave energy will be either reflected from the fore-reef or transmitted towards shore in the form of reformed waves. The ability of a submerged fringing reef to protect the coasts by dissipating wave energy has been long recognized in previous research. The knowledge of wave transmission and reflection provides a way to estimate the

amount of wave energy dissipated by wave breaking and bottom friction. Energy dissipation in the surf zone is essential for computing wave-induced setup and currents as well as the wave forces imposed on the back-reef beaches; it can also be applied to calibrate surfzone numerical models.

Transmission coefficient

Wave transmission characteristics of both submerged and emergent rubble-mound breakwaters have been studied by many researchers over decades (e.g., Seelig, 1980; Van der Meer and Daemen, 1994; Van der Meer et al., 2005). In general, the transmission coefficient is a function of the structure's geometry (crest height and width), front slope angle, surface roughness and porosity as well as wave parameters (incident wave height, incident wave period, angle of wave attack). For low-crested structures (LCS), there is a wealth of empirical formulae in the literature for design purposes. Van der Meer and Angremond (1991) suggested that K_t varies linearly with the relative crest submergence. Recently, Van der Meer et al. (2005) also considered the effects of crest width and the incident waves.

Van der Meer et al. (2005)'s formula for LCS reads

$$K_t = \begin{cases} -0.4\dfrac{F}{H_i} + 0.64\left(\dfrac{B_c}{H_i}\right)^{-0.31}(1-e^{-0.5\xi_i}) & \dfrac{B_c}{H_0} < 10 \\ -0.35\dfrac{F}{H_i} + 0.51\left(\dfrac{B_c}{H_i}\right)^{-0.65}(1-e^{-0.41\xi_i}) & \dfrac{B_c}{H_0} > 10 \end{cases} \tag{2.23}$$

where F is the structure crest freeboard and should be negative when the crest is submerged, B_c is the crest width, H_i is the incident wave height at the toe of the structure, ξ_i is the surf-similarity parameter defined as $\xi_i = s/\sqrt{H_i / L_o}$,where s is the slope of the structure's front face.

When the above equation is applied to the present fringing reefs, the long horizontal reef flat is taken as the crest in analogy to the breakwater by setting $B_c / H_i = +\infty$.

Consequently, the reef-flat submergence, h_r (which is always positive in this study) is used for F , and Eq. (2.23) is reduced to

$$K_t = 0.35\frac{h_r}{H_0} \tag{2.24}$$

where H_0 is used instead of H_i , the difference is due to the shoaling coefficient which is approximately 1 for all the tested cases (K_t ranges from 0.91 to 0.95 for present data).

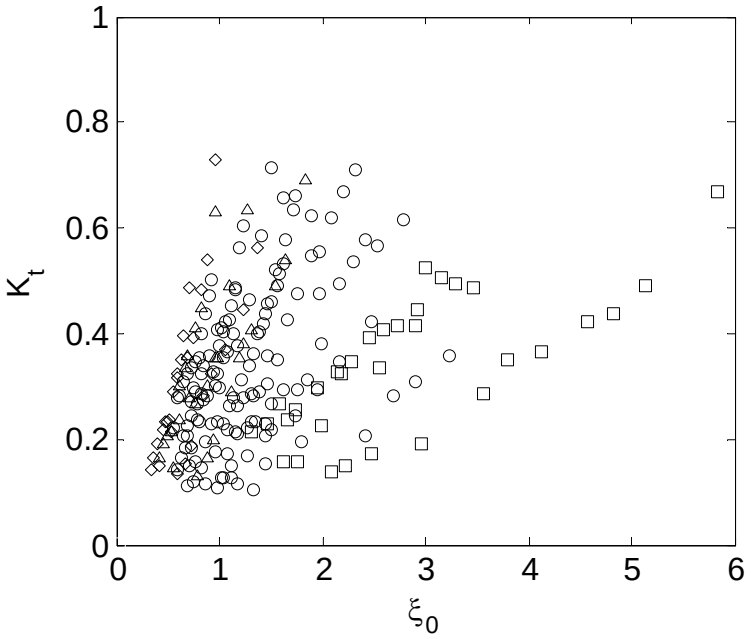

Fig. 2.17 Transmission coefficient (K_t) as a function of surf-similarity parameter (ξ_0). Squares: Exp., s=1/3; Circles: Exp., s=1/6; Triangles: Exp., s=1/9; Diamonds: Exp., s=1/12.

The effect of ξ_i or ξ_0 on K_t has been eliminated from the above equation due to the very large relative reef-crest width. However, the original equation, i.e., Eq. (2.23), indicates that K_t depends on ξ_i . To verify this, K_t against ξ_0 is plotted in Fig. 2.17. It appears that for a given fore-reef slope, K_t increases with increasing ξ_0 . However, K_t is slope-dependent and rises more rapidly under the

mild slope, suggesting that ξ_0 is not a suitable parameter to combine the effects of both fore-reef slope and incident waves on K_t for fringing reefs (it has shown in section 2.3.3 that K_t itself is almost slope-independent).

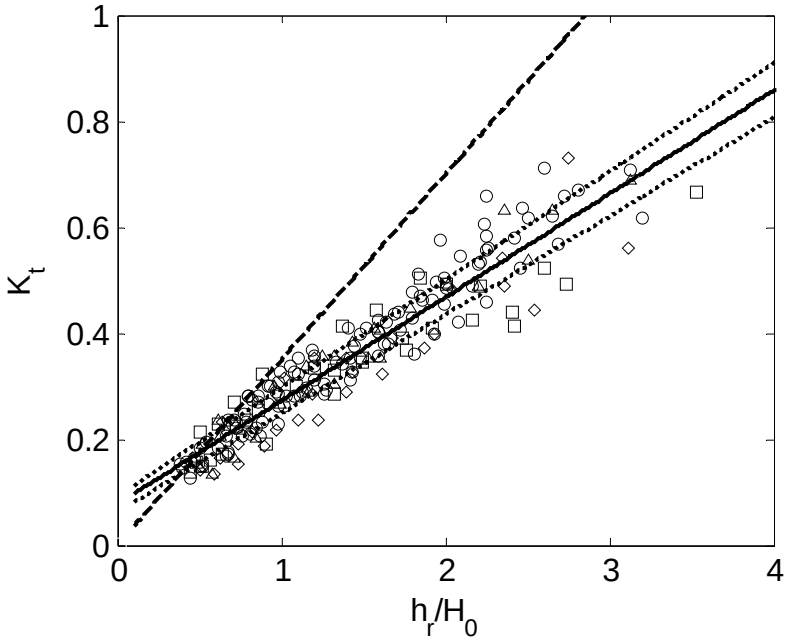

Fig. 2.18 Transmission coefficient (K_t) as a function of relative reef-flat submergence (h_r / H_0). Squares: Exp., s=1/3; Circles: Exp., s=1/6; Triangles: Exp., s=1/9; Diamonds: Exp., s=1/12. Dashed line: Pred. by Van der Meer et al. (2005); Solid line: Least-square fitting of Exp. data with linear relationship; Dotted lines represent the 95% confidence limits of the best fitting line.

Subsequently, the transmission coefficients are plotted as a function of the relative reef-flat submergence for different fore-reef slopes in Fig. 2.18, along with Eq. (2.24). It can be observed that K_t increases almost uniformly with increasing h_r / H_0, regardless of the fore-reef slopes. This is quite expected in that larger submergence means larger transmitted waves in view of the depth-limited breaking condition (see Eq. (2.12)). The values of K_t collapse approximately onto a straight

line except for certain scatter at very large h_r / H_0. A least-square fitting of the present data to a linear function gives

$$K_t = (0.08 \pm 0.01) + (0.20 \pm 0.01)\frac{h_r}{H_0} \tag{2.25}$$

The values of K_t for the present data are predominantly lower than those for submerged structures as given by Eq. (2.24), particularly for the cases with lager h_r / H_0, suggesting that Eq. (2.24) is not applicable to the seabed profiles (e.g., submerged steps, reefs) with relatively long crest widths.

Reflection coefficient

It is well studied in the literature that the reflection coefficient for a structure can be characterized by ξ_i. The most commonly used design formula is the one proposed by Seelig and Ahrens (1981)

$$K_r = \frac{a\xi_i^2}{b + \xi_i^2} \tag{2.26}$$

The values of a and b depend primarily on the structure geometry, porosity and surface roughness as well as wave type to certain extent. USACE (2003) recommends that $a = 1.0$, $b = 5.5$ for plane slopes under monochromatic waves and $a = 0.6$, $b = 6.6$ for rubble-mound breakwaters.

Again, the values of K_r measured from the experiments are plotted as a function of ξ_0 in Fig. 2.19, together with Eq. (2.26) for plane slopes and rubble-mound breakwaters. Fig. 2.19 shows that the reflection coefficient is generally very small for fringing reefs (less than 20%). The great scatter in the data is due partly to the error of the traditional two-point method used to separate the incident waves from the reflected waves, and partly to the multiple reflections existing in the flume (the reflection from wavemaker peddler, the two edges of the fore-reef and the back-reef beaches, etc.). Similar degree of the scatter in K_r was also found by Van der Meer et al. (2005) when they analyzed different datasets for LCS, although the error

sources may be different from the present). Comparison of the present data with the curve of the rubble-mound breakwaters shows that K_r is in an agreement with the predictions by Eq. (2.26) at smaller ξ_0, but the agreement becomes unsatisfactory as ξ_0 increases. However, the values of K_r for plane beaches are consistently larger than those for submerged breakwaters or fringing reefs.

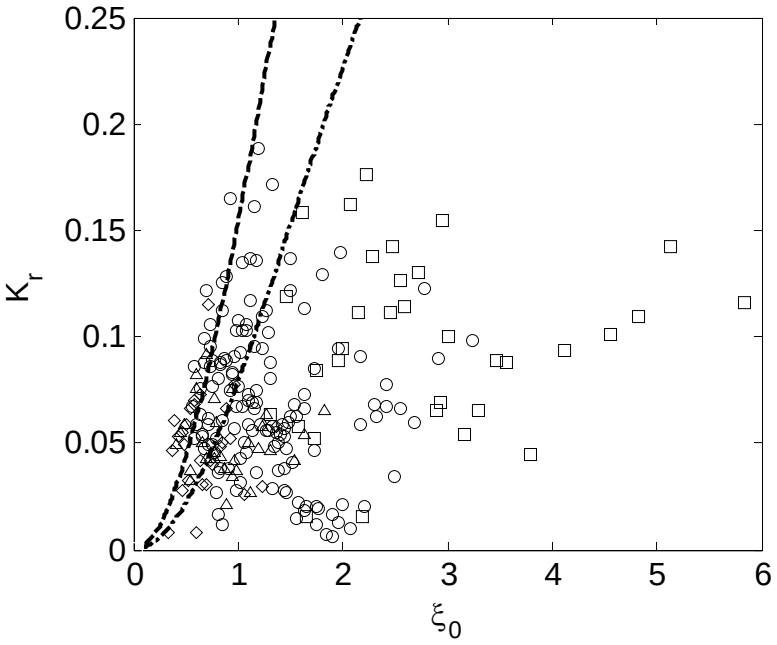

Fig. 2.19 Reflection coefficient (K_r) as a function of the surf-similarity parameter (ξ_0). Squares: Exp., s=1/3; Circles: Exp., s=1/6; Triangles: Exp., s=1/9; Diamonds: Exp., s=1/12. Dashed line: Pred. by Seelig and Ahrens (1981) for plane beach; Dash-dot line: Pred. by Seelig and Ahrens (1981) for rubble-mound breakwater.

The dependence of the reflection coefficient on the relative reef-flat submergence is shown in Fig. 2.20 for different fore-reef slopes, for which no clear trend in K_r can be seen, implying that K_r is almost independent of h_r / H_0. So far, it is not possible to obtain convincing formula to parameterize K_r based on the present data.

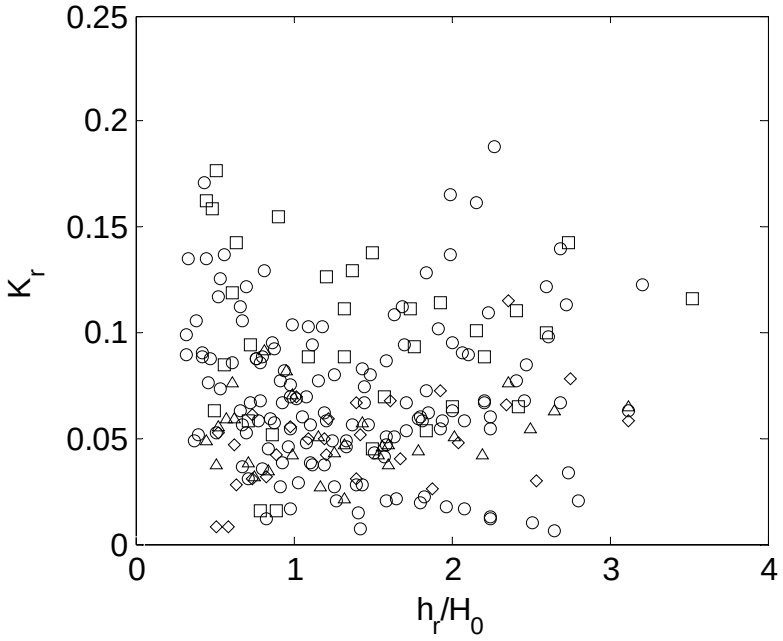

Fig. 2.20 Reflection coefficient (K_r) as a function of relative reef-flat submergence (h_r / H_0). Squares: Exp., s=1/3; Circles: Exp., s=1/6; Triangles: Exp., s=1/9; Diamonds: Exp., s=1/12.

Energy loss coefficient

The above analysis has shown that the relative reef-flat submergence, h_r / H_0, is a suitable parameter to predict the transmission coefficients. However, a suitable parameter to predict the reflection coefficients could not be found. In view that K_r is small (less than 20%), its contribution to the energy balance can be neglected when determining the energy loss coefficient, K_d, by Eq. (2.2). It is anticipated that h_r / H_0 is also a dominant parameter to describe K_d.

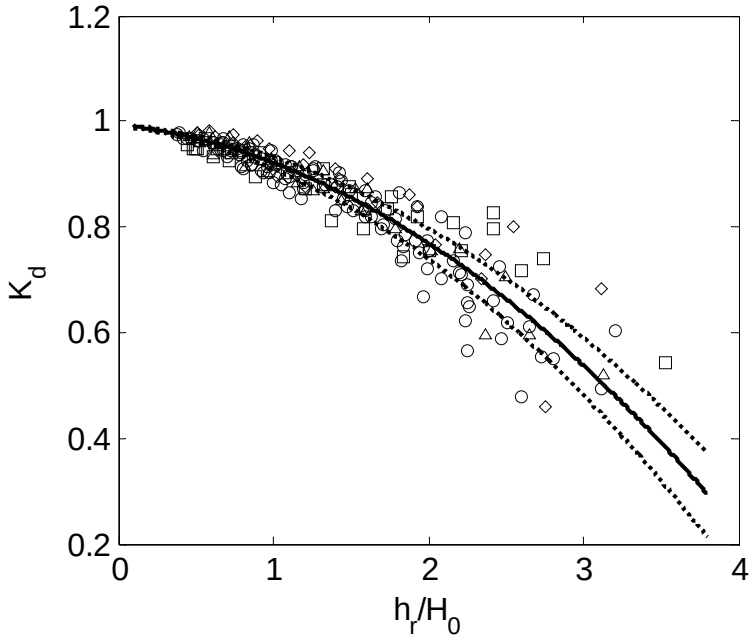

Fig. 2.21 Energy loss coefficient (K_d) as a function of relative reef-flat submergence (h_r / H_0). Squares: Exp., s=1/3; Circles: Exp., s=1/6; Triangles: Exp., s=1/9; Diamonds: Exp., s=1/12. Solid line: Least-square fitting of Exp. data with linear relationship; Dotted lines represent the 95% confidence limits of the best fitting line.

.

The calculated K_d as a function of h_r / H_0 is shown in Fig. 2.21 for different fore-reef slopes. It can be observed that more than 50% of incident wave energy can be dissipated by wave breaking on fringing reefs for all cases. Larger value of K_d appears for plunging breakers ($h_r / H_0 < 1.8$, see Eq. (2.6)), which is consistent with the well-accepted notion that plunging breakers dissipate more energy than spilling breakers. Also shown in Fig. 2.21 are the energy loss coefficients calculated by Eq. (2.27), which is obtained by combining Eq. (2.25) with Eq. (2.2), with the reflection coefficient being ignored because of its small contribution to the energy balance (less than 4%)

$$K_d = (0.994 \pm 0.002) - (0.032 \pm 0.006)\frac{h_r}{H_0} - (0.040 \pm 0.004)\left(\frac{h_r}{H_0}\right)^2 \qquad (2.27)$$

Eq. (2.27) suggests that h_r / H_0 approaches 0, K_d approaches to 1, i.e., if the reef flat is dry and almost all the wave energy can be dissipated through breaking; this might not be true if large wave reflection exists. Since wave breaking may cease if the reef flat is deeply submerged, Eq. (15) is valid only when $h_r / H_0 \leq 2.7$ according to Eq. (2.6). The non-zero K_d found for $h_r / H_0 > 2.7$ in Fig. 2.21 is due to the difficulty in the determination of the critical value of h_r / H_0 for non-breaking waves.

2.5 Concluding Remarks

A series of laboratory experiments were conducted in a wave flume to examine the effects of varying relative reef-flat submergence and fore-reef slopes on the properties of breaking waves over submerged idealized fringing reefs. Preliminary analysis of the data shows that deep-water wave height and reef-flat submergence are two key parameters to describe most of the breaking-wave properties investigated in this study. The influence of fore-reef slope appears to be insignificant. Dimensional analyses reveal that:

(1) The relative submergence of the reef flat has been found to be the determinating factor to characterize the breaker type for fringing reefs.

(2) The ratio of the reef-flat submergence to the breaker wave height has been found to be an appropriate parameter to classify the breaking locations.

(3) The breaker height index appears to be strongly dependent on the deep-water wave steepness in the same manner as that for plane beaches.

(4) The breaker depth index is found to be piecewise linearly related to the relative reef-flat submergence, resembling what is found for submerged breakwaters.

(5) The relative surfzone width is on the same order of magnitude as the length of local shallow water waves, and it has a linear correlation with the inverse of the relative reef-flat submergence.

(6) The transmitted coefficients increase almost linearly with increasing relative reef-flat submergence.

(7) More than 50% of incident wave energy can be damped by the fringing reef. Energy dissipation decreases with increasing relative reef-flat submergence.

(8) Some empirical formulae based on the findings listed above are proposed within the experimental data range ($0.32 < h_r / H_0 < 3.53$).

Natural reefs are far more complex than those that can be studied in laboratory; for a natural reef profile, the reef-crest submergence may become a primary controlling parameter on the nature of wave breaking. Spectral waves, coastal currents, fore-reef roughness, etc. might modify some conclusions in this study to a more or less extent. Comparisons with wave breaking observed in field conditions were not attempted in this chapter.

CHAPTER 3 A LABORATORY STUDY OF WAVE-INDUCED SETUP OVER A HORIZONTAL REEF WITH/WITHOUT A RIDGE

3.1 Literature Review

The shoaling and breaking of surface gravity waves on coral reefs play a central role in shaping the physical structure of coral reefs as well as serving biogeochemical function (Atkinson and Bilger, 1992; Madin et al., 2006). In many respects, the physics of waves on reefs parallels those of waves on beaches, although coral reefs are notably different from normal coastal beaches in many respects including the roughness of the substrate (Lowe et al., 2005), and the variety of geometries that are possible, e.g., barrier reefs vs. fringing reefs. As discussed in Chapter 1, many reefs are characterized by an inshore shallow reef flat with a steep offshore face (the fore-reef). The incident waves break on the fore-reef or the reef flat, dissipating their energy and generating a rise of mean sea level known as wave setup, a phenomenon first described by Munk and Sargent (1948). For a reef with an open lagoon (barrier reef or platform reef), this setup drives a current that exits the lagoon via gaps or channels between the lagoon and open sea, whereas for a reef with a closed lagoon or with no lagoon, the wave-induced setup on the reef flat is more or less constant and the wave-generated flow is always weak (Lowe et al., 2009a).

Although the reef-flat bathymetry varies from site to site, a ridge or similar configuration ("reef rim" or "reef crest" in some papers) is frequently observed at the edge of many coral reefs (Seelig, 1983; Kench et al., 2006; Jago et al., 2007; Hench et al., 2008; Péquignet et al., 2011). Ridges consisting of coral colonies, rubble algal, etc. might be formed due to long-term exposure under high energy dissipation at the reef edge where metabolic rates (nutrient uptake, photosynthesis, production etc.) and biomechanical tolerances of benthic organisms are significantly enhanced (Atkinson and Bilger, 1992; Madin et al., 2006). However, most previous investigations of waves and reef hydrodynamics (Gourlay, 1996a; Symonds et al.,

1995; Hearn, 1999; Gourlay and Colleter, 2005) have generally ignored these ridge structures, focusing on simple reef morphologies with constant fore-reef slopes and horizontal reef flats. In this chapter, laboratory results will be presented, showing that these ridge structures can significantly influence wave dynamics and thus alter the wave-induced setups and wave-driven flows.

While a number of field observations of waves on reefs have been reported in the literature (e.g., Young, 1989; Hardy and Young, 1996; Lugo-Fernandez et al., 1998a, 1998b; Brander et al., 2004; Lowe et al., 2005, 2009a; Hench et al., 2008), experimental investigations into wave interactions with reefs are scarce despite the fact that laboratory experiments can be used to isolate parametric dependencies on forcing parameters in a controlled environment. Early investigations can be found in Gerritsen (1980) and Seelig (1983). Notably, Gourlay (1994, 1996a) reported a series of laboratory experiments with idealized two-dimensional (2D) reef models, which were later compared to existing field observations (Gourlay, 1996b). He showed that wave setup was larger at both low reef-flat water depths and large deep-water wave heights. Using a fringing reef profile similar to that in Seelig (1983), Demirbilek et al. (2007) conducted laboratory investigations on the combined effects of wind and waves on wave setup and runup for spectral waves. More recently, Yao et al. (2009) reported preliminary laboratory experiments including a ridge structure located at the seaward edge of a horizontal reef flat, showing that the ridge could significantly increase the wave-induced setup, and may control the reef-flat setup in a way same as a broad-crest weir controls the water level in open channel flows.

Motivated by the field observations reported in Hench et al. (2008) and pursuing the hypothesis that the reef ridge plays an important role in determining wave setup, a series of experiments were carried out in a wave flume with a reef model that replicates a fringing reef (closed lagoon) system. The present laboratory experiments will also be used in the subsequent chapters to evaluate a numerical model and several analytical relations that have been developed to predict the wave setup on coral reefs. The rest of the chapter is organized as follows. In section 3.2,

the laboratory settings, instruments and experimental procedures are introduced. In section 3.3, the representative experimental results under both monochromatic and spectral waves in the absence/presence of a ridge are shown. Some nonlinear characteristics of cross-shore wave evolution (harmonic waves and radiation stress) are investigated in section 3.4 through a wave measurement with improved spatial resolution. The supplementary measurements of surfzone undertow are given by section 3.5. Some discussions are given in section 3.6. Main results are summarized and key conclusions are drawn in section 3.7.

3.2 Experimental Settings and Instruments

3.2.1 Wave flume and reef models

To examine the effects of ridges on wave-induced setup, a series of laboratory experiments were carried out in the Hydraulics Modeling Laboratory, Nanyang Technological University, Singapore. All tests were conducted in a glass-walled wave flume 36 m long, 0.55 m wide and 0.60 m deep. A servo-controlled piston type wavemaker which can generate both regular and irregular sea states was placed at one end of the flume to generate the designed waves. At the other end, a beach with a slope of 1:8 started at approximately 32 m from the wave maker and was covered with porous mats of 10 cm thick to reduce wave reflection. To construct an idealized 2D reef model that replicated a fringing reef, a plane slope of approximate 1:6 was built with PVC plates at 16.35 m from the wavemaker and it met the horizontal platform which was 0.35 m above the flume bottom. The horizontal platform was 7 m width with its length matching the inner width of the flume (see Fig. 3.1). The entire model was firmly held by stainless rods attaching to the two walls of the flume. A rectangular box 55 cm long, 50 cm wide and 5 cm high was placed on the reef flat with its front face aligned with the reef edge to model a ridge as shown in Fig. 3.2. The dimension (cross-shore width to height ratio is 1:10) of the ridge model was chosen to mimic the reef ridge existing on the Moorea reef studied by Hench et al. (2008).

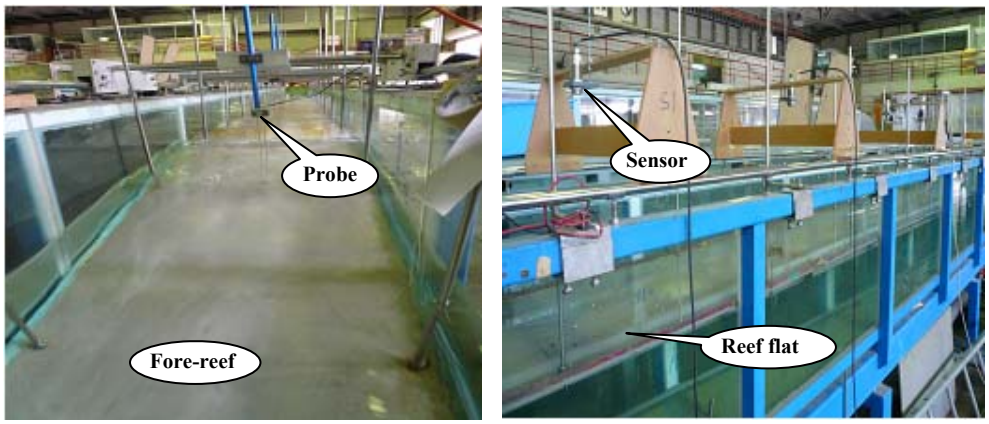

Fig. 3.1 The reef model. Left: Top view of fore-reef; Right: Side view of reef flat.

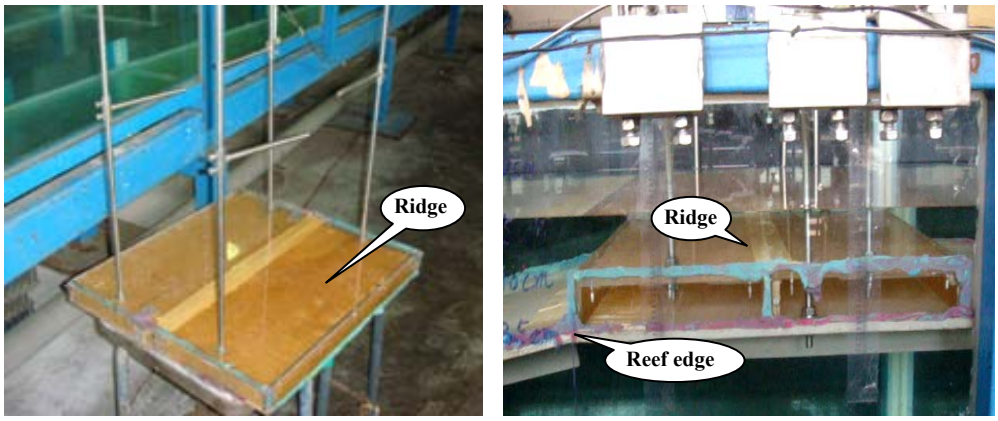

Fig. 3.2 The ridge model. Left: Top view; Right: Side view of ridge on reef flat.

Similar to the experimental setting in Chapter 2, the dimensions of the ridge, the water depth before the reef slope, and incoming wave height were designed according with Froude similarity with a targeted geometric scale factor of 1:20. Thus the dimensions of the prototype ridge are 1 m high and 10 m wide, which are in general agreement with what have been observed at Moorea reef, which is a typical barrier reef and includes a lagoon open to the ocean at the back of the reef. The experiments in this thesis were designed to provide insight into the effects of the ridge on wave transformation over fringing reef profiles rather than to mimic the Moorea reef at an exact model scale. For example, given the reef flat of 7 m in the laboratory setting, the corresponding reef-flat width at the prototype scale is 140 m, which is shorter than that of the Moorea reef (about 1 km). However, the width of

our reef-flat model is acceptable because the author will show latter in this chapter that: (1) it is longer than the maximum surf-zone width in our experiments; (2) the waves outside the surf zone is very small and the wave reflection from the final beach is weak; (3) the wave-induced setup is almost constant outside the surf zone, and (4) the mean current is very small outside the surf zone. The fore-reef slopes in the experiments were also slightly steeper than the average fore-reef slope of Moorea reef (1:8). The roughness and porosity of the reef flat have only minor effects on the wave-induced setups in the absence of the ridge, as shown in the Appendix C; the effects of roughness of porosity will be even smaller when a ridge is present since both the waves and mean current are very small behind the ridge. Therefore, reproducing hydraulic roughness and porosity of natural coral reefs at the model scale was not attempted in the experiments.

3.2.2 Experimental procedures

The schematic layout of the experimental arrangement is showed in Fig. 3.3. In the shallow region over the reef flat, four Ultralab® sensors (General Acoustics Ltd., see also Fig. 3.1) were used to measure the water surface elevation. These sensors transmit ultrasound pulses, which after reflection from the water surface are received by the sensor as an echo enabling the distance between the sensor and the moving water surface to be calculated based on the time of travel. These four sensors (G9 - G12) were almost equally spaced on the reef platform with the first sensor located 1.7 m away from the reef edge. However, in order to measure the wave setup in the zone across the ridge, where the acoustic sensors could not work well due to the sharp transformation of waves over the ridge and air bubbles in water, five resistance-typed probes (G4 - G8) (HR Wallingford Ltd., also shown in Fig. 3.1) were installed. In addition, two probes (G1 and G2) were placed upstream of the fore-reef to separate incident waves from the reflected waves (Goda, 2000) and one probe (G3) was placed on the slope itself to estimate wave shoaling. In principle, both types of wave gauges have accuracy up to 0.1 mm. Practically, it is estimated that the actual accuracy is ±1 mm due to various errors including calibration, weather conditions (the laboratory is open to the outdoors), fluctuation

of initial mean water level, etc.. All the wave gauges were sampled at 50 Hz through a personal computer based data acquisition system.

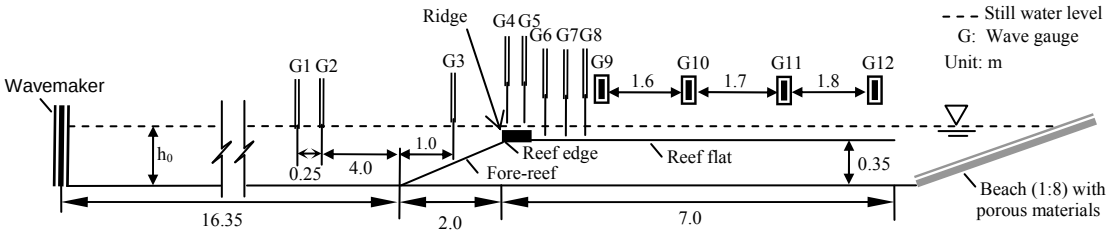

Fig. 3.3 Sketch of the experimental arrangement.

The design incident monochromatic wave conditions were selected from a combination of five incident wave heights (ranging from 0.05 m to 0.13 m) and four wave periods (ranging from 0.83 s to 1.67 s). The target waves (shown in Table 3.1) were slightly different from the actual incident waves in the experiments, due in part to the accuracy of the wavemaker and in part to the weak multiple reflections that existed in the wave flume. The actual incident waves, which were determined by separating the incident waves from the reflected waves using the wave records measured at G1 and G2, were converted to deep water waves for analyzing reef-flat wave setups.

Four water depths (h_0) were studied (40 cm, 41 cm, 42 cm and 45 cm) in this study. Those water depths were selected so that different submergences of the ridge-top ($h_c = 0$ cm, 1 cm, 2 cm and 5 cm) could be investigated. For comparison, three water depths (35 cm, 40 cm and 45 cm) were tested without the ridge; these water depths corresponded to the reef-flat /crest submergence of $h_c = 0$ cm, 5 cm and 10 cm.

Table 3.1 Test conditions[a]

Type	Range	
	Without ridge	With ridge
Reef-crest submergence: h_c (m)	0, 0.05, 0.1	0, **0.01**,0.02, 0.05
Deep-water monochromic wave height: H_0 (m)	0.046-0.131	0.035-0.135
Monochromic wave period : T (s)	0.83-1.67	0.83-1.67
Deep-water significant wave height: H_{s0} (m)	0.033-0.091	0.032-0.087
Peak wave period: T_p (s)	1.00-1.67	1.00-1.67
Reef-crest (ridge) height: d (m)	0	0.05
Cross-shore reef-crest (ridge) width: B (m)	0	0.5
Fore-reef slope: $s = \tan\theta$	1:6	*1:5*

[a] The italic value denotes the equivalent slope ($\tan\theta'$) as defined in Fig. 5.1 and the bold value was only tested under monochromatic waves.

The wave conditions for each water depth were varied so that a measurable mean water level profile could be obtained. During the experiments, each wave condition was repeated three times to ensure the repeatability of the experimental results. Wave breaking before the reef slope was observed when the deep-water wave steepness was very large; those cases were excluded from the following analysis. After the wavemaker was started, surface elevations were recorded by wave gauges through a data acquisition system for analyzing wave characteristics and wave setup. Based on the pilot tests, wave multiple reflections in the wave flume could reach a quasi-steady state (i.e., the wave amplitude does not have a significant variation in time) about 3 min after the start of the wavemaker. This can be explained by the following argument. For a representative water depth $h = 0.4\,m$ and wave period $T = 1.25\,s$, the wave celerity is $c \approx 1.6$ m/s in the experiments. The distance between the toe of the fore-reef and the wavemaker is about 16.35 m. It takes about 20.4 s for the waves to have a round trip between the wavemaker and the reef model. After 3 min, the waves have traveled about 9 round trips, which is enough for the waves to reach a quasi-steady state in the wave flume. Therefore, wave gauges were

sampled for 5 min and the last 100 wave cycles in wave records were used for calculating the wave setups. Between two subsequent tests, several minutes were allowed to elapse so that the water surface could become calm and the effects of residual currents were minimal.

The experiments were also extended to spectral wave conditions. The wave spectra were generated from JONSWAP spectra with peak enhancement factor $\gamma = 3.3$. The designed spectral wave condition was a combination of significant wave heights ranging from 0.03 m to 0.09 m and peak wave periods ranging from 1.0 s to 1.67 s (also shown in Table 3.1). The designed ranges for spectral waves were narrower compared with those for monochromic waves to avoid that steeper individual waves in the spectrum break offshore. The arrangement of wave probes (G1 - G8) was also slightly different from that for monochromic waves. G3 was moved offshore to form a three-probe array for wave spectrum separation (see Goda, 2000 for details). The significant wave height, H_s, was estimated by $H_s = 4\sqrt{m_0}$, where m_0 is the zeroth moment of measured spectrum, which was then converted to deep-water wave height; G4 and G5 were located on the fore-reef slope to capture the relatively wide surf zone of spectral waves and the remaining probes (G6 - G8) were put close to the ridges. The exact arrangement of all wave gauges (G1 - G12) for both wave conditions (monochromic and spectral) can be found in Fig. 3.7. The wave gauges were sampled for 20 min, wave analysis was performed using the data 4 min after the start of data collection to allow spectral waves to reach quasi-steady state. Unlike monochromic waves, only three water depths (40 cm, 42 cm and 45 cm) were investigated for spectral waves when the ridge was present.

According to Froude similarity, the scale factor for wave period would be 1:4.5 for a geometric scale factor of 1:20. For the test conditions listed in Table 3.1, the prototype scales are h_r = 0 m - 2 m, H_0 = 0.70 m - 2.70 m and T = 3.7 s - 7.5 s for monochromatic waves, and h_r = 0 m - 2 m, H_{s0} = 0.64 m - 1.82 m and T_p = 4.5 s - 7.5 s for spectral wave waves. Theses prototype scales are in general agreement

with those observed in field conditions (Bonneton et al., 2007; Hench et al., 2008; Lowe et al., 2009a; Vetter et al., 2010).

3.3 Results

3.3.1 Visualization of wave transformation over reef crest and reflection

Videos showing the breaking area were taken after the wave field had reached quasi-steady state. Plunging breakers were observed in most of the tested cases; spilling breakers were also observed in some of the cases with $h_0 = 0.45\,m$. The breaking point moves from the fore-reef slope onto the reef flat as water depth increases. Fig. 3.4 shows the representative features of wave transformation and breaking over the reef crest in the presence /absence of the ridge for incident monochromatic waves of $H_0 = 0.095\,m$ and $T = 1.25\,s$ in water of $h_0 = 0.45\,m$. Four different phases are displayed starting from the moment when the lip of breaker hit the water surface ($t/T = 0$). For the reef without the ridge, waves plunged onto the reef flat at $t/T = 0$, while at $t/T = 1/4$, the splash-up jet due to plunging breaker hit the water ahead of it, producing an air-water mixture of foam, bubbles and some subsequent white-capping. After half wave period ($t/T = 1/2$), the broken waves propagated across the surf zone as a fully turbulent bore. For the last phase ($t/T = 3/4$), the bore was mostly dissipated and a transmitted wave reformed on the reef flat. Strong reverse flow could be observed during this period before the next incoming wave arrived. When a ridge was present at the reef crest, the breaking point shifted seaward, the breaking waves stroke the front side or the edge of the ridge and then plunged onto the ridge-top, resulting in a stronger wave reflection and air entrainment. However, the transformation process was otherwise similar to that for the reef without the ridge under the same water depth and wave condition.

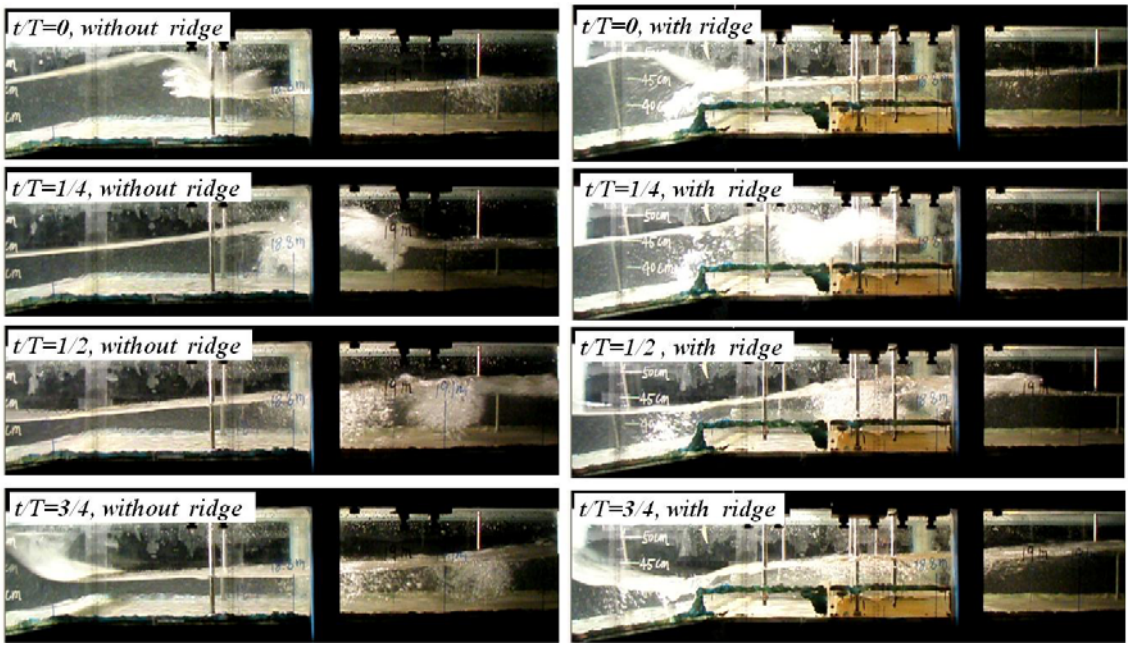

Fig. 3.4 Snapshots of monochromatic wave transformation over reef crest at different phases, the time interval between consecutive phases is one quarter of a wave period ($h_0 = 0.45\ m$, $H_0 = 0.095\ m$ and $T = 1.25\ s$).

Reflection coefficients determined by the two-probe method ranged from 2% to 25% without the ridge and from 6% to 55% with the ridge for monochromatic waves. For spectral waves, they ranged from 9% to 37% without the ridge and from 20% to 66 % with the ridge, respectively. Spectral waves have larger values of reflection coefficients than the comparable monochromatic waves because the low-frequency portion of wave spectra reflects more efficiently (Seelig, 1983). The effects of the ridge on the wave reflection were more evident for waves of small wave steepness. The enhanced wave reflection is expected since the ridge structure functions like a submerged breakwater, which is used widely to reflect ocean wave energy (Yao et al., 2009).

3.3.2 Wave evolution across reef profile

Time- series surface elevation for monochromatic waves

Sample wave records at selected wave gauges for model reefs with and without ridges (adjusted to be in phase) are given in Fig. 3.5. At the deep section of the

flume (G1), Stokes waves that have short, peaky crests and longer shallower toughs were observed in the intermediate depth of water ($kh_0 = 1.16$). When waves shoaled on the fore-reef slope (G3), they became more asymmetric and skewed. G6 was located in the surf zone for both cases; thus breaking waves with saw-tooth shape could be observed there. On the reef flat (G9), the reformed waves were very small and there were second peaks in the wave profiles due to the generation of higher harmonics. The phase discrepancy between the fundamental harmonics became substantial between the two reefs as waves propagated shoreward.

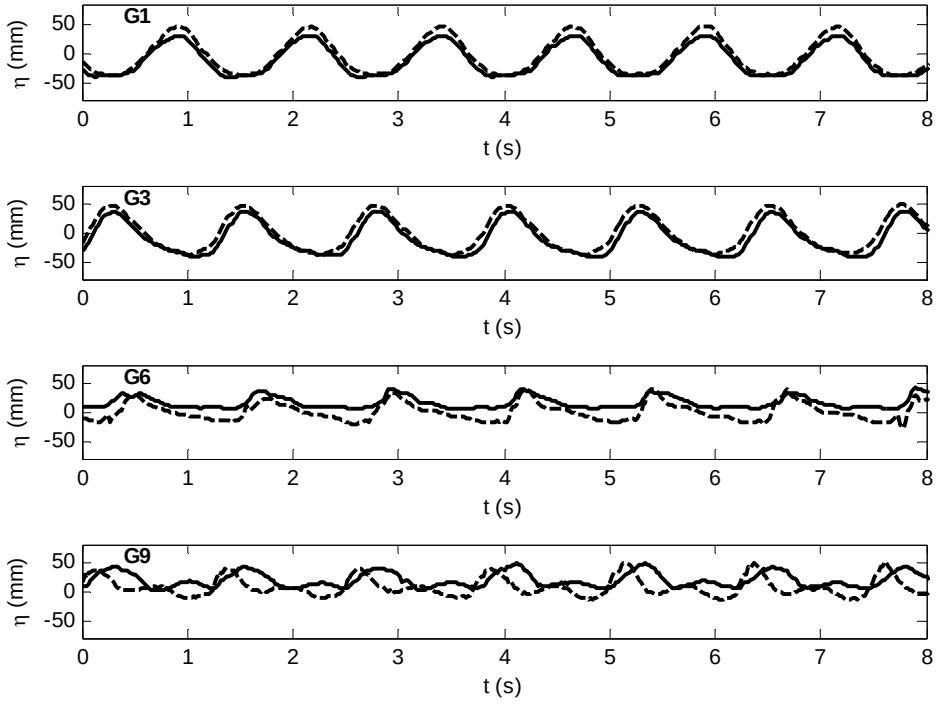

Fig. 3.5 Time-series wave records from selective wave gauges (G1, G3, G6 and G9) across different reef profiles under monochromatic waves ($h_0 = 0.45\,m$, $H_0 = 0.095\,m$ and $T = 1.25\,s$). Dashed lines - without ridge; solid lines - with ridge.

Wave spectra for spectral waves

Wave spectra for the case $H_{s0} = 0.087\,m$ and $T_p = 1.67\,s$ in water of $h_0 = 0.40\,m$ are shown in Fig. 3.6 to exemplify the behavior of spectral waves. As the waves

propagated over the fore-reef slope (G5) into the shallower water, wave energy was transferred from the peak frequency ($f_p = 0.612\ Hz$) to lower frequencies in the spectrum (shown by G5) for reefs both with and without the ridge. Wave breaking occurred either on the fore-reef slope or on the reef flat for the case without the ridge; hence there was still a considerable amount of wave energy around the peak frequency in the incident spectrum within the surf zone (G7). However at this location, a large portion of the wave energy near the peak frequency was dissipated when the ridge was present because the ridge-top was initially dry in water of $h_0 = 0.40\ m$ and all waves broke on the fore-reef slope or ridge edge. Shoreward of the reef-flat surf zone (G9), there was no notable difference in the wave spectra between the two reefs since the local water depths on the reef flat were both sufficiently shallow (0.05 m) so that most of wave energy was filtered through wave breaking.

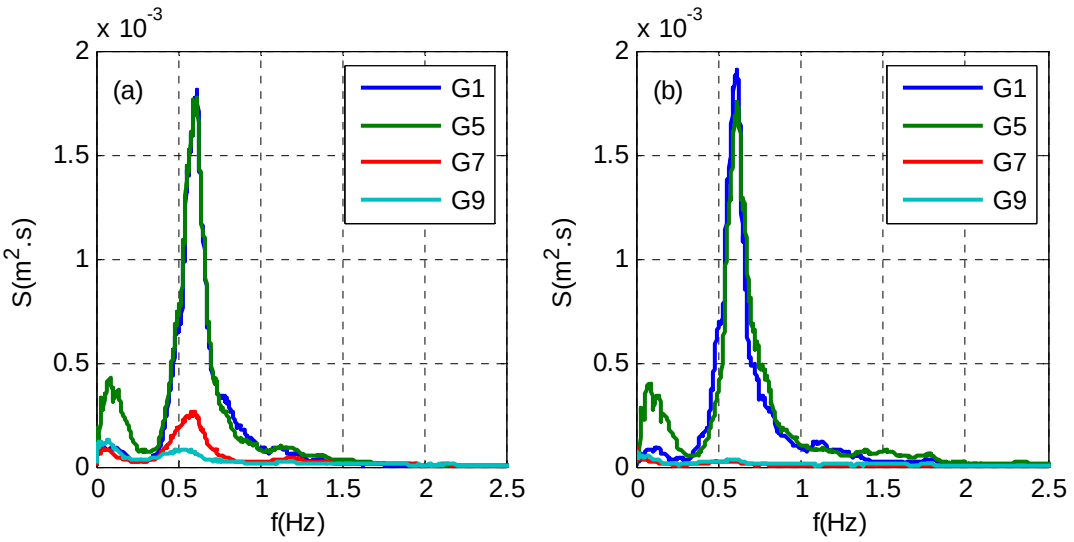

Fig. 3.6 Wave spectra ($h_0 = 0.40\ m$, $H_0 = 0.087\ m$ and $T = 1.67\ s$) from selective wave gauges (G1, G5, G7 and G9) across different reef profiles: (a) without ridge; (b) with ridge.

3.3.3 Mean water level across reef profile

Twelve wave gauges (G1 to G12) were used in the experiments, enabling us to construct reasonably detailed wave setup profiles across the reef models by a linear

interpolation. For example, two cases representing monochromatic and spectral wave conditions are illustrated in Fig. 3.7. As expected, for both waves, setdown occurred at the seaward side of the surf zone. In the surf zone itself, there was a monotonic increase of mean water level (MWL) due to wave breaking. The peak setup always appeared at G9. After the peak, the setup slightly decreased and then became almost constant. Under the same wave condition, the magnitude of setup in the presence of the ridge was significantly larger than that seen in the absence of the ridge. Moreover, the ridge also caused the lowest point of MWL to move seaward along with the point where waves broke.

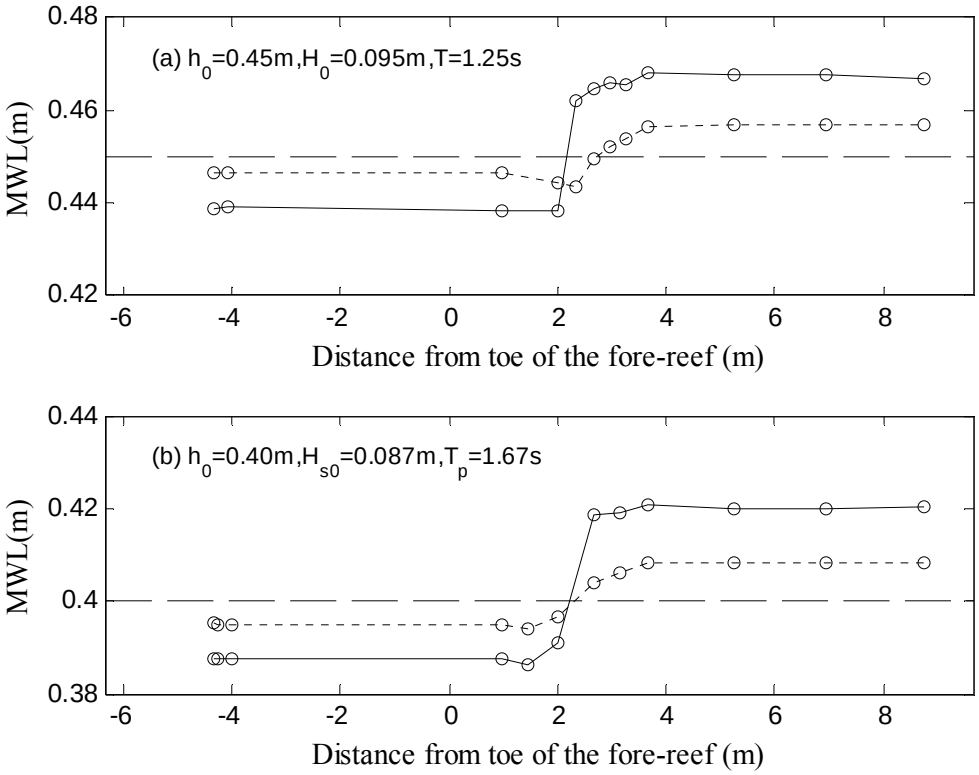

Fig. 3.7 Mean water level (MWL) offshore and across the reef profile under different wave conditions: (a) monochromatic waves; (b) spectral waves. Open circles - locations of wave gauges; dotted lines - without ridge; solid lines - with ridge; dashed lines - Still water level (SWL).

3.3.4 Wave setup as a function of deep-water wave height

The above analysis shows that the MWL always reached its maximum around G9 on the reef flat; thus, the setup at G9 is a good estimate of the maximum setup, $\overline{\eta}_r$. As an example, Fig. 3.8 shows this wave-induced setup as a function of deep-water wave height, H_0, for different wave periods, T, and for two water depths $h_0 = 0.40\ m$ and $0.45\ m$. The cases with and without the ridge under different wave conditions are also compared in this figure. All the measured data in the experiments can be referred to Appendix B.

A key issue arises that which wave height and wave period are selected as the representative wave parameters for spectral waves. There is no intrinsic relationship between regular and irregular wave parameters, and accordingly their equivalence depends on which wave feature is considered as the primary concern. Since wave setup is related to the radiation stress (thus the wave energy) as indicated in Eqs. (5.2) and (5.4), the deep-water root-mean-square wave height (H_{rms0}) is chosen so that an equivalent energy between the monochromatic and spectral waves is ensured. For wave period, the peak wave period (T_p) was used, the discrepancy between the peak wave period and the significant wave period is very small.

Under similar wave conditions, the ridge could cause a noticeable increase in the wave setup on the reef flat, particularly for the cases of longer wave period. In some cases, the wave-induced setup was as much as doubled by the ridge. With or without a ridge, the wave-induced setup on the reef flat increased almost linearly with increasing H_0. The relationship between $\overline{\eta}_r$ and T was less obvious. However, by comparing the wave setup under similar H_0, it could be found that $\overline{\eta}_r$ in general increased with increasing T, in agreement with the observations of Gourlay (1996a). Meanwhile, the setup variation for spectral waves has similar trend with that for monochromatic waves when H_{rms0} and T_p were used to characterize spectral waves.

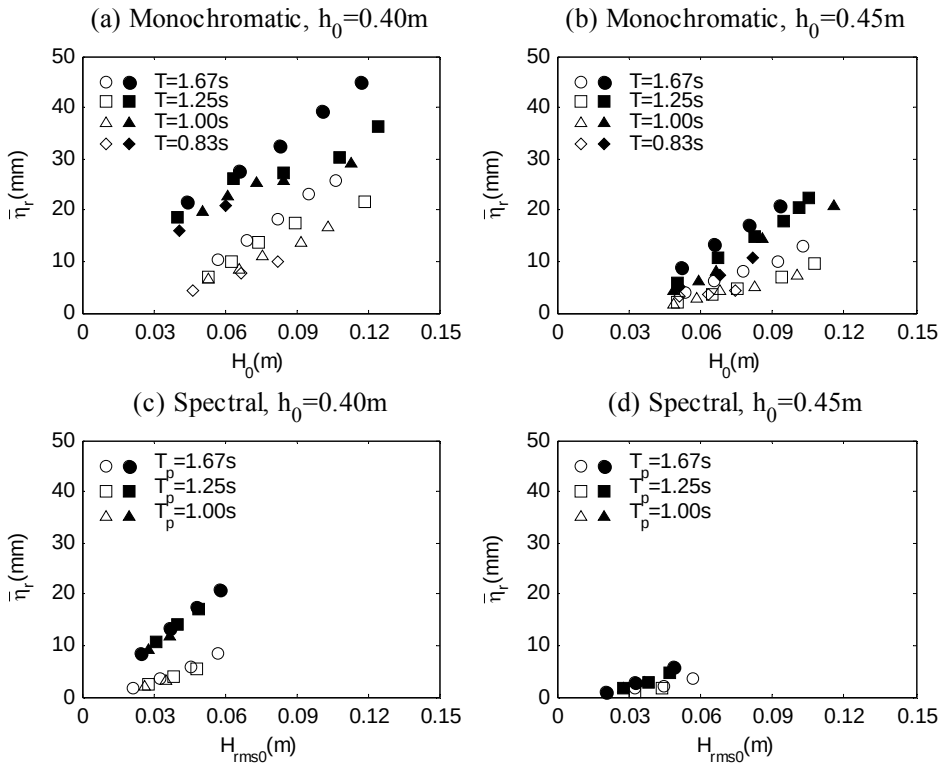

Fig. 3.8 Maximum wave setup on reef flat as a function of deep-water wave height for different wave periods, still water depths and incident wave conditions. Open markers - without ridge; solid markers - with ridge.

3.4 A Detailed Wave Measurement with Improved Spatial Resolution

3.4.1 Definition of the surf zone over reefs

As discussed in Chapter 2, for wave breaking over coral reefs, the surf zone is defined as the horizontal distance between the incipient breaking point to the point where propagating bores disappear and oscillatory waves reform. For the convenience of subsequent discussion, the author follows the division of surf zone over reefs by Gourlay (1994) which is based on the ideas of Svendsen et al. (1978):

Outer surf zone

In this region there is a significant change of wave shape as the surf roller develops. However, there is no significant change in momentum flux and the rapid reduction in wave height is associated with the transformation of potential energy into kinetic

energy. For plunging breakers, the width of this region is approximately identical to the plunging distance (described below) of the breaker.

Inner surf zone

In this region the surf roller developed in the outer region becomes a bore or moving hydraulic jump which travels landward over the seaward flowing undertow. Dissipation of wave energy and wave-induced setup begin at the transition between the inner and outer regions. On a horizontal or near horizontal reef, the inner region corresponds to the region where the bore propagates over the reef flat and this region ends where the bore disappears and an oscillatory wave reforms.

Unlike waves breaking on plane beaches described in Svendsen et al. (1978), there is no swash zone when waves break over coral reefs. The reformed oscillatory waves will continue to propagate over the shoreward region of the surf zone (starting from the endpoint of surf zone to the lagoon (if it exists) or to the coastline) until they break on the final beach. Frictional dissipation may be significant during the whole process.

Following Galvin (1969), the author defines the plunge distance as the distance from the breaking point (see section 2.3.1 for the definition) to the plunging point (the location where the wave crest curls over and touches the water surface in front of it). The splashing distance is defined as the distance from the plunging point to the splashing point (the location where the water mass displaced upward by the plunging wave strikes the water surface). See also Fig. 3.9 for all the definitions above.

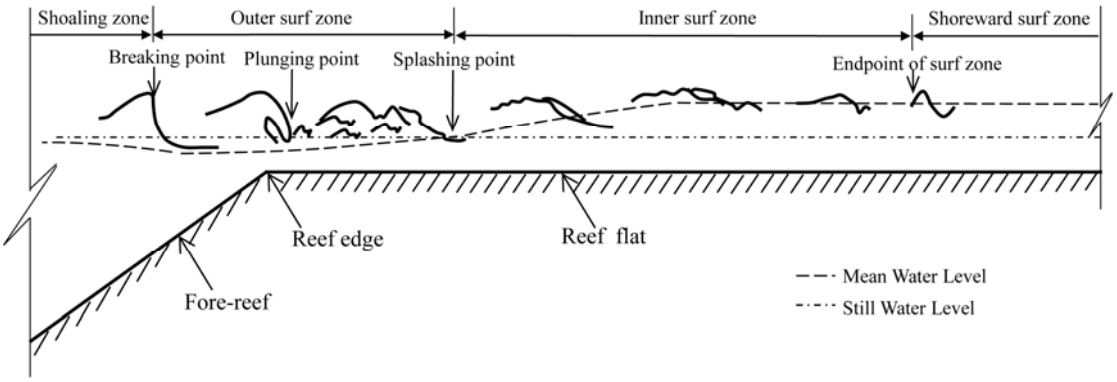

Fig. 3.9 Regions and locations in the surf zone (adapted from Svendsen et al., 1978).

3.4.2 Spatial variation of wave height and mean water level

Section 3.3.3 has compared the magnitudes of the MWL obtained in the absence /presence of a rectangle ridge for both monochromatic and spectral waves with limited sampling locations. In this section, to further understand the cross-shore distribution of wave height, MWL, higher harmonic waves and the momentum flux, a detailed wave measurement covering 60 sampling locations was carried out with a spatial resolution of 0.075 m in both the absence and presence of the ridge. The same monochromatic waves same as those in section 3.3 ($h_0 = 0.45\,m$, $H_0 = 0.095\,m$ and $T = 1.25\,s$) were selected. The studied area began from the shoaling zone on the fore-reef (0.75 m seaward of reef edge) and ended some distance shoreward of the surf zone on the reef flat (3.675 m shoreward of reef edge). The wave records were obtained by moving one resistance-type wave gauge along the flume within the same run. Wave measurements around the plunging points were not included in the analysis due to significant air-entrainment. Measurement locations relevant to subsequent discussions in this chapter are given in Table 3.2 for both cases (with and without the ridge).

Table 3.2 Selected measurement locations

Location name	Distance[a] from reef edge (m)	
	without ridge	with ridge
Breaking point	0.02	-0.04
Plunging point	0.25	0.20
Splashing point	0.78	0.48
Endpoint of surf zone	2.94	1.34

[a] positive if shoreward of the reef edge.

The measured local wave height and mean water level (MWL) are shown in Figs. 3.10(a) and 3.10(b) in both the absence and presence of the ridge. Also indicated in the figure are the sampling locations and seabed elevation. The origin of the abscissa is at the reef edge. The local wave height is obtained by averaging over about 50 waves determined by a zero-upcrossing method.

As it can be observed, wave breaking occurred almost at the same location (maximum wave height points) seaward of the reef/ridge edge for both profiles (with and without the ridge). For shoaling waves on the fore-reef, the wave height fluctuated due to partial wave reflection; the fluctuation was enhanced when the ridge was present. However, shoreward of the breaking point, the wave height decreased more rapidly for the reef with the ridge than without due to a narrower surf zone caused by the presence of ridge. Shoreward of the reef-flat surf zone, the wave height for the reef with the ridge was still slightly smaller although the still water depth (h_r) on the reef flat was the same for both profiles. The minor fluctuation of wave height on the reef flat might be due to the reflection of the beach at the end of flume. For the MWL, no fluctuation could be observed. MWLs reached the lowest points right in front of the reef/ridge edge due to wave setdown and began to rise in the surf zone. The estimated surfzone widths in the figure were about 2.7 m without the ridge and 1.2 m with the ridge, respectively, which were consistent with 2.92 m and 1.38 m (see Table 3.2) estimated by observation of the propagating bores. Shoreward of surf zone, the setups became nearly constant on the reef flat, which is typical for fringing reefs.

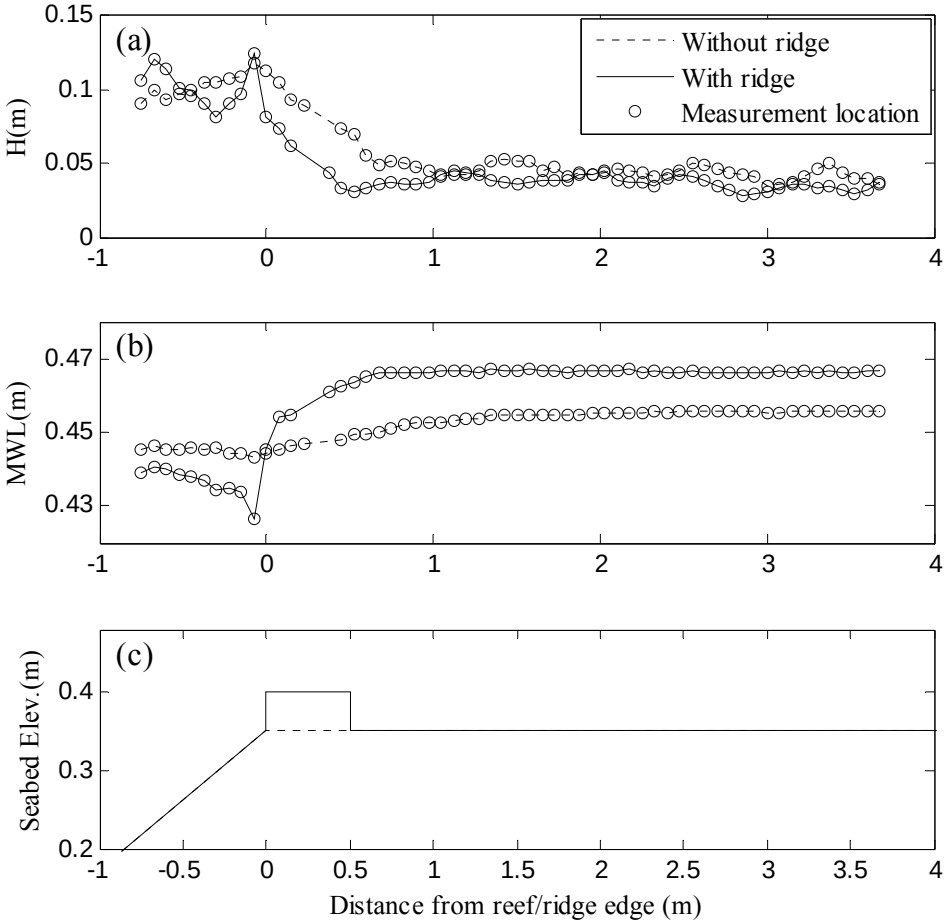

Fig. 3.10 Wave height and mean water level (MWL) across the reef profile ($h_0 = 0.45\ m$, $H_0 = 0.095\ m$ and $T = 1.25\ s$).

3.4.3 Generation of higher harmonics

The generation of higher harmonics when waves propagate over immersed obstacles (such as submerged steps, bars, breakwaters and plates) has been studied over decades (e.g., Beji and Battjes, 1993; Christou et al., 2008; Brossard et al., 2009). Previous experimental results and numerical simulations have shown that up to 60% of the incident wave energy can be transferred downstream of the structure through higher harmonic modes. The fringing-reef model resembles a sloping step, harmonic generation may occur above the fore-reef and over the reef crest. On re-entering deeper water on the downstream side of the reef crest (ridge), these higher harmonics may be released as free waves. The present experimental settings could not separate the free waves from the locked waves. In this section, the author

presents a preliminary harmonic analysis to quantify the energy transfer from the fundamental mode to higher harmonic modes in the measured cross-shore region.

Figs 3.11(a) and 3.11(b) show the cross-shore variation of harmonic waves in the absence/presence of the ridge, respectively. Up to the fifth harmonics (a_1 to a_5) are shown, and they are determined by a least-square fitting of the Fourier series to the measured surface elevations. Also shown in Fig. 3.11 is the seabed elevation.

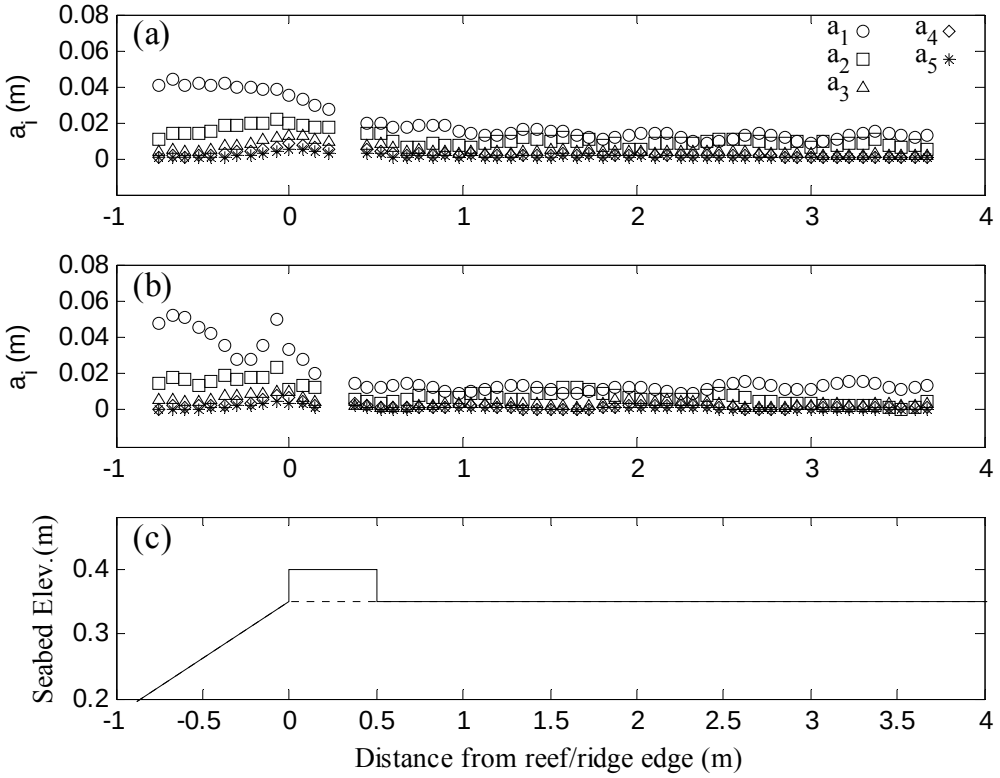

Fig. 3.11 Harmonic wave amplitudes across the reef profiles: (a) without ridge; (b) with ridge ($a_{i\,(i=1,2\cdots5)}$ - the i th harmonic wave amplitude; $h_0 = 0.45\ m$, $H_0 = 0.095\ m$ and $T = 1.25\ s$).

As it can be estimated in both Figs 3.11(a) and 3.11(b), for shoaling waves at the beginning of the measured region, the fundamental harmonic waves (a_1) reached up to 95% of the incident wave height ($H_0 / 2 = 0.048$) while the height of the second harmonic waves (a_2) was about 20% of a_1, and the third to fifth harmonic waves were very small in the shoaling zone. As wave shoaling continued on the fore-reef,

the higher harmonics continued to increase shoreward due to the energy transfer from the fundamental mode to higher harmonic modes. The fluctuation of a_1 on the fore-reef, particularly when the ridge was present, was due again to the strong wave reflection from the fore-reef. After the breaking points, the cross-shore evolution of harmonic waves was not significantly affected by the presence of the ridge: in the outer surf zone, there was a rapid decrease of a_1 due to the energy dissipation by wave breaking, but breaking dissipation only resulted in a slight decrease of high harmonic wave heights (a_2 to a_5). In the inner surf zone and the shoreward region of the surf zone on reef flat, wave attenuation slowed down, and the second harmonic waves became comparable with the fundamental harmonic waves. The third to fourth harmonics remained very small on the reef flat. The spatial oscillations in the amplitudes of the fundamental and higher harmonic waves on the reef flat are due partly to the coexistence of the locked and free waves (the bound and free modes propagating downstream have the same pulsation but different wave numbers; this may be true when the ridge is present, but may not be true in the absence of the ridge) and due partly to a resonant behavior caused by the multi-reflection between the two ends of the reef flat.

The above analysis is based only on one wave condition, and further studies are needed in the future to examine different wave conditions, different reef-crest submergences and different reef/ridge widths. Nevertheless, the above simple analysis does show that the generation of higher harmonics can have a significant impact on the transmitted wave energy over reefs. This highly nonlinear phenomenon becomes more significant as waves transform from the fore-reef to the reef flat; as a result, the validity of the existing analytical models that are based on linear monochromatic waves needs to be revisited using newly obtained experimental data.

3.4.4 Calculation of radiation stress

The radiation stress concept as introduced by Longuet-Higgins and Stewart (1962) is defined as the excess flux of horizontal momentum due to the presence of waves.

This concept is important in nearshore hydrodynamics because the spatial gradients of the radiation stress can generate a variation of mean water level (MWL) (setup and setdown), currents alongshore and long waves (Longuet-Higgins and Stewart, 1964).

The cross-shore component of the radiation stress can be defined as (Svendsen, 2006)

$$S_{xx} = \overline{\int_{-h}^{\eta} (\rho u_w^2 - \rho w_w^2) dz} + \frac{1}{2} \rho g \overline{\eta^2} \tag{3.1}$$

where u_w and w_w are the horizontal (normal to shore) and vertical components of wave orbital velocity, and the over-bar indicates a wave-average over one wave period. The effects of turbulence and viscosity are neglected in the above definition.

Radiation stress cannot be directly measured with the existing measuring techniques due to the difficulties in obtaining wave orbital velocity information in the trough-crest region. Therefore radiation stress has been traditionally determined in three different ways (Torres-Freyermuth et al., 2007): (1) using analytical and/or parametric results from constant depth wave theories; (2) making estimations based on MWL spatial measurements, and (3) by using detailed velocity and free surface measurements or simulations.

Longuet-Higgins and Stewart (1964) approximated Eq. (3.1) using shallow-water linear wave theory to give

$$S_{xx} = \frac{3}{16} \rho g H^2 = 0.1875 \rho g H^2 \tag{3.2}$$

This expression for the radiation stress has been widely used in wave-driven current models, since it relies only on wave height. However, this expression was obtained for small-amplitude, non-breaking monochromatic waves propagating over a mild slope bottom. Since the waves in the surf zone are highly nonlinear, Svendsen and Putrevu (1993) determined the radiation stresses by analyzing measured wave-height and MWL profiles for monochromatic waves, and calculated

the dimensionless radiation stress, $P = S_{xx} / \rho g H^2$, which was supposed to contain the effect of both roller and nonuniform velocity and pressure distribution in the surf zone. They observed a common feature in all calculated P (independent of the beach slope and incident waves): P has a value of about 0.1 at the breaker point, and increases to a maximum value of about 0.4 somewhere between the breaker point and the shoreline, and eventually reduces to 0.1 again near the shoreline. The relatively small values of P at or before wave breaking is attributed to the fact that near-breaking waves have sharp crests and relatively flat troughs in comparison with a sine wave of the same height (Svendsen, 1984a). However, Svendsen (1984a) also found that in the surf zone, the contribution from the rollers becomes significant, resulting in relatively large values of P (above 0.1875 as shown in Eq. (3.2)). A representative value of P for surf-zone waves resembling saw-tooth waves is $P = 0.22$ (Svendsen, 2006). A common issue with this approach is that the interpolation errors may lead to errors in predicted setups (Svendsen and Putrevu, 1993). More recently, Johnson and Smith (2005) and Torres-Freyermuth et al. (2007) have used detailed measured or simulated velocities to evaluate the cross-shore and long-shore radiation stress components. However, owing to the difficulties in measuring the motion of water above the wave trough, the velocity field in this region was obtained by extrapolation based on the continuity equation.

In this section, S_{xx} is evaluated using the exact definition, i.e., Eq. (3.1) to avoid the aforementioned difficulties and assumptions. Since only the wave measurements are available, following the convention of analyzing irregular waves, the waves measured at a location are assumed to be a sum of all harmonic waves (the waves are assumed to be nonlinear waves with a discrete spectrum). In addition, all higher harmonics are supposed to be phase-locked (locked waves), i.e., free waves are not considered. Since we have obtained both the amplitudes and phase angles from the harmonic analysis (up to five harmonic waves are considered here), thus the free surface of each harmonic mode (η_i) is known from the harmonic analysis; according to linear wave theory, the corresponding velocities (u_w^i and w_w^i) can be computed. The total velocity or the surface elevation (η, u_w and w_w as appear in Eq.

(3.1)) is simply the summation of all the harmonic contributions, i.e., $\eta = \sum_{i=1}^{5} \eta_i$, $u_w = \sum_{i=1}^{5} u_w^i$ and $w_w = \sum_{i=1}^{5} w_w^i$. Finally, S_{xx} can be calculated according to Eq. (3.1), first carrying out the integration with respect to z and then carrying out the time average over one wave period.

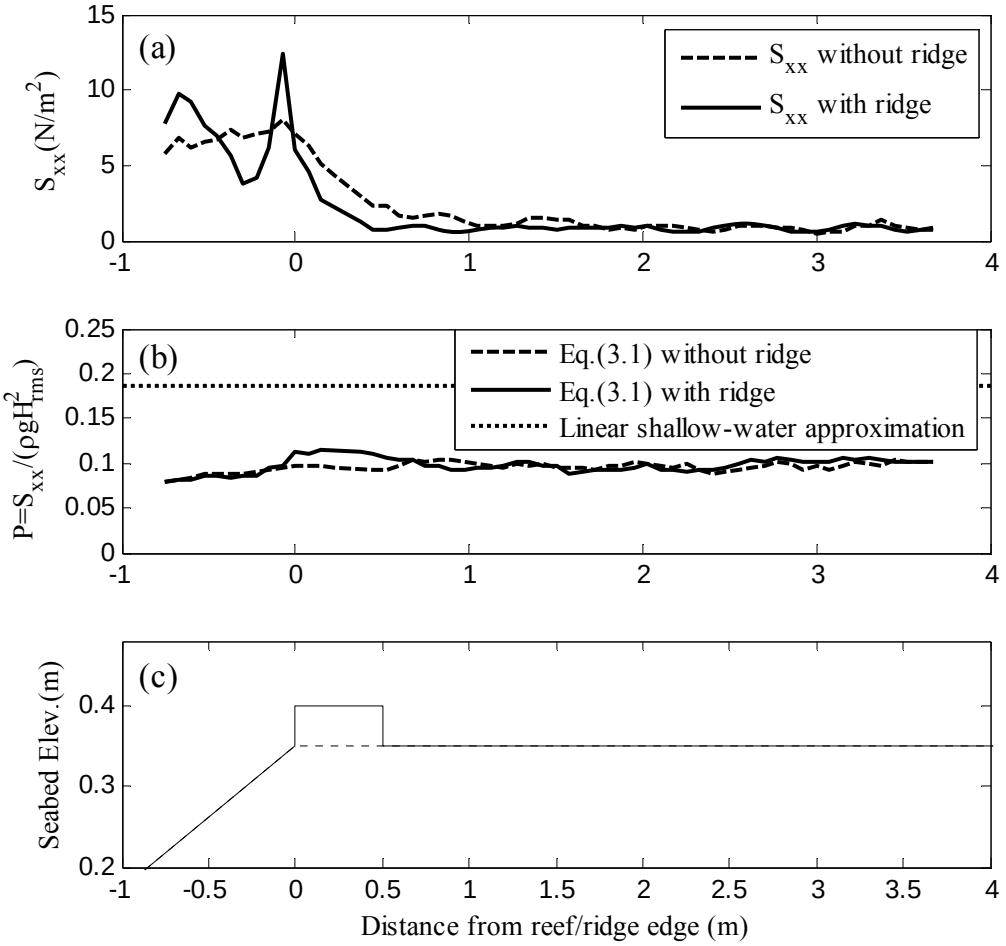

Fig. 3.12 Cross-reef variation of: (a) dimensional radiation stress (S_{xx}); (b) the dimensionless radiation stress (P) ($h_0 = 0.45\ m$, $H_0 = 0.095\ m$ and $T = 1.25\ s$).

The computed dimensional radiation stress (S_{xx}) and the non-dimensional radiation stress (P), i.e., S_{xx} normalized by $\rho g H_{rms}^2$ (H_{rms} is the local root-mean-square wave height and computed by $H_{rms} = \sqrt{\sum_{i=1}^{5} (2a_i)^2}$, it is employed here because H_{rms} is related to wave energy, and thus the radiation stress.) are shown in Figs 3.12(a)

and 3.12(b), respectively, also shown in the figure is the value of P (0.1875) obtained from traditional shallow-water approximation for linear waves.

As depicted in Fig. 3.12(a), for shoaling waves on the fore-reef, particular in the presence of the ridge, the cross-shore values of S_{xx} were affected by the fluctuation of the amplitudes of those harmonic waves (see Fig. (3.11)), but the increase of S_{xx} before the breaking points can still be identified for both cases with and without the ridge, which in fact generated the wave setdown in Fig. 3.10(b). After the breaking points, the value of S_{xx} becomes smaller when the ridge was present because the height of the transmitted waves was controlled by the water depth above the ridge top; whereas, the cross-shore gradient of S_{xx} was significantly increased by the ridge, forcing a larger setup on reef flat (see also Fig. 3.10(b)). For the dimensionless value P, Fig. 3.12(b) shows that P generally remained to be a constant around 0.1 within the entire measured region (from the shoaling zone on the fore-reef to the shoreward region of the surf zone on reef flat), which was generally smaller than the radiation stress ($P = 0.1875$) predicted by linear wave theory. The value of P close to the 0.1 near the breaking point was in agreement with previous studies on monochromatic waves breaking on plane slopes (Svendsen and Putrevu, 1993; Torres-Freyermuth et al., 2007). However, unlike previous studies, an observable increase of P value in the surf zone was not found in our experiments, indicating that there is a fundamental difference in the surfzone momentum flux between the fringing reefs and plane beaches. Meanwhile, there was almost no difference in the values of P with and without the ridge, except in the outer surf zone around the ridge where a slight increase of P could be observed.

3.5 Undertow Measurements

The one-dimensional vertical (1DV) flow structure in the surf zone is a subject of great importance in understanding many coastal processes and has probably received the most attention in the past. The undertow is the below-surface rush of water returning to sea after the water comes inshore as breaking waves. During the last two decades, new measurement techniques have become available (e.g., Laser

Doppler Anemometry (LDA), and Particle Image Velocimetry (PIV)), which have successfully been applied in numerous laboratory experiments for undertow measurements for both plane beaches (Ting and Kirby, 1994; Govender et al., 2002; Cowen et al., 2003; Huang et al., 2009) and barred beaches (Hass and Svendsen, 2002; Govender et al., 2009). See Christensen et al. (2002) for a review.

For coral reefs, wave-driven currents have a major influence on lagoon flushing. The wave-driven flow over the reef and through the lagoon is also a critical factor in determining community distribution and production rates in coral reef ecosystem by controlling both the supply of nutrients and the level of turbulence on the reefs (Hearn, 1999). Field studies on this topic are numerous (e.g., Kraine et al., 1999; Lugo-Fernández et al., 2004; Luick et al., 2007; Hench et al., 2008 ; Lowe et al., 2009a).

The most comprehensive laboratory measurements of wave-driven currents over the reef flat to date were obtained by Gourlay (1996a). He found that wave-generated flow across a reef increased with increasing both wave height and wave period similar to what was found for the wave setup. In contrast to the wave setup, the wave-generated flow was small at lower reef-flat water level and increased to its maximum value at higher water level. However, it can be reduced to zero when the water level was further increased. However, the velocity measurements in these experiments were only taken at a single depth and limited locations. In this section, the goal is to investigate the wave-averaged mean velocity profiles (undertow) that describe the circulation current in the vertical plane of the surf zone. It was performed as a supplement to the wave setup experiments in this chapter.

The monochromatic waves with $h_0 = 0.45\,m$, $H_0 = 0.095\,m$ and $T = 1.25\,s$ were again selected to represent a typical plunging breaker on the reef flat. The vertical variation of the flow structures under the breaking waves was measured by an electromagnetic flow meter (EFM) (Kenek, Ltd.). This type of flow meter has been successfully used to measure the flow field around breakwaters (e.g., Mory and Hamm, 1997; Cáceres et al., 2008; Vicinanza et al., 2009). The probe of EFM used

in the experiments is 5 mm in diameter and 55 cm in length with an L-shape tip (See Fig. 3.13), and it could be adjusted both horizontally and vertically with a trolley seated on the sidewalls of the flume. Two instantaneous velocity components, $u(t)$ (horizontal and normal to shore) and $w(t)$ (vertical), were measured at the tip of the probe. EFM probes are generally more flexible than ADV probes for flow measurement in very shallow water. The measurements could only be performed beneath the wave trough level and outside the air-entrainment region. Detailed vertical profiles from 0.5 cm above the bottom to 0.5 cm below the wave trough with a vertical interval of 0.5 cm were measured at 13 selected cross-shore locations along the centerline of the flume (L1 - L3 in the shoaling zone, L4 - L11 in the surf zone, L12 - L13 shoreward of surf zone). The exact positions of those locations are varied according to the observed breaking, plunging, splashing points and surfzone widths in the absence/presence of the ridge, see Table 3.3 for details. Special attention was paid to the vicinity of reef/ridge edge where the flow variation was supposed to be large. However, the region between the plunging and splashing points was avoided due to strong air entrainment.

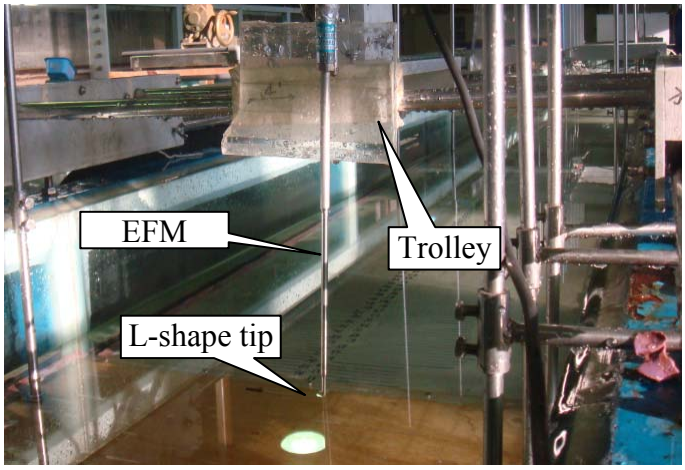

Fig. 3.13 The setting of electromagnetic flow meter (EFM).

Velocity measurements with a frequency of 50 Hz started after the wavemaker ran for about 10 min. This was done in order to ensure that waves and mean current were in a state of equilibrium. Flow measurement at one location was conducted within the same run, and then it was started at another location in a new run. At

least a half hour elapsed between the two runs to eliminate possible residual currents. The mean velocity was deduced by averaging the measured velocity over a period of time. A recording time of 1.5 min was usually sufficient to obtain mean velocity beneath the trough of breaking waves, except around the splashing point where the velocity profile was not periodic (e.g., L9 in Fig.3.14), the sampling duration was extended to 3 min at those locations.

Sample records of measured flows at selected measurement locations are given in Fig. 3.14 for reefs with and without the ridge (adjusted to be in phase). The u-velocity component measured at mid-depth is shown for each location.

Table 3.3 The arrangement of flow measurement locations

Location No.	Distance[a] from reef edge (m)		Surfzone position	
	without ridge	with ridge	without ridge	with ridge
L1	-0.75	-0.75	shoaling zone	shoaling zone
L2	-0.45	-0.45	shoaling zone	shoaling zone
L3	-0.15	-0.15	shoaling zone	shoaling zone
L4	0	0	outer surf zone	outer surf zone
L5	0.15	0.075	outer surf zone	outer surf zone
L6	0.6	0.15	inner surf zone	outer surf zone
L7	0.825	0.45	inner surf zone	inner surf zone
L8	1.125	0.6	inner surf zone	inner surf zone
L9	1.5	0.825	inner surf zone	inner surf zone
L10	1.95	1.125	inner surf zone	inner surf zone
L11	2.55	1.5	shoreward surf zone	shoreward surf zone
L12	3.15	1.95	shoreward surf zone	shoreward surf zone
L13	3.675	2.55	shoreward surf zone	shoreward surf zone

[a] positive if shoreward of the reef edge.

Fig. 3.14 shows that at each location, the maximum instantaneous velocity within one wave period in the presence of the ridge was comparable to that in the absence of the ridge: At the location L1 observed in shoaling zone, the measured velocities had identifiable periods and similar magnitudes. In the outer surf zone and before the plunging point (L5), the instantaneous flows became more asymmetric and skewed, and a saw-tooth shape could be observed. In the inner surf zone shoreward

of splashing points (L9), the flows became somewhat irregular, due partly to the effect of the turbulence generated by breaking waves on the measurements and partly to the generation of higher harmonics. Thus there was a notable mismatch between the two velocity time-series. The maximum velocities at L9 for both reef profiles were also reduced compared with those at L1 and L5. Moving further shoreward of the surf zone (L13), the flows became more organized and there were secondary peaks because of the higher harmonic waves. However, the velocity magnitudes were almost the same as those at L9.

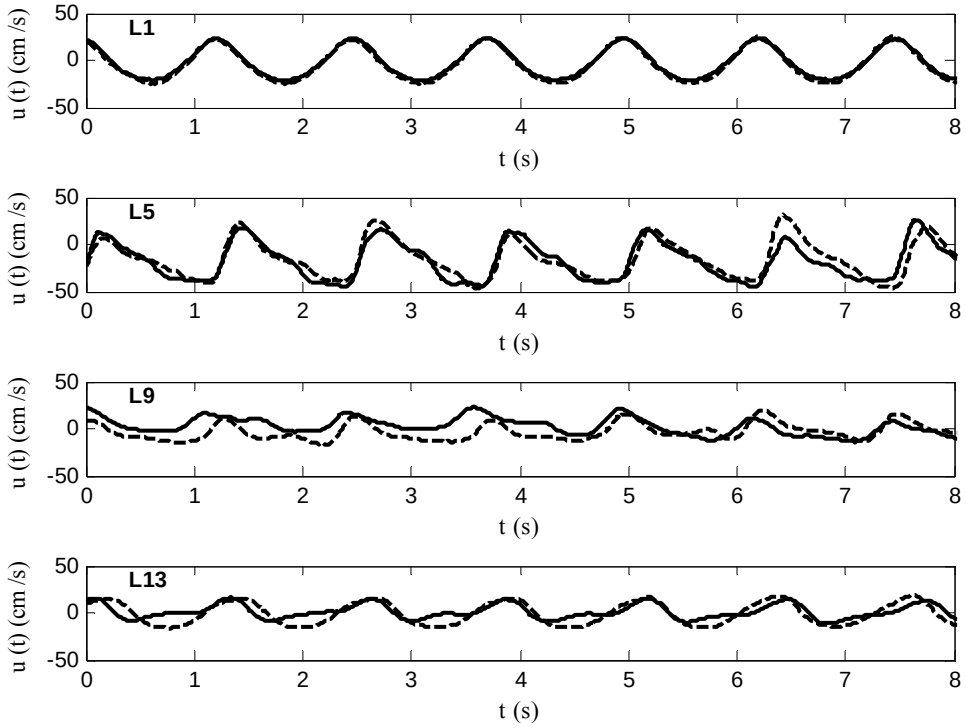

Fig. 3.14 Time-series of flow records from selective measurement locations (L1, L5, L9, L13) across different reef profiles. Dash lines - without ridge; solid lines - with ridge. See Table 3.3 for the distances between those locations and reef edge.

The time-averaged horizontal velocities (u component) are shown as a function of water depth in Fig. 3.15 for the reef without the ridge and Fig. 3.16 for the reef with the ridge. In the present study for monochromatic waves, the ensemble average method was implemented by phase-averaging the measured records at each sampling point over a number of wave cycles. These values were averaged to yield

the time-averaged u velocity. The standard deviation of these values is also indicated in the figure as an error bar for that sampling point. The position of each sampling point is specified by the distance from the reef edge (x , positive if shoreward of reef edge) and the relative elevation, z/h (where z is the local water depth of sampling point with $z=0$ on the still free surface and h is the local still water depth). Exact measurement locations may be varied due to the difference in surf zone width for the two reef profiles. The undertow velocity is normalized by the local shallow wave celerity, $c=\sqrt{gh}$. The magnitudes of the velocities under the trough of breaking waves were generally in the range 0 - 50 cm/s in present experiments and the measurement error (see the error bars in both figures) is generally larger at those locations near the splashing points (e.g., L7 and L8) due to the air bubbles entrained in water.

For the horizontal reef flat without the ridge, Fig. 3.15 shows that the undertow was offshore-directed at the shoaling locations (L1 - L3); it increased almost linearly from the bed upwards, which is typical for non-breaking waves. L4 and L5 were in the outer surfzone but before the plunging point, the velocity profiles were not linear, showing values close to zero near the bed and being the maximum near the trough of breaking waves. Maximum velocities both at L4 and L5 were approximately 0.15c near the trough level. In the inner surf zone (shoreward of splashing region) where initial wave breaking was completed with fully developed bores, most of the velocities were negative at the measurement locations (L6 - L11), i.e., offshore directed, and their magnitudes decreased almost linearly from the bottom to the trough. Close to the wave trough, they may become positive, i.e., onshore directed, due to the mass transport above the wave trough as well as in the bore (Svendsen, 1984b). From L6 to L11, wave breaking reduced in intensity and there was a gradual reduction in the bore size by visual observation. The reduction in bore size was accompanied by a decrease in the magnitudes of undertow. Outside the surf zone (L12 and L13) where the wave setup was almost constant, the vertical velocity became almost zero, indicating that there was no reef-flat circulation shoreward of the surf zone for fringing reefs. The correlation between the setup and

undertow at all these locations can be justified by the cross-shore momentum balance as will be discussed in Chapter 7.

When the ridge was present, the offshore undertow profiles at L1 and L2 were similar to those in the absence of the ridge, see Fig. 3.16. However, the flow structure at L3, where the waves were near-breaking, was significantly altered by the ridge. At those locations beneath the breaking waves on the shallow ridge top (L4 - L6), the offshore-directed nonlinear curve profiles again could be observed; their magnitudes were almost doubled (around $0.3c$) compared with those without the ridge. The maximum velocity occurs at the reef/ridge edge and was approximately $0.45c$. L7 was close to the splashing point on the ridge-top, the velocity profile at this location resembled that at L6, but the magnitudes were significantly smaller. From L8 to L11 (inner surf zone), the vertical flow structure gradually evolved from the nonlinear curve to a linear profile, followed by a reduction of velocity magnitudes further shoreward of the ridge. The linear profiles had a seaward current near the bottom and a shoreward current near the trough. Beyond the surf zone, the magnitudes of undertow at L12 and L13 were again very weak. By comparing the overall flow pattern in the presence of the ridge with that in the absence of the ridge, it can be concluded that the ridge behaves in a similar way to a weir in an open channel flow, which can act to block the flow (undertow) upstream (leeside of the ridge). From an energy point of view, it means that more kinetic energy (in the form of undertow velocity) is converted to potential energy (in the form of wave setup), but the total energy pumped by breaking waves onto the reef flat might be conserved.

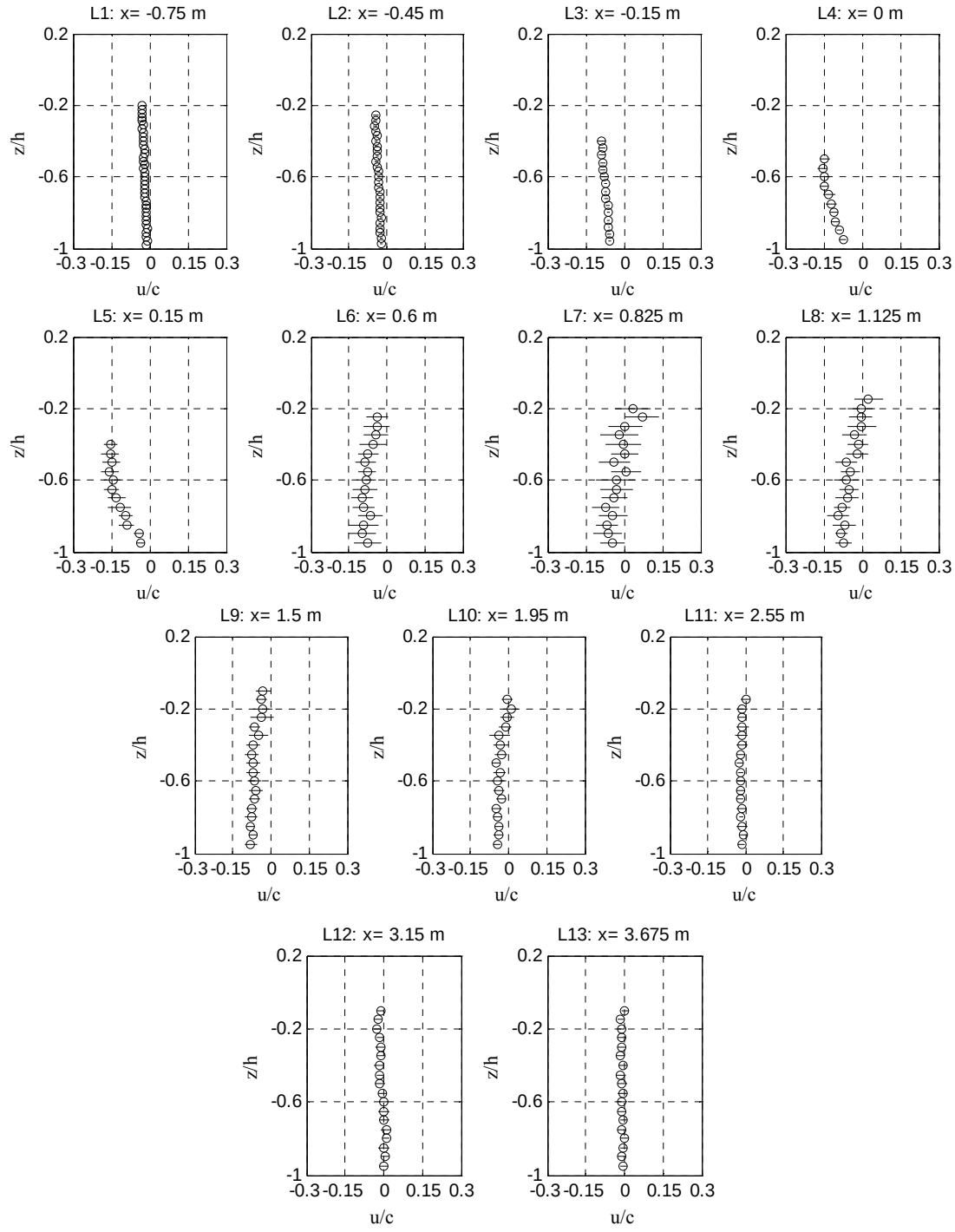

Fig. 3.15 Variation of time-averaged horizontal velocity as a function of depth in the absence of the ridge ($c = \sqrt{gh}$ is the local shallow-water wave celerity; Solid lines indicate the error bars based on the standard deviation of phase-averaged velocity).

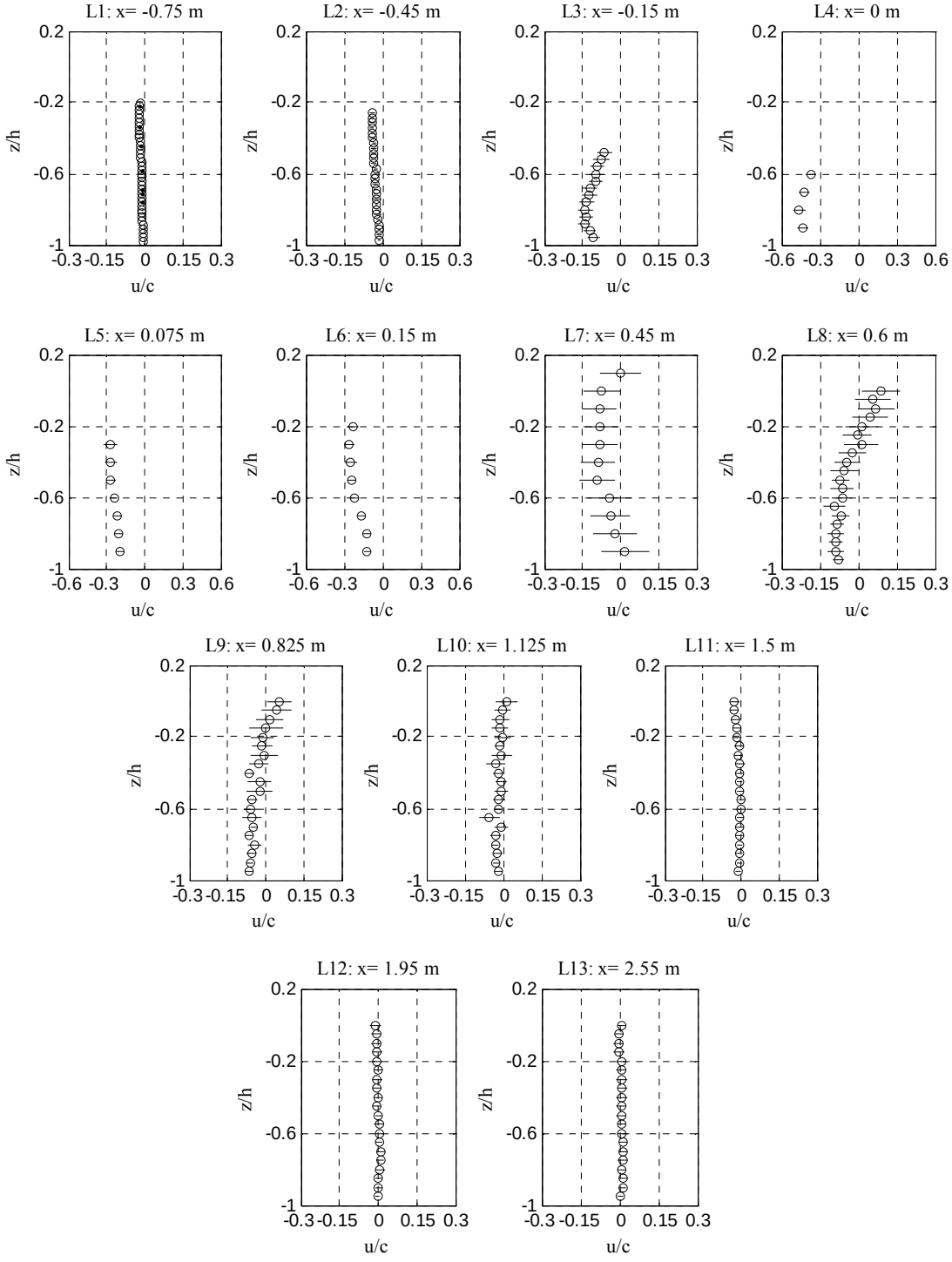

Fig. 3.16 Variation of time-averaged horizontal velocity as a function of depth in the presence of the ridge ($c = \sqrt{gh}$ is the local shallow-water wave celerity; Solid lines indicate the error bars based on the standard deviation of phase-averaged velocity).

Generally speaking, the observations without the ridge in this section are in agreement with the measurements for a plane slope with a plunging breaker (Ting and Kirby, 1994). The predominant offshore-directed undertow currents are largely because of the closed laboratory flume, which requires that the wave-induced mass transport above wave trough level is compensated by a seaward flow below this level so that the depth-averaged net flux is zero. If there is a circulating pipe connecting both ends of the flume or a gap in the fore-reef or ridge model, the undertow may be significantly smaller or even directs towards the shore as found from the horizontally two-dimensional (2DH) flow measurements (e.g., Drønen et al., 2002). An analytical modeling of the 2DH flow pattern for the reef system will be given by section 7.7 although the present laboratory experiments did not go that far.

3.6 Discussions

In this section, some discussions on the possible effects of the laboratory settings on the experimental results is given.

In the experiments, there is a setdown of the mean water level seaward of the fore-reef resulting from the mass conservation in a closed flume (see e.g., Fig. 3.7). However, the magnitude of this setdown is generally less than 1 cm. For a typical test condition with a wave period of 1.25 s and a water depth of 40 cm, this only causes of a decrease of wave length by 1% according to the liner dispersion relationship, thus it has a negligible effect on the incident wave characteristics and does not change the breaking conditions on the fore-reef. It is stressed that the same still water level is ensured when comparing wave-induced setups and that the setup is defined as the deviation of the mean water surface from the still water level. Therefore, the higher setup is not affected by the setdown in front of the reef model. In fact, a larger setdown in front of the shoaling zone is actually the result of a larger setup, not the other way around, as there is no driving force in the water in front of the shoaling zone.

One may also wonder whether this seaside setdown leads to a stronger offshore flow near the reef crest or not, which again might impact the breaking process. In the closed flume, since the offshore mean current (undertow) is balanced by shoreward wave-induced mass transport, its magnitude should depend largely on the breaking-wave characteristics rather than the setdown. Within one wave period, there is an inflow phase and an outflow phase; each has duration of about half the wave period. When water rushes up the reef flat, it is the inflow phase, and when water retreats from the reef flat, it is the outflow phase. The wave breaking process is largely controlled by the incoming wave meeting with the outflow at the breaking point. When waves break, the wave orbital velocity is of $O(\sqrt{g(h_b+\overline{\eta})}$, i.e., the inflow velocity is of $O(\sqrt{g(h_b+\overline{\eta})}$, which is of $O(1m/s)$ for the test case in section 3.5. The outflow depth is much smaller than the inflow depth in the experiments, i.e., the outflow is basically a sheet flow, which has a velocity much larger than $O(\sqrt{g(h_b+\overline{\eta})}$. The undertow at the reef edge for the test case is just about 0.3 m/s even when the ridge is present. Therefore, the outflow velocity is much stronger than the mean current and the effect of the mean current on the wave breaking process is secondary.

For the fringing reef model in this study, the reef or ridge structure "block" water exchange between the back reef (shoreward of reef flat) and the seaside of the fore-reef). Wave breaking will dissipate most wave energy within the surf zone, and the waves outside the surf zone on the reef flat are very weak. For a fringing reef with a closed lagoon, the net flow rate is always zero with or without the ridge, even though a circulation (a forward mean flow above the wave trough and a backward mean flow near the bottom (undertow)) is possible on the reef flat. Figs. 3.15 and 3.16 show that the undertow is weak in the shoaling zone and shoreward of the surf zone for both reef models with and without the ridge, thus the water exchange between the seaward side of fore-reef and the lagoon is always weak. However, in the surfzone when the ridge is present, the undertow velocity significantly is increased in the vicinity of the ridge and decreased on the leeside of the ridge, suggesting that there is indeed a certain degree of blocking effect introduced by the

ridge, but it is difficult to quantify how much water is blocked by the ridge. For a barrier reef without an open lagoon, the wave-induced setup could force the water to the back lagoon and the net flow rate is not zero on the reef flat; the non-zero flow in turn could affect the magnitude of setup in the surf zone. Gourlay (1996a) studied experimentally the wave-induced setup over both fringing reefs and platform (barrier) reefs (open lagoon), and he found that the magnitude of the wave-induced setup on a platform reef (with a net mean flow) was smaller than that on a fringing reef (with zero net flow) by an amount equal to the velocity head of the mean flow on the reef platform (i.e., a mean current of 0.5 m/s on the reef flat may reduce the wave-induced setup by about 1.2 cm). The difference between the wave-induced setups for barrier reefs and fringing reefs should be the upper bound of the effects of the mean flow on wave-induced setups. In our experiments, the net mean flow rate is zero and the undertow is weak, thus the influence of the mean current should be negligible.

3.7 Concluding Remarks

In this chapter, a series of experimental results for reef profiles with and without a seaward edge ridge and for both monochromatic and spectral waves have been presented. The experimental data show that the behavior of the wave transformation and wave breaking in the presence of a ridge are significantly different from those in the absence of the ridge. In particular, a ridge near the reef edge can cause an increase in the wave-induced setup over the reef flat. Furthermore, the ridge drastically increases the reflection coefficients of the reef model. Experimental results also show that the energy dispassion due to wave breaking results primarily from the fundamental harmonic waves, and that the second harmonic waves may become comparable to the fundamental harmonic waves on the reef flat. The distribution of the momentum flux in surf zone for fringing reefs is different from that for plane beaches, and a measured value of radiation stress below that obtained by using linear shallow-water approximation is consistently observed. The cross-shore undertow velocity profile for fringing reefs in the absence of the ridge is similar to that for plane beaches if plunging breakers occur on both bed profiles are similar; the existence of the ridge may cause a retention of the flow on the leeside of

the ridge. The generality of above remarks needs to be further verified by more experiments with different reef/ridge configurations under various wave conditions.

CHAPTER 4 NUMERICAL STUDY OF WAVE TRANSFORMATION OVER FRINGING REEFS

4.1 Literature Review

Hydrodynamics associated with waves on fringing coral reefs is more complex than that on plane beaches. As introduced in Chapter 1, a typical fringing coral reef involves a transition of bottom profile from deep to shallow waters over a long distance, and a porous reef surface which may provide high resistance to the waves. Numerical modeling of nearshore coral reef hydrodynamics faces several challenges such as the steep fore-reef slopes (e.g., Seelig, 1983; Gourlay, 1996a; Hench et al., 2008), the complex configurations of reef crest and reef flat (e.g., Seelig, 1983; Hench et al., 2008), the spatially-varied roughness of reef surface (e.g., Lowe et al., 2005). Also, the wave transformation usually needs to be modeled over long time scales (several hundred waves) and large space scales (over the entire reef profile).

Over decades, analytical models frequently deal with the one-dimensional horizontal (1DH) idealized reef profiles (a typical idealized reef profile has a plane sloping fore-reef and a horizontal platform reef flat). Conventionally, in analogy to the wave-driven cross-shore flows and the wave-induced setup/setdown on beaches (e.g., Svendsen, 2006), analytical solutions based on the radiation stress concept introduced by Longuet-Higgins and Stewart (1964) had been used frequently in the past to study 1DH reef hydrodynamics (Gourlay, 1996a; Symonds et al., 1995; Hearn, 1999; Gourlay and Colleter, 2005). In recent years, the effects of complex bathymetry and different forcing mechanisms have been modeled by using two-dimensional horizontal (2DH) and three-dimensional (3D) models to study both the waves and the mean flows, and usually the radiation stress concept is used to couple the waves and the mean flows (Kraines et al., 1998, 1999; Douillet et al., 2001; Luick et al., 2007; Storlazzi et al., 2011). The modeling results presented by Lowe et al. (2009b) look very promising, even though the predicted mean water level was not as accurate as the computed wave heights and currents. Compared to field

studies, fewer numerical models have been applied to well-controlled, small-scale laboratory investigations in the literature.

The most advanced approaches based on Navier–Stokes equations and various turbulence closures, e.g., the models with RANS-based turbulence closure. (Lin and Liu, 1998; Losada et al., 2005; Lara et al., 2008; Torres-Freyermuth et al., 2010), are well suited for simulating breaking waves and wave-structure interactions in small confined regions. However, Navier-Stokes approaches are still very computationally expensive to run, especially for the nearshore zones where a large number of grid points and a fine mesh are needed to accurately capture the fine turbulence structures, thus its use is generally restricted to a small number of waves and small regions. Currently, applying Navier-Stokes models to field scale reef profiles is not feasible.

Another type of prevailing model, which is more computationally efficient, is based on Boussinesq-type equations. This depth-integrated modeling approach employs a polynomial approximation to the vertical profile of velocity field, thereby reducing the dimensions of a three-dimensional problem by one. It has been proven to be able to account for both nonlinear and dispersive effects at different degrees of accuracy. After the first introduction of Boussinesq equations by Peregrine (1967), considerable efforts have been made in different ways to extend the Boussinesq equations to deeper waters (e.g., Madsen and Sørensen, 1992; Nwogu, 1993; Wei et al., 1995; Lynett et al., 2002) and to surf zones or swash zones (e.g., Madsen et al., 1997; Kennedy et al., 2000; Veeramony and Svendsen, 2000). One of the pioneer studies of extending Boussinesq-type model to coral reef studies was conducted by Skotner and Apelt (1999), who studied the wave-induced setup by monochromatic waves propagating onto a submerged fringing coral reef which consisted of a relatively steeper fore-reef. They found that a Boussinesq-type model could simulate satisfactorily the patterns of mean water level for 1DH reef profiles subjected to small waves, but there was a tendency to underestimate the wave-induced setup as the incident wave height was increased. Demirbilek and Nwogu (2007) used a different set of Boussinesq equations to study spectral waves

transforming over a reef profile that was similar to the one used by Skotner and Apelt (1999). They confirmed the ability of their Boussinesq model in describing the variation of significant wave height, the mean water level across the reef profile, the evolution of the wave spectrum, the generation of infragravity oscillations and shoreline runups. More recently, Roeber et al. (2010) employed a shock-capturing Boussinesq-type model to simulate the solitary wave transformation over fringing reefs, which involved energetic wave breaking, bore propagation and the transition from subcritical to supercritical flows under an initially dry reef crest.

The main objective of this study is to implement and validate a weakly dispersive and fully nonlinear depth-integrated Boussinesq-type model[1] to help interpret some of the previous laboratory work (Chapter 3, also see Yao et al., 2009) and other similar published work on wave transformation over fringing reefs. The present numerical model is chosen because it is capable of simulating a wide range of long and short wave problems (Lynett et al., 2002; Hsiao et al., 2005; Lynett, 2006). The model has also been applied to wave overtopping over a levee system by Lynett et al. (2010). This chapter will first report a preliminary validation of the adopted model for an idealized reef profile, then present comprehensive comparisons between numerical simulations and available published data for various wave conditions and different fringing reef configurations. The effects of the fore-reef shapes and sloping angles on the mean water levels and wave heights will also be investigated using the validated numerical model.

The remainder of this chapter is organized as follows. In section 4.2, the mathematical formulation, numerical scheme, boundary conditions and energy dissipation sub-models are described. In section 4.3, calibration and validation of the numerical model are performed. Numerical simulations are compared with available experimental data for four representative scenarios to show the robustness of the model in section 4.4. In section 4.5, a revisit of two published numerical works on wave transformation over ringing reefs is reported. In section 4.6, the

[1] CoulWave code V.2.0. was modified for this study. See Lynett and Liu (2008) for details of CoulWave.

validated model is applied to study the effects of the inclination of a plane fore-reef and the shape of fore-reef on the wave dynamics over the fringing reefs. The main conclusions drawn from this study will be given in section 4.7.

4.2 Description of the Numerical Model

4.2.1 Governing equations

Let x-coordinate be pointing in the direction of wave propagation with its origin at the toe of the fore-reef, and z-coordinate pointing upward with its origin at the still water level. The 1DH equations in non-conservative form are expressed as

$$\begin{aligned} &\eta_t + \left[(\eta+h)u_\alpha\right]_x \\ &-\left\{(h+\eta)\left[\left(\frac{1}{6}\left(\eta^2-\eta h+h^2\right)-\frac{1}{2}z_\alpha^2\right)u_{\alpha xx}+\left(\frac{1}{2}(\eta-h)-z_\alpha\right)(hu)_{\alpha xx}\right]\right\}_x = 0 \end{aligned} \tag{4.1}$$

$$\begin{aligned} &u_{\alpha t}+u_\alpha u_{\alpha x}+g\eta_x+\frac{z_\alpha^2}{2}u_{\alpha xxt}+z_\alpha\left(hu_{\alpha t}\right)_{xx} \\ &+z_\alpha\left[u_\alpha\left(hu_\alpha\right)_{xx}\right]+z_\alpha z_{\alpha x}u_\alpha u_{\alpha xx}+\frac{z_\alpha^2}{2}\left(u_\alpha u_{\alpha xx}\right)_x \\ &+\left(u_\alpha z_{\alpha x}\right)\left(hu_\alpha\right)_{xx}+\left(hu_\alpha\right)_x\left(hu_\alpha\right)_{xx}-\left[\eta\left(hu_{\alpha t}\right)_x\right]_x \\ &+\left[\eta u_{\alpha x}\left(hu_\alpha\right)_x-\frac{\eta^2}{2}u_{\alpha xt}-\eta u_\alpha\left(hu_\alpha\right)_{xx}+\frac{\eta^2}{2}\left(u_{\alpha x}^2-u_\alpha u_{\alpha xx}\right)\right]_x = 0 \end{aligned} \tag{4.2}$$

where η is the water surface elevation; h is the still water depth; g is the gravitational acceleration and $u_\alpha\left[x, z=z_\alpha(x,t)\right]$ is a reference horizontal velocity in the x-direction at a specified depth of $z_\alpha(x,t) = -0.531h$ (Nwogu, 1993). The complete derivation of above equations was given by Lynett and Liu (2008) and their conservative form can be found in Kim et al. (2009).

For 1DH problems, there are two sources of energy dissipation: bottom friction and wave breaking. Adding the dissipation terms to the momentum equation gives

$$\frac{\partial Du_\alpha}{\partial t}+\cdots+R_f-R_b=0 \tag{4.3}$$

where $D = h + \eta$ is the total water depth, R_f and R_b are ad-hoc dissipative terms accounting for the bottom friction and the wave breaking, respectively. Sub-models for R_b and R_f will be discussed in section 4.2.4 and 4.2.5, respectively.

4.2.2 Numerical scheme

The numerical solver for the above equations has been described in details in Kim et al. (2009). A third-order Adams-Bashforth predictor and a fourth-order Adams-Moulton corrector scheme are used for time marching. For the spatial discretization, a shock-capturing Finite Volume (FV)-based approach is used. The leading order terms are solved with the fourth-order MUSCL-TVD (monotone upstream-centered scheme for conservation laws-total variation diminishing) scheme, while for the second-order terms, a cell-averaged finite volume method is implemented. Compared with traditional Finite Difference (FD)-based methods, FV formulations in conservative form are generally very stable and accurate, thus appropriate for the present problems which may have complex flow conditions and rapid bottom variations. The numerical scheme is accurate to $O(\Delta t^4)$ in time and $O(\Delta x^4)$ or $O(\Delta x^2 \mu^2)$ in space, where μ is the wave length scaling parameter defined by $\mu = h / L$, with L being the incident wave length. For the present model, a value of 0.5 for the Courant number (C_r) will typically yield stability and convergence, but for simulations with highly nonlinear waves, a value as low as 0.1 may be required for stability (Lynett and Liu, 2008).

4.2.3 Boundary and initial conditions

Numerical boundary conditions

Two types of numerical boundary conditions can be applied at the two ends of the computational domain: the reflective (or no-flux) boundary condition and the radiation (or open) boundary condition. For the latter, sponge layers are frequently used to effectively damp the energy of outgoing waves. The sponge layer is usually applied in a manner similar to that recommended by Kirby et al. (1998). For completeness, the implementation of sponge layers in CoulWave is given in

Appendix D. The moving boundary can be simulated using the "slot technique" (Tao, 1983), the Lagrangian method by Zelt (1991), or the extrapolating boundary algorithm (Lynett et al., 2002); the latter is used here to describe wave runup and rundown processes. It utilizes a linear extrapolation of free surface and velocity through the wet-dry boundary and into the dry region, thereby allowing the real boundary location to exist in-between nodal points. The technique is also simple to implement and numerically stable, does not require any sort of additional dissipative mechanisms or filtering (Lynett et al., 2002). The moving boundary algorithm is needed only when the initially dry reef flats are studied.

Wave generation and initial conditions

Internal source methods are frequently employed as efficient and accurate methods for numerical wave generations (e.g., Lin and Liu, 1999; Wei et al., 1999; Hsiao et al., 2005). The method using a distributed source function in the continuity equation as proposed by Wei et al. (1999) is adopted in this study. Irregular waves are generated by summing up many regular waves with different frequencies, amplitudes and random phases for a given spectrum. The initial condition assumes no wave or current motion in the computational domain.

4.2.4 Wave breaking (R_b)

It is well-known that the depth-integrated Boussinesq-type models cannot describe the overturning of a free surface and the detailed breaking process. Hence several empirical models have been proposed for the wave breaking in surf and swash zones. The most common approach is to add an ad-hoc dissipation sub-model to the momentum equation. There are two primary types of breaking models: roller models (e.g., Schäffer et al., 1993; Madsen et al., 1997; Veeramony and Svendsen, 2000) and eddy viscosity models (e.g., Zelt, 1991; Karambas and Koutitas, 1992; Kennedy et al., 2000). Even though the two approaches stem from different ideas and have different controlling parameters, their overall effects in the momentum equation are similar: both require an energy dissipation mechanism and a trigger mechanism for the initiation of wave breaking. One of the basic requirements on empirical breaking models is that they must ensure conservation of mass and

momentum as well as preserve some nonlinear wave properties in surf zones. In this study, the simple eddy viscosity-type formulation proposed in Kennedy et al. (2000) is used to model the wave energy dissipation caused by wave breaking. It has been proven that the adopted wave breaking model can adequately predict the energy dissipation for both spilling and plunging breakers (Kennedy et al., 2000; Lynett, 2006; Roeber et al., 2010). For completeness and the convenience of discussing the numerical results, the breaking model in CoulWave is summarized below.

The 1DH form expression for R_b is given by

$$R_b = \left[\nu \left(H u_\alpha \right)_x \right]_x \tag{4.4}$$

where ν is an empirical eddy viscosity and given by the following zero-equation turbulence model

$$\nu = \Phi \delta H \eta_t \tag{4.5}$$

where δ is an empirical coefficient to correct both the mixing-length and friction-velocity scales. The parameter Φ accounts for the trigger mechanism to ensure a smooth transition between breaking and non-breaking states. The expression for Φ is given by

$$\Phi = \begin{cases} 1 & \eta_t \geq 2\eta_t^* \\ \eta_t / \eta_t^* - 1 & \eta_t^* < \eta_t \leq 2\eta_t^* \\ 0 & \eta_t \leq \eta_t^* \end{cases} \tag{4.6}$$

where η_t^* determines the onset and stoppage of the breaking process and is evaluated by

$$\eta_t^* = \begin{cases} \eta_t^{(F)} & t - t_0 \geq T^* \\ \eta_t^{(I)} + \dfrac{t - t_0}{T^*} \left(\eta_t^{(F)} - \eta_t^{(I)} \right) & 0 \leq t - t_0 < T^* \end{cases} \tag{4.7}$$

where $\eta_t^{(I)}$ is a threshold value at the breaking inception ; $\eta_t^{(F)}$ is a saturated value for the breaking cessation; t_0 is the time at which the breaking event starts; $t - t_0$ is the age of breaking event; T^* is the duration of the breaking event. Determination

of the four empirical parameters in the breaking model (i.e., $\delta, \eta_t^{(I)}, \eta_t^{(F)}, T^*$) will be discussed later.

4.2.5 Bottom friction (R_f)

The bottom friction term R_f can be calculated by the following quadratic friction law

$$R_f = f u_b |u_b| \tag{4.8}$$

where u_b is the bottom velocity and can be evaluated from u_α; f is an empirical fiction coefficient, which can be related to Manning coefficient (n_M) by

$$f = \frac{g n_M^2}{H^{1/3}} \tag{4.9}$$

Values of n_M for surfaces of commonly used materials can be found in any standard text book for hydraulics or fluid mechanics.

4.3 Model Calibration and Validation

4.3.1 Experimental and numerical settings

Experimental setting

The laboratory experiments in Chapter 3 are re-summarized in this section for the convenience of the following simulations: the measurements were conducted in a closed wave flume in the Hydraulics Modeling Laboratory, Nanyang Technological University, Singapore. The flume is 36 m long, 0.55 m wide, and 0.60 m deep. The experiments were designed to study the hydrodynamic characteristics of two types of reef-crest profile subjected to both monochromatic and spectral waves: (1) an idealized fringing reef without a ridge and (2) a fringing reef with an idealized ridge. The first reef model had a relatively steep fore-reef (V:H=1:6) as well as a 7 m-long horizontal reef flat. For the second model, a rectangular box was placed (55 cm long, 50 cm wide and 5 cm high) on the reef flat with its front face aligned with the reef

edge to mimic an idealized ridge (see Fig. 4.1). The dimensions of the ridge model were chosen to mimic the reef ridge existing on the Moorea reef studied by Hench et al. (2008). The detailed experimental settings and preliminary data results for the experiments examined in this chapter have been reported in Chapter 3 as well as in Appendix B. To measure the cross-reef wave transformation, 12 wave gauges (G1 - G12) were used and their arrangement is shown in Fig. 4.1: G9 - G12 were equally spaced over the reef flat with the first gauge being located behind the surf zone. For monochromatic waves, G4 - G8 were located in the vicinity of the reef edge to measure the surfzone waves; G1 and G2 were placed seaward of the reef slope to separate the incident waves from the reflected waves and G3 was placed on the slope to measure the shoaling waves. For spectral waves, the arrangement of wave gauges is slightly different: G3 was moved further seaward to form a three- probe array for wave spectrum separation and G4 was located on the fore-reef to observe wave shoaling; the remaining gauges (G5 - G8) were put close to the reef edge to capture the spectral waves in the surf zone. Exact locations of the wave gauges will be specified later. At the shoreward end of the flume, waves were effectively damped by a porous wave absorber to reduce the wave reflection. A series of monochromatic and spectral wave conditions were tested in the experiments with a range of reef-flat submergences. Spectral waves were generated from the widely-used JONSWAP spectrum with a peak enhancement factor $\gamma = 3.3$.

Numerical settings

Referring to Fig. 4.1, the computational domain, in terms of the dimensions of the flume and the location and shape of the idealized reef model, were designed to reproduce the main aspects of the laboratory settings. The 1DH numerical domain is also 32 m long. Dissipative sponge layers, typically of a width of 1.25 times the incident wavelength, (i.e., $W = 1.25L$, where L is the wave length), were placed at the two ends of the computational domain to ensure that the outgoing waves can be absorbed satisfactorily. The incident wave field was generated by using the aforementioned internal source method. The internal source was placed close to the seaward sponge layer, i.e., $L_1 = 0$. The fore-reef was $b_0 = 2.1\,m$ wide with its toe starting at $L_2 = 16.35\,m$ from the wave generation point. The reef flat, which was

extended all the way to the shoreward sponge layer, had a width of $L_3 = 9.8\ m$; the elevation of the reef flat was fixed at 0.35 m above the flume bottom for all experiments. A representative case of monochromatic waves of $H_0 = 0.057\ m$, $T = 1.25\ s$ and $h_0 = 0.4\ m$ transforming over the horizontal reef flat (i.e., in absence of the ridge) is used for numerical calibrations. The chosen wave condition gives $kh_0 = 1.23, ka = 0.09$ and a positive reef-flat submergence of 0.05 m. For this case, the model parameters were calibrated by using the R-square value (R^2) to minimize (through a trial-and-error procedure) the global error between the measured mean water level and the predicted mean water level at the 12 measurement locations. Friction was not considered in the calibrations. A steady wave field could be reached about 60 s after the start of the simulation, which is shorter than 3 min observed in the laboratory experiments reported in Chapter 3; this is because of the use of sponge layer which reduces the multiple reflections in the computational domain. A total number of 200 waves were simulated for each case to ensure that the last 100 wave cycles in wave records could be used to calculate the wave height and mean water level. The main purpose of this section is to understand the effects of different numerical model parameters on the computed results.

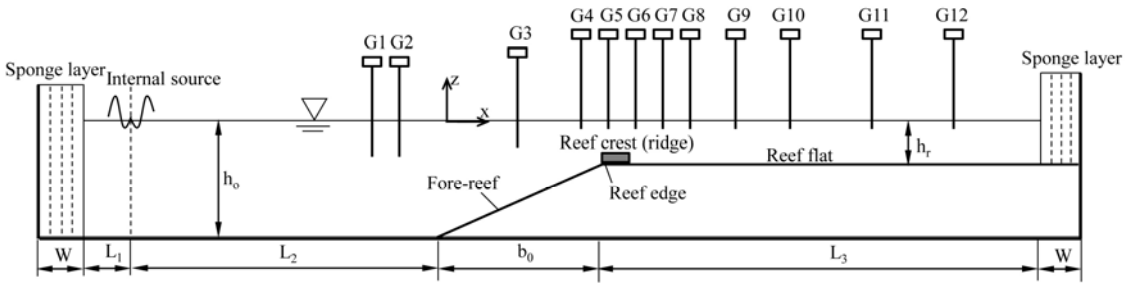

Fig. 4.1 Computational domain for waves propagating over a fringing reef (the exact locations of the wave gauges for all relevant laboratory experiments are given in Table 4.2).

4.3.2 Grid size

The grid size is determined by a predefined grid number per incident wave length (N). A variety of grid number ranging from $N = 25$ to 100 were tested, leading to

the grid size ranging from $\Delta x = 0.02\ m$ to $0.08\ m$, Numerical instability may occur for a finer grid resulting from higher frequency oscillations. Since the time step during the tests is fixed at 0.005 s, the Courant number changes with grid size. The cross-shore variations of wave height and mean water level (which are the primary concerns of this study) are calibrated. Fig. 4.2 shows that a value of $N = 75$ seems to be sufficient to discretize the computational domain, significant improvement on the prediction of the wave height or MWL profile is not found by further reducing the grid size. The values of the transmitted wave height (H_t) as well as the maximum wave setup ($\overline{\eta}_r$) on the reef flat as a function of the grid size are shown in Figs. 4.3(a) and 4.3(b), respectively. It can be observed that the predictions converge with increasing N: both $\Delta H_t / H_t$ and $\Delta \overline{\eta}_r / H_t$ are about 1% when increasing N from 75 to 100. Thus $N = 75$ is used in the subsequent simulations, which gives a grid size of $\Delta x = 0.04\ m$.

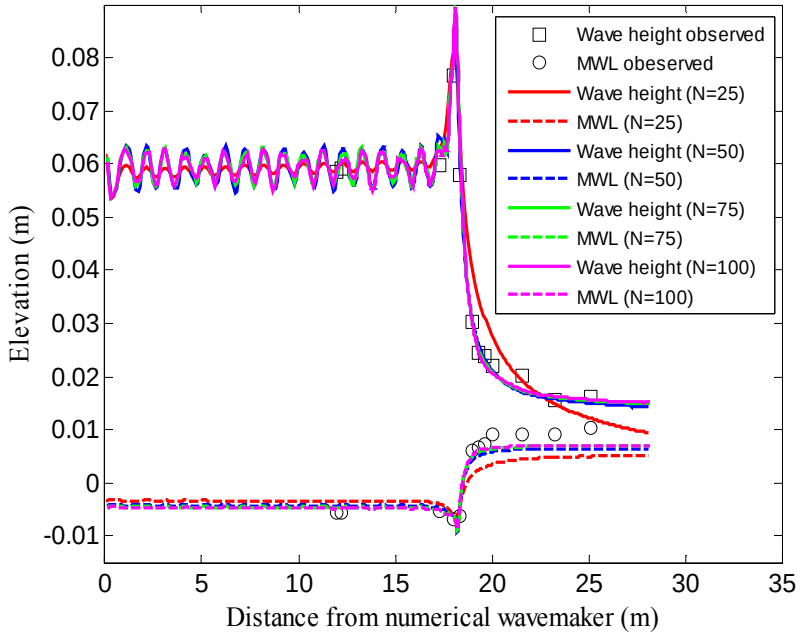

Fig. 4.2 Variation of wave height and MWL across the flume with different grid sizes.

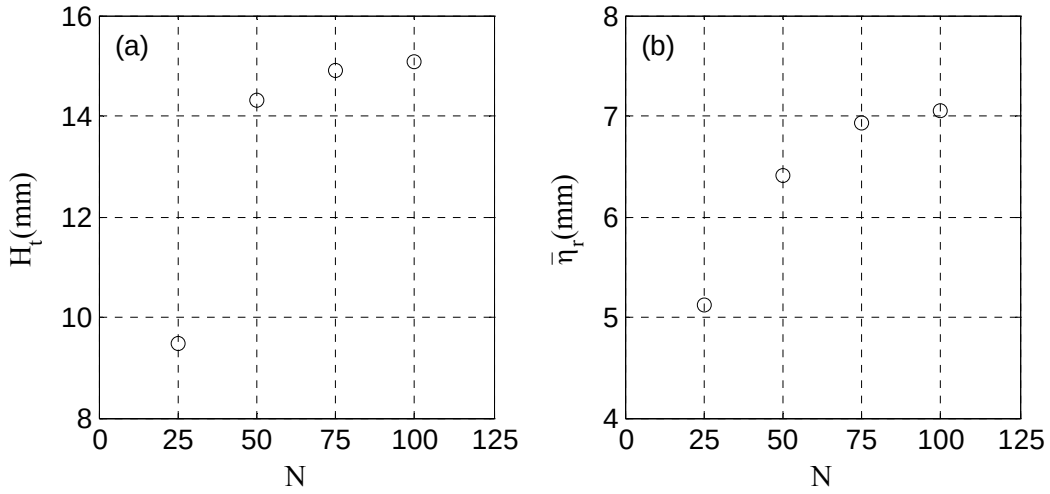

Fig. 4.3 Transmitted wave height (H_t) and maximum wave setup on the reef flat ($\bar{\eta}_r$) as a function of grid number per incident wave length (N).

4.3.3 Boundary conditions

Sponge layers were used to reduce the wave reflection from the numerical boundaries. Since waves are generated internally by using an internal source method in the present model, sponge layer needs to be added to the left boundary to absorb the reflective waves. For the right boundary, different settings may be attempted. To implement the sponge layer concept, both the mass and momentum equations need to be modified by adding artificial damping terms. Pilot test also found during the numerical experiments that the damping terms in the mass balance could significantly affect the computed MWL, which indicated a change of total mass in the computational domain. This was especially true for very shallow reef-flat submergences. Therefore, the following three types of boundary conditions have been studied in order to implement the appropriate numerical boundary conditions for the problem:

BC1: For this type of boundary conditions, sponge layers are used on both sides of the computational domain, and the damping terms are used in both the momentum and mass balance equations;

BC2: For this type of boundary conditions, sponge layers are used on both sides of the computational domain, but the damping term is used only in the momentum equation;
BC3: For this type of boundary conditions, a sponge layer is implemented on the left boundary but only in the momentum equation, and a 1:8 slope combined with high bottom friction ($n = 0.1$) is used for the right boundary to reduce the reflection.

The grid size for this test was kept at $\Delta x = 0.04\ m$. A comparison of the MWLs and wave heights using these three boundary conditions is shown in Fig. 4.4. Results show that the simulated MWL agrees better with the measurement under BC2 than that under BC1; the improvement can be substantial for very shallow reef-flat submergences (not reported here). However, the wave heights obtained using BC1 and BC2 are almost the same. BC3 in principle should perform the best since it mimics the actual laboratory experiment most closely. However, it is difficult to model wave motion in the porous mats placed on the sloping beach to dissipate wave energy. For example, using a high friction coefficient for the final slope to model the porous wave absorber could cause some fluctuation in the wave height on reef flat as indicated by Fig. 4.4. Therefore, BC2, i.e., the sponge layers are used only in the momentum equation, is selected in the following simulations.

This calibration reveals that the damping term in the continuity equation would behave like a sink/source term, causing a significant change of the total amount of water in the computational domain and resulting in an incorrect mean water level. An explanation can be given in view of Appendix D, Eq. (D.1) could remove mass from the computational domain at the boundary through η; this may be of no concern for open boundary problems. However, using Eq. (D.1) in continuity equation to simulate waves in a closed laboratory flume will eventually cause an imbalance or loss of mass in the flume.

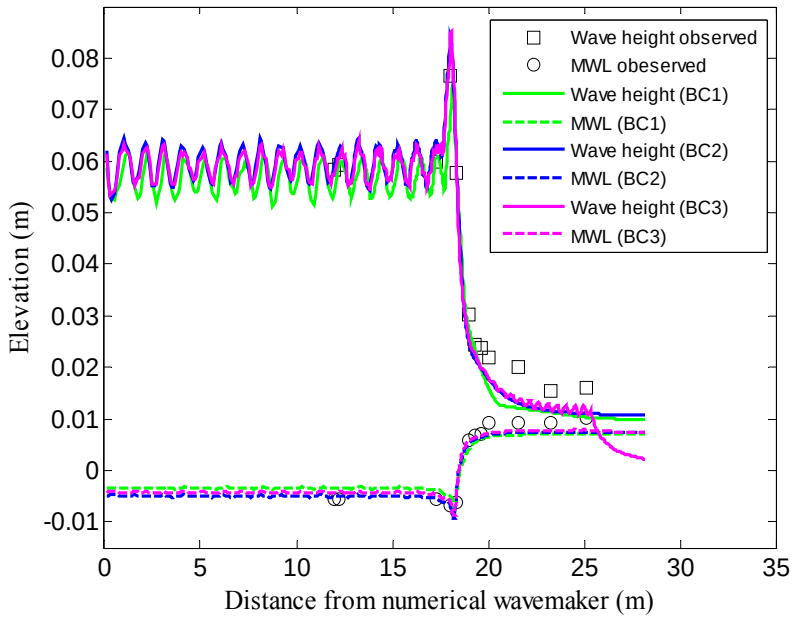

Fig. 4.4 Variation of wave height and MWL across the flume with different boundary conditions.

4.3.4 Breaking model

It is believed that the under-prediction of both the reef-flat MWL and the wave height are attributed to the empirical breaking model used in the simulation. Numerical experiments suggested that δ, which is related directly to the turbulence intensity, is the most important parameter among the four model parameters. Values of δ ranging from 1.4 to 10 can be found in the published literature (Kennedy et al., 2000; Lynett, 2006; Lynett and Liu, 2008). The value depends on the dispersive and nonlinear properties of a given numerical model (Lynett, 2006). For example, Kennedy et al. (2000) used $\delta = 1.2$ for the model of Wei et al. (1995) with linear dispersion and nonlinear properties up to $kh = 3$, and Lynett (2006) used $\delta = 10$ for the model of Lynett and Liu (2004) with linear dispersion and nonlinear properties up to $kh = 6$. However, in practice, a trail-and-error procedure is needed to calibrate this value with measurements. Thus δ was varied from 0 to 10 during the present calibration. For the trigger-related parameters in Eq. (4.7), the following values suggested by Lynett and Liu (2008) were adopted in this study

$$\eta_t^{(I)} = \alpha_1 \sqrt{gH}; \quad \eta_t^{(F)} = \alpha_2 \sqrt{gH}; \quad T^* = \alpha_3 \sqrt{H/g} \tag{4.10}$$

where $\alpha_1 = 0.65, \alpha_2 = 0.08, \alpha_3 = 8$ for plane beaches. Kennedy et al. (2000) used the still water depth, h in place of the instantaneous water depth, H.

Results obtained with different values of δ are given in Fig 4.5. The best agreement is obtained with $\delta = 2$, which is employed to perform the numerical experiments in the rest of the chapter for all idealized fringing reefs without a ridge. For fringing reefs with the ridge, model calibration is needed in order to find a suitable value of δ. However, the wave-induced setup is not sensitive to the change of δ.

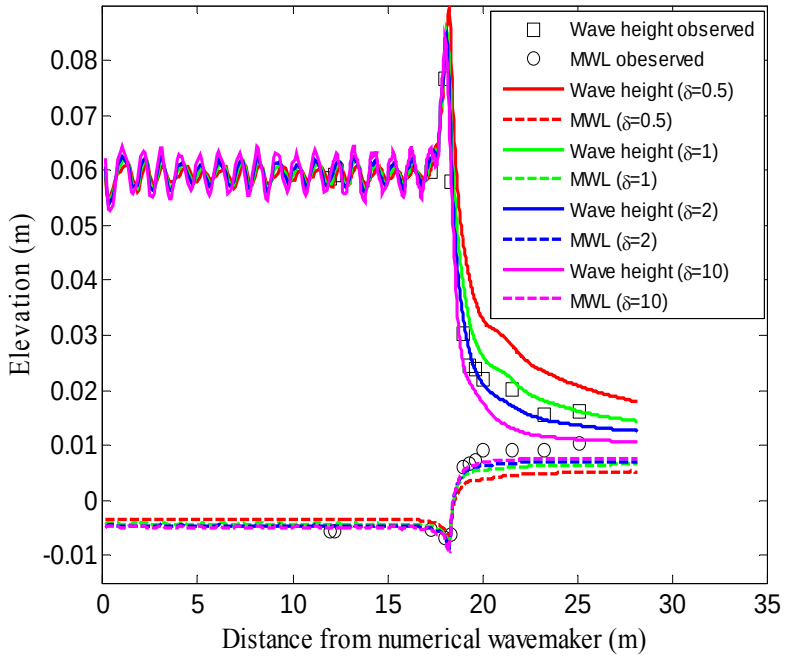

Fig. 4.5 Variation of wave height and MWL across the flume with different turbulence intensities.

4.3.5 Model validation for rapidly varying bathymetry

Unlike beaches, which typically have mild slopes, a typical coral reef often forms a steep transition from the relatively deep to shallow waters. One major concern with applying Boussinesq models to fringing coral reefs is the relatively steep fore-reef

slopes; this is because derivatives of the water depth are included in the higher order terms of Boussinesq equations.

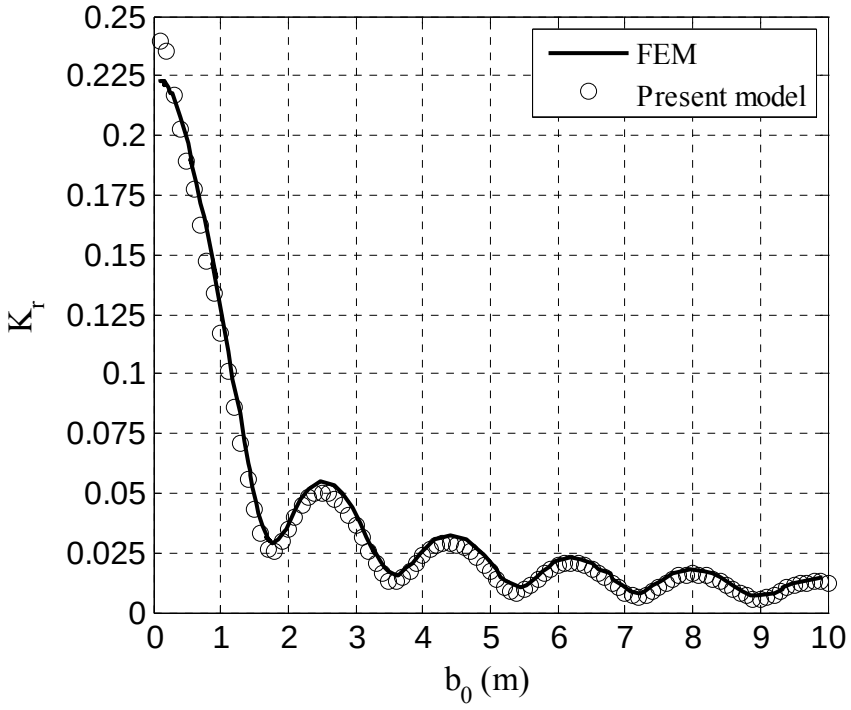

Fig. 4.6 Variation of reflection coefficient (K_r) with the slope width (b_0). Solid line: FEM solution of Suh et al. (1997); Open circles: present model.

As a verification of the capability of the present model to deal with rapidly varying bathymetry, a train of monochromatic waves propagating over a plane shelf are considered here. This problem was first studied by Booij (1983), who investigated the accuracy of a mild-slope equation by comparing the predicted reflection coefficients with Finite Element Method (FEM) solutions. Since then, this problem has become a benchmark against which the accuracy of a hydrodynamic model can be verified. An example for testing Boussinesq-type models using this benchmark is given in Madsen et al. (2006). The bottom profile for this benchmark problem consists of a plane slope connecting two constant-depth regions, which is similar to the idealized fringing reef model (shown in Fig. 4.1). The offshore water depth is $h_o = 0.6\ m$, while the reef-flat water depth is $h_r = 0.2\ m$. A train of monochromatic waves with a period of 2.0 s was studied. The width of the fore-reef

slope varied from $b_0 = 0.1$ m to 10 m, corresponding to the slopes of V:H=4:1-1:25. To resolve the steepest slope numerically, a grid size of 0.04 m and a constant Courant number of 0.5 for all simulations were used.

The computed reflection coefficients are shown in Fig. 4.6, together with the FEM solutions by Suh et al. (1997). The figure clearly shows that the present numerical results are accurate up to the slope width of $b_0 = 0.3\,m$, i.e., a slope of V:H=4:3, but slightly under-predicts the reflection coefficients for very steep slopes. The fluctuation of reflection coefficient with b_0 is due to the multiple reflections between the two edges of the fore-reef.

4.3.6 Results after calibration

Wave height and MWL across the reef profile

The cross-shore variations of MWL and wave height are shown in Fig. 4.7, where the BC2 type boundary conditions, $\Delta x = 0.04\,m$ and $\delta = 2$ were used, also included in the figure is the seabed profile. Overall, the numerical model gives a good prediction ($R^2 = 0.93$) of the variation of MWL across the numerical flume: both the off-reef setdown due to shoaling and the breaking points (the location where the wave height reach its maximum) are reasonably captured by the numerical model despite that the measured location is not sufficient for detailed comparison. However, there is a slight under-prediction of the reef-flat setup. The variation of the wave height along the numerical flume is also satisfactorily predicted. The wavy feature of the computed wave height seaward of the reef model is due to the partial wave reflection, which produces a partial standing wave pattern in front of the reef model. Theoretically, the length of standing waves formed by a supposition of the incident and reflected waves should be one half of the wave length of the incident waves. For this case, the incident wave length is about 2.05 m in the fore-reef region, the estimated wave length of the partial standing wave pattern seaward of fore-reef is 1.03 m, which is in agreement with the observation shown in Fig. 4.7. The rapid decrease of wave height in the surf zone is well captured by the numerical simulation, suggesting that the simple empirical breaking model is appropriate for

this study. There is still a slight under-prediction of the heights of the reformed waves on the reef flat; this under-prediction might be improved if further calibrations of other parameters in the breaking mode were conducted. The calculated reflection coefficient for the first harmonic wave is $K_r = 0.045$, which agrees reasonably well with the measured reflection coefficient $K_r = 0.038$. When calculating the reflection coefficients using the measured or calculated surface displacements, 4th order Stokes wave theory was used to find the amplitudes of the fundamental waves.

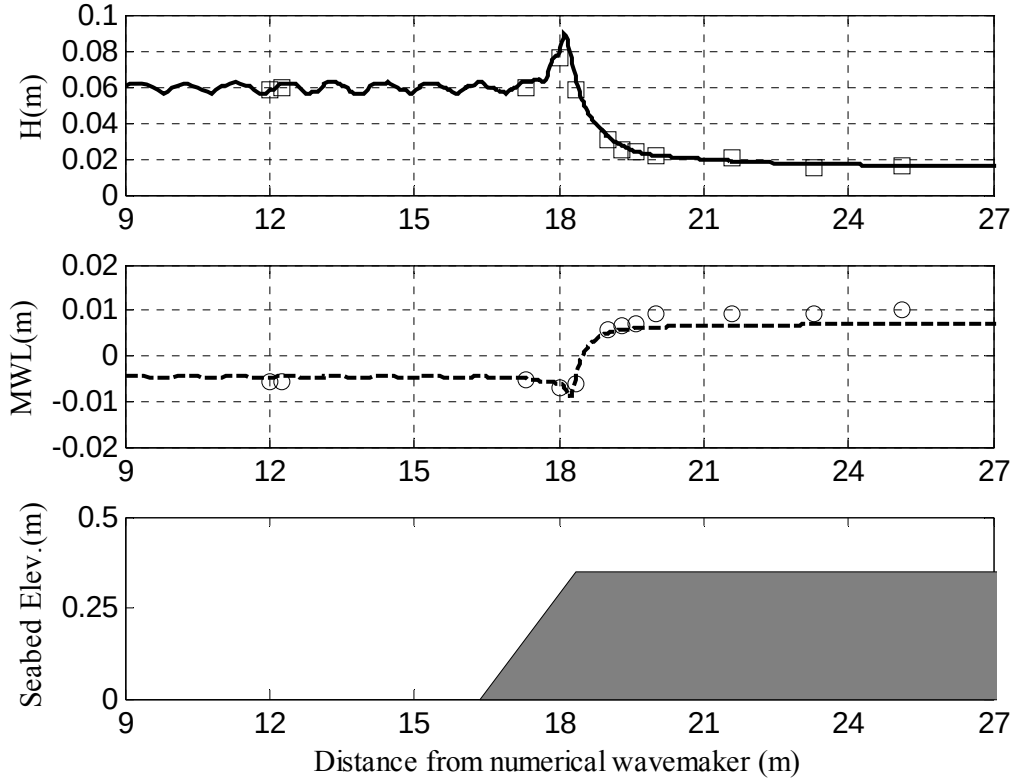

Fig. 4.7 Variation of wave height and MWL across the flume with calibrated numerical settings. Solid lines: predictions by present model; Open circles: laboratory measurements.

Wave transformation across reef profile

Measured and calculated water surface elevations are compared in Fig. 4.8 at six locations, also indicated in the figure is the root-mean-square error (rmse) at each location. It can be observed that very good agreements between predictions and measurements are obtained at most sampling locations (where the rmse is small): off the reef in the deeper water section (G1), the waves are Stokes waves. When waves are on the slope (measured by G3 and G4), wave shoaling makes the wave form asymmetric and skewed. Gauges G5 and G7 are located in the surf zone, thus breaking waves with saw-tooth shape are observed there. These results suggest that the proposed breaking model could reasonably simulate some nonlinear properties such as asymmetry and skewness of the wave form in the surf zone when the incident wave height is relatively small (0.057 m for the case used in calibration). On the reef flat (G9), both numerical and experimental results show that the reformed waves are very small. The generation of the higher harmonic waves can be best seen from the wave amplitude spectrum, which is shown in Fig. 4.9. Up to the fifth harmonics are shown here. It shows that at locations G1, G3 and G9, the numerical model under-predicts the amplitudes of the higher harmonic components. However, in the surf zone (G4, G5 and G7), there is a tendency to over-predict the amplitudes of the higher harmonic components.

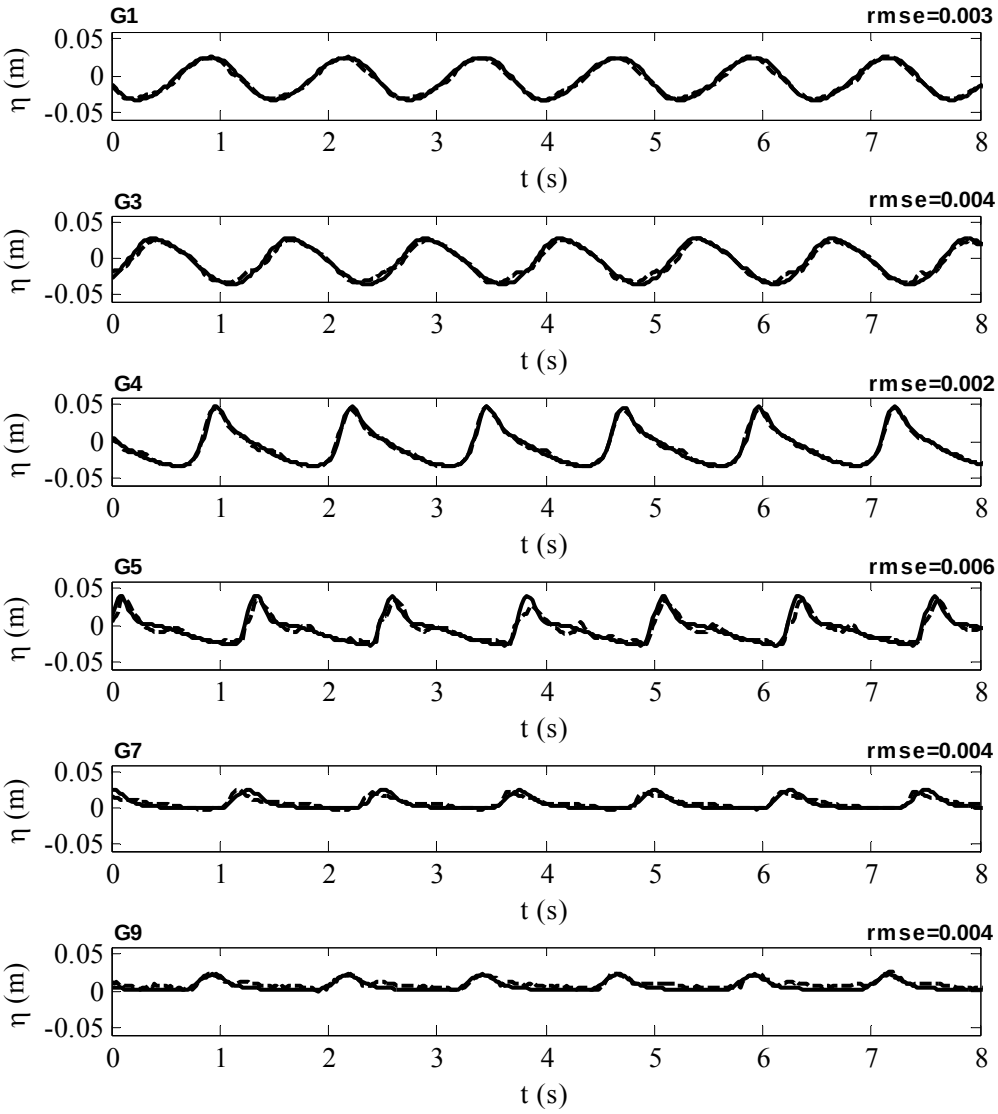

Fig. 4.8 Time-series of surface elevations at six locations (G1, G3, G4, G5, G7 and G9). Dashed lines: laboratory measurements; solid lines: predictions by present model; rmse: root-mean-square error.

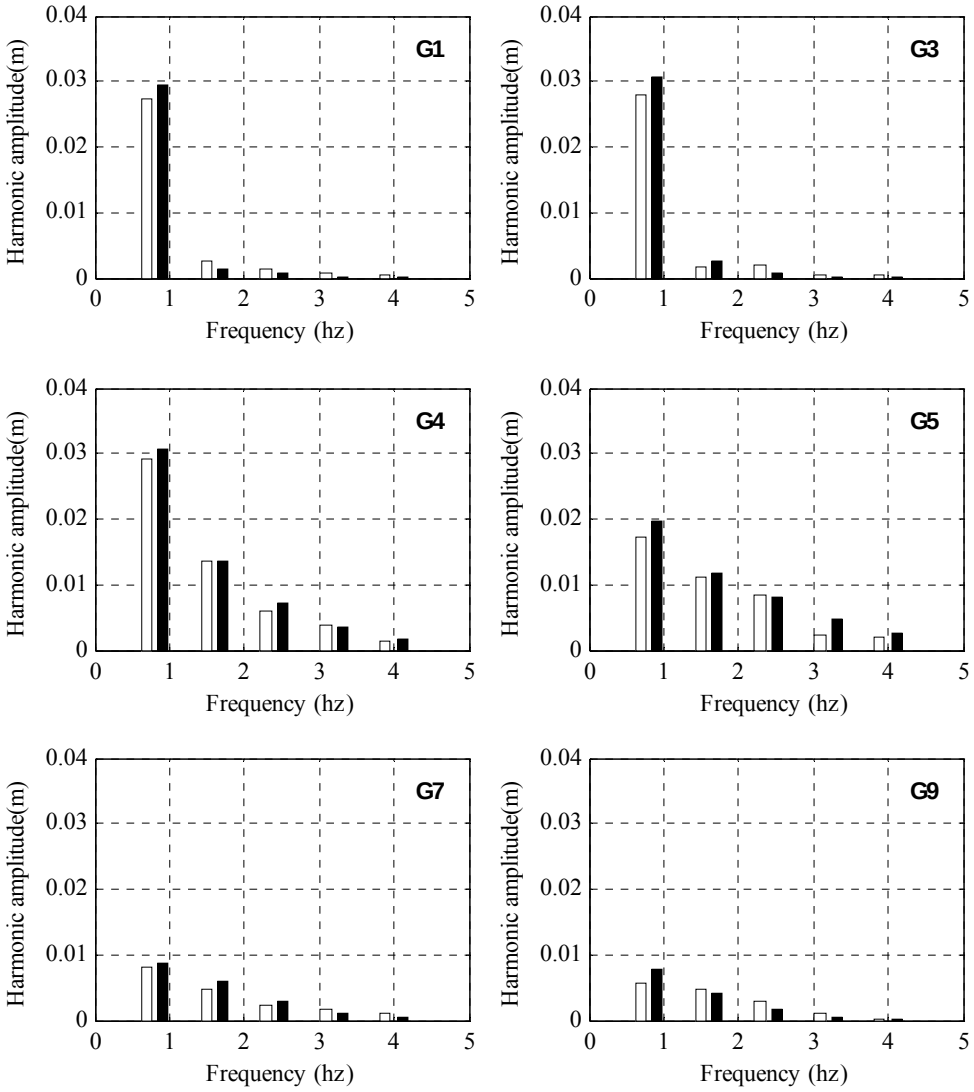

Fig. 4.9 Amplitude spectra from selective wave gauges (G1, G3, G4, G5, G7 and G9). Open bar: observed results; solid bar: predicted results.

4.4 Cases Studies

4.4.1 Case selection and numerical input

Four representative cases are simulated in this study and these are summarized in Table 4.1. Case 1 is identical to the calibration case for monochromatic waves over an idealized horizontal reef flat except that both incident wave height and the reef-flat submergence are increased. Case 2 is different from Case 1 in that a rectangular ridge is present to investigate the model capability to deal with the complex geometry with a reef crest. Since higher order derivatives of water depth are

included in the higher order terms of the Boussinesq equations, abrupt variation in bathymetry such as the seaside and leeside vertical faces of the ridge would cause some high order terms in the Boussinesq equations to grow to infinity. Thus even with shock-capturing scheme and FVM method, the rectangular ridge still need to be smoothed for numerical simulation. In the simulations, both seaside and leeside vertical faces of the ridge were modified to V:H=1:1 slopes to ensure numerical stability. Since the height of the ridge is just 5 cm, the smoothing does not significantly affect the wave transformation in the vicinity of the ridge. The application of the model to an initially dry reef flat, which corresponds to the conditions where a reef flat is exposed to air at low tides, is tested in Case 3. For Case 4, the idealized reef profile subjected to spectral waves is studied. The water depth in the deeper section of the flume (i.e., h_0 in Fig. 4.1) varied from $0.35\,m$ to $0.45\,m$ for the four cases studied here, giving a change of kh_0 from 0.84 to 1.54 and a change of kh_r from 0.27 to 0.53 (see Table 4.1). Numerical wave gauges were placed at the same positions as their laboratory counterparts in the flume. Their exact locations measured from the toe of the fore-reef for the four test cases are given in Table 4.2.

Table 4.1 A summary of the four simulated laboratory experiments

Case No.	T [a] (s)	H_0 [a] (m)	h_r (m)	kh_o	kh_r	ka	Wave type	Reef crest
1	1.25	0.095	0.1	1.33	0.53	0.14	monochromatic	plane
2	1.25	0.095	0.1	1.33	0.53	0.14	monochromatic	ridge
3	1.0	0.101	0 [b]	1.54	0	0.22	monochromatic	plane
4	1.67	0.087	0.05	0.84	0.27	0.09	spectral	plane

[a] For spectral wave height, H_0 and T refers to the deep-water significant wave height and peak wave period, respectively;

[b] $h_r = 0$ corresponds to an initial dry reef flat.

Table 4.2 The distances of the wave gauges (G1 - G12) from the toe of fore-reef for the four simulated experiments (Unit: m)

Case No.	G1	G2	G3	G4	G5	G6	G7	G8	G9	G10	G11	G12
1	-4.35	-4.1	0.95	2	2.35	2.65	2.95	3.25	3.65	5.25	6.95	8.75
2	-4.35	-4.1	0.95	2	2.35	2.65	2.95	3.25	3.65	5.25	6.95	8.75
3	-4.35	-4.1	0.65	1.25	2	2.35	2.75	3.15	3.65	5.25	6.95	8.75
4	-4.35	-4.25	-4	0.95	1.45	2	2.45	2.95	3.65	5.25	6.95	8.75

The previously calibrated grid spacing $\Delta x = 0.04\,m$ was used to discretize the computational domain, leading to a variable grid points per wave length $N = 50$ - 100. The numerical model was run for 200 waves using a Courant number of 0.50 for monochromatic waves and for 1000 waves with a Courant number of 0.35 for spectral waves, respectively, which yields a time step ranging from 0.004 s to 0.007 s. Also, to ensure numerical stability, all simulations described in this section used a 4-point filter to reduce the curvature of the rapidly varying bathymetry. To ensure that the transient effects are insignificant in computing the wave height and the mean water level, the initial 75 wave cycles for monochromatic waves and the initial 100 significant wave cycles for spectral waves were not used in the data analysis. For empirical parameters in the surfzone model, the suggested values in section 4.3.4 were used, except $\delta = 10$ for the reef with the ridge (Case 2). The value $\delta = 10$ was obtained by calibrating the model against the experimental results; an explanation for the increased value of δ when a ridge exists at the reef crest is given in the next section.

Since the wave flume and the reef model were made of glass and PVC, respectively, a constant Manning coefficient $n_M = 0.01$, as suggested in the literature, was used to estimate the friction coefficient in Eq. (4.9). A summary of the model parameters for the simulated cases is given in Table 4.3.

Table 4.3 A summary of model parameters for all the simulations

Case No.	Gird size Δx	Courant number C_r	Sponge layer width W [c] (m)	δ [d]	α_1 [e]	α_2 [e]	α_3 [e]
1	0.04	0.5	2.65	2	0.65	0.08	8
2	0.04	0.5	2.65	2	0.65	0.08	8
3	0.04	0.5	1.78	10	0.65	0.08	8
4	0.04	0.35	3.73	2	0.65	0.08	8
S&A [a]	0.04	0.5	4.10	10	0.65	0.08	8
D&N [b]	0.05	0.35	3.60	2	0.65	0.08	8

[a] S&A stands for Skotner and Apelt (1999);

[b] D&N stands for Demirbilek and Nwogu (2007);

[c] $W = 1.25L$, where L is the incident wave length;

[d] Definition is given in Eq. (4.5);

[e] Definition is given in Eq. (4.10).

4.4.2 Effects of the ridge on wave breaking

Videos of breaking waves were taken after the wave fields had reached steady states. Plunging breakers were observed in Cases 1 to 3; spilling breakers were predominant in Case 4. Fig. 4.10 shows snapshots when the lips of the breakers hit the water surface for Cases 1 and 2. In the absence of a ridge, the localized breakers plunged onto the horizontal reef flat at certain location downstream of the reef edge. In the presence of a ridge, the breaking point shifted seaward: the breaking waves first stroke the front side of the ridge and then plunged onto the ridge top, accompanying a stronger wave reflection.

The surfzone locations and widths were estimated from the video recordings of the experiments (see Table 3.2). The observed surf zones extended approximately from 0.02 m shoreward from the reef edge to 2.94 m shoreward from the reef edge for Case 1, and from 0.04 m seaward from the reef edge to 1.34 m shoreward from the reef edge for Case 2, giving surfzone widths of 2.92 m and 1.38 m, respectively. The seaward shift of the breaking point for Case 2 is due to the alteration of the

wave field by the ridge. The calculated surf zone ranges approximately from 0.1 m seaward from the reef edge to 2.0 m shoreward from the reef edge for Case 1 and from 0.3 m seaward from the reef edge to 0.4 m shoreward from the reef edge for Case 2. Therefore, the surfzone width is greatly reduced by the ridge. The predicted reduction of surf zone width by the reef ridge can be explained by the breaking model used in the simulations. With a ridge, the average surfzone water depth is 0.05 m, which is just 50% of that without the ridge, therefore according to Eq. (4.10), the breaking duration T^*, which is proportional to the square-root of the surfzone water depth, is reduced by approximately 30%, indicating that the breaking process would complete within a shorter distance.

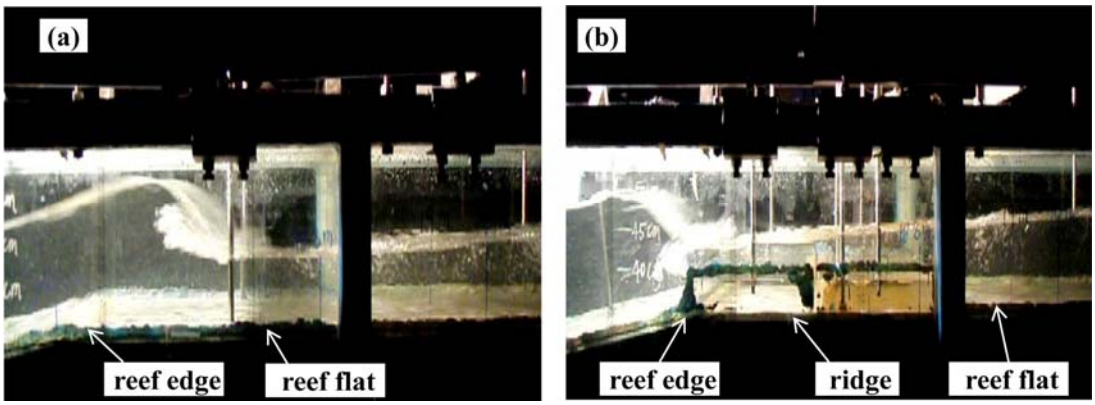

Fig. 4.10 Snapshots of the breaking waves over the reef crest: (a) Case 1 without ridge; (b) Case 2 with ridge.

Based on the present numerical simulations, both the breaker wave heights and reformed wave heights are almost the same for these two cases: about 0.12 m for breaker wave height and 0.04 m for the reformed wave height. Consequently, about the same amount of wave energy in the incident waves needs to be dissipated within a relatively narrower surf zone when a ridge exists. Therefore, when a ridge is present at the edge of a reef crest, the correction factor δ needs to be increased to adjust the incorrect mixing length and friction velocity scales in the eddy viscosity model. Of course, other factors such as flow separation and vortex shedding at both the sharp edges of the ridge may also contribute to a larger δ, but it is believed that these contributions are not substantial.

4.4.3 Wave height, mean water level and wave reflection

The main concern in this chapter is the mean quantities such as wave heights and mean water levels. The cross-reef variations of wave height and mean water level, together with the bottom profiles for the four experiments listed in Table 4.1, are displayed in Figs. 4.11 to 4.14 for the convenience of the following discussion. The R-square values (R^2) of mean water level as well as the measured and predicted maximum setups on the reef flat for all four cases are listed in Table 4.4.

Wave height

The simulated wave heights agree reasonably well with the measurements for all the cases, indicating that the empirical breaking model can simulate the energy dissipation well. Simulations show that the wave height first increases on the fore-reef due to shoaling, then reaches a peak (which is the breaking point), and finally decreases rapidly in the surf zone due to wave breaking. The peak value of the wave height was not captured by the measurements in Figs. 4.11 and 4.12 because of limited number of measurement stations and the resulting coarse spatial resolution in the experiments. A set of results obtained with a higher spatial resolution is shown in Fig. 3.10, where a peak in the measured wave height can be clearly seen. The modulation of the simulated wave height seaward is again due mainly to the partial wave reflection from the reef model, which may produce a partial standing wave pattern in front of the reef model. This phenomenon is enhanced by the presence of the ridge in Case 2, and was nearly invisible in the Case 4 for spectral waves due mainly to the fact that there is no organized partial standing wave pattern that can be formed in front of the reef model.

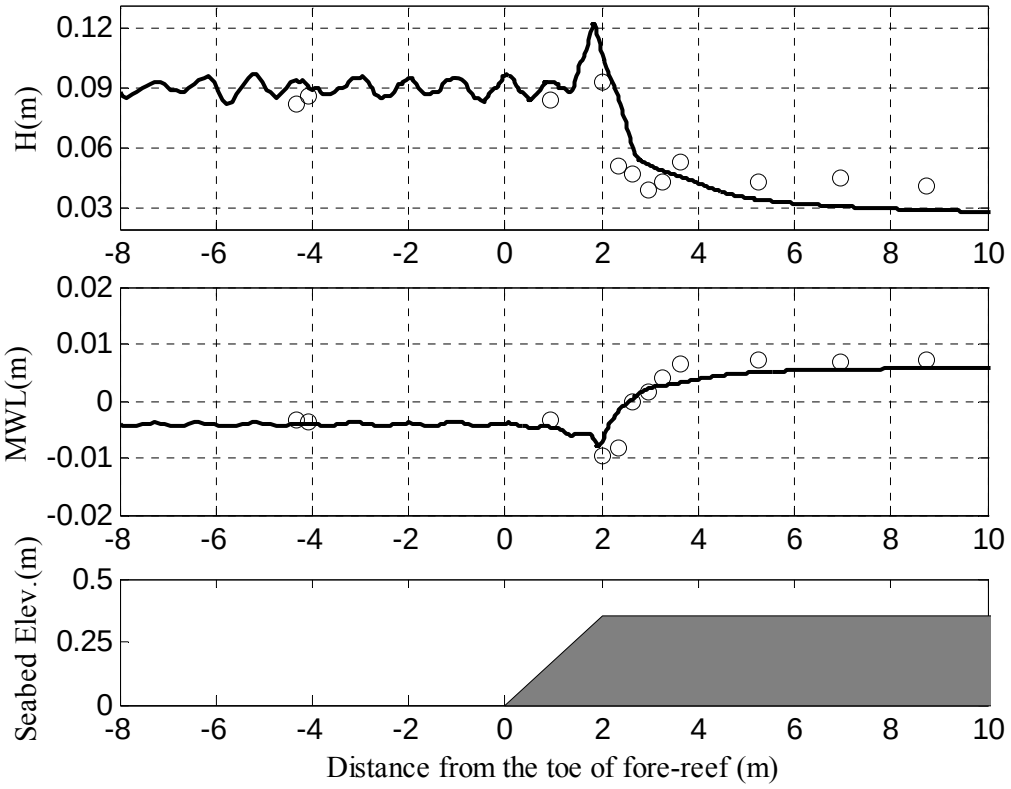

Fig. 4.11 Variations of the wave height and mean water level (MWL) over the reef profile for Case 1. Solid lines: predictions by present model; Open circles: laboratory measurements.

Some minor discrepancies in the reformed wave heights over the reef flat can be observed for both Case 1 and Case 2, although the scatter in the measurements is noticeable. These discrepancies may be attributed partly to the empirical value used to define the saturated breaking cessation in Eq. (4.10). Since the wave energy density is proportional to the wave height squared, the minor differences found in the reformed wave heights do not have a significant effect on the accuracy of the predicted energy dissipation.

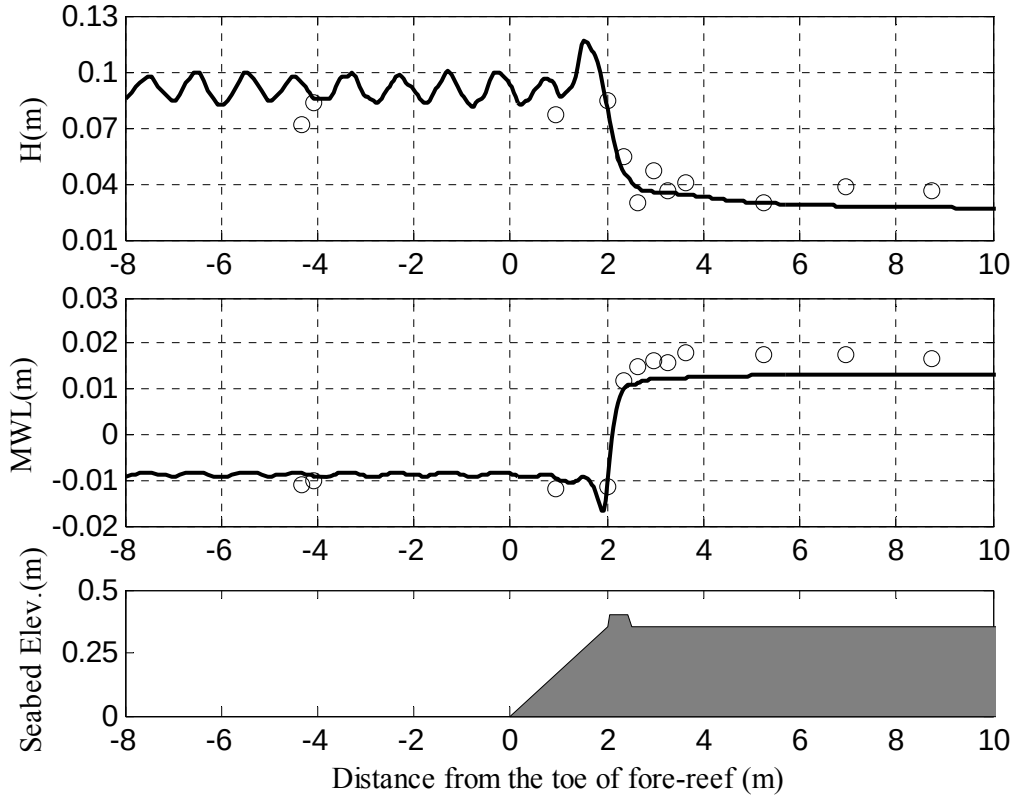

Fig. 4.12 Variations of the wave height and mean water level (MWL) over the reef profile for Case 2. Solid lines: predictions by present model; Open circles: laboratory measurements.

The reef flat with zero submergence in Case 3 was rarely studied in the existing literature. For this case, wave breaking first occurred on the fore-reef and then pumped water onto the reef flat through overtopping. The very good agreement between the simulated and measured wave heights for this case is very impressive (shown in Fig. 4.13). As the flow on the reef flat might be supercritical (Gourlay and Colleter, 2005), the stability and the accuracy of the numerical simulation were achieved with the help of shock-capturing FV-based solver and the moving boundary algorithm.

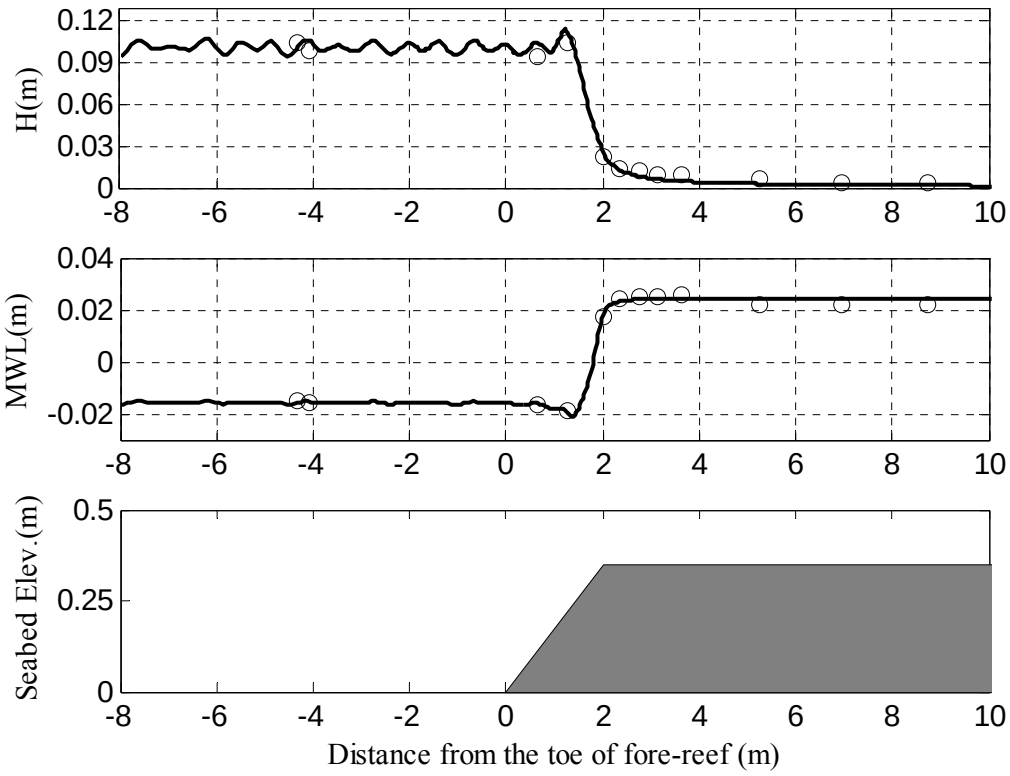

Fig. 4.13 Variations of the wave height and mean water level (MWL) over the reef profile for Case 3. Solid lines: predictions by present model; Open circles: laboratory measurements.

As shown in Fig. 4.14, the agreement between the numerical and experimental results is remarkable for Case 4 (spectral waves), suggesting that the proposed surfzone model also work well for spectral waves over fringing reefs. For this case, the surf zone is wider and spilling breakers are predominant.

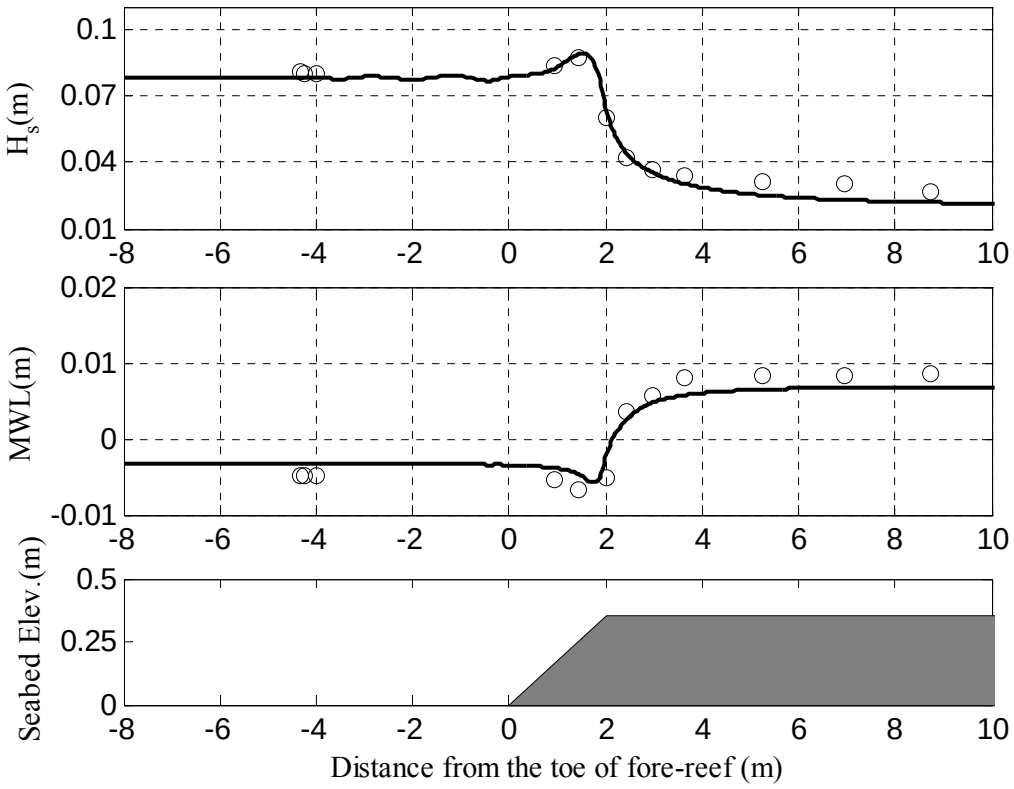

Fig. 4.14 Variations of the significant wave height and mean water level (MWL) over reef profile for Case 4. Solid lines: predictions by present model; Open circles: laboratory measurements.

Mean water level

Overall, the model gives very good predictions of the variation of mean water level for all cases, with all R^2 being larger than 0.85 as shown in Table 4.4. The setdowns over the fore-reef are due mainly to wave shoaling before breaking. The breaking points (locations where the magnitude of wave setdown reaches its maximum) and the setups over reef flat are all reasonably predicted by the simulations (see Table 4.4). The setdowns in the water in front of the fore-reef are related to the requirement on the conservation of mass for a closed flume: the wave-induced setup over the reef flat must be balanced by the setdown in the other part of the flume. The slight underestimation of the wave-induced setups over the reef flat for Case 1 and Case 2 was directly related to the under-prediction of the local wave heights for these two cases. A comparison of the predicted wave-induced setups

over reef flat for these two cases reveals that a ridge-like reef crest can increase the wave-induced setup by narrowing the surf zone as discussed in the previous section. Since the cross-shore wave height evolutions for both cases are well reproduced by the present model, the excellent agreement between the numerical and experimental mean water levels for Case 3 and Case 4 are not surprising given the radiation stress concept.

Table 4.4 The R-squares (R^2) of mean water level at all measurement locations, the measured maximum setup ($\overline{\eta}_r^o$) and the predicted maximum setup ($\overline{\eta}_r^p$) on the reef flat

Case No.	R^2	$\overline{\eta}_r^o$ (mm)	$\overline{\eta}_r^p$ (mm)	$\overline{\eta}_r^p / \overline{\eta}_r^o$
1	0.87	7.1	5.9	0.83
2	0.93	18.0	13.3	0.74
3	0.99	25.6	24.3	0.95
4	0.96	8.3	7.7	0.93

Reflection coefficient

The calculated and measured reflection coefficients for the first harmonic waves are compared in Table 4.5. Satisfactory agreements are obtained between the numerical and laboratory results in view that: (1) the small differences between laboratory and numerical boundary conditions (e.g., the reflection from paddle of wavemaker was not modeled in all numerical simulations), (2) the minor difference in the shapes of the ridges used in the experiments and the simulations (the sharp edges of the ridge have been smoothed in the numerical simulations for numerical stability considerations), and (3) the error arises from the empirical breaking model which may not reflect the real physics of surfzone process. The influence of the ridge on the wave reflection is evident for Case 2; the enhanced wave reflection is expected since the ridge structure functions like a submerged breakwater, which has been widely used to reflect the wave energy for shore protections. For spectral waves, frequency averaged reflection coefficients as defined by Goda (2000) are used

$$K_r = \sqrt{E_r / E_i} \tag{4.11}$$

where E_i and E_r are the total energy contained in the incident and reflective spectra, respectively.

The results for Case 4 show that spectral waves generally have larger values of reflection coefficient than the equivalent monochromatic waves do; this is because low-frequency wave components tend to have larger reflection coefficients than higher-frequency components (Seelig, 1983).

Table 4.5 The measured (K_r^m) and predicted (K_r^p) reflection coefficients

Case No.	K_r^m	K_r^p
1	0.07±0.01	0.03
2	0.22±0.02	0.11
3	0.03±0.00	0.08
4	0.12±0.01	0.10

4.4.4 Wave transformation

Monochromatic waves

The computed surface elevations at six locations for Case 1 and Case 2 are compared with the experimental data in Figs. 4.15 and 4.16, respectively, also indicated in the figures is the root-mean-square error (rmse) at each location. It can be observed that very good agreements are obtained at most locations (where the rmse is small) for these two cases. Wave shoaling makes the wave form asymmetric and skewed at G3 on the fore-reef; at this location, the simulation for Case 1 agrees better with experiments than for Case 2 because the smoothed ridge profile near the reef edge may have slightly affected the reflected waves and the wave dispersion in the water above the ridge. G5 and G7 are located in the surf zone, thus breaking waves with saw-tooth shape are again observed there; a relatively larger error in the measured waves in the surf zone is expected because of the entrained bubbles in the surfzone water. On the reef flat (G9), both the numerical and laboratory results show that the reformed waves are very small and resemble cnoidal waves.

Fig. 4.17 presents a comparison of the measured and simulated surface elevations for Case 3 (dry reef flat). The wave form is satisfactorily predicted seaward of the fore-reef (G2) and in the shoaling zone (G3); the reformed waves are quite small (G9 and G11), therefore, most of the wave energy has been dissipated by wave breaking and bottom friction.

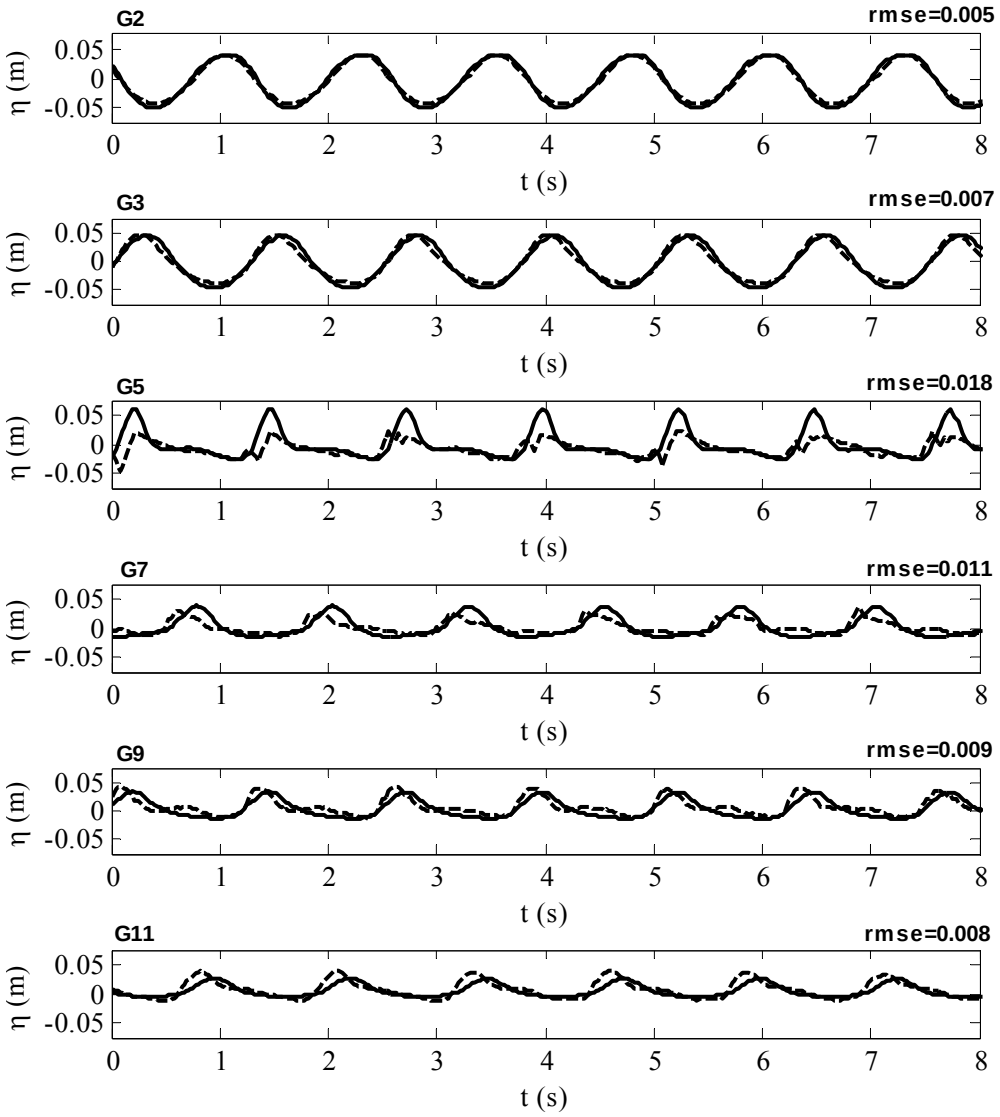

Fig. 4.15 Time-series of surface elevations at six locations (G2, G3, G5, G7, G9 and G11) for Case 1. Dashed lines: laboratory measurements; solid lines: predictions by present model; rmse: root-mean-square error.

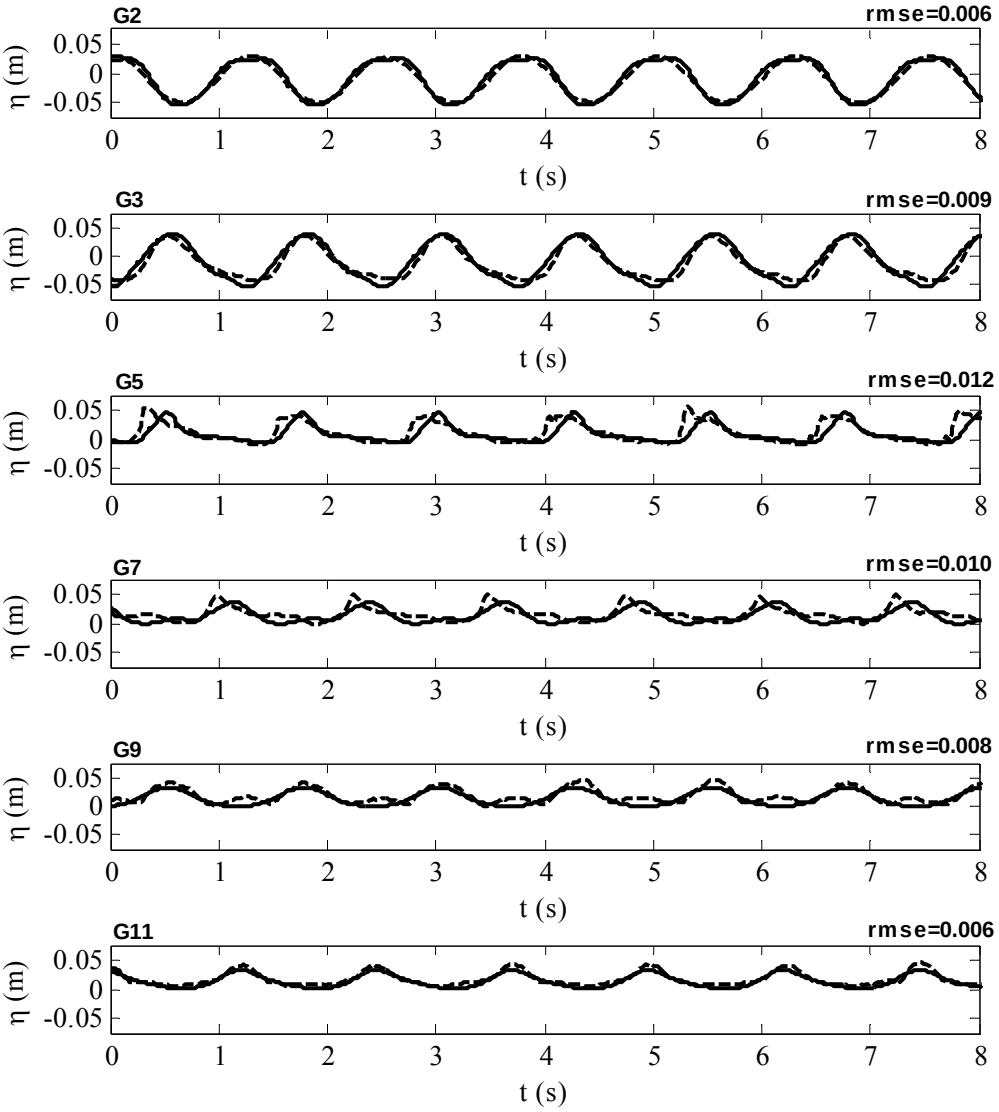

Fig. 4.16 Time-series of the surface elevations at six locations (G2, G3, G5, G7, G9 and G11) for Case 2. Dashed lines: laboratory measurements; solid lines: predictions by present model; rmse: root-mean-square error.

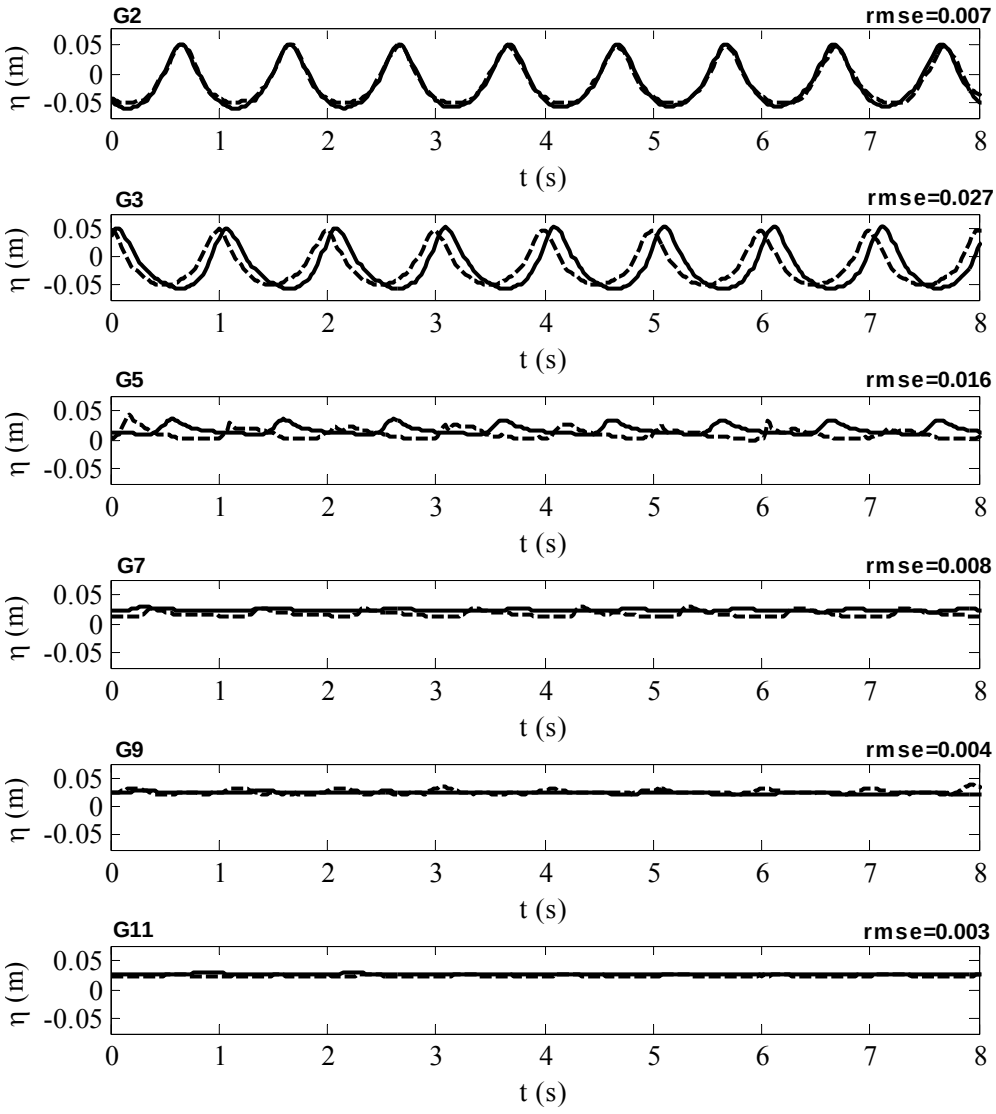

Fig. 4.17 Time-series of the surface elevations at six locations (G2, G3, G5, G7, G9 and G11) for Case 3. Dashed lines: laboratory measurements; solid lines: predictions by present model; rmse: root-mean-square error.

Spectral waves

A comparison of the measured and simulated wave spectra is presented in Fig. 4.18. Good agreement can be observed at G2. For spectral waves, individual wave breaking occurs either on the fore-reef or on the reef flat, thus at G5 (located at the seaward side of the reef edge), there is still a considerable amount of wave energy around the peak frequency. The numerical model slightly over-predicts the wave energy at the peak frequency near the reef edge (G5) as well as during the shoaling process (G4). Waves first shoal on the fore-reef and break in the shallow water

above the reef flat, transferring part of the energy from the fundamental waves to higher and lower harmonic waves. The numerical model also satisfactorily captures the energy transfer from the peak frequency to both higher and lower frequency waves, and the predicted wave spectra at G6 to G9 and G11 are satisfactory. Shoreward of the surf zone, there is no noticeable difference between the computed and measured wave spectra since the local water depth on the reef flat is sufficiently shallow to filter out most of short waves through bottom friction. The low-frequency motions on the reef flat are probably due to infragravity waves (Demirbilek and Nwogu, 2007).

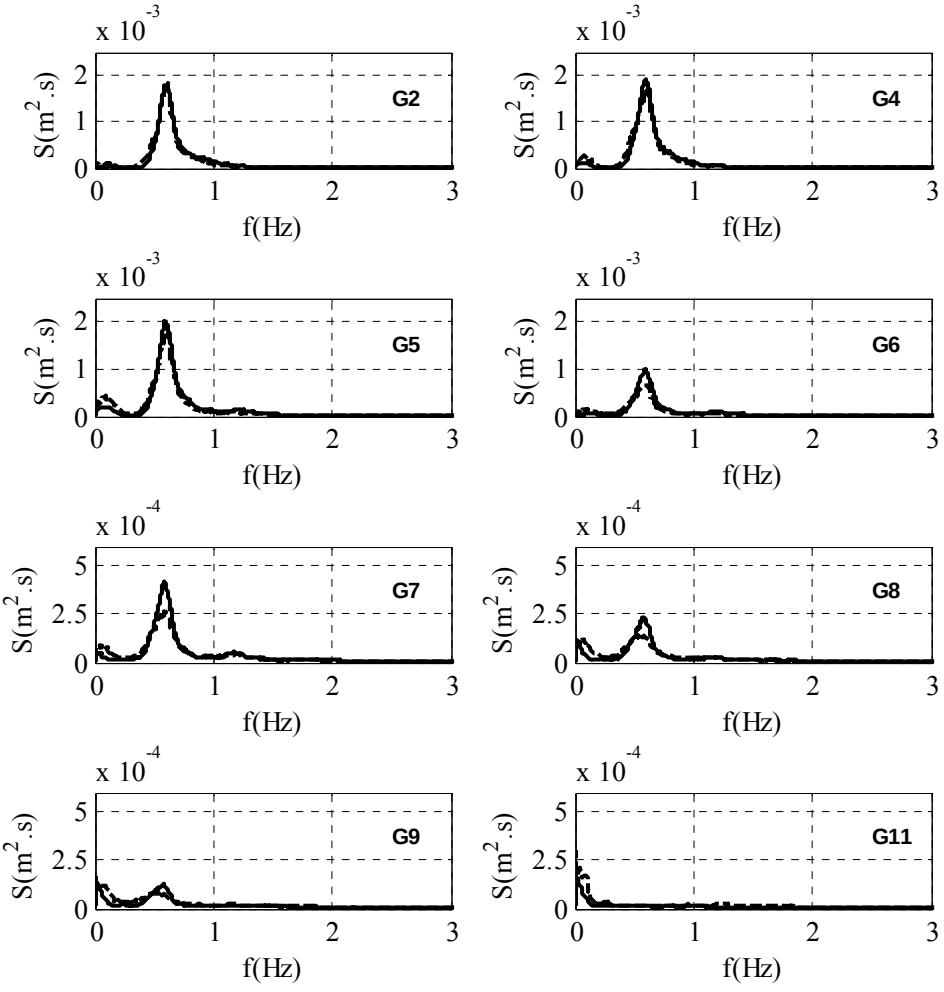

Fig. 4.18 Wave spectra at eight locations (G2, G4 - G9, and G11) for Case 4. Dashed lines: laboratory measurements; solid lines: predictions by present model.

4.5 Revisits of Other Numerical Studies

In this section, two other published laboratory and numerical studies on wave transformation over fringing reefs are revisited. The purpose is to investigate whether highly nonlinear Boussinesq equations can improve the predictions from the weakly nonlinear Boussinesq equations and to demonstrate the effects of numerical boundary conditions on the mean water levels.

4.5.1 Revisit of Skotner and Apelt (1999)

Skotner and Apelt (1999) reported both experimental data and numerical simulations for setdowns and setups induced by monochromatic waves propagating onto a submerged fringing coral reef as described by Seelig (1983). The reef profile consisted of a steep composite fore-reef with an average slope of V:H=1:12, which was followed by a small sharp ridge-like reef crest, and a 7 m-long horizontal reef flat. For their numerical simulations, they used the weakly nonlinear Boussinesq model originated by Nwogu (1993) with a roller-based surfzone model proposed by Schäffer et al. (1993). Nwogu (1993)'s equations could be recovered by neglecting the nonlinear dispersive terms in Eqs. (4.1) and (4.2)

$$\eta_t + hu_{\alpha x} + \left(\eta u_\alpha\right)_x + \left(\frac{1}{3}h^3 + h^2 z_\alpha + \frac{1}{2}hz_\alpha^2\right)u_{\alpha xxx} = 0 \qquad (4.12)$$

$$u_{\alpha t} + u_\alpha u_{\alpha x} + g\eta_x + \left(\frac{1}{2}z_\alpha^2 + hz_\alpha\right)u_{txx} = 0 \qquad (4.13)$$

Monochromatic waves were generated internally with the sponge layers being used only in the momentum equation on both sides of the computational domain to reduce the wave reflection. Six tests were simulated, covering a range of breaker types. They found that their numerical model could predict the trend of the mean water level reasonably well, but there was an increasing discrepancy in the magnitude of setup or setdown when the height of incident waves was increased. Their Test 6 with a wave height of 0.079 m and a wave period of 1.7 s had the poorest agreement. Hence, it is selected in this study to see if the present model can provide an improved prediction. The same boundary conditions and numerical inputs as theirs were used in the simulation with a grid size of $\Delta x = 0.04\ m$, Courant

number $C_r = 0.5$, and friction coefficient $f = 0.015$. For the correction coefficient in the breaking model, the value $\delta = 10$ gave the best fit to the laboratory data. Details of the simulation parameters are given in Table 4.3.

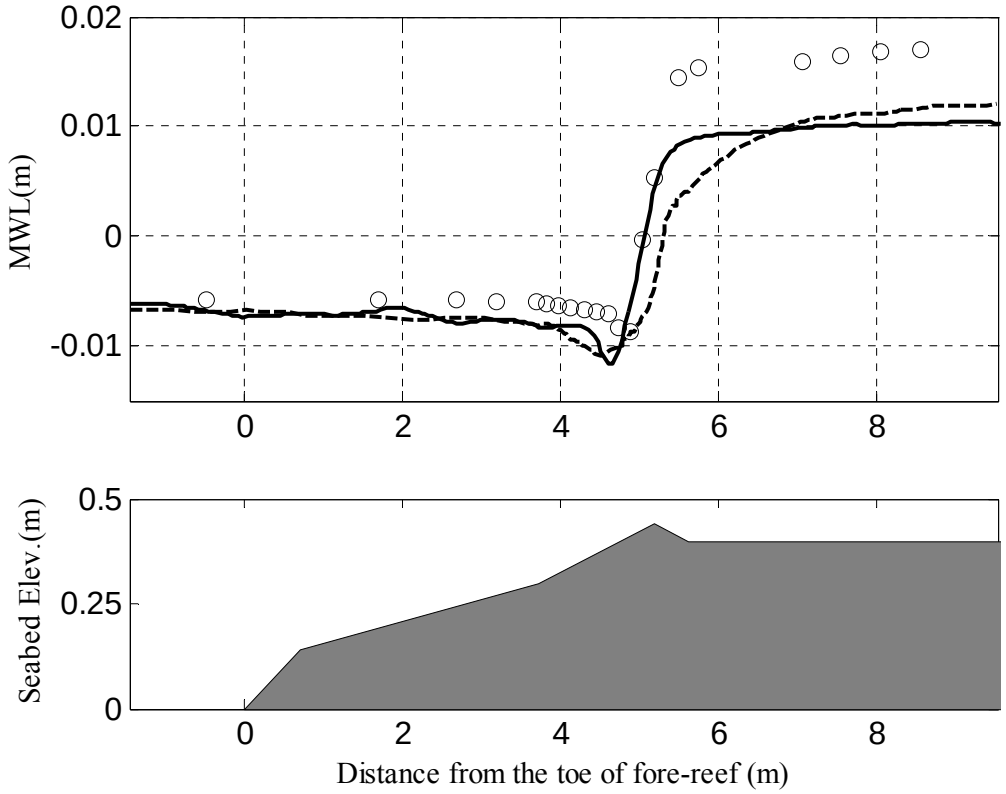

Fig. 4.19 Variation of the mean water level (MWL) over the reef profile for the Test 6 of Skotner and Apelt (1999). Dashed line: prediction by Skotner and Apelt (1999); Solid line: prediction by present model; Open circles: laboratory measurements by Skotner and Apelt (1999).

A comparison among the results of laboratory, numerical simulations of Skotner and Apelt (1999) and the present model is given in Fig. 4.19, where the seafloor profile is also shown. In general, the wave-induced setdowns predicted by the present model are in agreement with the numerical results of Skotner and Apelt (1999). The simulation in this study gives a better prediction of the change of mean water level in the surf zone. However, both models underestimate the magnitude of the setup over the reef flat. Skotner and Apelt (1999) suspected that the under-

productions might result from the lack of highly nonlinear terms in their governing equations, but the present results show that the inclusion of the higher order nonlinear terms in the Boussinesq model does not necessarily improve the prediction of the mean water level over the reef flat.

4.5.2 Revisit of Demirbilek and Nwogu (2007)

Demirbilek and Nwogu (2007) presented a combined laboratory and numerical study for a typical fringing reef without any ridge structure. Their tests were run for a wide range of irregular sea states generated from JONSWAP spectra. Their numerical model was based on the weakly nonlinear Boussinesq equations derived by Nwogu (1993). The effect of wave breaking was also parameterized using an eddy-viscosity concept based on a one equation turbulence closure model. Since the intention of this section is to investigate the effects of boundary settings, the weekly nonlinear version of the present model was used (i.e., Eqs. (4.12) and (4.13)). Only a representative case (their Test 48) with $H_s = 7.5\,m$, $T_p = 1.5\,s$ and $h_r = 0.031\,m$ was revisited in this section. Following their report, the present simulations were carried out using a grid spacing $\Delta x = 0.05\,m$ a time step $\Delta t = 0.01\,s$ and an equivalent friction coefficient $f = 0.011$ which was converted from their Chezy coefficient. The present physical simulation time was 900 s, and the initial 100 s surface elevations were not used in computing the mean water levels. The major difference in the numerical settings is: they used sponge layers in both the continuity and momentum equations at the seaward boundary and a plane beach at the shoreward boundary while in this study the sponge layers were used only in momentum equation at both boundaries. Parameter δ in the present breaking model needs to be calibrate with experiments; the value suggested in section 4.3.4 was used, i.e., $\delta = 2$ for this case. A summary of all the simulation parameters is given in Table 4.3.

The measured and computed significant wave heights (H_s) and the mean water level variations are compared in Fig. 4.20. Both simulations predicted similar wave heights over the reef. However, the simulation of Demirbilek and Nwogu (2007)

failed to capture the wave-induced setdown seaward of the fore-reef, which was well predicted by the present simulation. Demirbilek and Nwogu (2007) attributed the difference between the measurements and their simulations to the sponge layer damping term used in their continuity equation. From the comparisons in Fig. 4.20, it can be concluded that the mean water level over the reef is sensitive to the types of the boundary conditions used and that the damping terms should not be included in the continuity equation when simulating the mean water levels in a closed flume.

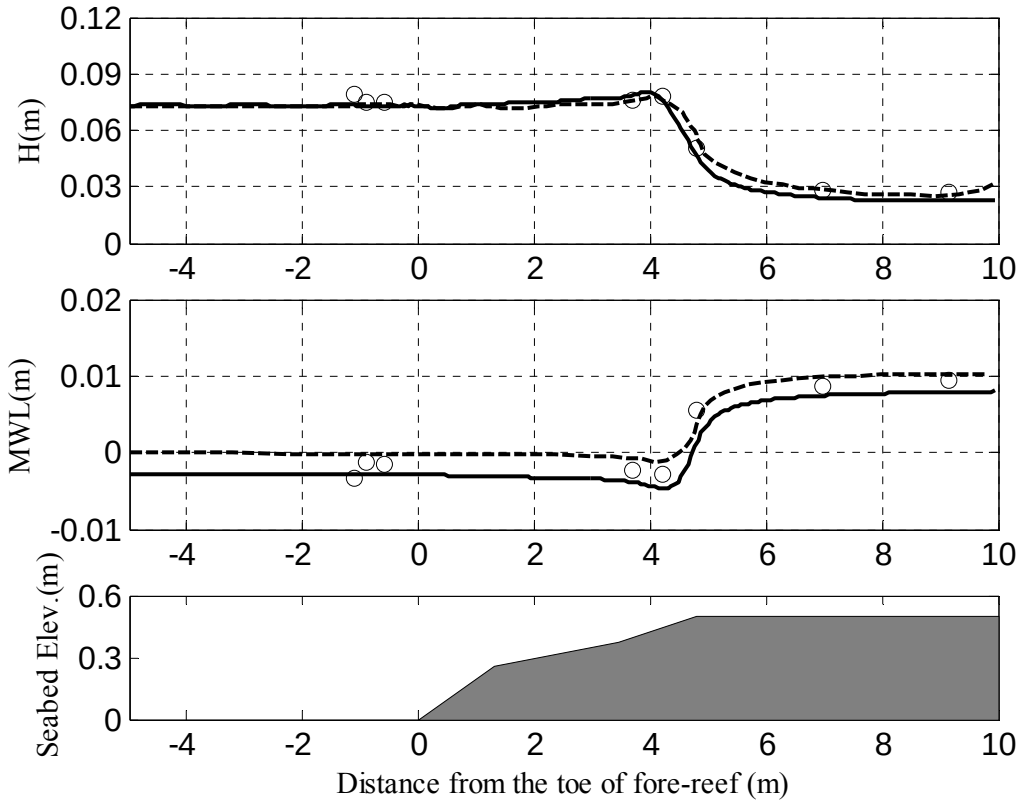

Fig. 4.20 Variations of the wave height and mean water level (MWL) over the reef profile for the Test 48 of Demirbilek and Nwogu (2007). Dashed lines: predictions by Demirbilek and Nwogu (2007); Solid lines: predictions by present model; Open circles: laboratory measurements by Demirbilek and Nwogu (2007).

4.6 Model Application to Different Fore-reef Slopes and Profiles

The influences of offshore wave conditions and reef-flat submergences on the mean quantities such as wave height and the wave-induced setup over reef flat have been

investigated experimentally by, e.g., Gourlay (1994, 1996a) and numerically by, e.g., Skotner and Apelt (1999) and Demirbilek and Nwogu (2007). However, to the best of the author's knowledge, neither existing laboratory nor numerical work has studied the influence of the inclination angle of a plane fore-reef or the shape of fore-reef. In this section, the numerical model is applied to examine a series of fore-reefs numerically. Case 1 (a plane fore-reef with a slope of V:H=1:6) in section 4.4 is taken as the benchmark against which the comparisons and discussion are made. Two types of numerical tests were conducted: (1) plane fore-reefs with slopes varying from V:H=1:1 to 1:20, and (2) combinations of two types of circular arc profile (convex and concave) and two values of arc curvature (0.075, 0.15). For the circular arc profiles, the chords are the same as the fore-reef length in Case 1. For both types of numerical tests, the numerical settings were the same as those used for Case 1.

4.6.1 Effect of the inclination angle of plane fore-reef

The effects of fore-reef slope on the cross-shore variation of wave height and mean water level are summarized in Fig. 4.21. While the computed reflection coefficient, transmission coefficient, breaking location relative to the toe of fore-reef and maximum setup/setdown are plotted against the surf-similarity parameter (ξ_0), defined by Eq. (2.4), in Figs. 4.22(a), 4.22 (b), 4.22 (c) and 4.22(d), respectively.

Fig. 4.21 shows that seaward of the reef model, the fluctuation of wave height caused by the partial standing waves is generally amplified as the fore-reef becomes steeper, indicating an enhanced wave reflection. However, Fig. 4.22(a) shows that when the fore-reef slope becomes relatively gentle (small ξ_0), there is no trends for the variation of reflection coefficient with slope; the same is also found in Fig. 4.6. The fluctuation of the seaward mean water level for steeper slopes can also be observed in Fig. 4.21. Similar phenomenon can also be observed in the simulations of Skotner and Apelt (1999) and Ranasinghe et al. (2009). Currently the author cannot provide a convincing explanation for it.

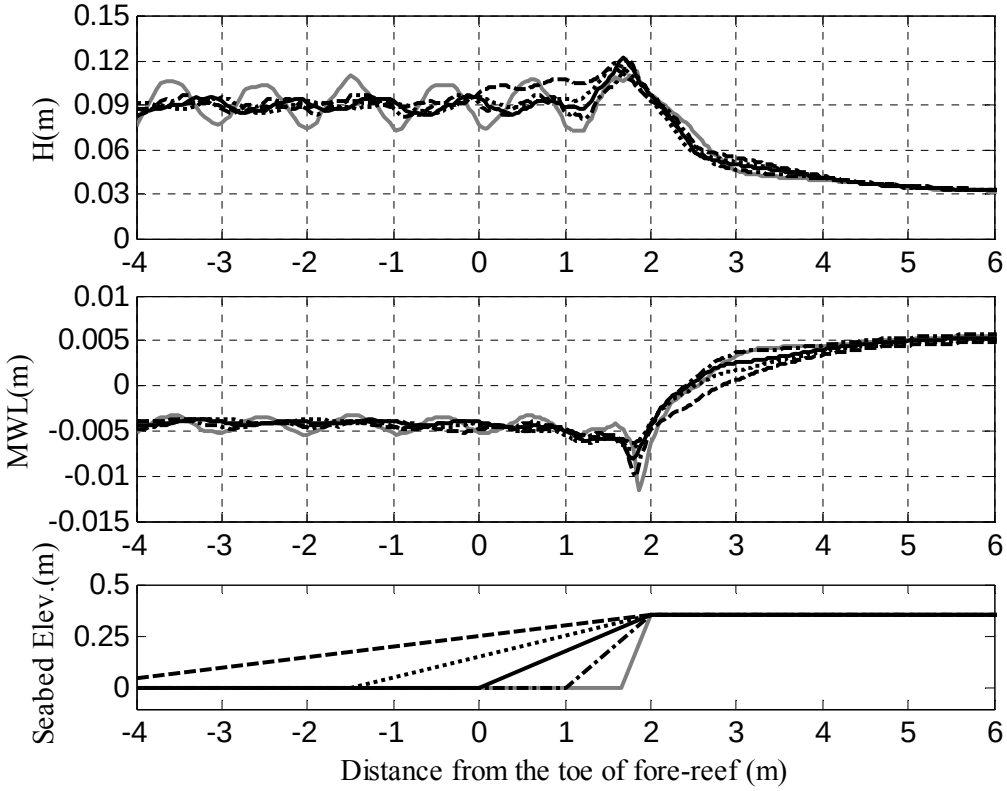

Fig. 4.21 Variations of the wave height and mean water level (MWL) over reef profile with different fore-reef slopes. Light black solid line: V:H=1:1; Dash-dot line: V:H=1:3; Dark black solid line: V:H=1:6; Dotted line: V:H=1:10; Dashed line: V:H=1:20.

The predicted wave heights on reef flat are almost the same as indicated by the transmission coefficients in Fig. 4.22(b), which is controlled mainly by the breaking cessation criteria in the breaker model. Wave breaking occurs on the seaside of the reef edge and breaker wave heights are almost the same for all simulations. However, the breaking points are shifted slightly seaward as the slope varies from V:H=1:1 to 1:20; this is because an increasing distance between the breaking location and the toe of fore-reef slope with the increasing ξ_0, as shown in Fig. 4.22(c) .

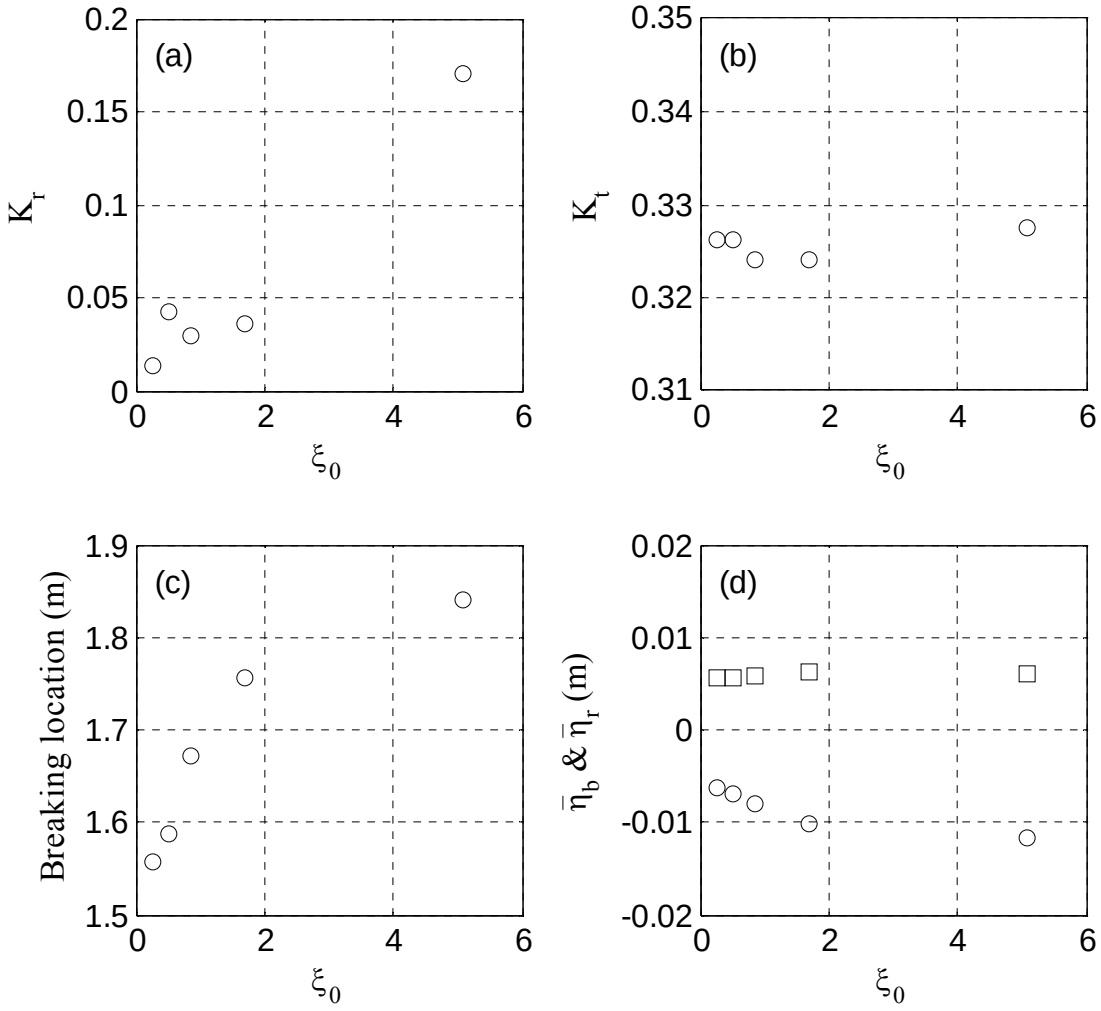

Fig. 4.22 Reflection coefficient (K_r), transmission coefficient (K_t), breaking location related to the toe of fore-reef (positive if shoreward), maximum wave setdown ($\overline{\eta}_b$) and maximum wave setup on the reef flat ($\overline{\eta}_r$) as a function of surf-similarity parameter (ξ_0).

Fig. 4.22(d) shows that the wave-induced setdown at the breaking point decreases with the increase of ξ_0 and the fore-reef slope. However, the wave-induced setups are about the same for all simulations on the reef flat. This is due to the fact that the total amount of energy dissipated in the surf zone is about the same for different slopes. However, the spatial variation of the setup in surf zone depends on the surfzone width, which is related to the slopes of fore-reef. The calculated wave

setup increases more rapidly for steeper slopes due to the reduction in the overall water depth in surfzone and in surfzone width. When waves shoal on a milder slope over a longer distance, the bottom friction may also affect the wave-induced setup. However, the additional tests by varying the Manning's coefficient have found that the frictional dissipation is negligible for your problems since the fore-reef is not long enough. The fore-reef slope for Case 2 was also adjusted (in the presence of the ridge), similar observations (not reported here) were obtained. It seems that the slope of a plane fore-reef can have noticeable influence on the wave-induced setdown and setup only in the shoaling zone and surf zone.

4.6.2 Effect of the shape of fore-reef profile

The influences of the shape of fore-reef profile are summarized in Fig. 4.23, which reveals that seaward of the fore-reef, there is no notable difference among different simulations in both the wave height and mean water level. However, the location of the breaking point is affected by the slope profiles: the concave profiles (in analogy to mild slopes) move the breaking point seaward, while the convex profiles (in analogy to steep slopes) move it shoreward. Physically, wave breaking in coastal waters is always depth-limited. When a wave shoals on a fore-reef slope, there is a ratio of the wave height to water depth beyond which the wave will break. The ratio has been found to be almost slope-independent for reef profiles as discussed in Chapter 2. Since the breaker wave height depends only on the local water depth, the breaker water depth should be similar for all investigated slopes. For a milder slope, achieving such a depth requires that the breaking point moves further offshore if the reef edge is kept at the same location.

The wave-induced setdown is larger for the convex profiles than for the concave profiles or plane profile. However, the wave setup on the reef flat remains nearly unchanged as the fore-reef profile varies from the concave configurations to the convex configurations: this may be because the wave breaking dissipation is almost the same for all cases. The near-constant reef-flat setup indicates that the shape of the fore-reef profile is not a key parameter contributing to the wave-induced setup

over the fringing reef and the results obtained for the plane fore-reef are representative of other shapes.

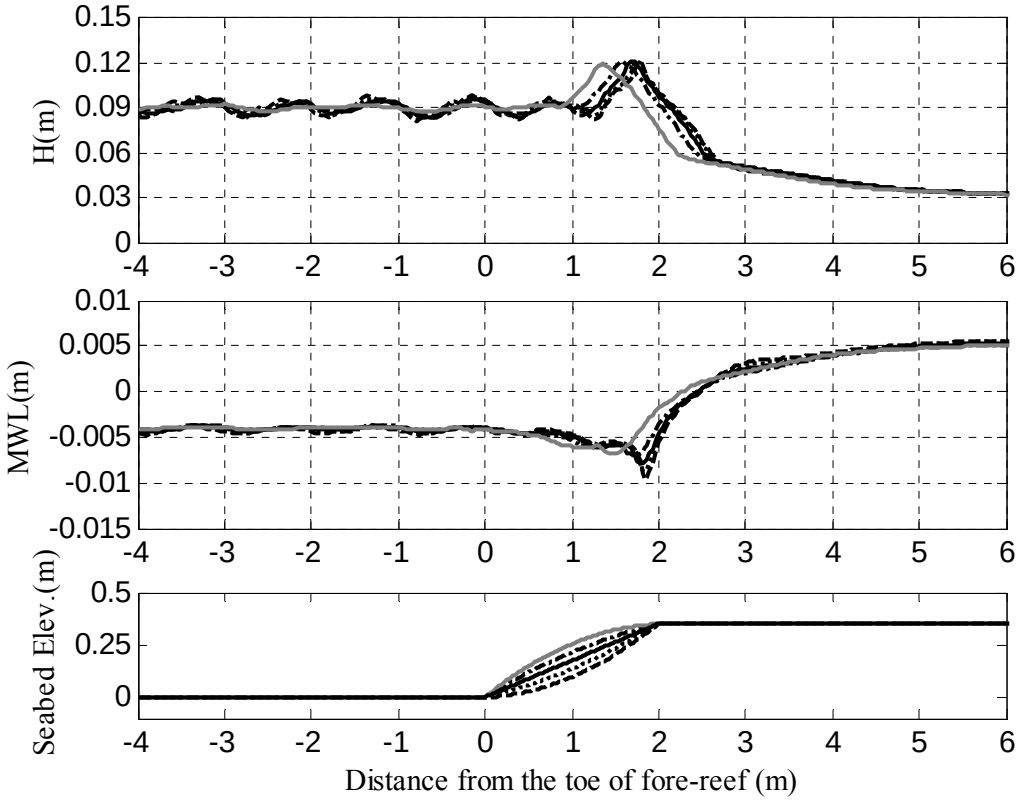

Fig. 4.23 Variations of the wave height and mean water level (MWL) over reef profile with different fore-reef profiles. Light black solid line: concave arc with the curvature=0.15; Dash-dot line: concave arc with the curvature=0.075; Dark black solid line: plane slope; Dotted line: convex arc with the curvature=0.075; Dashed line: convex arc with the curvature=0.15.

4.7 Concluding Remarks

Numerical experiments based on weakly dispersive, fully nonlinear Boussinesq-type equations with a FV-based solver have been performed to study the wave transformation over various fringing reef profiles. Comparisons with published laboratory measurements and other numerical studies lead to the following conclusions:

In order to conserve the mass in a closed wave flume, the numerical damping layer can only be used in the momentum equation.

The zero-equation eddy viscosity model, with its model parameters being calibrated using measurements, can reasonably simulate the key characteristics (wave reflection, wave height, wave-induced setup/setdown) of both monochromatic and spectral waves over various fringing reef profiles and conditions, including the dry reef-fat condition and a ridge at the reef edge.

The reef crest profile, especially the existence of a ridge at the reef edge, may significantly affect the wave-induced setup/setdown over the fringing reef.

The increase of the wave-induced setup over the fringing reef with a ridge located at the reef edge is due mainly to the reduction of the surfzone water depth and the surfzone width.

Both the inclination angle of plane fore-reef and the shape of fore-reef profile have negligible effects on the wave-induced setup/setdown outside the shoaling zone and surf zone. The results for plane fore-reef are representative of other profiles.

.

Natural reefs are far more complex than can be studied in the laboratory. Coastal currents, fore-reef roughness and gaps in the reef ridges might affect the wave transformation over reefs. A numerical study of the effects of reef-surface roughness on the wave dynamics over fringing reefs is under way and the results will be reported elsewhere.

CHAPTER 5 MODELING WAVE-INDUCED SETUP OVER FRINGING REEFS WITH SELECTED EXISTING ANALYTICAL MODELS

5.1 Introduction

The numerical simulations based on Boussinesq-type equations in Chapter 4 have been proven to be able to adequately reproduce the wave setups under different reef profiles (with and without a ridge) and wave conditions (monochromatic and spectral). However, the applicability of the numerical model is believed to be related to the FV-based numerical scheme and the parameterization of wave breaking. Simple parameterizations are still desired for use in wave models since it is not practical to solve the Boussinesq equations for most problems of interest. It is preferable if some analytical solutions can be devised to describe the wave setups under certain special conditions, particularly for the case in which a ridge is located at the reef edge, so that more insight into the underlying physical processes can be revealed.

In analogy to wave-driven cross-shore flows and setup/setdown on beaches (e.g., Svendsen, 2006), the hydrodynamics of wave setup on reefs has been described using the radiation stress concept proposed by Longuet-Higgins and Stewart (1964). Traditionally, two main groups of analytical models are commonly used in the existing literature to predict the maximum wave-induced setup on a reef flat. The first group is to derive an analytical solution by integrating the momentum equation in the surf zone, and energy balance is supplemented to estimate some boundary values. Tait (1972) was the first to achieve such a solution. Similar approaches can be found in e.g., Symonds et al. (1995), Hearn (1999) and Vetter et al. (2010). Importantly, this type of model was usually developed for horizontal reef flats without the ridge. This is for a good reason: the sudden depth change and shallow water on the reef ridge renders the analytical formulation nearly intractable. The other group is established according to the cross-shore energy balance; this idea was originally proposed by Gourlay (1996b) and improved later by Gourlay and Colleter

(2005). In this group of methods, the energy flux of incident, transmitted, and reflected waves are parameterized, separately. The cross-shore momentum balance is supplemented to estimate the energy flux associated with wave breaking and the surfzone morphologic effects are also addressed through an empirical coefficient, see section 5.2 for details.

Field observations have often been cast in terms of a simple scaling parameter connecting the maximum wave-induced setup on reef flat, $\overline{\eta}_r$, the offshore wave height, H_0, and wave period, T,

$$\overline{\eta}_r \propto (H_0^2 T)^p (H_0 / T^2)^q = H_0^m T^n \tag{5.1}$$

where m and n can be determined by using field or experimental data (Hench et al., 2008). The first parameter ($H_0^2 T$) represents the deep-water (offshore) wave energy flux towards the reef whereas the second (H_0 / T^2) represents the deep-water (offshore) wave steepness. The radiation-stress type model of Hearn (1999) gave $m = 1$ and $n = 0$, although it was unclear in his model which incident wave height it referred to, since the wave shoaling was not considered. In contrast, the model of Gourlay and Colleter (2005) gave $m = 2$ and $n = 1$ when the reef-flat water level was very high. For spectral wave conditions, the offshore root-mean-square (rms) wave height, $H_{rms0} = (1/\sqrt{2}) H_{s0}$ (where H_{s0} is significant offshore wave height) and the peak wave period, T_p, may be used instead of the monochromatic wave height, H_0, and the monochromatic wave period, T, in Eq. (5.1). Hench et al. (2008) found that $m = 3.2$ and $n = 3$ for the Moorea reef, a natural reef with a ridge. In contrast, Lowe et al. (2009a) reported that for the reef system in Kaneohe Bay, a natural reef with no ridge, m and n ranged between 1.6 to 2.7 and 0.6 to 0.8, respectively.

In this chapter, the performances of the offshore scaling parameter (i.e., Eq. (5.1)) and two aforementioned representative 1DH analytical models (the models of Tait (1972) and Gourlay and Colleter (2005)) are investigated using the experimental

data for wave setup presented in Chapter 3. Their performances for different reef profiles (with and without the ridge) and wave conditions (monochromatic and spectral) are compared. The rest of the chapter is organized as follows: the theoretical background of the existing analytical models is described in section 5.2. The offshore scaling parameter is validated in section 5.3. The model of Tait (1972) is tested in section 5.4 while the model of Gourlay and Colleter (2005) is examined in section 5.5. Some discussions on the model implementations and results are given in section 5.6. The conclusions are drawn in section 5.7.

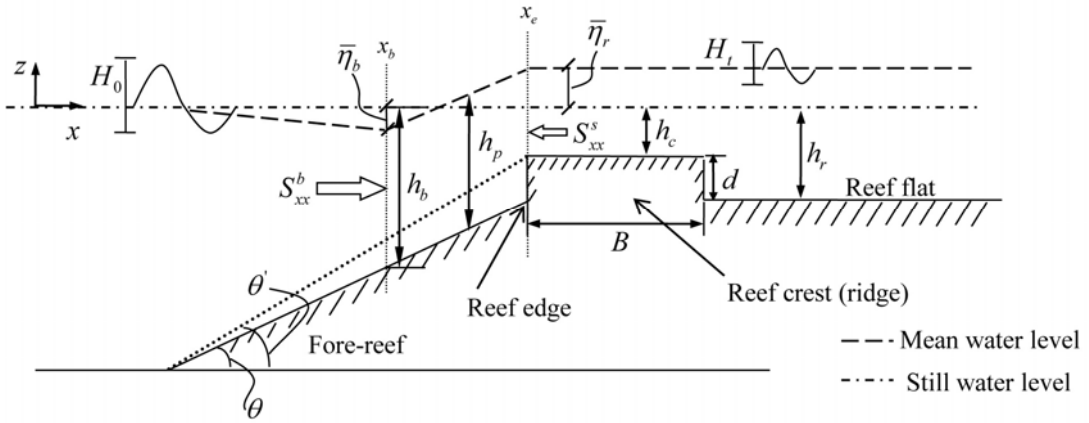

Fig. 5.1 Configuration of an idealized fringing reef with a rectangle ridge and some notations adopted in this chapter.

5.2 Theoretical Considerations

Although several theories proposed to predict wave setup over reefs differ in many respects (see Lowe et al., 2009a), they all rely fundamentally on four principles describing waves and mean flows:

(1) The mean momentum balance can be expressed using the radiation stress theory of Longuet-Higgins and Stewart (1964), which can be written for steady 1D flows as (see Eq. (1.3) after ignoring the convection term)

$$g(h+\bar{\eta})\frac{d\bar{\eta}}{dx}+\frac{\tau_x^b}{\rho}=-\frac{1}{\rho}\frac{dS_{xx}}{dx} \tag{5.2}$$

where h is the undisturbed water depth, $\bar{\eta}$ is the wave-induced change in mean water level which has a maximum value of $\bar{\eta}_r$ at the shoreward end of the surf zone, τ_x^b is the cross-shore bottom shear stress and S_{xx} is the cross-shore radiation stress for unidirectional long-crested waves. Some relevant parameters are shown in Fig. 5.1.

(2) Wave evolution is modeled by a simplified form of conservation of wave energy (e.g., Svendsen, 2006)

$$\frac{d}{dx}(c_g E) = -\varepsilon_b - \varepsilon_f \tag{5.3}$$

where c_g is the group velocity, E is the energy density, ε_b and ε_f are energy dissipation rates due to wave breaking and bottom friction, respectively.

(3) The wave-averaged quantities S_{xx} and E, and group velocity c_g (and implicitly the dispersion relation) can be evaluated using linear wave theory for shallow water waves

$$\begin{aligned} S_{xx} &= \frac{3}{16}\rho g H^2 \\ E &= \frac{1}{8}\rho g H^2 \\ c_g &= \sqrt{gh} \end{aligned} \tag{5.4}$$

where H is the local wave height.

(4) In shallow water, where waves break under the depth-limited condition, the breaker height is estimated by

$$\frac{H}{h+\bar{\eta}} = \gamma(s, kh, S) \tag{5.5}$$

where γ is the empirical breaker depth index, k is the wave number, $s = \tan\theta$ is the fore-reef slope with θ being the fore-reef slope angle as shown in Fig. 5.1. (For

a reef with the ridge, an equivalent fore-reef slope angle can be defined as the angle between the toe of the beach and the seaward edge of the ridge (see the angle θ' in Fig. 5.1). Note that the mean water level, $(h+\overline{\eta})$, is used here instead of the still water level, h, in Eq. (1.1). The deep-water wave steepness, S, is written here in terms of the deep-water wave height, H_0, and either the wave period, T or the deep-water wavelength, L_0 (see e.g., Raubenheimer et al., 1996)

$$S = \frac{H_0}{gT^2} = \frac{1}{2\pi}\frac{H_0}{L_0} \tag{5.6}$$

The simplest model described first by Tait (1972) assumed that: (a) $\tau_x^b = 0$; (b) γ is a constant on the fore-reef slope, and (c) the energy flux is conserved until breaking. In this case, Eq. (5.2) can be integrated exactly to give

$$\overline{\eta}_r = -\frac{\gamma^2 h_b}{16} + \frac{1}{1+8/3\gamma^2}(h_b - h_r) \tag{5.7}$$

where h_b is the breaker depth for monochromatic waves and h_r is the still water depth on the reef flat (reef-flat submergence). See Appendix E for the derivation of Eq. (5.7).

Eq. (5.7) is the original form of the model proposed by Tait (1972). However, Tait (1972) did not give any analytical solution of h_b. In fact, h_b can be estimated based on the cross-shore energy balance without considering frictional dissipation (see also Appendix E). After ignoring the first term in Eq. (5.7) for wave setdown, Tait (1972)'s model in its dimensionless form reads

$$\frac{\overline{\eta}_r}{H_0} = \frac{1}{1+8/3\gamma^2}\left[\frac{(1-K_r^2)^{0.4}}{(4\pi\gamma^2)^{0.4}S^{0.2}} - \frac{h_r}{H_0}\right] \tag{5.8}$$

where K_r is the reflection coefficient. Similar approaches have also been used by Symonds et al. (1995), Hearn (1999) and Vetter et al. (2010).

Alternatively, using conservation of energy and momentum, Gourlay and Colleter (2005) suggested that the wave-induced setup in the water above the reef flat (without considering the reef-flat mean current) could be calculated with

$$\frac{\overline{\eta}_r}{T\sqrt{gH_0}} = \frac{3}{64\pi} K_p \left[1 - K_r^2 - 4\pi\gamma^2 \left(\frac{\overline{\eta}_r + h_r}{H_0} \right)^2 \frac{1}{T} \sqrt{\frac{\overline{\eta}_r + h_r}{g}} \right] \left(\frac{H_0}{\overline{\eta}_r + h_r} \right)^{3/2} \qquad (5.9)$$

where K_p is a free parameter that describes the effects of reef profile shape. The breaker depth index, γ, was supposed to apply on or near the reef flat and was believed to be smaller than that used in Eq. (5.8) on the fore-reef (see also Appendix E for the derivation of Eq. (5.9)). It is important to note that Gourlay and Colleter (2005) also used a radiation stress concept to model the surf zone. Instead of carrying out an exact integration of the momentum equation across the surf zone, Gourlay and Colleter (2005) assumed that the change of radiation stress would take place at an effective depth, $h_p = (1/K_p)(\overline{\eta}_r + h_r)$. In essence, by assuming a constant γ on the reef flat, they were able to use K_p to parameterize wave breaking.

5.3 Offshore Scaling Parameter

Using Eq. (5.1) to analyze the experimental data in Chapter 3 obtained with and without the ridge for both monochromatic and spectral wave conditions (H_{rms0} and T_p were used for spectral waves), the correlation coefficients between data and the scaling parameter fitted for various exponents were computed, and the values of *m* and *n* corresponding to maximum correlation coefficient are listed in Table 5.1.

Table 5.1 shows that the values of *m* and *n* for wave setup experiments in Chapter 3 fall in the range of 0 to 3, which is consistent with the range observed in field as reviewed in section 5.1. For reefs both with and without the ridge, no obvious relation can be observed between m or n and the still water depth on the reef crest, h_c. In general, the value of p is one order of magnitude larger than that of q for

most cases, which means that the maximum wave-induced setup on the reef flat has a strong dependence on the offshore wave energy. Note also that there is an increase of q/p with decreasing h_c for both reefs (with and without the ridge) subjected to monochromatic waves, indicating an increasing dependence on the wave steepness for those cases.

Table 5.1 Maximum correlation between wave-induced setup ($\overline{\eta}_r$) and offshore scaling parameter ($H_0^m T^n$)

h_c (m)	m	n	p^*	q^*	q/p	Correlation coefficient	With ridge	Wave condition
0	0.25	0.19	0.14	-0.03	-0.21	0.99	no	monochromatic
0.05	1.06	0.66	0.56	-0.05	-0.09	0.99	no	monochromatic
0.1	2.28	1.39	1.19	-0.1	-0.08	0.98	no	monochromatic
0	1.33	1.24	0.78	-0.23	-0.29	0.98	yes	monochromatic
0.01	0.17	0.10	0.09	-0.01	-0.11	0.99	yes	monochromatic
0.02	0.32	0.14	0.16	0.01	0.06	0.99	yes	monochromatic
0.05	1.19	0.53	0.58	0.03	0.05	0.99	yes	monochromatic
0	0.67	0.52	0.37	-0.07	-0.19	1	no	spectral
0.05	1.76	0.59	0.82	0.12	0.15	1	no	spectral
0.1	1.64	1.63	0.98	-0.32	-0.33	1	no	spectral
0	1.01	0.20	0.44	0.12	0.27	1	yes	spectral
0.02	0.91	0.33	0.43	0.05	0.12	1	yes	spectral
0.05	2.18	0.49	0.97	0.24	0.25	0.99	yes	spectral

* Referring to Eq. (5.1) for dentitions.

Since both the water depths above the reef flat and the presence of a ridge can significantly change the values of *m* and *n*, the dimensional parameter group $H_0^m T^n$ is not sufficient to describe the predicted wave setup on the reef flat. Moreover, there is a clear discrepancy in the values of *m* and *n* obtained from the laboratory observations and those from existing theories, indicating that the existing analytical solutions, which were developed for simpler reef models, may not fully account for

the effects of ridge on the wave breaking and the wave setup. For example, casting the Tait (1972)'s model, i.e., Eq. (5.8), into the offshore scaling parameter gives $m = 0.8$ and $n = 0.4$, values that differ somewhat from what have been shown in Table 5.1.

5.4 Comparison of Experimental Data with the Model of Tait (1972)

The performance of Eq. (5.8) can be assessed with the wave setup data in Chapter 3. For the experiments with a ridge, the still water depth on the ridge-top should be used instead of the water depth on the reef flat (Yao et al., 2009). Hence, the reef-crest submergence, h_c (the minimum water depth across the reef flat), is used in Eq. (5.8) instead of h_r for the reefs with and without a ridge. K_r is obtained from measurements since there is no well-accepted approach to predict K_r for reefs. For a given reef profile and h_c, values of γ can be obtained from a least-square fitting of the laboratory data to Eq. (5.8) for both monochromatic and spectral waves. The comparisons of the predicted and observed setups are shown in Fig. 5.2.

Overall, the model of Tait (1972) provides a seasonable prediction of wave-induced setups up to $h_c = 0.02m$. However, when h_c is further increased, the values of $\overline{\eta}_r$ are generally under-predicted, particularly for the cases with larger incident wave heights, suggesting that a global value of γ may be inappropriate for a given water depth due to the dependence of γ on wave characteristics. For both profiles, Fig. 5.2 also shows that γ falls between 0.3 and 1.7, i.e., the (relatively wide) range previously found for natural beaches (e.g., Guza and Thornton, 1981; Nelson, 1994; Raubenheimer et al., 1996, Péquignet et al., 2011). However, even for a given reef profile, smaller γ must be used for larger h_c, i.e., γ depends on the reef-crest submergence. It also implies that the assumption of a constant value of γ, as is done in similar existing models (e.g., Symonds et al., 1995; Hearn, 1999), may not be appropriate. Note that the author did not include wave setdown in the above

results as Tait (1972) originally did (see Eq. (5.7)). Preliminary tests have shown that the overall under-prediction would be enhanced if it were included.

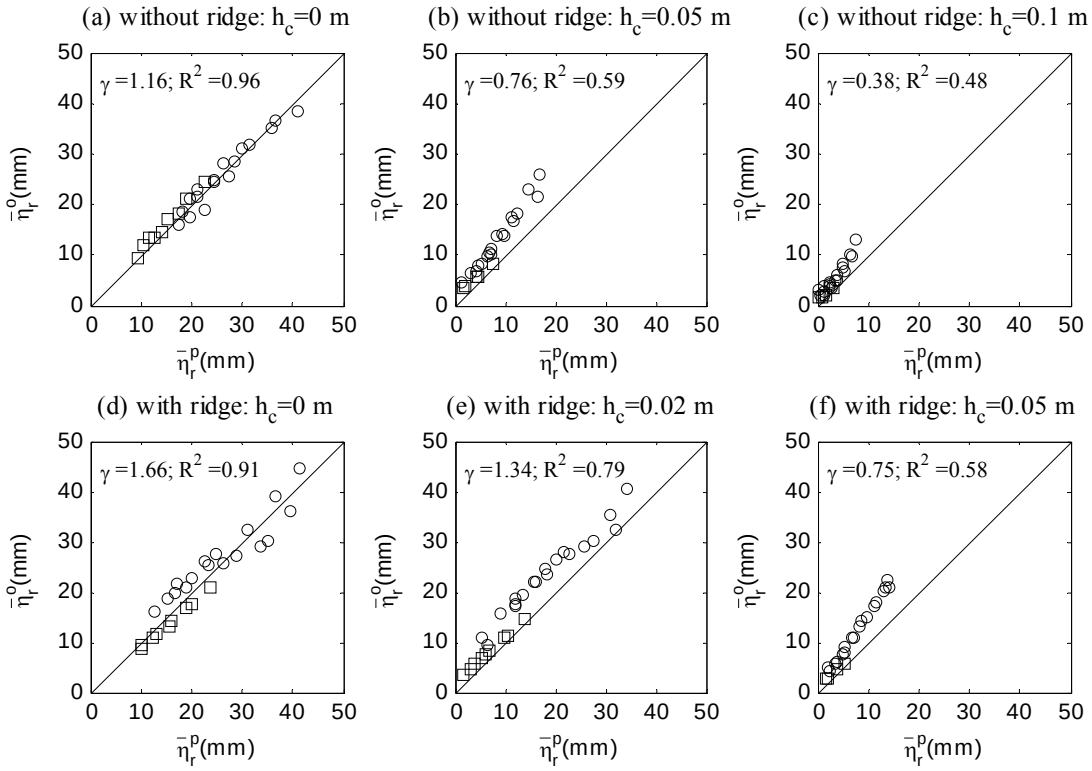

Fig. 5.2 Predicted wave setup ($\overline{\eta}_r^p$) vs. observed wave setup ($\overline{\eta}_r^o$) using the model of Tait (1972) for different reef-crest submergences, reef profiles and wave conditions (h_c - reef-crest submergence; γ - empirical parameter in the model; circles - monochromatic waves; squares - spectral waves; R^2 - R-square; Solid line - $\overline{\eta}_r^p = \overline{\eta}_r^o$).

5.5 Comparison of Experimental Data with the Model of Gourlay and Colleter (2005)

In this section, the theory of Gourlay and Colleter (2005) is used to analyze the wave setup data in Chapter 3. The author used $\gamma = 0.4$ in the model as suggested by Gourlay (1996a). Instead of ignoring K_r as Gourlay and Colleter (2005) did, K_r is included in the present analysis since the measured values of K_r can be as large as

0.6. Again, h_r in Eq. (5.9) is replaced by the still water depth over the reef crest, h_c. By doing so, Eq. (5.9) can be solved for wave setups. The comparisons between the calculated wave setups and the observed setups are shown in Fig. 5.3. Here the shape-dependent parameter K_p is taken as the average of all values obtained for both monochromatic and spectral wave conditions.

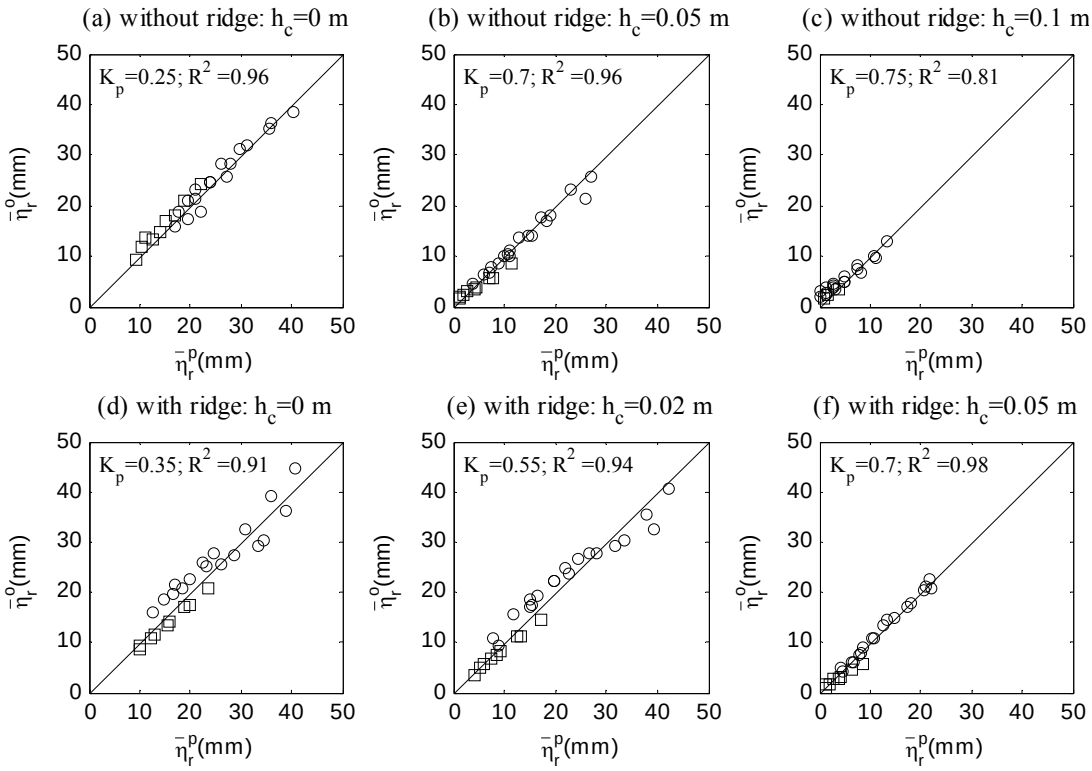

Fig. 5.3 Predicted wave setup ($\overline{\eta}_r^p$) vs. observed wave setup ($\overline{\eta}_r^o$) using the model of Gourlay and Colleter (2005) for different reef-crest submergences, reef profiles and wave conditions (h_c - reef-crest submergence; K_p - empirical parameter in the model; circles - monochromatic waves; squares - spectral waves; R^2 - R-square; Solid line - $\overline{\eta}_r^p = \overline{\eta}_r^o$).

Overall, comparing Fig. 5.3 with Fig. 5.2, it appears that the model of Gourlay and Colleter (2005) hindcasts the wave setup data more accurately than does the model of Tait (1972). In the absence of a ridge, Gourlay and Colleter (2005) gives good predictions of the wave-induced setup for both wave conditions (monochromatic

and spectral). For the reef with a ridge, there is a slight over-prediction of $\overline{\eta}_r$ when the incident wave height is large and h_c is small. K_p falls between 0.2 and 0.8 for both reefs (with and without the ridge), in agreement with the range of values suggested by Gourlay (1996b). However, even for the same reef profile (with or without the ridge), there is a systematic increase of K_p with increasing h_c, indicating that K_p is not a constant as originally proposed by Gourlay and Colleter (2005).

5.6 Discussions

To reproduce the experimental results in Chapter 3 using both approaches of Tait (1972) and Gourlay and Colleter (2005), the empirical parameter γ is required. In addition to the reef-crest submergence, laboratory and field studies (e.g., Raubenheimer et al., 1996; Goda, 2010) also reported that γ depends on seabed slope, i.e., fore-reef slope for coral reefs, and a constant of 0.4 to 0.6 has been found to be more appropriate for flat bottoms like reef flats (Nelson, 1994; Gourlay, 1994; see also the experimental results indicated by Eq. (2.20)).

By assuming wave breaking on the fore-reef and ignoring wave setdown, Tait (1972)'s model (i.e., Eq. (5.7)) arrived at the conclusion that the wave setup was controlled by the difference of wave depth between the breaking point and the reef crest (i.e., $h_b - h_c$), modulated by a factor $1/(8/3\gamma^2+1)$. It has been shown by Eq. (2.20) that γ is altered by h_c. When $h_c / H_0 = 0$, the values of γ at both breaking location and reef-crest were about the same, resembling the emerged slopes. Therefore, the agreement between the predictions and the observations was good as shown in Figs. 5.2(a) and 5.2(d). The fitted value of γ in the absence of the ridge (see Fig. 5.2(a)) gave $\gamma = 1.16$, which was closer to experimental observations of $\gamma = 1.04$ (see Eq. (2.20)) than the engineering value of $\gamma = 0.78$. However, as h_c increased, the fitted values of γ decreased because waves broke further shoreward where the seabed was milder (e.g., on the reef flat). γ is also modified by H_0 as

indicated by Eq. (2.20). Smaller waves may break further shoreward, resulting in a smaller γ. Consequently at a given h_c, there was considerable mismatch between the predictions and the observations when $h_c > 0$ as shown in Fig. 5.2. Therefore, different values of γ should be used to parameterize wave breaking on the fore-reef slope and the reef flat, respectively, as attempted by other investigators (e.g., Gourlay, 1996a; Hearn, 1999).

In Gourlay and Colleter (2005), transmitted waves on the horizontal reef flat were assumed to be controlled by the depth-limited breaking condition (i.e., Eq. (5.5)), and a single value of γ appropriate to a flat bottom was adopted. Gourlay and Colleter (2005) avoided the determination of breaking locations by introducing an additional fitting parameter, K_p. It can be shown that the relationship between K_p and the parameter γ, which was used in Tait (1972) on the fore-reef (for $K_r = 0$), is

$$K_p = \frac{16}{3}\frac{\overline{\eta}_r(\overline{\eta}_r + h_c)}{(4\pi)^{-0.8}\gamma^{0.4}H_0^2 S^{-0.4} - \gamma^2 h_c^2} = fn(h_c / H_0, S, \gamma) \qquad (5.10)$$

(See Appendix E for the derivation of Eq. (5.10)). Since Eq. (5.5) indicates that γ is related to incident wave conditions, it is possible that K_p, as shown in Eq. (5.10), is independent of incident wave conditions for a given profile. Therefore, the model of Gourlay and Colleter (2005) outperformed that of Tait (1972) in view of its ability to reproduce all the experimental data using a constant K_p at a given h_c. However, a dependence of K_p on h_c is evident in Fig. 5.3.

Reef porosity and bottom roughness may also affect the results given by the models of Tait (1972) and Gourlay and Colleter (2005). Gourlay and Colleter (2005) have pointed out that their shape-dependent coefficient K_p is also related to the porosity and roughness of the reef crest. The relative importance of bottom friction in the surf zone should depend on the fore-reef slope. For a steep fore-reef with waves breaking at the reef-edge, bottom friction should be negligible, while for a mild

fore-reef, frictional dissipation can be comparable with breaking dissipation (Lowe et al., 2005). More importantly, Gourlay (1996a) reported that wave-induced cross-shore currents on the reef flat caused a reduction in the magnitude of wave setup, an effect that should depend on the geometry of the reef system, in particular the nature of connections of the reef flat and back-reef lagoon to the open ocean.

The geological significance of ridges may also be important. Blanchon[2] pointed out that wave reflection from high algal ridges adjacent to reef-flat islands is likely responsible for accelerated rates of reef-flat progradation through time. The progradation in turn would increase reef-flat width which would reduce wave setup due to lateral flow away from the barotropic pressure gradient. That would reduce the algal ridge height and further reduce setup, and this process would continue until setup approached open or unconfined reef-flat values. A gradual "emergence" of the reef flat would be produced over geological time, which is a common feature of Indo-Pacific reefs. However, the impacts of lateral flow out of the confined system on wave setup need to be considered in order to understand this process. An attempt will be made in section 7.7 where a 2DH analytical mode is presented.

5.7 Concluding Remarks

The performance of selected existing models is evaluated using the experimental data in Chapter 3. The offshore scaling parameter shows that the maximum wave-induced setup on the reef flat has a stronger dependency on offshore wave energy flux than wave steepness, but it is generally insufficient to analyze the experimental data. The model of Tait (1972) can reproduce the experimental results with certain success, especially at relatively smaller reef-crest submergences. The model of Gourlay and Colleter (2005) can almost account for all experimental data, but with the use of an additional empirical parameter. The primary drawback in both models is that both have empirical parameters that vary with reef-crest submergence.

---

[2] Personal communication with Dr. Blanchon P. Marine Geosciences Lab., Reef Systems Unit, Institute of Marine Sciences & Limnology, National Autonomous University of Mexico (UNAM).

CHAPTER 6 WAVE SETUP OVER FRINGING REEFS UNDER CRITICAL FLOW CONDITION: AN ANALYTICAL MODEL BASED ON MASS BALANCE

6.1 Introduction

It has shown in Chapter 5 that there is a dependence of the shape-related parameter (K_p) on reef-crest submergence. This suggests that the model of Gourlay and Colleter (2005) has limited predictive values if a constant K_p is assigned for a given reef profile. Similarly, the model of Tait (1972) treated γ (the breaker depth index) as an empirical parameter that depends on both wave characteristics and reef-crest submergence. One normally anticipates that for a given reef profile (with or without the ridge), an analytical model could adequately reproduce the maximum wave-induced setup on the reef flat with a single empirical parameter relating only to reef morphology. To achieve this, a kinematic model based on mass balance will be considered in this chapter. A more sophisticated dynamic model will be introduced in next chapter.

The reviewed models (empirical, numerical or analytical) in Chapters 4 and 5 did not address the flow conditions when the reef-crest submergence is very small or the reef crest is even emerged. Under such conditions, wave breaking first occurs on the fore-reef and then pumps water onto the reef flat through overtopping. Motivated by broad-crested weir hydraulics, an analytical model is presented in this chapter to describe the setup induced by both monochromatic and spectral waves with very small reef-crest submergence. The weir-like scheme originally proposed by Gourlay (1996a) is adopted and improved. The present model does not directly consider wave breaking or other energy dissipation sources.

The rest of the chapter is organized as follows: the analytical model is formulated based on the mass conservation in section 6.2. The model is validated in section 6.3 by the experimental data for wave setup in Chapter 3 under monochromatic waves.

Model extension to spectral waves is discussed in section 6.4, and then applied to other published data with different reef configurations in section 6.5. A discussion on the model coefficient is given in section 6.6. Model comparison with that proposed by Gourlay (1996a) is conducted in section 6.7. Some conclusions are drawn in section 6.8.

6.2 Theoretical Consideration

6.2.1 Conservation of mass

The derivation of the model starts with the requirement of mass balance. From the one-dimensional (1D) continuity equation for monochromatic water waves, we have

$$\frac{\partial \overline{\eta}}{\partial t} + \frac{\partial q}{\partial x} = 0 \tag{6.1}$$

where η is the free surface elevation and the over-bar means time-averaging over a wave period and $q = U\overline{D}$ is the mean volumetric flux. $\overline{D} = h + \overline{\eta}$ is the total mean water depth and the depth-averaged mean velocity U is defined by

$$U = \frac{1}{\overline{D}} \overline{\int_{-h}^{\eta} u_w dz} \tag{6.2}$$

where h is the local water depth and u_w is cross-shore wave orbital velocity.

Eq. (6.1) indicates that when monochromatic waves interact with 1DH fringing reefs (laterally confined conditions as in a closed wave flume), the mass flux associated with breaking waves causes a "piling-up" of water (the increase of $\overline{\eta}$) on the leeside of reef crest (ridge), the baratropic pressure associated with this "piling-up" will force a current seaward. Initially, the water mass transported into the leeside of the ridge is not balanced by an equal return flow. This mass-flux difference allows the mean water level to continuously rise at the leeside of the ridge on the reef flat, until an equilibrium level is reached when the returning flow globally equals the shoreward mass flux. In this chapter, we only consider the equilibrium state.

For steady state, Eq. (6.1) reduces to

$$\frac{\partial q}{\partial x} = 0 \tag{6.3}$$

For fringing reef backed by a coastline, Eq. (6.3) requires that the mean volumetric flux through any vertical plane is zero within a wave period, i.e.,

$$q = U\bar{D} = 0 \tag{6.4}$$

which means that within one wave period, the mass flux of the forward flow must be balanced by the mass flux of the backward flow

$$Q_F = Q_B \tag{6.5}$$

where Q_F is the total forward volumetric flux during the up-rush phase of the wave breaking process over the reef crest and Q_B is the total backward volumetric flux during the backwash phase over the reef crest if we impose Eq. (6.4) on the reef crest.

.

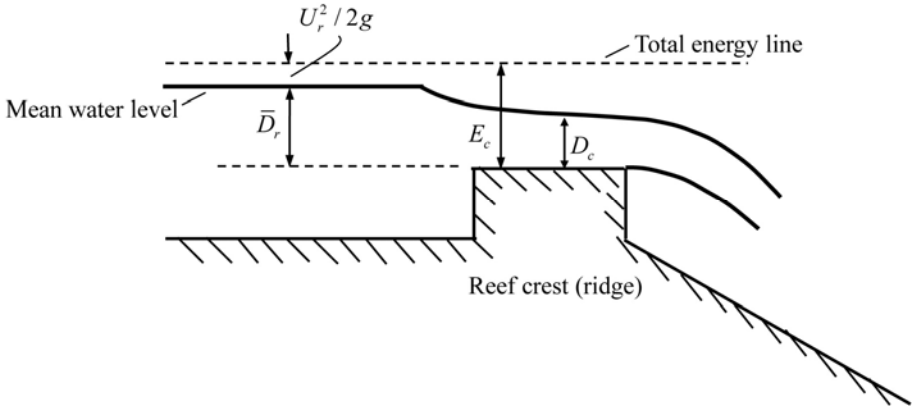

Fig. 6.1 Backward flow over the reef crest which resembles the flow over a broad-crested weir.

6.2.2 Expression for Q_B

For the backward flow over the crest of the ridge, it is assumed that the critical flow condition (free fall) exists, i.e., the water level over the reef flat is controlled by the critical water depth above the crest for a given flow rate. The flow is in analogy to

the flow over a broad-crested weir as shown in Fig. 6.1, where energy loss is ignored. For a broad-crested weir, it is well-known that the critical flow depth for the water flow above the crest is

$$D_c = \left(\frac{q_c^2}{gb^2} \right)^{1/3} \tag{6.6}$$

(See Munson et al., 2002) where q_c is the critical volumetric flow rate per unit width, b is the lateral width of the broad-crested weir (ridge), and g is the gravitational acceleration. Assuming no energy losses, the specific energy E_c measured above the crest of the weir is equal to $\bar{D}_r + U_r^2 / 2g$, where U_r is the depth-averaged velocity in the water upstream of the weir and $\bar{D}_r$ is the upstream (mean) water level above the crest (see Fig. 6.1). It is assumed that $U_r << \sqrt{2g\bar{D}_r}$ or $U_r^2 / 2g << \bar{D}_r$, thus in terms of the specific energy, E_c, the critical depth is

$$D_c = \frac{2}{3} E_c \approx \frac{2}{3} \bar{D}_r \tag{6.7}$$

Combining Eq. (6.6) and Eq. (6.7) and rearranging yields

$$q_c \approx b\sqrt{g} \left(\frac{2}{3} \bar{D}_r \right)^{3/2} \tag{6.8}$$

In terms of the still water depth above the crest, h_c, the water depth upstream of the ridge can be written as $\bar{D}_r = h_c + \bar{\eta}_r$, where $\bar{\eta}_r$ is the maximum wave-induced setup in the water upstream. Thus the flow rate q_c can be written as

$$q_c \approx b\sqrt{g} \left(\frac{2}{3} (h_c + \bar{\eta}_r) \right)^{3/2} \tag{6.9}$$

Consequently, the total volumetric flux during the wave backwash phase (half wave period) is estimated as

$$Q_B \approx b\sqrt{g} \left(\frac{2}{3} (h_c + \bar{\eta}_r) \right)^{3/2} \frac{T}{2} \tag{6.10}$$

where T is the wave period.

6.2.3 Expression for Q_F

Suppose that deep-water waves with wave height H_0 and period T approach the reef, and cause a setup over the fringing reef. In deep water, the flux of the forward flow over one half of wave period can be calculated by

$$Q_{F0} = b\int_0^{T/2}\int_{-\infty}^{\eta} |u_w| dz dt \tag{6.11}$$

Using linear wave theory and taking wave reflection into consideration gives

$$Q_{F0} = b\int_0^{T/2}\int_{-\infty}^{0} |u_w| dz dt = (1-K_r) b \frac{gH_0T^2}{4\pi^2} \tag{6.12}$$

where K_r is the reflection coefficient of the fringing reef.

A scaling factor β is introduced to account for the change of forward mass flux when waves propagate from the offshore to the ridge-top where critical depth occurs. The forward flow at the critical water depth can be expressed as

$$Q_F = \beta Q_{F0} = \beta(1-K_r) b \frac{gH_0T^2}{4\pi^2} \tag{6.13}$$

Note that all other factors that the present theory does not consider explicitly (for example, the energy loss due to the sharp edges of reef crest, the asymmetry of the wave profile near breaking point, the unsteadiness of the weir flow, the flux contribution from the bore, etc.) are implicitly included in the parameter β.

6.2.4 Expression for wave setup

After equating Eq. (6.10) to Eq. (6.13), the following non-dimensional wave setup arrives

$$\frac{h_c + \overline{\eta}}{H_0} = \frac{3/2}{(2\pi^2)^{2/3}} \frac{[(1-K_r)\beta]^{2/3}}{S^{1/3}} \tag{6.14}$$

where $S = H_0 / gT^2$ is the offshore wave steepness. Note that the reflection coefficient K_r may be related to the surf-similarity parameter for plane beaches. However, as discussed in section 2.4.4, the author is currently unable to find an empirical expression for K_r, thus the measured K_r is used in this chapter.

6.3 Model Validation

6.3.1 Overview of experimental setting

The model is validated with the laboratory experiments reported in Chapter 3. The experiments were designed to study the wave-induced setup over two types of reef profiles subjected to both monochromatic and spectral waves: (1) an idealized fringing reef model, which had a relatively steep fore-reef slope (1:6) and a horizontal platform reef flat (7 m long); (2) a fringing reef with a ridge, which was formed by placing a rectangular box (55 cm long, 50 cm wide and 5 cm high) on the reef flat with its front face aligned to the reef edge to simulate the ridge. For monochromatic waves, there are three tested reef-flat submergences (0 cm, 5 cm and 10 cm) in the absence of the ridge and four tested ridge-top submergences (0 cm, 1 cm, 2 cm and 5 cm) in the presence of the ridge, respectively. For spectral waves, there are three tested reef-flat submergences (0 cm, 5 cm and 10 cm) in the absence of the ridge and three tested ridge-top submergences (0 cm, 2 cm, 5 cm) in the presence of the ridge, respectively (see also Appendix B for the original experimental data). Note that in this chapter, the unified definition of "reef-crest submergence" (denoted as h_c) refer to both the "reef-flat submergence" and "ridge-top submergence". More details of the experimental settings can be found in section 3.2.

6.3.2 Visualization of the wave breaking process

Fig. 6.2 shows representative snapshots of wave transformation and breaking over the reef crest in the absence/presence of the ridge for monochromatic incident waves of $H_0 = 0.102\,m$ and $T = 1.25\,s$ with the zero reef-crest submergence ($h_c = 0$). Four different phases are displayed, starting from the moment when the lip

of the breaker hits the water surface ($t/T=0$). For the reef without the ridge, waves started to break on the fore-reef at $t/T=0$. At $t/T\approx 1/4$, the broken waves were rushing up the slope, producing a strong shoreward turbulence flow on the reef flat. At $t/T\approx 1/2$, water on both the fore-reef and reef flat retreated. At $t/T\approx 3/4$, strong reverse flow could be observed before the next wave breaking. The critical flow could occur on the reef edge as indicated by the arrows in the figure. When a ridge was present at the reef edge, the breaking waves stroke the front side of the ridge and then plunged onto the ridge-top, resulting in strong shoreward flow over the ridge top. Starting from $t/T\approx 3/4$, free fall seawards was observable at the edge of the ridge (also indicated by the arrows).

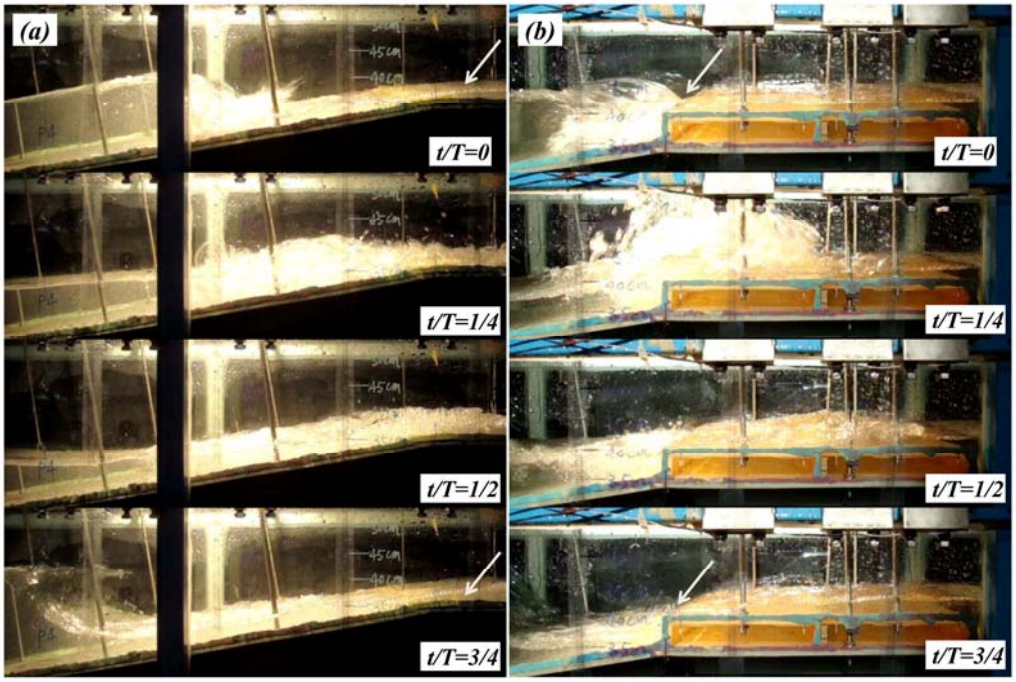

Fig. 6.2 Snapshots of monochromatic wave transformation over reef crest at different phases: (a) without ridge; (b) with ridge. The arrows indicate the occurrence of the free falls.

6.3.3 Comparison between model predictions and measurements

The wave setup predicted by the present analytical model, i.e., Eq. (6.14), is plotted against the measured ones in Figs. 6.3(a) and 6.3(b) for the reefs in the absence and presence of the ridge, respectively, under monochromatic waves. The measured

reflection coefficients are used in the calculations. The scaling factor β is obtained by a least-square fitting to the experimental dataset for each reef-crest submergence, h_c. For a clear presentation of the data, only those datasets with good prediction by the model are shown in the figures.

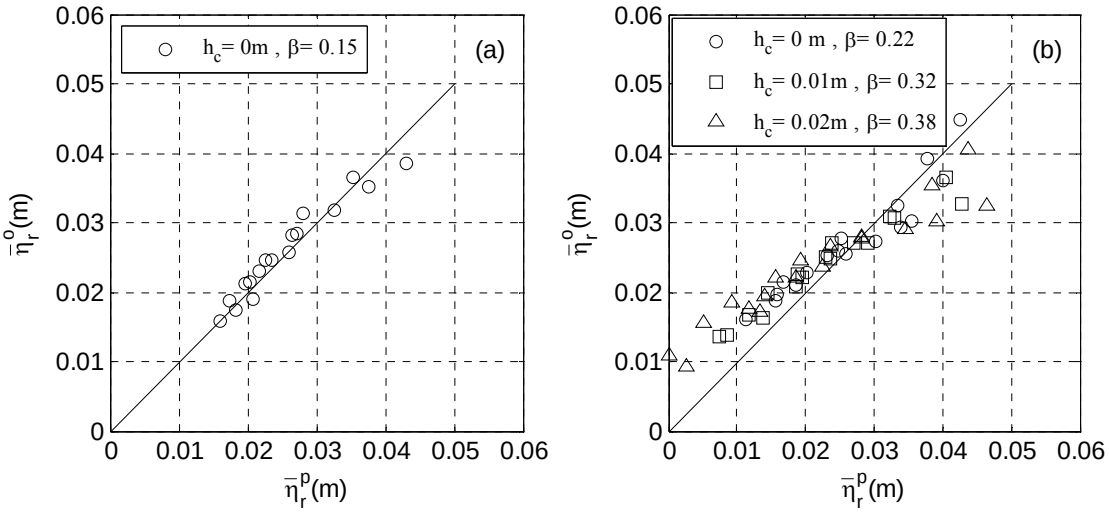

Fig. 6.3 Predicted wave setup ($\overline{\eta}_r^p$) vs. observed wave setup ($\overline{\eta}_r^o$) for different reef-crest submergences (h_c) under monochromatic waves: (a) without ridge; (b) with ridge (β - scaling factor in the model; Solid line - $\overline{\eta}_r^p = \overline{\eta}_r^o$).

It can be seen from Figs. 6.3(a) and 6.3(b) that for both reefs, with and without the ridge, the predicted setup agrees well with the measurements when the reef-crest submergence, h_c, is relatively small. Good fit is obtained for the initial dry reef crests ($h_c = 0$), which is anticipated since the critical flow is more likely to occur when reef-crest water level is small enough to allow a free fall during the backwash period. However, as h_c increases, the agreement becomes less satisfactory and some unphysical negative setups are predicted, indicating the hydraulic control at the reef/ridge edge imposed by critical depth is no longer valid in those cases (not shown in the figures). Comparisons between Figs. 6.3(a) and 6.3(b) show that the analytical model could provide better predictions for the experiments with the ridge, as long as h_c is not too large. This is expected because the vertical edge of the ridge increases the duration of free fall during backward phase and the sloping fore-reef

may impose a downstream effect if the ridge is absent. It is also observed that the value of β increases with increasing of h_c.

6.4 Extension to Spectral Waves

Extension of the present model to the spectral waves tested in Chapter 3 is straightforward provided that the representative wave height and wave period are selected. H_{rms} and T_p for spectral waves, as discussed in Chapter 5, are used here. The results are shown in Figs. 6.4(a) and 6.4(b), respectively, for the reefs without and with the ridge. It can be seen again that for both reefs, the predicted setups agree very well with the measurements when $h_c = 0$. As h_c further increases, model predictions break down due to the lack of critical flow condition at the reef crests (not shown in the figures).

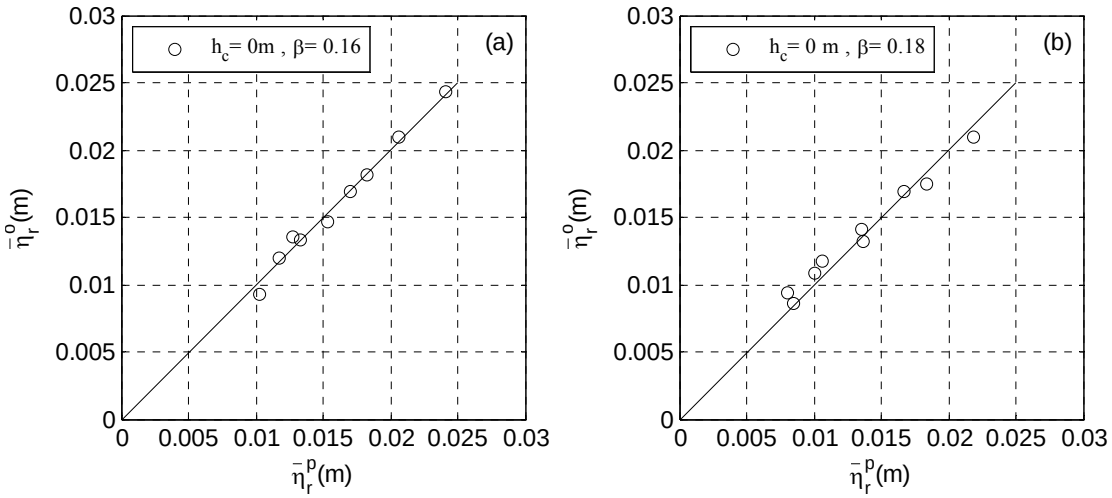

Fig. 6.4 Predicted wave setup ($\overline{\eta}_r^p$) vs. observed wave setup ($\overline{\eta}_r^o$) for different reef-crest submergences (h_c) under spectral waves: (a) without ridge; (b) with ridge (β - scaling factor in the model; Solid line - $\overline{\eta}_r^p = \overline{\eta}_r^o$).

6.5 Applications to Other Published Experimental Data

In this section, the present model is applied to three other published laboratory work, i.e., Seelig (1983), Gourlay (1996a) and Demirbilek et al. (2007), which have different fringing reef profiles and wave conditions. Seelig (1983)'s reef profile consisted of a steep composite fore-reef with an average slope of 1:9.6, a small sharp reef crest, and a horizontal reef flat. The reef profile of Demirbilek et al. (2007) was identical to that of Seelig (1983), except for the sharp reef crest, which was not present in their model. The fore-reef of Gourlay (1996a)'s profile was very steep (1:1) compared with that of Seelig (1983). It had a sloping reef flat without the reef crest. Several reef-crest submergences were tested in these experiments. Experiments conducted by Seelig (1983) and Gourlay (1996a) were under monochromatic waves while those by Demirbilek et al. (2007) were under spectral waves. The reflection coefficients in Seelig (1983)'s experiments were not available, thus $K_r = 0$ was assumed in the calculations. For both experiments of Gourlay (1996a) and Demirbilek et al. (2007), the measured reflection coefficients were used. The predicted wave setups using the present theory, together with the measured setups of Seelig (1983), Gourlay (1996a) and Demirbilek et al. (2007), are shown in Figs. 6.5(a), 6.5(b) and 6.5(c), respectively. Again, only those data with good agreement are presented in the figures.

For Seelig (1983)'s data shown in Fig. 6.5(a), the agreement between prediction and measurement is satisfactory when the reef crest is initially dry ($h_c = 0$). Fig. 6.5(b) shows excellent agreement between the predictions and measurements for Gourlay (1996a)'s experiments under $h_c = 0$; good agreement is also found when h_c reached 0.05m. These should be attributed to the very steep fore-reef slope in his model, which ensured a critical flow condition for those cases. Under the spectral wave condition tested by Demirbilek et al. (2007), good agreement is again found for cases with smaller h_c (see Fig. 6.5(c)). Comparisons among the three figures show that the presence of a steep reef crest may significantly change the value of β, thus altering the flow pattern.

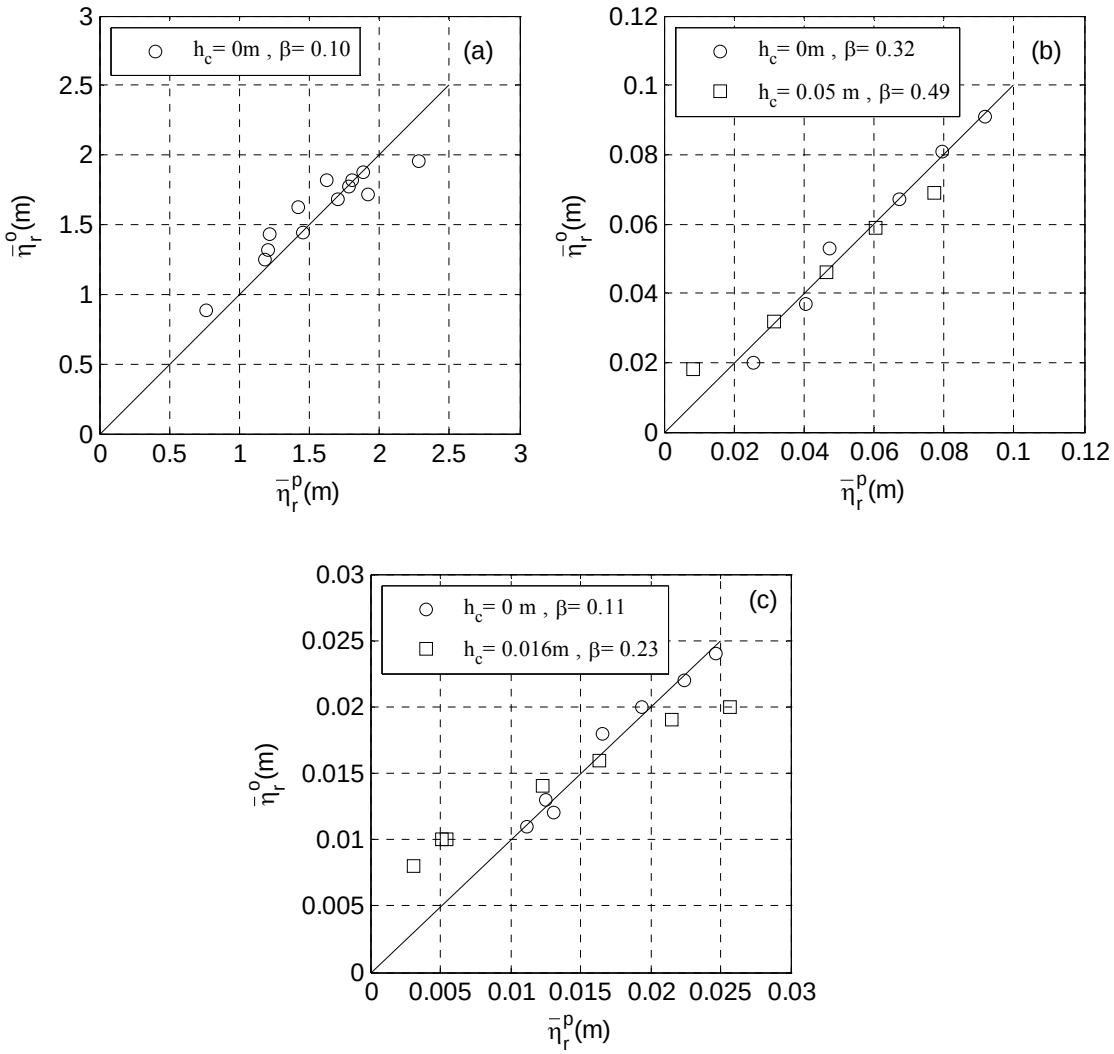

Fig. 6.5 Predicted wave setup ($\overline{\eta}_r^p$) vs. observed wave setup ($\overline{\eta}_r^o$) for different reef-crest submergences (h_c): (a) Dataset from Seelig (1983); (b) Dataset from Gourlay (1996a); (c) Dataset from Demirbilek et al. (2007) (β - scaling factor in the model; Solid line - $\overline{\eta}_r^p = \overline{\eta}_r^o$).

6.6 More on the Scaling Factor

Previous discussion has shown that β in the model increases with increasing h_c until a certain value at which the model is no longer valid. This is due to the fact that as the reef-crest submergence becomes larger, seaward water may affect the free fall and critical flow condition (backwater effect). In this section, the variation

of β with different reef profiles is investigated. The fitted values of β for each dataset at $h_c = 0$ is summarized and shown in Table 6.1; also shown in the table are the values of fore-reef slope (s) , which is believed to be related to both the fore-reef configuration and the reef-crest shape.

Table 6.1 The values of β in present model for different experimental data with $h_c = 0$

Dataset	Wave type	s	β	R^2 [e]
Chapter 3 data without ridge	monochromatic	1:6	0.15	0.92
Chapter 3 data with ridge	monochromatic	1:5[b]	0.22	0.81
Chapter 3 data without ridge	spectral	1:6	0.16	0.99
Chapter 3 data with ridge	spectral	1:5[b]	0.18	0.96
Seelig (1983)	monochromatic	1:9.6[a,c,d]	0.10	0.73
Gouraly (1996a)	monochromatic	1:1	0.32	0.98
Demirbilek et al.(2007)	spectral	1:9.6[a]	0.11	0.97

[a] Averaged slope of the composite fore-reef slope;

[b] The equivalent slope as defined in Fig. 5.1 in the present of the reef crest (ridge) ;

[c] The slope without considering the presence of the reef crest;

[d] Reflection is ignored in the calculations;

[e] R^2 - R-square.

Table 6.1 reveals that the values of β are generally within the range of 0 to 0.5. The primary reason for the smaller β should be the reduction of forward mass flux associated with wave propagation from offshore to the reef crest. However, it may also be affected by the unsteadiness, the application of linear wave theory, the lack of energy dissipation, etc.. Further investigation on this issue may be needed. Meanwhile, the values of β generally increase with increasing fore-reef slope

within the investigated data range. Through trial and error, the relationship between s and β is found to be best described by the following power law

$$\beta = -0.13 s^{-0.45} + 0.45 \quad \text{for } h_c = 0 \text{ and } 1/9.6 < s < 1/1 \tag{6.15}$$

with $R^2 = 0.94$. The upper limit $\beta = 0.45$ may correspond to the case where the fore-reef becomes vertical, resembling a submerged step. A lower limit may also exist, and it should be related to the reef profile whose fore-reef slope is so gentle that the backwater can affect the free fall. However, this conjecture cannot be validated with the available datasets.

The present approach shows that wave setup is dependent on both deep-water wave steepness and fore-reef slope (through β) when the wave depth over reef-crest is sufficiently small. However, there may be a transition region of h_c in which the theory is not valid.

6.7 Comparison with the Model of Gourlay (1996a)

To the best of the author's knowledge, similar kinematic models in existing literatures can only be found in Gourlay (1996a). The present model differs from that in Gourlay (1996a) mainly in the estimation of the forward flow, Q_F. In Gourlay (1996a)'s theory, Q_F was computed at the reef edge by assuming a saw-tooth profile for breaking waves. The wave height was converted to offshore by a shoaling coefficient which was approximately equal to one. Wave reflection was not considered in the formulation, thus he arrived at a more complicated expression than Eq. (6.14) as

$$\frac{\bar{\eta}_r}{H_0} = \frac{0.391}{K^{2/3}} \left[2\left(\frac{h_c}{H_0}\right)^{5/2} - \left(2\frac{h_c}{H_0} - 3K\right)\left(\frac{h_c}{H_0} + K\right)^{2/3} \right] - \frac{h_c}{H_0} \tag{6.16}$$

where the wave-crest asymmetry factor, K (ranging from 0.5 to 1.0) was introduced in his model as a fitting parameter.

The results obtained from the Eq. (6.16) for all the aforementioned datasets with $h_c = 0$ are listed in Table 6.2.

Table 6.2 The values of K in model of Gourlay (1996a) for different experimental data with $h_c = 0$

Dataset	Wave type	s	K	R^2 [e]
Chapter 3 data without ridge	monochromatic	1:6	0.25	0.74
Chapter 3 data with ridge	monochromatic	1:5[b]	0.29	0.60
Chapter 3 data without ridge	spectral	1:6	0.32	0.87
Chapter 3 data with ridge	spectral	1:5[b]	0.28	0.97
Seelig (1983)	monochromatic	1:9.6[a,c,d]	0.22	0.38
Gouraly (1996a)	monochromatic	1:1	0.38	0.96
Demirbilek et al.(2007)	spectral	1:9.6[a]	0.32	0.82

[a] Averaged slope of the composite fore-reef slope;

[b] The equivalent slope as defined in Fig. 5.1 in the present of the reef crest (ridge) ;

[c] The slope without considering the presence of the reef crest;

[d] Reflection is ignored in the calculations;

[e] R^2 - R-square.

Comparing Table 6.1 with Table 6.2, it can be found that overall the present model outperformed that of Gourlay (1996a) in view of lager values of R^2 in Table 6.1 than those in Table 6.2. Gourlay (1996a) only gave equivalently good predictions for both the spectral wave data in Chapter 3 with the ridge and his data. The poorer performances of Gourlay (1996a)'s model for most datasets cannot be explained by the missing wave reflection in Eq. (6.16): the reflection coefficients were not available for Seelig (1983)'s data but the present model still worked better. Meanwhile, the fitted values of K are generally in the range of 0 - 0.5 which is

quite different from his suggested range of 0.5 - 1.0 as the wave asymmetry factor. The author believes that the role of K in his model is equivalent to β in the present model: both include not only the effects of waves, but also other factors such as fore-reef slope, flow unsteadiness, energy dissipation, etc.. However, Table 6.2 shows that a definite variation of K with the fore-reef slope (s) as that of the β in the present model cannot be identified.

Finally, it is worth mentioning that the present theory should be suitable for emerged reef crest where the critical flow condition is more likely to be satisfied. In such case, wave overtopping is responsible for the forward flow, Q_F. There is a wealth of existing empirical formulae to estimate overtopping discharge over emerged seawalls and breakwaters (Owen, 1980; Van der Meer and Janssen, 1995; Pullen et al., 2007; Goda, 2009 and others), most of them are exponentially related to the relative freeboard and additional empirical parameters are always needed in those equations. However, the available data for fringing reefs are limited to the submerged or zero-submerged conditions thus the applicability of those formulae for wave overtopping cannot be examined in this chapter.

.

6.8 Concluding Remarks

A kinematic analytical model based on the mass balance is proposed in this chapter to study the wave setup over fringing reef profiles that can allow critical conditions (free-fall conditions) to occur. It is found that wave setup can be described by deep-water wave steepness and a scaling factor. The present model is successful in reproducing the maximum wave-induced setup on reef flats with and without the presence of the ridge as long as a free-all condition approximately exists. The predictions match equivalently well with measurements under both monochromatic and spectral wave conditions. Model applications to other published experiments also show that the model is capable of predicting the available laboratory data provided that the reef-crest submergences are sufficiently small. The scaling factor in the model is found to increase with both increasing reef-crest submergence and fore-reef slope. The present model outweighs Gourlay (1996a)'s model in terms of

its simpler analytical form, better predictions and the systematic variation of the empirical parameter with fore-reef slope. Further understanding on the scaling factor is needed.

CHAPTER 7 WAVE SETUP OVER FRINGING REEFS: AN ANALYTICAL MODEL BASED ON MOMENTUM BALANCE

7.1 Introduction

Previous discussions have shown that for 1DH experiments in a closed flume without circulation, experimental results may be interpreted either by wave-averaged momentum balance and energy balance (e.g., the models of Tait (1972) and Gourlay and Colleter (2005) in Chapter 5) or by mass balance over one wave period (the hydraulic theory in Chapter 6). These two methods approach the same problem from different theoretical considerations: the former is a dynamic theory which studies the driving forces that maintain the equilibrium state, while the latter is in fact a kinematic theory which examines the equilibrium state itself. When a reef crest (ridge) is present, two main forces exist: (1) the radiation stress that drives the mean flow, and (2) the forces on the ridge that reflect waves and resist the returning mean flow. Both forces contribute to the wave setup over the reef flat and it is difficult to differentiate their individual contributions. It is desirable to have an analytical approach (at least in 1DH form) that can be devised to account for the experimental results in Chapter 3 as well as other published laboratory data discussed in Chapters 6. Additional benefits could be obtained if it could be applied to field observations with acceptable accuracy.

The necessity to develop a 2DH model has been emphasized in the previous chapters in that coral reef flows observed in the field are essentially 2DH. The effects of currents (wave-driven currents or/and tidal currents) together with the roughness of the reef surface on wave-induced setup may be significant in the context of a 2DH reef system. The modification of currents to the wave setup across the reef has been reported in laboratory experiments (Gourlay, 1996a) and field observations (Lugo-Fernández et al., 2004; Hench et al, 2008; Lowe et al., 2009a). Some 1DH analytical models (Symonds et al., 1995; Hearn, 1999; Gourlay and Colleter, 2005) have considered the effects of current as well. Analytical models for

2DH flows around reefs are rare. Lowe et al. (2009a) is one of the pioneers to propose a simple 2DH model that used the mass and momentum balances to study the wave setup and circulation in the cross-reef direction (both over the reef flat and within the lagoon-channel region); they included in their model both bottom friction and reef morphological features. However, there is a rich literature in barred beaches (Bellotti, 2004) and submerged breakwaters (Calabrese et al., 2008; Zanuttigh et al., 2008; Vicinanza et al., 2009), from which some useful ideas can be borrowed to study 2DH reef flow problems.

Reef-flat surfaces are often very rough compared to sandy beaches because of the presence of canopy-forming benthic organisms and the irregular morphology of the platforms on which they grow. Field measurements of reef-flat surface roughness showed that coral reefs have very high drag coefficients, being some orders of magnitude higher than those associated with normal sandy shelves (Falter et al., 2004; Lowe et al., 2005; Hench et al., 2008). The bottom friction can play an important or even dominant role in the overall wave energy dissipation on the mild slope fore-reefs (e.g., Lowe et al., 2005), which could significantly reduce the wave setup (e.g., Longuet-Higgins, 2005; Dean and Bender, 2006; Apotsos et al., 2007). However, for 1DH fringing reef models with a very rough reef flat, the influence of frictional dissipation in water over the reef flat can be ignored as shown by experimental work reported in Appendix C.

Motivated by the work in previous chapters, an analytical model based on 1DH cross-shore momentum balance is derived in this chapter and validated by both laboratory and field data. The model is extended to 2DH in analogy to “rip current” systems around barriers or breakwaters. The rest of the chapter is arranged as follows: the 1DH analytical model is formulated in section 7.2. The model is validated in section 7.3 by the experimental data presented in Chapter 3 and other published experimental data. An analysis of model sensitivity is conducted in section 7.4. Model applications to some published field data are presented in section 7.5. Some discussions on the model are given in section 7.6. An extension to 2DH problem is performed in section 7.7 and major conclusions are drawn in section 7.8.

7.2 Theoretical Consideration

7.2.1 Governing equations

The cross-shore depth-integrated momentum equation, i.e., Eq. (1.3), is applied in the surf zone for a general fringing reef profile (a seaward fore-reef followed by a reef flat with/without a reef crest (ridge) being located at the reef edge). The reef crest must be submerged ($h_c > 0$) or at least initially dry ($h_c = 0$) (see Fig. 7.1 for an illustration). Assuming alongshore uniform waves and bathymetry, we have

$$g(\overline{\eta}+h)\frac{\partial \overline{\eta}}{\partial x}+\frac{1}{\rho}\frac{\partial S_{xx}}{\partial x}+\frac{\partial[U^2(\overline{\eta}+h)]}{\partial x}+\frac{\tau_x^b}{\rho}=0 \tag{7.1}$$

or

$$\frac{\partial\left[U^2(h+\overline{\eta})\right]}{\partial x}+\frac{g}{2}\frac{\partial(h+\overline{\eta})^2}{\partial x}+\frac{1}{\rho}\frac{\partial S_{xx}}{\partial x}+\frac{\tau_x^b}{\rho}-g(h+\overline{\eta})\frac{\partial h}{\partial x}=0 \tag{7.2}$$

See section 1.1.3 for the definitions of the symbols in the equations above. Some assumptions need to be made in order to further simplify Eq. (7.2). The first assumption is that waves break on a fore-reef location (x_b), but the surf zone process might cease beyond the reef crest (x_c). This is consistent with our laboratory observations where the inner surf zone might occupy a region shoreward of the reef crest (see e.g., Fig. 3.4).

Integrating Eq. (7.2) from the breaking point (the start of the surf zone), $x = x_b$, to the end of the surf zone, $x = x_s$, gives

$$(h_s+\overline{\eta}_r)U_s^2-h_bU_b^2+\frac{g}{2}(h_s+\overline{\eta}_r)^2-\frac{g}{2}h_b^2+\Delta S-\Delta\Pi+\Upsilon=0 \tag{7.3}$$

where h_b is the breaker wave height, h_s is the water depth at the end of the surf zone, U_b and U_s are the depth-averaged mean velocities at the breaking point and the end of surf zone, respectively. $\Delta S=(S_{xx}^s-S_{xx}^b)/\rho$ is related to the wave

radiation stress, with S_{xx}^{b} and S_{xx}^{s} being the x components of the radiation stress tensor at x_b and x_s, respectively; $\Upsilon = \int_{x_b}^{x_s} \tau_b / \rho dx$ is the frictional force in the surf zone. $\Delta\Pi = \int_{x_b}^{x_s} g(h+\bar{\eta})(dh/dx)dx$ can be viewed as a reaction of the bottom to the water above (Bellotti, 2004).

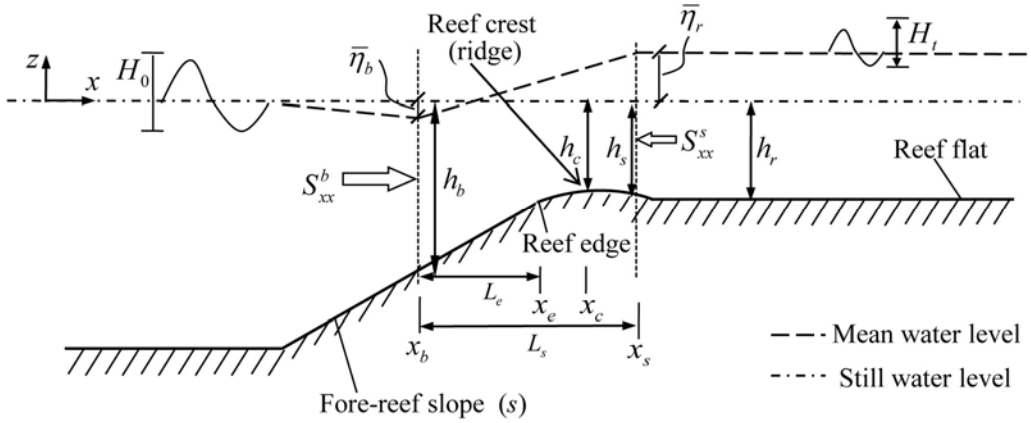

Fig. 7.1 Configuration of a fringing reef with a ridge and some notations adopted in this chapter.

7.2.2 Approximation for 1D fringing reefs

For a closed flume without circulation, the wave-driven current terms in Eq. (7.3) are approximately zero. Frictional force term can be ignored in view that the laboratory reef profiles are relatively smooth and the mean current is very weak as measured in section 3.5. The effects of those terms on wave setup will be discussed later. After neglecting the mean current and bottom friction, Eq. (7.3) reduces to

$$\frac{g}{2}(h_s+\bar{\eta}_r)^2 - \frac{g}{2}h_b^2 + \Delta S - \Delta\Pi = 0 \tag{7.4}$$

where the wave-induced setdown at breaking point ($\bar{\eta}_b$) has been neglected since $\bar{\eta}_b / h_b << 1$ (see Eq. (7.8) below).

For laboratory experiments, the following assumptions can be justified when computing the radiation stresses: (1) simple progressive waves are assumed shoreward of the surf zone; (2) generation of both high and low frequency waves can be ignored; (3) a partial standing wave pattern (see Fig. 3.10 and Fig. 4.11) exists before waves break. The approximate expression for S_{xx}^{b} based on the linear shallow wave approximation, neglecting the shift of the phase constant between incident and reflected waves (Calabrese et al., 2008), is

$$S_{xx}^{b} = S_{xx}^{b0}(1+K_r^2) = \frac{3}{16}\rho g H_b^2 (1+K_r^2) = \frac{3}{16}\rho g \gamma_1^2 h_b^2 (1+K_r^2) \tag{7.5}$$

where $S_{xx}^{b0} = 3\rho g H_b^2 / 16$ is the *x*-component of the radiation stress tensor at the breakpoint without considering wave reflection. K_r is the reflection coefficient, which needs to be obtained from measurements since no empirical formula is available for fringing reefs. The depth-limited breaking condition ($H_b = \gamma_1 h_b$) is used in Eq. (7.5) to estimate H_b, with γ_1 being the breaker depth index for the fore-reef. Assuming normal incident waves, the breaker water depth, h_b, can be derived from a simple 1D energy balance after neglecting the frictional dissipation (see Appendix E)

$$h_b = \frac{H_0 (1-K_r^2)^{0.4}}{(4\pi\gamma_1^2)^{0.4} S^{0.2}} \tag{7.6}$$

where $S = H_0 / gT^2$ is the offshore (deep-water) wave steepness. Therefore, h_b is a function of both incident wave condition and relative reef-flat submergence (implicitly included in γ_1 as indicated by Eq. (5.5)).

On the reef flat, S_{xx}^{s} is evaluated by

$$S_{xx}^{s} = S_{xx}^{b0} K_t^2 = \frac{3}{16}\rho g H_t^2 = \frac{3}{16}\rho g \gamma_2^2 (h_s + \overline{\eta}_r)^2 \tag{7.7}$$

where $H_t = H_b K_t$ is the transmitted wave height and K_t is the transmission coefficient. Unlike submerged breakwaters, there is no well-established empirical

formula to estimate K_t for reefs, thus a similar depth-limited breaking condition $H_t = \gamma_2(\overline{\eta}_r + h_s)$ is employed in the water over the reef flat, where the value of γ_2 is different from that of γ_1 since the breaker depth index for a horizontal bottom is smaller than that for a slope (see section 5.6).

The wave-induced setdown ($\overline{\eta}_b$) can be estimated by (see Longuet-Higgins and Stewart, 1964)

$$\overline{\eta}_b = -\frac{H_b^2}{16h_b} = -\frac{\gamma_1^2 h_b}{16} \tag{7.8}$$

This setdown is approximately 20% of $\overline{\eta}_r$, thus will be kept when approximating the variation of $\overline{\eta}$ in the surf zone.

In principle, the integral of $\Delta\Pi = \int_{x_b}^{x_s} g(h+\overline{\eta})(dh/dx)dx$ in Eq. (7.4) can be computed numerically if detailed information in the surf zone (x_b, x_s, $h(x)$) is known. Subsequently, the wave-induced setup can be computed based on Eqs. (7.5) to (7.8). However, in practice, particularly in field conditions, detailed measurements of surfzone area and the seabed topography underneath are non-trivial. There is also no well-accepted formula to predict x_s so far, thus a further approximation of this term is necessary for some special cases.

(1) Idealized profile in the absence of a ridge

For an idealized fringing reef profile without a ridge (a seaward planar fore-reef followed by a horizontal reef flat, where the reef edge coincides with the reef crest, i.e., $x_e = x_c$ and $h_s = h_r = h_c$), Fig. (3.10) shows that MWL increased rapidly right after the breaking point and became asymptotic to a more or less constant further shoreward. Therefore different expressions (the polynomial and the power law) that are possible to approximate such variation of $\overline{\eta}$ from x_b to x_s are investigated in this study (Note that Bellotti, 2004 used a linear variation of $\overline{\eta}$ over a barrier).

Detailed derivation is given in Appendix F, where a unified general expression for $\Delta\Pi$ has been given in the following form (See Eq. (F.24))

$$\Delta\Pi = \frac{g}{2}\left(h_r^2 - h_b^2\right) + g\overline{\eta}_b\left(h_r - h_b\right)\left(1-\lambda\right) + g\overline{\eta}_r\left(h_r - h_b\right)\lambda \tag{7.9}$$

where

$$\lambda = \begin{cases} \dfrac{\beta_0}{2} & \textit{linear polynomial} \\ -\dfrac{1}{3}\beta_0^2 + \beta_0 & \textit{quadratic polynomial} \\ -\dfrac{1}{2}\beta_0^3 + \beta_0^2 & \textit{cubic polynomial} \\ \dfrac{3}{5}\beta_0^4 - 2\beta_0^3 + 2\beta_0^2 & \textit{quartic polynomial} \\ \dfrac{C}{1+C}\beta_0^{\frac{1}{C}} \quad C = 2,3,\cdots N & \textit{power law} \end{cases} \tag{7.10}$$

and β_0 is a dimensionless parameter defined by

$$\beta_0 = \frac{x_e - x_b}{x_s - x_b} = \frac{L_e}{L_s} \tag{7.11}$$

Comments on Eq. (7.10) will be given in section 7.3.3. Physically, β_0 is the ratio of the distance between the breaking point and the reef edge (L_e) to the total surf zone width (L_s). Since $L_e \le L_s$, β_0 must be within the range of 0 to 1 ($\beta_0 = 0$ indicates that wave breaking occurs on the reef edge and $\beta_0 = 1$ reduces the present model approximately to Eq. (5.8)). For a given reef profile, $L_e = (h_b - h_r)/s$ (s is fore-reef slope) is a function of both wave condition and reef-flat submergence. In section 2.3.3, it has also been shown that L_s depends both on the incident waves and reef-flat submergence.

Based on all derivations above, substituting Eqs. (7.5), (7.7) and (7.9) into Eq. (7.4) leads to the following second-order algebraic equation for $\overline{\eta}_r$

$$\overline{\eta}_r^{\,2} + b\overline{\eta}_r + c = 0 \tag{7.12}$$

which has a unique positive solution

$$\overline{\eta}_r = \frac{-b + \sqrt{b^2 - 4c}}{2} \tag{7.13}$$

with

$$b = 2h_c + \frac{16(h_b - h_r)\lambda}{(8 + 3\gamma_2^2)} \tag{7.14}$$

$$c = \frac{3\gamma_2^2 h_r^2 - 3\gamma_1^2 h_b^2 (1 + K_r^2) + 16\overline{\eta}_b (h_b - h_r)(1 - \lambda)}{8 + 3\gamma_2^2} \quad (c < 0) \tag{7.15}$$

where the parameter λ is related to β_0 by Eq. (7.10); h_b and $\overline{\eta}_b$ are given by Eqs. (7.6) and (7.8), respectively; K_r needs to be obtained from measurements since no well-established empirical expression for K_r is available; the model parameters γ_1, γ_2 and β_0 will be discussed later. The requirement on $c < 0$ is satisfied when $h_r < h_b$ if both wave reflection and setdown are ignored. When waves propagate over the reef crest without breaking, the present approach is no longer valid (the setup is always zero).

(2) Idealized profile in the presence of an idealized ridge

For an idealized ridge profile such as the rectangular one tested in Chapter 3 (shown in Fig. 5.1), the ridge is low-crested with a wide horizontal ridge-top, thus for most cases, breaking actually ceases on the ridge-top, i.e., $h_c = h_s$. Meanwhile, both seaside and leeside slopes are vertical, showing the singular points in dh/dx, thus the expression for $\Delta\Pi$ (see Eq. (G.7) in Appendix G) will be slightly different from Eq. (7.9). Detailed derivations for this case are given in Appendix G based on the power law approximation of $\overline{\eta}$ in surf zone (the polynomial approximations can also be derived in a similar way but the expressions are more complicated and thus are not included in this thesis). For fringing reefs with an idealized ridge, the maximum setup on the ridge-top can be calculated by Eq. (7.13) with

$$b = 2h_c + \frac{16(h_b - h_r)\lambda + 16\dfrac{C+1}{C}(h_r - h_c)\lambda}{(8 + 3\gamma_2^2)} \tag{7.16}$$

$$c = \frac{3\gamma_2^2 h_c{}^2 - 3\gamma_1^2 h_b^2\left(1 + K_r^2\right) + 16\bar{\eta}_b\left(h_b - h_r\right)(1-\lambda) + 16\bar{\eta}_b\left(1 - \dfrac{C+1}{C}\lambda\right)\left(h_r - h_c\right)}{8 + 3\gamma_2^2} \tag{7.17}$$

where $\lambda = C\beta_0^{1/C}/(1+C)$ is from Eq. (7.10) for power law approximation and β_0 is defined by Eq. (7.11).

(3) Idealized profile in the presence of a general ridge (extension of the theory)

When there is a ridge with arbitrary shape on a reef, it is anticipated that the above approximation, i.e., Eq. (7.9), for $\Delta\Pi$ in the absence of the ridge can still be used, provided that a suitable representative h_r can be selected since wave breaking may cease at different locations for different waves and geometries. The water depth h_c has been proven to be the key parameter in controlling the reef-flat hydrodynamics throughout the previous chapters (Chapters 2, 3, 5 and 6) and other studies (e.g., Gourlay, 1996b; Blenkinsopp, and Chaplin, 2008), and h_c is also easy to be measured, thus it will be used for h_r in Eq. (7.9). Consequently, the value of β_0 depends on the choice of h_c and the physical interpretation of β_0 could be different from what we understand for the idealized reefs with/without the rectangular ridge, i.e., defined by Eq. (7.11).

7.2.3 Upper and lower limits of the model validity

For a given water depth over the reef crest, incident waves of sufficiently small amplitude can propagate onto the reef crest without breaking, hence generating no setup. Under such circumstances, the theory outlined above (Eqs. (7.3) - (7.17)) will no longer be valid. Therefore, there must be an upper limit for h_c / H_0 above which wave breaking ceases for a given reef profile. This transition can be estimated by

assuming that the maximum allowable local wave height at the reef crest (H_t) is controlled by the local water depth, i.e., $H_t = \gamma_2 h_c$ and that the energy dissipation due to bottom friction can be ignored. Conservation of the cross-shore energy flux between a station offshore and a station at the reef crest (using linear deep and shallow-water wave approximations at these two locations) gives

$$\frac{gT}{4\pi}\frac{\rho g H_0^2 (1-K_r^2)}{8} = \sqrt{g h_c}\,\frac{\rho g H^2}{8} = \sqrt{g h_c}\,\frac{\rho g \gamma_2^2 h_c^2}{8} \tag{7.18}$$

Rearranging Eq. (7.18) gives an expression for the relative reef-crest submergence, h_c / H_0, as

$$\frac{h_c}{H_0} = \sqrt{\frac{1-K_r^2}{4\pi\gamma_2^2}}\left(\frac{h_c}{gT^2}\right)^{-1/4} \tag{7.19}$$

Note that the maximum value of h_c / H_0 is independent of the offshore wave height. For example, for the laboratory conditions in Chapter 3 with monochromatic waves, if one uses $\gamma_2 = 0.4$ as recommended by Gourlay (1996a) and since the maximum value of h_c is 0.1 m and the minimum value of T is 0.83 s in the experiments, one can arrive $h_c / H_0 = 2.0$ through Eq. (7.19) (after ignoring K_r), which could represent the upper bound for any wave breaking in the experiments.

To further validate Eq. (7.19), a limited series of laboratory tests were carried out to identify the boundary between non-breaking and breaking waves for different offshore monochromatic waves. These observations along with the theoretical curves are shown in Fig. 7.2 for $h_c = 0.05\,m$ and $0.1\,m$ in the absence of the ridge and for $h_c = 0.05\,m$ in the presence of the ridge. Four wave periods (T) were investigated. For each pair of water depth and wave period, the critical condition for which waves began to break was determined by varying the incident wave height by an interval of 1mm, the corresponding deep-water wave heights (H_0) were then obtained by converting the measured incident wave heights to deep-water ones. Using this set of data, Eq. (7.19) can be used to estimate γ_2 via a least-square fitting.

As seen in Fig. 7.2, virtually all of the critical breaking cases lie within the 95% confidence limits of the theoretical curves, indicating that Eq. (7.19) is adequate to estimate the transition from non-breaking waves to breaking waves. The average value of γ_2 for these three sets of conditions is about 0.4, which is consistent with the value suggested by Gourlay (1996a).

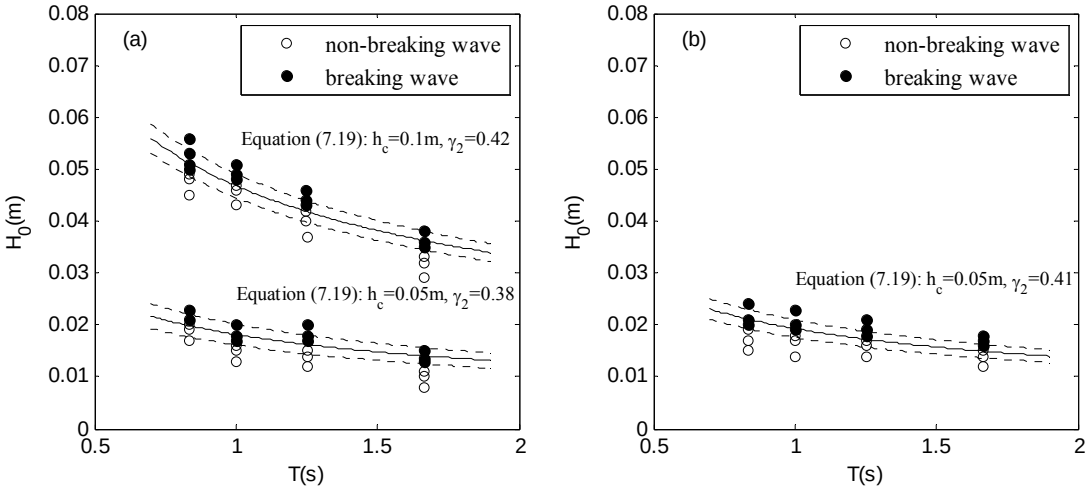

Fig. 7.2 Comparison of breaking state transition of laboratory observations with theoretical predictions for different reef-crest submergence: (a) without ridge; (b) with ridge. Solid lines represent least-squares fits of Eq. (7.19); Dotted lines represent the 95% confidence limits of the best fitting line.

As aforementioned, a requirement to use the above model is that the reef crest is submerged, i.e., ($h_c \geq 0$), thus the lower limit of the proposed model is $h_c / H_0 \geq 0$ in terms of the relative reef-crest submergence. In reality, the reef crests may occasionally emerge during low tides, thus negative reef-crest submergence ($h_c < 0$) can occur; under such conditions, wave overtopping and run-up may be important which are beyond the scope of this thesis. However, the analytical model in Chapter 6 does show some potential to deal with such situations.

7.2.4 Estimation of the breaker depth indices

In Eq. (7.13), there are three parameters in the proposed analytical solution: β_0, γ_1 and γ_2. The approach to estimate β_0 will be discussed later. For γ_2 on the reef flat, a constant value was found suitable from the experiments in section 2.4.2 as well as other laboratory observations (Nelson, 1994; Gourlay, 1994), thus $\gamma_2 = 0.4$, as verified in the previous section, will be adopted herein. The value of γ_1 is more tricky to choose, since it is related to both wave conditions and seabed slope. It was found that the reef-flat submergence affected the values of γ_1 (see both sections 2.4.2 and 5.6). For given offshore waves, γ_1 should approach the value for an emerged plane slope (denoted by γ_m) under $h_c / H_0 = 0$ (zero submergence); whereas for large enough reef-crest submergence where waves are about to cease breaking, γ_1 equals to γ_2 when $h_c / H_0 = (1-K_r^2)^{0.5}(4\pi)^{-0.5}\gamma_2^{-1}g^{0.25}T^{0.5}h_c^{-0.25}$ (see Eq. (7.19)). Thus by assuming a linear variation of γ_1 with h_r / H_0, one arrives

$$\gamma_1 = \gamma_m - \frac{h_c}{H_0}\frac{(4\pi)^{0.5}\gamma_2 h_c^{0.25}}{(1-K_r^2)^{0.5}g^{0.25}T^{0.5}}(\gamma_m - \gamma_2)$$
$$\textit{when} \quad 0 \le \frac{h_c}{H_0} \le (1-K_r^2)^{0.5}(4\pi)^{-0.5}\gamma_2^{-1}g^{0.25}T^{0.5}h_c^{-0.25} \tag{7.20}$$

Existing empirical formulae to estimate γ_m are commonly available for slopes smaller than 1/10 (see section 2.4.2). Some fore-reef slopes are relatively steep (> 1/10), thus in the current model, to be consistent with the laboratory observations in Chapter 2, the value of $\gamma_m = 1.0$ (see Eq. (2.20)) will be used as a first approximation in the 1DH modeling in this chapter. A model sensitivity analysis will be presented later in this chapter.

7.3 Model Validation by Experimental Data

7.3.1 Classification of the investigated reef profiles

The proposed model is tested against the laboratory datasets investigated in Chapter 6, the reef profiles used in previous laboratory studies have been described in Chapter 6 and are illustrated in Fig. 7.3 for reference in this chapter.

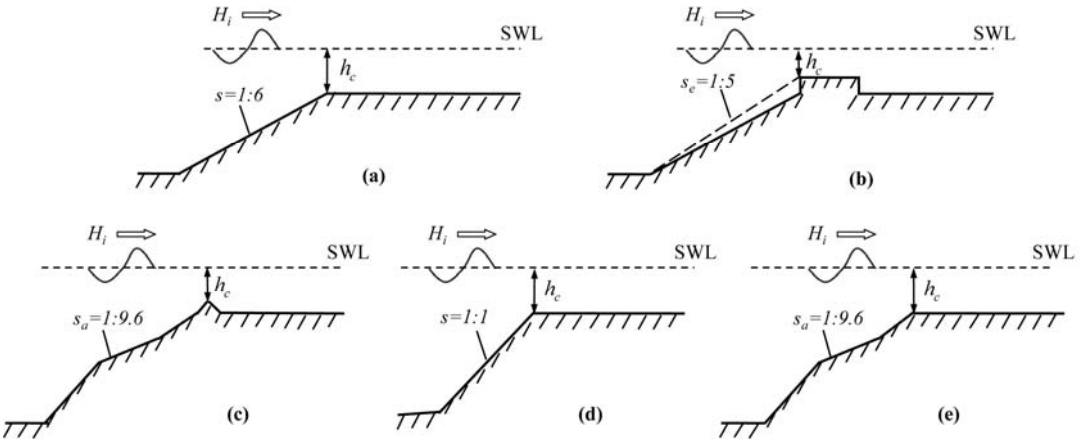

Fig. 7.3 Laboratory reef profiles investigated in this chapter: (a) experimental setup in Chapter 3 without ridge; (b) experimental setup in Chapter 3 with ridge; (c) Seelig (1983); (d) Gouraly (1996a); (e) Demirbilek et al. (2007) (h_c - reef-crest submergence; s - fore-reef slope; s_e - equivalent fore-reef slope; s_a - average fore-reef slope; H_i - incident wave height; SWL - still water level).

The author has listed three categories of reef profiles in section 7.2.2 for which the wave setups are computed by different equations. To facilitate discussion in this section, the classification of each profile in Fig. 7.3 will be given and the physical meaning of its β_0 will be examined. Theoretically, the values of β_0 lie in the range of 0 to 1. For reefs shown in Figs. 7.3(a), 7.3(d) and 7.3(e), a common feature is that the bottom topography near the reef edge (where the surfzone process occurs) is idealized (a planar slope followed by a horizontal reef flat), thus the physical meaning of β_0 for those profiles is the ratio of the two length scales (L_e and L_s) in the surf zone as indicated by Eq. (7.11). They fall into the category of "idealized

profile without the ridge" and the wave setup will be computed by Eq. (7.13) with Eqs. (7.14) and (7.15). For the reef in Chapter 3 when the ridge is present (Fig. 7.3(b)), the ridge-top is horizontal and relatively wide (50 cm) so that wave breaking actually completes (see e.g., Fig. 3.10) on the ridge-top where the water depth is known, resembling the surfzone process on the horizontal reef flat without a ridge. However, the seaside vertical slope of the ridge has some impact on the model results (See Appendix G), thus it belongs to the category of "idealized profile with an idealized ridge" and the wave setup will be computed by Eq. (7.13) with Eqs. (7.16) and (7.17). β_0 in both Eqs. (7.16) and (7.17) again represents the ratio of L_e / L_s. For the reef in Seelig (1983) (see Fig. 7.3(c)), the effect of profile shape on the value of β_0 may be substantial because his reef crest (ridge) was narrow and steep, thus it lies in the category of "idealized profile with a general ridge" and the wave setup will be computed by Eq. (7.13) with Eqs. (7.14) and (7.15), but the reef-crest submergence (h_c) will be used instead of h_r as the representative water depth in Eqs. (7.14) and (7.15).

7.3.2 The measured β_0 for an idealized reef without ridge

To estimate the magnitude of β_0, the data in Chapter 2 were investigated. To calculate β_0, L_s was obtained from measurements (See Appendix A), and L_e could be estimated by $L_e = (h_b - h_r)/s$ (h_b is given by Eq. (7.6) with Eq. (7.20) and s is the fore-reef slope). The values of β_0 as a function of deep-water wave height (H_0) are presented in Figs. 7.4(a) and 7.4(b) for different reef-crest submergences (h_r) and fore-reef slopes (s), respectively.

Fig. 7.4(a) shows that at a given s, the values of β_0 increase with decreasing h_r while Fig. 7.4(b) shows that at a given h_r, they increase with decreasing s; both figures indicate a monotonic increase of β_0 with increasing H_0. Overall, the measured values of β_0 are within a relatively narrow range (0 to 0.25) compared to its theoretical range (0 to 1). For practical use of the theory, it is undesirable if the

theory requires measured values of β_0 to predict wave setup. It will be shown that the predicted $\overline{\eta}_r$ is not very sensitive to small variations of β_0. In view of the uncertainties in β_0 resulting from extending the theory to non-idealized reef profiles (discussed in section 7.2.2) or from the uncertainties in the measured or observed x_s in both laboratory and field data to be investigated in this chapter, a constant representative β_0 for a given reef profile will be used in the model, the validity of this simplification will be shown in the following sections.

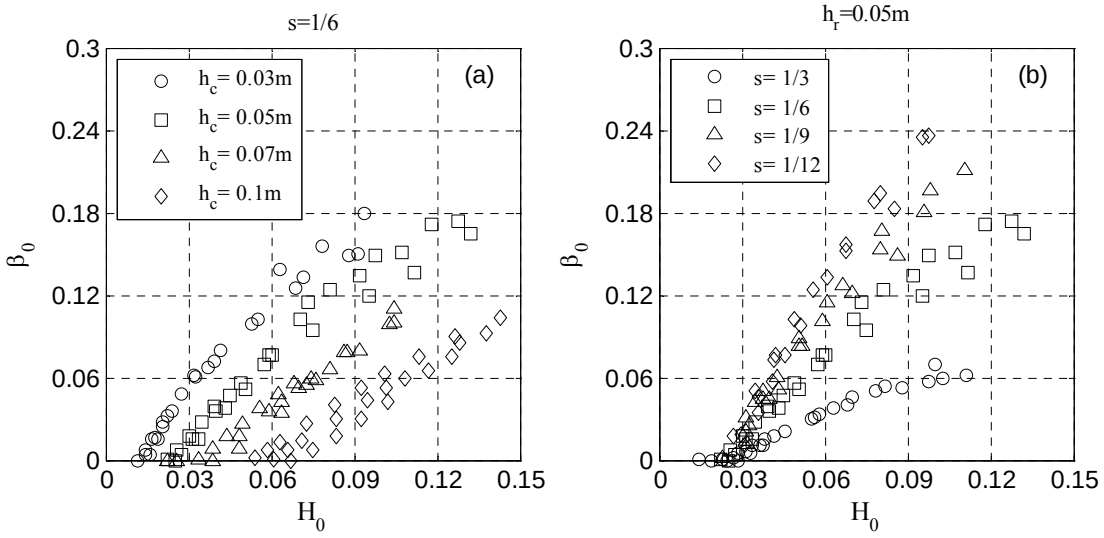

Fig. 7.4 The measured β_0 as a function of deep-water wave height (H_0) for: (a) different reef-crest submergences (h_c) and (b) different fore-reef slopes (s).

7.3.3 Comparisons among different approximations to the variation of $\overline{\eta}$ in the surf zone

Different approximations to the variation of $\overline{\eta}$ in the surf zone (given in Eq. (7.10)) are compared in this section using the measured wave setups in Chapter 3 for the cases in the absence of the ridge (both monochromatic and spectral waves are included and the H_{rms0} and T_p are used to characterize the spectral waves), since the wave measurements in Chapter 2 did not focus on the maximum setup across the reef flat. A single value $\beta_0 = 0.044$, obtained by averaging the dataset in Chapter 2 (shown in Fig. 7.4(a)) for the idealized reef with $s = 1/6$ (similar to the

experimental settings in Chapter 3 without the ridge), was used as a reference value. The representative β_0 for each approximation is obtained by a best fit between the measured setups in Chapter 3 and the model predictions based on Eq. (7.13) with Eqs. (7.14) and (7.15). Different values of C (up to $C=8$) were tested for the power law. All the fitted values of β_0 together with those from polynomial variations (from linear to Quartic) are compared in Table 7.1. The performances of the proposed model are measured by two parameters (also listed in the table): (1) R-square (R^2), and (2) the Bias (the mean of the difference between measured and predicted values of wave setup, which is to measure the tendency of under-predicting (positive bias) or over-predicting (negative bias) against the experimental data). A model will have the best performance if it is practically unbiased and has R^2 near 1.

Table 7.1 shows that very good agreement ($R^2=0.98$ and Bias=-2.62×10^{-4}) between observations and predictions was obtained for all approximations to $\overline{\eta}$, indicating that treating β_0 as a constant for a given reef profile is reasonable. All approximations give the same R^2 and bias because they share the same expression (i.e., Eq. (7.9)), in which λ is the sole parameter, but their corresponding values of β_0 are different because of Eq. (7.10). Overall, the fitted $\beta_0=0.054$ according to the power law with $C=7$ has the best agreement with the measured β_0; thus hereafter, all the results for the idealized fringing reefs without the ridge are presented based on $\lambda=7\beta_0^{1/7}/8$, which is to be used in Eq. (7.9). Note that using other approximations listed in the table can also provide the same quality of prediction but may result in a non-physical β_0 (e.g., greater than 1) for the given reef profile.

Table 7.1 Model parameter β_0 for different approximations to the variation of $\overline{\eta}$ in surf zone[a]

Polynomial	β_0	Power law	β_0
Linear	1.15	C=2	0.75
Quadratic	0.78	C=4	0.27
Cubic	1.46	C=6	0.092
Quartic	0.94	**C=7**	**0.054** [b]
		C=8	0.031

[a] Tests are preformed against the dataset in Chapter 3 without the ridge;

[b] This is the best agreement with the laboratory observation.

For the measured setups in Chapter 3 in the presence of an idealized rectangular ridge, Figs. 3.10, 4.10 and 4.11 have shown that when the ridge was present, wave setups increased more rapidly in the surf zone and the surfzone width, L_s, became narrower, indicating that the variation of $\overline{\eta}$ in the surf zone depends on the geometry of the seabed profile and the value of β_0 for the reef with the ridge is expected to be larger than that without. To achieve this, a smaller C for the power law approximations is expected according to Table 7.1. It was found that a best fit between the model results (using Eq. (7.13) with Eqs. (7.16) and (7.17) as well as the power law parameter $C = 4$, i.e., $\lambda = 4\beta_0^{1/4}/5$) and the experimental data gave $\beta_0 = 0.093$, which is reasonable and will be applied for the cases where a rectangular ridge exists at the reef edge.

7.3.4 Comparison between experimental data and model predictions

Predicted and measured wave setups are compared in Figs. 7.5(a) and 7.5(b) for the wave setup experiments in Chapter 3 in the absence and presence of the ridge, respectively. The predicted setups were computed based on Eq. (7.13) with Eqs. (7.14) and (7.15) using the power law approximation ($C = 7$) for the reef profile without the ridge, and on Eq. (7.13) with Eqs. (7.16) and (7.17) using the power law

approximation ($C = 4$) for the reef profile with the ridge. For the other two model parameters, $\gamma_m = 1.0$ and $\gamma_2 = 0.4$ were adopted for both profiles.

For the reef without the ridge as shown in Fig. 7.5(a), very good agreement is found, with $R^2 = 0.98$ (see Table 7.2). The under-predictions for those cases with very small setups are due primarily to the measurement error for smaller waves. For the reef with the ridge as shown in Fig. 7.5(b), although there is a consistent slight over-prediction for the cases under spectral waves, the overall agreement is still satisfactory ($R^2 = 0.94$, see Table 7.2). Note that H_{rms0} and T_p have been used to characterize the spectral waves in the simulations.

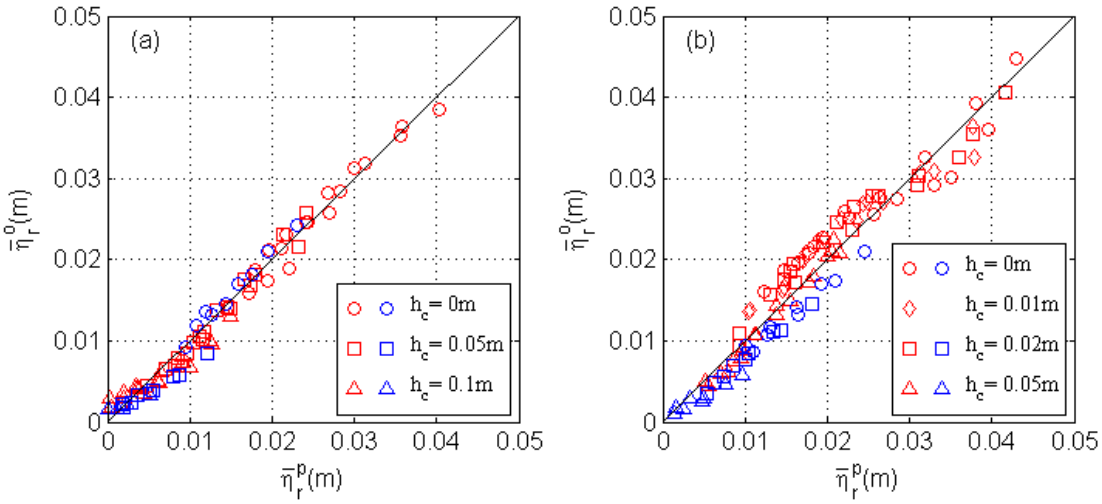

Fig. 7.5 Predicted wave setup ($\bar{\eta}_r^p$) vs. observed wave setup ($\bar{\eta}_r^o$) for different reef-crest submergences (h_c): (a) without ridge; (b) with ridge (Red markers - monochromatic waves; Blue markers - spectral waves; Solid line - $\bar{\eta}_r^p = \bar{\eta}_r^o$).

Model applications to two other published monochromatic wave datasets (Seelig, 1983, Gourlay, 1996a) and one spectral wave dataset (Demirbilek et al., 2007) are shown in Figs 7.6(a), 7.6(b) and 7.6(c), all model results were computed based on Eq. (7.13) with Eqs. (7.14) and (7.15) as well as the power law approximation ($C = 7$) with $\gamma_m = 1.0$ and $\gamma_2 = 0.4$. The values of β_0 for these datasets will be discussed in the next section. Very good predictions can be observed for the two

monochromatic wave datasets ($R^2 > 0.95$, see Table 7.2). Slightly poorer agreement was found for the spectral wave dataset ($R^2 = 0.91$), the agreement can be improved if γ_m is reduced.

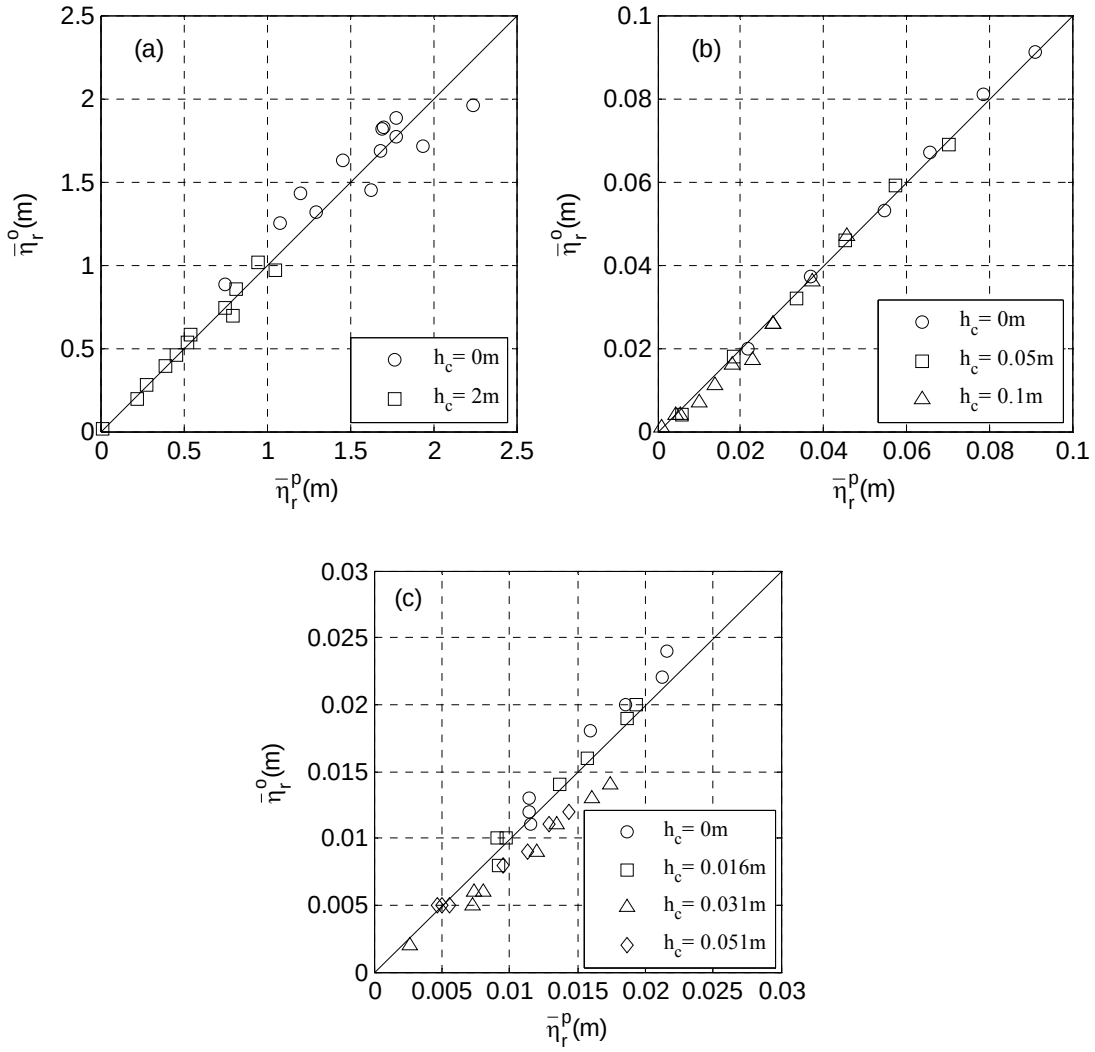

Fig. 7.6 Predicted wave setup ($\bar{\eta}_r^p$) vs. observed wave setup ($\bar{\eta}_r^o$) for different reef-crest submergences (h_c): (a) Dataset from Seelig (1983); (b) Dataset from Gourlay (1996a); (c) Dataset from Demirbilek et al. (2007) (Solid line - $\bar{\eta}_r^p = \bar{\eta}_r^o$).

7.3.5 More on the model parameter β_0

The values of the model parameter β_0 for all above laboratory datasets, obtained by matching observations with model predictions using the power law approximation of $\overline{\eta}$, are summarized in Table 7.2.

Table 7.2 Model parameter β_0 for available data

Dataset	Wave type	Fore-reef slope (s)	Power law	β_0	Bias(m)	R^2
Chapter 3 data without ridge	monochromatic and spectral	1:6	C=7	0.054	-2.62×10^{-4}	0.98
Chapter 3 data with ridge	monochromatic and spectral	1:5[b]	C=4	0.093	1.85×10^{-5}	0.94
Seelig (1983)	monochromatic	1:9.6[a,c,d]	C=7	0.21	-0.0027	0.96
Gouraly (1996a)	monochromatic	1:1	C=7	0.0003	-0.0013	0.99
Demirbilek et al. (2007)	spectral	1:9.6[a]	C=7	0.11	-5.90×10^{-4}	0.91

[a] Averaged slope (s_a in Fig. 7.3) of the composite fore-reef;

[b] The equivalent slope (s_e) as indicated in Fig. 7.3 in the present of the reef crest (ridge) ;

[c] The slope without considering the presence of the reef crest;

[d] Reflection is neglected in the calculations.

Table 7.2 reveals that generally, for most datasets, the values of β_0 are relatively small, closer to the physical lower limit of 0. For those datasets in the absence of a ridge, a systematic decrease of β_0 with increasing fore-reef slope (s) among the investigated datasets can be identified, and this decrease is more evident for very steep slopes, in that a steeper slope moves the breaking point shoreward, reducing L_e and thus β_0. This trend is consistent with the variation of the measured β_0 for different values of s as indicated in Fig. 7.4(b). For the datasets in the presence of a ridge, similar to the data in Chapter 3, the value of β_0 for Seelig (1983)'s data is also relatively large, which was supposed to be due to the shape effect of his steep

ridge as discussed in section 7.3.1 and Appendix G. However, overall the robustness of the model to each dataset using just a single model parameter (β_0) can be validated. The reason for this will be investigated by the model sensitivity analysis (see section 7.4). Since Table 7.2 shows that the model is nearly unbiased (bias close to zero) and has values of R^2 near one, it can be applied for practical use if the characteristics of waves and the reef geometry are known and the reef crest is submerged ($h_c \geq 0$).

7.4 Model Sensitivity Analysis

The sensitivity analysis in this section is carried out in two steps. The first step was to consider the sensitivity of the model to parameters that can be measured, and thus may be used as input parameters such as the reflection coefficient, K_r. Model runs were re-conducted by setting K_r to zero for all datasets except for Seelig (1983), and the results are given in Table 7.3. Comparing Table 7.3 with Table 7.2, which has been obtained with the measured K_r, no significant difference can be observed in view of the model performances (see the Bias and R^2 in both tables). However, the effect of K_r on the empirical parameter β_0 is evident: Table 7.3 shows that the values of β_0 were slightly reduced when wave reflection was excluded from the model, particularly for the data in Chapter 3 with the ridge where the values of K_r can be as large as 0.55 for monochromatic waves and 0.66 for spectral waves, β_0 was reduced by about 12% (from 0.093 to 0.084). Therefore, due to the lack of reliable equations for calculating K_r at present, neglecting wave reflection in the model may be possible in that its consequence can be compensated by different value of β_0.

The second step of the analysis is to check the sensitivity of the model to other three parameters (β_0, γ_m and γ_2) that have been calibrated or empirically determined. Fig. 7.7 shows the average of all the wave setups ($\overline{\eta}_r^{ave}$) predicted by the proposed

model divided by the average of all the wave setups ($\overline{\eta}_{r0}^{ave}$) obtained with reference parameters ($\beta_0 = 0.054$ as given in Table 7.2 for the best fit, $\gamma_m = 1.0$ and $\gamma_2 = 0.4$ as suggested in section 7.2.4) for the data in Chapter 3 without the ridge (see Fig. 7.5a). Each model run was carried out by changing only the value of the selected parameter. The parameters are varied with the following constraints:

- $\beta_0 = 0 - 0.30$, based on the measurements shown in Fig. 7.4;
- $\gamma_m = 0.6 - 1.4$ based on a number of experimental and field data for plane beaches (e.g., Camenen and Larson, 2007; Goda, 2010);
- $\gamma_2 = 0.2 - 0.7$ based on laboratory or field observations for horizontal reef flat (i.e., Gourlay, 1994; Nelson, 1994; Lowe et al., 2009a; the results in sections 2.4.2 and 7.2.3).

Table 7.3 Model parameter β_0 for available data by excluding wave reflection

Dataset	Wave type	Power law	β_0	Bias(m)	R^2
Chapter 3 data without ridge	monochromatic and spectral	C=7	0.051	-2.53×10^{-4}	0.98
Chapter 3 data with ridge	monochromatic and spectral	C=4	0.084	2.70×10^{-5}	0.94
Gouraly (1996a)	monochromatic	C=7	0.0003	-0.0013	0.99
Demirbilek et al.(2007)	spectral	C=7	0.11	5.90×10^{-4}	0.91

It can be observed that the model is very sensitive to γ_m and the predicted setups vary almost linearly with γ_m; however, the model results are less sensitive to γ_2: $\overline{\eta}_r^{ave}$ varies more or less within ±20% of $\overline{\eta}_{r0}^{ave}$ for the tested range of γ_2. Most importantly, the model is the least sensitive to β_0. For example, when β_0 rises to 5 times of or reduces to 1/5 of its reference value, $\overline{\eta}_r^{ave}$ decreases or increases by only about 10%. This should be why β_0 can be treated as a constant in the model as in

the previous sections. Fig. 7.7 also indicates that both a decrease of β_0 and an increase of γ_m will result in an over-prediction of wave setup, and vice versa. Thus even if the previous selection of $\gamma_m = 1.0$ might not be exact for a specific fringing reef, its consequence on the predictions could be compensated by adjusting β_0; however, the adjusted value of β_0 may no longer reflect its real physical meaning. Note that the ability to change the predicted wave setup by adjusting β_0 or γ_m does not mean that γ_m can be used as the sole fitting parameter instead of β_0 in the present model. Preliminary tests revealed that adjusting γ_m alone could not yield a global satisfactory prediction if β_0 was not properly chosen.

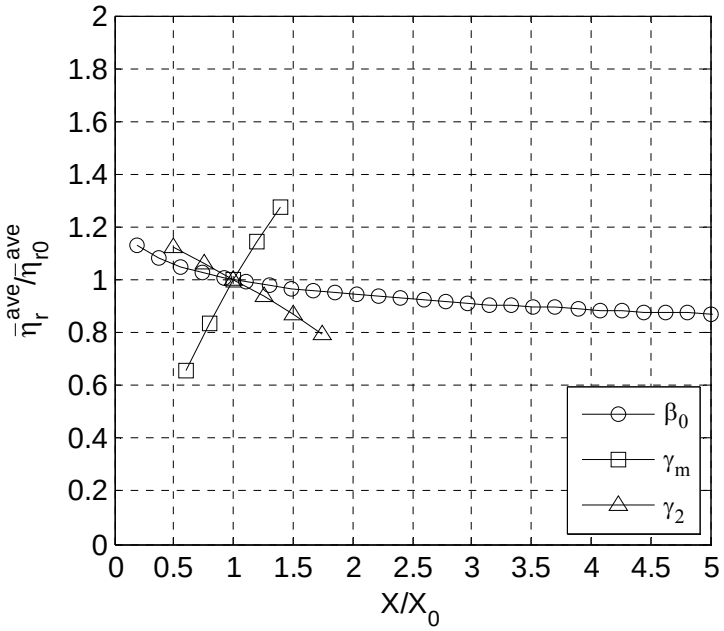

Fig. 7.7 Sensitivity of the model results to the reference parameters. On the abscissa, the value of each parameter X is divided by its calibrated value X_0. On the ordinate, the average wave setups ($\bar{\eta}_r^{ave}$) are normalized by their corresponding average value under reference conditions ($\bar{\eta}_{r0}^{ave}$) (X represents β_0, γ_m or γ_2; X_0 represents $\beta_0 = 0.054$, $\gamma_m = 1.0$ or $\gamma_2 = 0.4$; $\bar{\eta}_{r0}^{ave}$ is obtained by averaging the data in Fig. 7.5a).

7.5 Applications to Field Data

7.5.1 Background

In contrary to the 1DH flow in a closed laboratory flume, the flow patterns at natural reef sites are essentially 2DH: currents may be driven by different forcing mechanisms such as waves, winds, tides or even buoyancy (Monismith, 2007). As for waves, the wave-induced setup creates a mean pressure gradient over the reef flat and throughout the lagoon, which can drive a current that eventually exits the lagoon via channels in the reef (Hearn, 1999). This kind of reef-lagoon-channel system is often termed as "barrier reef". Meanwhile, many natural fringing reefs, which form adjacent to coastal landmasses, have enclosed lagoons in which water exchange with the surrounding ocean is often restricted by friction through narrow, rough, and sometimes tortuous gaps, thus a weak cross-shore current and 2DH circulation may still exist. The reduction of wave setup due to the presence of such currents has been reported in the literature (e.g., Gourlay, 1996a). Moreover, the alongshore currents on the reef flat also result in an alongshore distribution of the wave setup (e.g., Jago et al., 2004).

The overall dynamics controlling wave-driven flows on coastally bounded reefs may be similar to those, for example, rip currents that are formed around submerged bars on sandy beaches or around detached submerged low-crested breakwaters. In this case, spatially non-uniform wave setup can drive a flow over a shallow bar/breakwater crest that returns to the ocean through narrow channels. However, natural reefs may have much wider reef-flat, lagoon and channel geometries than those of barred beach or breakwater systems.

The bottom frictional force in the presence of waves and currents is usually parameterized by a quadratic friction law

$$\tau_x^b = \rho C_d u_{ref} \left| u_{ref} \right| \tag{7.21}$$

where C_d is a representative drag coefficient, u_{ref} is a reference velocity. For different selections of u_{ref}, C_d has different values. Note that in wave-dominated

coastal regions (i.e., $|u_w| >> u_{ref}$, where $|u_w|$ is the magnitude of wave orbital velocity), a linear drag law may be more appropriate (Hearn et al., 2001).

Finally, it is worthy to mention that although the 1DH simulations based on linear wave theory could provide satisfactory predictions for the laboratory data, an alternative wave model may be needed for field conditions to recast cross-shore variation of S_{xx} in Eq. (7.1) where the friction dispassion may be important. A number of 1D wave models have been developed to predict wave transformation on beaches (e.g., Thornton and Guza, 1983; Svendsen, 1984a); these models are more appropriate for reefs with relatively mild fore-reef slopes (e.g., less than 1:10). However, it is not the focus of the present study to conduct a detailed evaluation of such wave models.

7.5.2 Results

In this section, four recent field studies on the wave setup over coral reefs covering a variety of reef profiles and wave conditions are examined. Noting that aside from waves, the mean water level may also be affected by tides and winds at a specific site. By considering that wind effects on the mean water depth are reported to be negligible for most datasets, the reef-crest submergence (h_c) in the present model represents the mean water depth plus the tide modulation in field conditions. The details for each dataset related to model application are listed below.

Bonneton et al. (2007)

The measurements were conducted at a barrier reef, New Caledonia. The reef profile consisted of a fore-reef with an average slope of 1:10, a relatively horizontal reef flat and a lagoon. The offshore wave conditions (H_{rms0}, T_p) were converted from their measurements (H_s, T_{02}, which is the mean zero-upcrossing period) at their station A_0 on the fore-reef; the reef-crest submergence (h_c) and wave setup ($\overline{\eta}_r$) were obtained from their station P_1 on the reef flat.

Hench et al. (2008)

The measurements were conducted at a barrier reef, Paopao Bay, Moorea. The reef profile consisted of a fore-reef with an average slope of 1:8, a reef crest (ridge), a horizontal reef flat and a lagoon, The values of H_{rms0} and T_p were converted from their measured H_s and T_s at the fore-reef station B, while h_c and $\overline{\eta}_r$ were obtained from the reef-crest station C. The observed tides at Moorea were remarkably small (on the order of 0.2m at spring tide), thus tide effect was ignored and a constant $h_c = 2m$ (the mean water depth at the station C) was applied in the model.

Lowe et al. (2009a)

The measurements were conducted at a barrier reef in Kaneohe Bay, Hawaii. The reef profile consisted of a fore-reef with an average slope of 1:60, a horizontal reef flat and a lagoon. Their H_{rms0} and T_p were measured at a fore-reef station, and then converted to offshore values. Values of h_c and $\overline{\eta}_r$ were extracted from the measurements at the reef-flat station A_2. Since tide modulation was found to be small and the reported data had been filtered to sub-tidal frequencies, tide effect was ignored and a constant $h_c = 2m$ (the mean water depth at the station A_2) was applied in the model

Vetter et al. (2010)

The measurements were conducted at a fringing reef, Ipan, Guam. The reef profile consisted of a fore-reef with an average slope of 1:15, a reef crest and a horizontal reef flat backed directly by the shoreline. The H_{rms0} and T_p were measured at a fore-reef station S_8. $\overline{\eta}_r$ was obtained from their measurements near the reef-crest station S_6. h_c was obtained from the measured mean water depth at S_8 minus the relative seabed elevation between S_6 and S_8. Two sub-datasets were reported: a normal swell event (denoted as N-deployment) and a storm event (denoted as G-deployment)

Wave directions were not considered in the model for all four datasets because they were measured from remote offshore stations, which may not be accurate estimation of the wave directions at those fore-reef stations where the observed H_{rms0} and T_p came from. Finally, reflection coefficients were not measured in field observations thus reflection was not included in the model computations; its influence will be incorporated into β_0 as discussed in section 7.4.

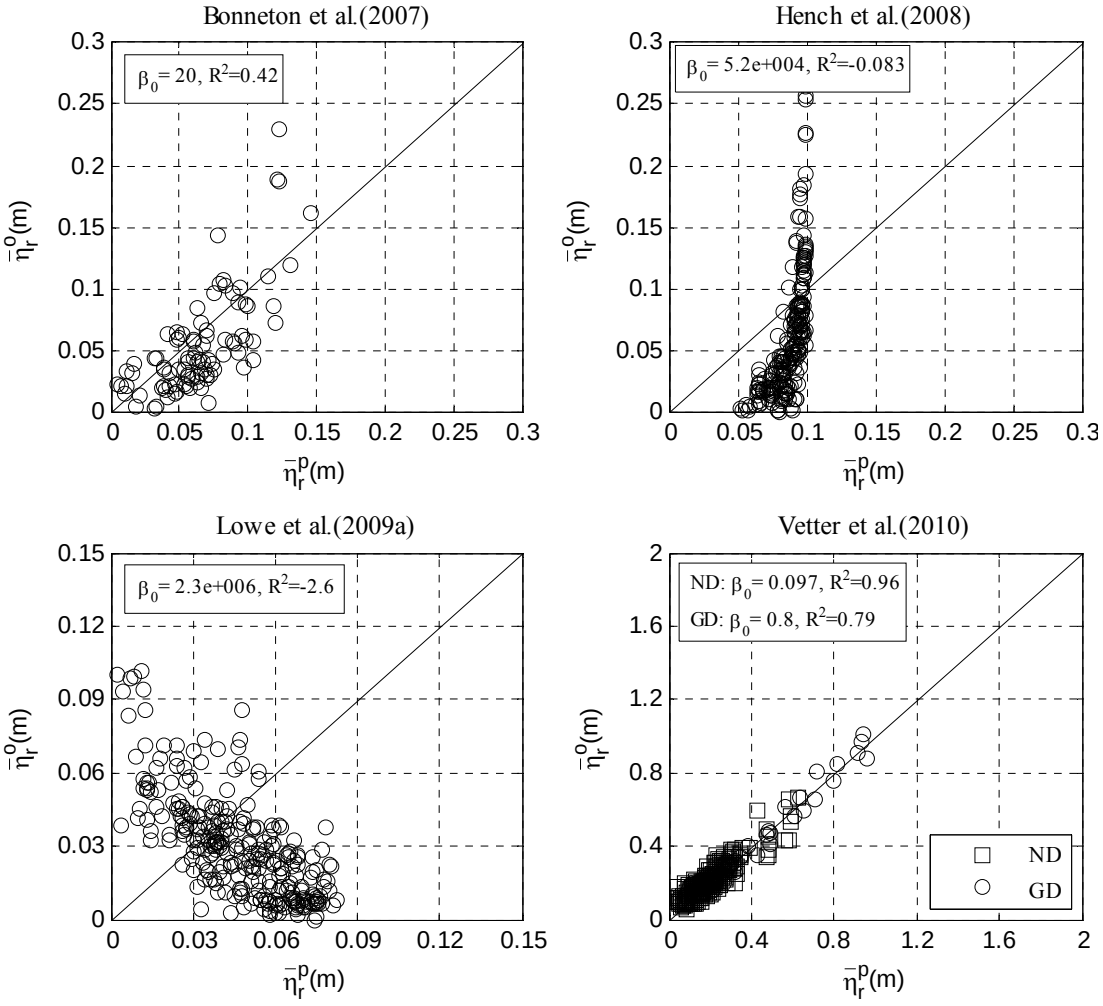

Fig. 7.8 Predicted wave setup ($\bar{\eta}_r^p$) vs. observed wave setup ($\bar{\eta}_r^o$) for different field studies (β_0 - parameter in the proposed model; R^2 - R-square; Solid line - $\bar{\eta}_r^p = \bar{\eta}_r^o$; ND - N-deployment; GD - G-deployment).

For the field applications, all model results were again computed based on Eq. (7.13) with Eqs. (7.14) and (7.15) as well as the power law approximation ($C = 7$), using the model parameters $\gamma_m = 1.0$ and $\gamma_2 = 0.4$. The predicted setups are plotted against the observed setups in Fig. 7.8 for the four datasets. It can be seen that the best agreement appears in the N-deployment for the dataset of Vetter et al. (2010), with $R^2 = 0.96$. This is expected since the reef in Vetter et al. (2010) is a fringing reef and the current modification to the wave setup is supposed to be small. Moreover, the characteristics of observed wave breaking on the fore-reef are consistent with the theoretic hypothesis of the present model. In fact, Vetter et al. (2010) also reproduced their data using a dynamic model similar to Eq. (5.8). However, as for the G-deployment (the storm event), the predictions are not as good ($R^2 = 0.79$) compared with those for the N-deployment; this is possibly due to the current and non-wave-related sea level changes caused by winds during the storm (Péquignet et al., 2011). Consequently, the observed wave setups at the reef crest were reduced, which resulted in a dramatic increase of the fitted value of β_0 in the model (see section 7.4 for the sensitivity analysis). For this dataset, an increase of β_0 from 0.097 (N-deployment) to 0.80 (G-deployment) could be found. The magnitude of β_0 for N-deployment was consistent with the laboratory observations in Table 7.2.

The predictions for Bonneton et al. (2007)'s data are reasonable ($R^2 = 0.42$). Bonneton et al. (2007) found that their observations were mainly controlled by the difference between the water depth at the breakpoint and the water depth over the reef, which is in fact partly embodied in Eq. (7.9) of the present model. The model failed to reproduce the data in Hench et al. (2008), but a trend can still be identified in Fig. 7.8 and this trend could be best described by Eq. (5.1) with $m = 3.2$ and $n = 3$ as found by Hench et al. (2008). The reef-lagoon-channel system existed at both reef sites, in which the setup reduction due to the current (which was typically on the magnitude of $0.2 m/s$ for those sites) may be substantial, thus non-physical values of β_0 larger than the upper limit of 1.0 were obtained for both datasets.

Model application to the data of Lowe et al. (2009a) is unsuccessful. This might be explained by the observations that the mild fore-reef slope of Kaneohe Bay reduced setup through a combination of frictional wave damping and its relatively wide surf zone compared to steep reefs. Lowe et al. (2009a) had shown that the observed wave setup was correlated to the offshore wave power. The effect of the mean current at this reef site was relatively weak (typically less than $0.2m/s$) due to the presence of significant wave setup inside its coast-bounded lagoon, which reduced cross-reef setup gradients by 60% - 80%. Therefore, very large value of β_0 was found by the model. The influences of current, frictional dissipation and lagoon setup will be included in the 2DH formulation of the present model in section 7.7.

Therefore, unlike the model applications in the previous laboratory data, for which the fore-reef slope as well as reef-crest shape contribute the value of β_0, the increase of β_0 for field datasets seems to be controlled by the reduction of observed wave setups caused by the aforementioned factors (current, bottom friction, lagoon setup, etc.). The level of the amplification of β_0 depends on the degree of the setup reduction at a specific reef site. Thus among the three barrier reefs in Fig. 7.8, the wave setups in Lowe et al. (2009a) deviated from those for fringing reef most, while the reef in Bonneton et al. (2007) was most like the fringing reef. Adjusting γ_m or γ_2 in the model can slightly improve the predictions for some datasets. In general, the present 1DH model works quite well not only for the field fringing reefs on which its theoretical foundation relies, but also works reasonably well for some barrier reefs where the setup reduction is relatively weak. For completeness of this section, the applicability of the two selected existing models in Chapter 5 is also evaluated against the four field datasets above, see Appendix H for details.

7.6 Discussions on the 1DH Model

In this section, some comments are made here for the model implementations and parameters:

(1) The approach to estimate L_s in the model is based on the power law variation of $\bar{\eta}$ in surf zone satisfying the boundary conditions $\bar{\eta}(x_b) = \bar{\eta}_b$ and $\bar{\eta}(x_s) = \bar{\eta}_r$, which may be different from visual observation method in Chapter 2 for the measured L_s. There is no detailed wave measurements other than the one shown in Fig. 3.10, but the numerical results in Chapter 4 indicate that wave setdown is unlikely to occur on the reef flat, thus the calculated h_b (always on the fore-reef slope, which is consistent with the model requirement that wave breaking should occur on the fore-reef) rather than the measured h_b (some may be on the reef flat as observed in Chapter 2, depending on the breaking criteria used) was adopted in section 7.3.2 to estimate L_e. Therefore, the measured β_0 in section 7.3.2 based on above L_s and L_e may deviate somewhat from the β_0 defined in the model;

(2) The author has calibrated a power law based on the experimental data in this thesis. However, it has been shown in section 7.3.3 that other relations such as the polynomials listed in Table 7.1 could also provide the same quality of predictions as long as β_0 was treated as a fitting parameter, which has less obvious physical meaning;

(3) In principal, β_0 obtained from the measured $\bar{\eta}$ in the surf zone should be used in the model to predict wave setup, although doing so is undesirable. As a first approximation, a representative β_0 can be selected by referring to the values of β_0 listed in Table 7.2 according to the reef morphology (fore-reef slope and reef-crest configuration) to be investigated, since β_0 generally falls in a narrow range (0 - 0.25) and is insensitive to the model results. Alternatively, a fitted representative value of β_0 may be obtained from the model based on some pilot measurements of the wave setup;

(4) Both model parameters γ_m and γ_2 are empirical and they may affect the results in a more or less same degree as shown by the model sensitivity analysis. Compared to γ_2 which is almost constant, γ_m is in fact related to the fore-reef slope (see section 2.4.2) thus it may be more appropriate to assign a value according to the slope of the given reef profile rather than using a constant as did in previous

sections. Using a different γ_m requires recalibrating β_0 as well as the power law parameter C. An example will be shown by a case study for the 2DH model in section 7.7.2.

Similar to previous models (Tait ,1972; Gourlay and Colleter, 2005), the proposed model is essentially a dynamic model. However, it differs from the model of Tait (1972), i.e., Eq. (5.8), and the model of Gourlay and Colleter (2005), i.e., Eq. (5.9), in the following aspects:

(1) It can accommodate all the investigated reef profiles even if there is a ridge at the reef edge;

(2) It does not require that the surf-zone process ends at the reef crest, which is more consistent with the laboratory observations;

(3) In contrast to both γ in Eq. (5.8) and K_p in Eq. (5.9), the model parameter β_0 has a clear physical meaning;

(4) In contrast to both γ and K_p, a representative constant β_0, which is independent of the reef-crest submergence and offshore waves, can be used in the model applications for a given reef profile;

(5) The effect of reef-crest submergence on γ is considered (see Eq. (7.20)), and different values of γ are employed for the fore-reef and reef flat, respectively;

(6) It includes the shoaling-induced setdown on the fore-reef rather than treating it separately as Tait (1972) did.

The present model differs from the kinematic model in the Chapter 6 in the following respects:

(1) It explicitly includes wave shoaling, breaking, reflection and transmission;

(2) It is applicable to all laboratory data used in the previous chapters.

7.7 Model Extension to 2DH

7.7.1 Formulation

The aim of this section is to present a simplified model based on the approach of Bellotti (2004) for an easy estimate of the 2DH hydrodynamic characteristics of natural reefs. An idealized reef-lagoon-channel cell (barrier reef) similar to Lowe et al. (2009a) is considered where setup generated by wave breaking drives flow across a shallow reef flat, through a deeper lagoon, and finally exits through a channel (see Fig. 7.9). Note that the considered domain is half of complete reef-channel topography; for symmetry reasons, it is sufficient to model an area extending from the middle of the channel to the middle of the reef. The cross-shore reef profile is assumed to be idealized as discussed in section 7.2.2.

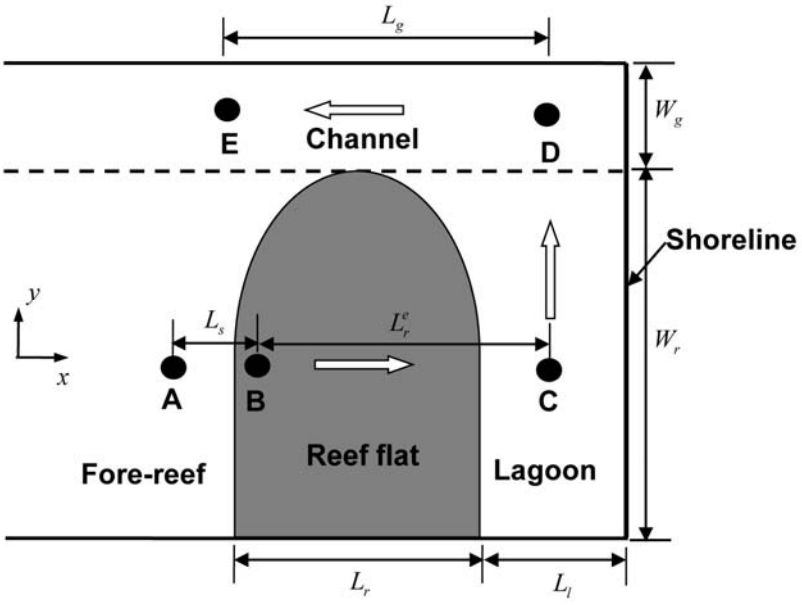

Fig. 7.9 Plan view of an idealized reef-lagoon-channel system, including a shoreline, a reef (below the dashed line) and a channel (above the dashed line). Flow moves from points A through E.

The momentum balance Eq. (7.3) in the surf zone (from A to B) is recalled. In contrast to the previous 1DH form, both flow-related terms and the friction term are retained here to give

$$(h_r+\overline{\eta}_r)U_r^2-h_bU_b^2+\frac{g}{2}(h_r+\overline{\eta}_r)^2-\frac{g}{2}h_b^2+\Delta S-\Delta\Pi+C_d^r\left(\frac{U_b+U_r}{2}\right)^2L_s=0 \qquad (7.22)$$

where U_b and U_r are the depth-averaged mean velocities at the breaking point and on the reef flat, respectively. the velocity $(U_b+U_r)/2$ averaged between the breaking point and the end of the surf zone is employed in the quadratic friction law for a shoreward current; h_r is the still water depth along the horizontal reef flat; C_d^r is a representative drag coefficient for the reef profile and L_s is the total surfzone width which varies with incident waves and can be estimated by the definition of β_0 as $L_s=(h_b-h_r)/(s\beta_0)$ (see section 7.2.2), where s is the fore-reef slope. Both ΔS and $\Delta\Pi$ are determined in the same way as did for the 1DH problems. Interpretation of the role of bottom friction in Eq. (7.22) is important. From a mathematical point of view, this term induces a decrease of wave setup if the depth-averaged velocity is shoreward directed.

The integrated cross-section continuity equation in the surf zone (A to B) reads

$$U_r(h_r+\overline{\eta}_r)-U_bh_b=0 \qquad (7.23)$$

For this reef-channel geometry, an alongshore continuity equation can be derived by requiring that the inflow over the barrier (reef flat) must be balanced by the outflow through the channel

$$U_rh_rW_r-U_gh_gW_g=0 \qquad (7.24)$$

where h_g is the still water depth along the channel; W_r and W_g are the alongshore reef and channel widths, respectively, and U_g is the depth-averaged velocity in the channel. The above equation also implies that both U_r and U_g are uniform cross-shore. However, in practice, the channel may be fed locally by the alongshore (lateral) current on the reef flat. This is more likely to occur when the value of W_g/W_r or L_r/L_l is large. When this happens, an alongshore momentum balance may be included to predict the alongshore setup gradient that drives this flow. Nevertheless, the present model assumes that flow originating near the reef crest

crosses the entire reef flat before entering the lagoon since most reefs have relatively wide reef flat (on the order of magnitude of 100-1000m) and narrow channels (on the order of magnitude of 10 m). If W_g / W_r approaches zero, the model is expected to approach its 1DH form.

Different from the simple barrier-gap system (e.g., Bellotti, 2004), an additional momentum equation is introduced here to describe the cross-reef flow on the reef flat, which is driven mainly by the barotropic pressure gradient resulting from the setup in the surf zone.

Since the wave forcing is very small on the reef flat (i.e., $\Delta S = 0$), Eq. (7.3) can be integrated across the horizontal reef flat ($\Delta \Pi = 0$) from the endpoint of surf zone (B) to the lagoon (C) to give

$$(\overline{\eta}_L - \overline{\eta}_r)U_r^2 + \frac{g}{2}(h_r + \overline{\eta}_L)^2 - \frac{g}{2}(h_r + \overline{\eta}_r)^2 + C_d^r U_r^2 L_r^e = 0 \tag{7.25}$$

where $\overline{\eta}_L$ is the wave setup in the lagoon. As shown by Lowe et al. (2009a), $\overline{\eta}_L$ may not be zero as commonly assumed in existing 1DH models (Tait 1972; Hearn, 1999; Gourlay and Colleter, 2005), L_r^e is the effective cross-shore reef-flat width (distance between B and C in Fig. 7.9) and can be estimated by $L_r^e = L_r - L_s(1-\beta_0)$ since that part of the surf zone is located on the reef flat. L_r is the practical cross-shore reef-flat width as shown in Fig. 7.9. The above equation indicates the importance of the bottom friction on the reef flat.

The energy equation for the lagoon-channel return flow (D to E in Fig. 7.9) relates the water head (setup) in the lagoon to the channel current. It is assumed that: (1) the lagoon can be treated as a reservoir, i.e., $\overline{\eta}_L$ is constant in the deep lagoon; (2) the wave forcing is negligible in this deep channel region (i.e., $\Delta S = 0$), and (3) $\overline{\eta} = 0$ just offshore of the channel (i.e., ignoring wave setdown). Following the expression by Lowe et al. (2009a) gives

$$\frac{\overline{\eta}_L}{L_g} = C_d^g \frac{U_g^2}{g h_g} \tag{7.26}$$

where C_d^g is a representative drag coefficient for the channel path. Standard methods in the open channel hydraulics may be used to estimate C_d^g . To consider the lateral flow and setup distribution in the lagoon, the flow dynamics from C to D can be treated as part of the channel dynamics (Lowe et al., 2009a) or be solved by introducing additional alongshore momentum balance in the lagoon and imposing mass balance between the lagoon and the channel.

Eqs. (7.22), (7.23), (7.24), (7.25) and (7.26) represent a closed set of equations, and can be used to solve for the five unknown variables ($\overline{\eta}_r, \overline{\eta}_L, U_b, U_r, U_g$) for given wave characteristics (H_{rms0} , T), morphological properties of the reef-lagoon-channel system ($W_L, W_g, L_r, L_g, h_r, h_g, s$), roughness of the system (C_d^r, C_d^g) and the aforementioned model parameters ($\gamma_m, \gamma_2, \beta_0$). Parameters such as C_d^r , C_d^g and β_0 are difficult to be measured thus may be obtained by a best fit between the field data and model predictions.

Some features of the present model are: (1) Bellotti (2004) did not consider the barrier (corresponding to the reef flat) width, although it is believed to have an influence on the rip current system as pointed out by Drønen et al. (2002). Both the reef flat dimensions and the lagoon setup are accounted for in the present model; and (2) Lowe et al. (2009a) assumed in their model $\overline{\eta}/h << 1$ from the offshore to the lagoon, which may not be valid when reefs are exposed to very low tides; there is no such assumption for the present model. Meanwhile, the model of Lowe et al. (2009a) needs to be solved numerically from offshore to the lagoon which prevents from derivation of simple analytical solutions.

7.7.2 Case study

The field data of the southern circulation at Kaneohe Bay (Lowe et al., 2009a, hereafter L09) is revisited by the proposed 2DH model in this section. The

morphological properties in L09 were reported with a range of values in view of the error in the field estimation. The aim of the study is not to seek optimized model inputs to achieve a best model performance, but to validate the model's ability to predict the field data. Therefore, the author used their estimated mean values, which are: $W_r/(W_r+W_g)=0.71$, $h_g=5m$, $L_g=5000m$, $L_g=1500m$, $s=1/60$, $C_d^r=0.02$ and $C_d^g=0.02$. For the model parameters, a γ_m smaller than 1.0 may be more appropriate in view of very gentle fore-reef slope at Kaneohe Bay (1:60). The value of $\gamma_m=0.78$, which is widely adopted for wave breaking in constant water depth (USACE, 2003), will be used together with the power law given in Eq. (7.10). Recalibrating the power law in the same procedures as shown in sections 7.3.2 and 7.3.3 based on the laboratory reef without the ridge in Chapter 3 (the cross-shore reef profile for this case study has been assumed to be idealized without the ridge by L09) gives $C=4$ and $\beta_0=0.085$. Pilot tests have shown that the results were not very sensitive to β_0 when β_0 varied in the range of 0 to 1. For γ_2 , the value of 0.3 was adopted according to L09's measurements. The parameters h_r , H_{rms0} and T_p were obtained in the same way as described in section 7.5.2.

The author has emphasized in section 7.5.1 the importance of choosing a suitable 1D wave model to calculate the radiation stress term in the model. Both L09 and Péquignet et al. (2011) used the model of Thornton and Guza (1983), which needs to be solved numerically. L09 has reported a 40% energy reduction resulting from the frictional dispassion prior to the breaking point due to the very gentle fore-reef at Kaneohe Bay. Frictional dissipation could be further increased in the shallower surf zone. Meanwhile, the wave reflection was not measured in their observations. To estimate h_b, the original form of Eq. (7.6), i.e., Eq. (E.4), should be used. For simplicity, the author introduced an energy reduction coefficient κ to account for both frictional dissipation and reflection in Eq. (E.4), which gives $\kappa^2=\alpha^2+K_r^2$ (see Appendix E). Preliminary simulations have shown that κ is the most sensitive parameter in the present case study, thus it will be used as a fitting parameter instead of β_0 in this section.

A total of 56 days (from 22 Jan to 19 Mar.) observed wave setup ($\overline{\eta}_r$), lagoon setup ($\overline{\eta}_L$) and reef-flat current (U_r) were reproduced by the present model. The results together with the observations and the model results of L09 based on quadratic friction law are shown in Fig. 7.10.

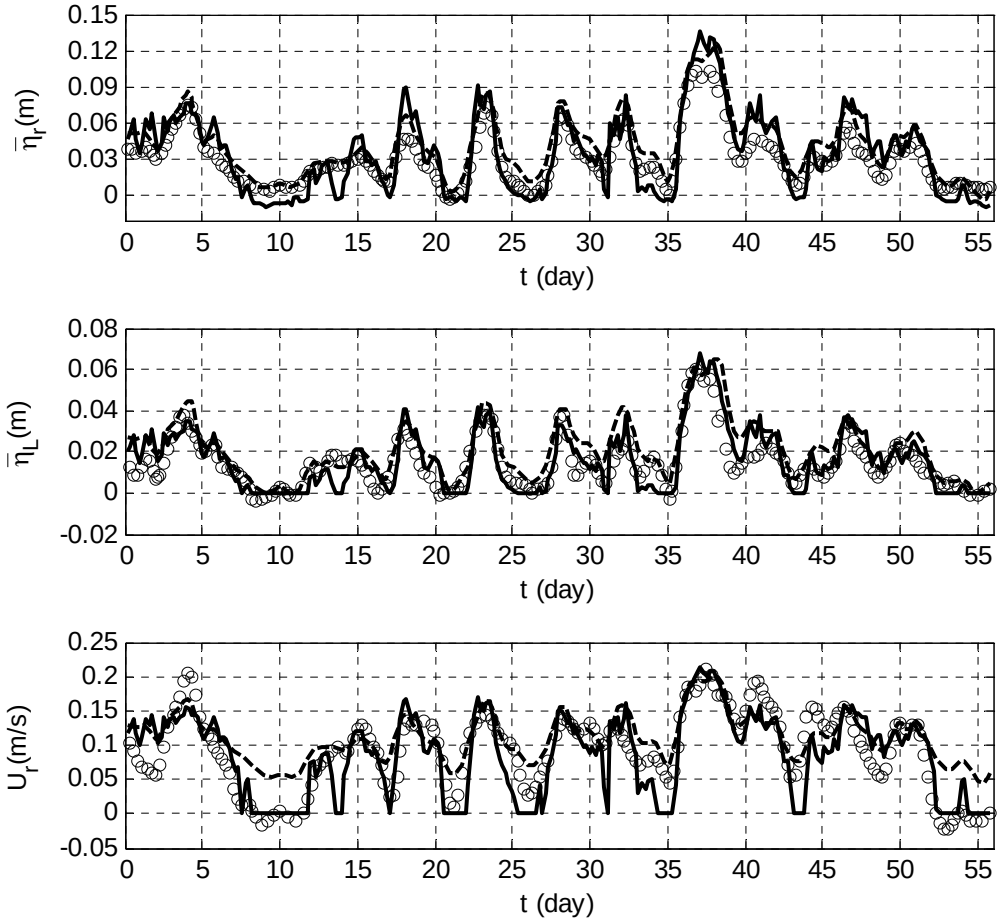

Fig. 7.10 Time-series of field observations and model predictions (Open Circles: Observations; Dashed line: Predictions by L09; Solid line: Predictions by the present model).

$\kappa = 0.94$ was obtained from a best fit between the observations and predictions, indicating the combined effect of frictional dissipation and reflection at Kaneohe Bay was significant. Fig. 7.10 shows that the proposed 2DH model adequately

predicted the overall pattern of the time-series field observations. The model skill values are estimated by (Wilmott, 1981)

$$skill = 1 - \frac{\sum \left| X_{model} - X_{obs} \right|^2}{\sum \left(\left| X_{model} - \overline{X_{obs}} \right| + \left| X_{obs} - \overline{X_{obs}} \right| \right)^2} \tag{7.27}$$

Perfect agreement will yield a skill of one, whereas complete disagreement will yield a skill of zero. The comparison gives 0.93 (present model) and 0.94 (L09) for $\overline{\eta}_r$; 0.91 (present model) and 0.90 (L09) for $\overline{\eta}_L$, and 0.89 (present model) and 0.84 (L09) for U_r. Corresponding R^2 values were 0.62 (present model) and 0.94 (L09) for $\overline{\eta}_r$; 0.54 (present model) and 0.82 (L09) for $\overline{\eta}_L$, and 0.60 (present model) and 0.80 (L09) for U_r. The skill values of the present model are comparable to those of L09, but R^2 values of the present model are lower. The R^2 values can indeed to be increased if the input values are further calibrated. For example, if one uses $h_g = 5.5m$ which is still in L09's suggested range, the R^2 values for $\overline{\eta}_L$ and U_r can rise to 0.69 and 0.62, respectively, without affecting the R^2 value for $\overline{\eta}_r$. However, it is not the focus of this section to seek the best performance of the model by adjusting the input parameters. Overall, the proposed 2DH model could improve the predictions of the field data in L09 over its 1DH form.

Through this case study, the importance of the frictional dispassion has been recognized when the model in its present form is used for some field reef with a mild fore-reef. Although adding a damping coefficient can account for dissipation in a simple way, it will introduce the additional free parameter κ. A wave model may be more favorable to estimate the wave transformation across the fore-reef and in the surf zone even though the model computation is time-consuming. The present model needs to be further validated by well-controlled 2DH laboratory experiments. Nevertheless, it provides a useful tool for illustrating how the wave-driven current, reef morphology and bottom roughness crucially affect the setup and circulation in coastally bounded reef-lagoon-channel systems.

7.8 Concluding Remarks

A 1DH analytical model based on the cross-shore momentum balance is proposed in this chapter to study the wave-induced setup over submerged fringing reefs. A power law is found to sufficiently approximate the wave setup profile in the surf zone. The model explicitly accounts for wave transformation processes over reefs such as shoaling, breaking, reflection and transmission. It allows surfzone process to extend shoreward of the reef crest. The effect of reef-crest submergence on the breaker depth index is considered. Comparisons with different laboratory data show that the model is capable of reproducing the maximum wave-induced setup on the reef flat under a variety of reef profiles (with and without a ridge at the reef edge), a range of reef-crest submergences (from zero to the upper limit where waves cease to break), and two types of wave conditions (monochromatic and spectral). The 1DH model is also successfully applied for some field reefs. The defined model parameter (β_0) is physically related to surfzone length scales and it has been proven to be the most suitable free parameter in the model. The value of β_0 , typically within the range of 0 to 0.25, is found to decrease with increasing fore-reef slope in the laboratory experiments, but the detailed reef-crest configuration is also important. β_0 also accounts for the reduction of wave setup commonly observed at field reefs. The model formulation has been extended to 2DH in analogy to the existing conceptual approaches for "rip current" and validated by a field case study. The 2DH form requires further validation with more laboratory and field data.

CHAPTER 8 CONCLUTIONS AND FUTURE WORK

8.1 Conclusions

This thesis has presented a comprehensive study of the surface gravity wave dynamics over fringing coral reefs with/without a ridge, including experimental studies, numerical modeling and theoretical analyses.

In Chapter 2, a series of laboratory experiments have been conducted in a wave flume to examine the effects of varying reef-flat submergence and fore-reef slopes on the properties of breaking waves (the breaker type and location, breaker height and depth indices, surfzone width, as well as wave reflection and transmission) over submerged idealized fringing reefs subjected to monochromatic waves. Dimensionless analysis has shown that the relative submergence of the reef flat is the determining factor to characterize most breaking characteristics over fringing reefs. The influence of fore-reef slope appears to be insignificant. The idealized reef profile investigated in this chapter serves as a first approximation to natural fringing reefs. Their hydrodynamic response to waves has been proven to resemble submerged structures (e.g., breakwaters) rather than plane beaches. Some empirical formulae have been proposed within the experimental data range. The findings obtained in this chapter are referred to in subsequent chapters

In Chapter 3, the laboratory work was diverted to the effects of a reef crest (a "ridge" structure located at the reef edge as is frequently observed in the field) on the wave-induced setup. Experimental results for reef profiles with and without a rectangular idealized ridge subjected to both monochromatic and spectral waves have been compared. It is shown that the behavior of the wave transformation in the presence of a ridge is significantly different from that in the absence of the ridge. In particular, a ridge near the reef edge can cause an increase in the wave-induced setup on the reef flat as well as wave reflection seaward of the fore-reef. Additional wave measurements with higher spatial resolution allow the investigation of the cross-shore evolution of harmonic waves and momentum flux. These measurements

show that the second harmonics become comparable to the fundamental harmonics on the reef flat after dissipation due to breaking. The momentum flux, with a value consistently lower than the theoretical value based on the linear shallow-water approximation, was found to be different from that for plane beaches in existing studies. Simple cross-shore undertow measurements were also obtained. It has been found that the cross-shore undertow profile in the absence of a ridge is identical to that for plane beaches under similar plunging breakers and the presence of a ridge blocks the flow in the leeside of the ridge in a way similar to how broad-crested weir controls the water level and flow in open channel flows.

Numerical experiments based on fully nonlinear, weakly dispersive, Boussinesq-type equations with a FV-based solver have been performed to study the wave transformation over various fringing reef profiles in Chapter 4. Model validations by the wave data presented in Chapter 3 and other similar studies have shown the necessities of an appropriate treatment of boundary conditions and a fine-tuned eddy-viscosity model. The numerical model can efficiently reproduce the key characteristics (wave reflection, generation of higher and lower frequency waves, wave height variation, wave-induced setup/setdown) of both monochromatic and spectral waves over various fringing reef profiles and reef-crest submergences, including a ridge at the reef edge and the dry reef-flat condition. Numerical tests have also been extended to reef topographies with which existing laboratory experiments are not concerned. Both the slope and the shape of fore-reef have been examined, and they were found to have notable effects on the variation of wave-induced setup inside the surf zone.

To gain more insight into the underlying physical processes, some analytical modeling approaches were attempted. The performance of different existing models to simulate the measured wave setups have been evaluated in Chapter 5. The offshore scaling parameter, commonly used for field data, has been found to be insufficient to describe the experimental data. It has also been shown that the model of Tait (1972) is able to reproduce the experimental results with some success, especially at relatively small reef-crest submergences. The model of Gourlay and

Colleter (2005) can account for most of the experimental data with the addition of an empirical parameter. The inadequacies of existing 1DH analytical models have been discussed. It was pointed out that the primary drawback of both models of Tait (1972) and Gourlay and Colleter (2005) is that both have free parameters that vary with reef-crest submergence.

An analytical model based on the mass balance has been presented in Chapter 6 to study the wave setup over fringing reef profiles where free fall (critical flow) conditions exist at the crest of the reef. It was based on the kinematics of the flow around the reef crest. The model has indicated that wave setup can be described by the deep-water wave steepness and a flux adjustment factor. The kinematic model has been proven to reproduce the maximum wave-induced setup on reef flat with/without the presence of a ridge subjected to both monochromatic and spectral waves. Model applications to other published experiments were also successful. The scaling factor in the model has been found to be a function of both the reef-crest submergence and the fore-reef slope. The model is ready to be extended to the emerged reef-crest conditions which occasionally occur for field reefs during low tides. A key requirement for this model is that the reef-crest submergence must be sufficiently small or emerged so that a critical flow condition exists.

A dynamic approach has been introduced in Chapter 7. The 1DH analytical model based on the cross-shore momentum balance is formulated to study the wave-induced setup over fringing reefs. Validation with various laboratory data has shown that the model is capable of reproducing the maximum wave-induced setup on a reef flat under a variety of reef profiles (with and without the presence of a ridge) and reef-crest submergences (from zero submergence to the upper limit where waves cease to break) as well as under both monochromatic and spectral conditions. The 1DH model has also been successfully applied for some field reefs, especially for the "fringing" type. The model parameter β_0 is related to some physical length scales in the surf zone and it has been found to be dependent on both the fore-reef slope and the reef-crest shape for the laboratory data. For natural reefs, it also accounts for factors (current, friction, etc.) that cause reduction of

wave setup. The model formulation has been extended to 2DH to study the idealized "barrier" reef system and validated by a case study. Aside from superior model performance for the data investigated, the proposed model has some distinctive features compared to existing dynamical approaches (e.g., Tait (1972) and Gourlay and Colleter (2005)) in that: (1) It allows surfzone processes on the reef flat; (2) The modulation of reef-crest submergence on the breaker depth index is considered; (3) The primary model parameter is independent of reef-crest submergence. Moreover, it differs from the kinematic theory in Chapter 6 in that it explicitly accounts for the primary 1DH transformation processes associated with waves such as wave shoaling, breaking, reflection and transmission.

To summarize, the major concern of this thesis is 1DH wave interactions with idealized fringing reefs at laboratory scale. It has shown the similarities and discrepancies of important aspects of wave dynamics (wave transformation, wave-induced setup and flow, etc.) with other coastal systems in engineering perspectives. It has enriched the existing data on the wave transformation over fringing reefs, especially over the fringing reef with a ridge. The laboratory data provided in this thesis can be used in validation of a variety of numerical wave and circulation models. The ability of the proposed numerical and analytical approaches in reproducing wave-induced setup is well addressed in this thesis. The analytical models discussed in this thesis are substitutes for some direct measurement and experimentation and provide us a tool to understand and the observed phenomena in the laboratory and underlying physical processes in a more general and objective way. Application of the proposed 1DH/2DH model to field data also enables us to understand some fundamental differences in wave dynamics between the laboratory reefs and the natural reefs.

8.2 Future Work

Three possible future research directions can be recommended here:

8.2.1 Experimental work

The wave-induced setup and flow over the reef flat could be investigated in a more systematic way in a laboratory wave-current flume or wave basin, particularly, the fundamental differences between the fringing reef and barrier reef could be studied. Moreover, flow measurements with advanced techniques such as Particle Image Velocimetry (PIV) could provide a high-resolution flow field on the shallower reef flat to investigate turbulence characteristics in the surf zone. Meanwhile, effects of the roughness and porosity of the fore-reef surface on wave-induced setup require further systematic experimental investigation.

8.2.2 Numerical simulation

Nature reel profiles are subjected to many other processes in addition to wave forcing. The adopted Boussinesq model in Chapter 4 can also be applied to conditions with an ambient current; the wave-current interaction as well as wave-generated currents can be modeled. The polynomial approximation of vertical velocity profile and the multi-layer concept (Lynett, 2006) provides a tool to investigate surf zone mean flow quantities such as the mass flux, undertow, etc., although some improvements on the breaking model may be needed. Extension of this approach to 2DH laboratory experiments or field cases is straightforward and the inclusion of subgrid lateral turbulence diffusion may be necessary. All of these could be attempted with more detailed flow measurements.

8.2.3 Analytical modeling

The potential of the kinematic theory in Chapter 6 to deal with emerged reef-crest conditions (negative reef-crest submergence) has not been validated by experimental data; this could be further examined. The magnitude of the scaling factor in the model has been found to be surprisingly small (bellow 0.5), and the underlying reasons should be further understood. The dependence of the model parameter in the dynamic model of Chapter 7 on the reef-crest shape is not very conclusive since a uniform trend has not been obtained due to a lack of data; more work on this issue is needed. Furthermore, an alternative wave model rather than

using the simple shallow-water wave approximation to parameterize the radiation stress could be attempted. Lastly, the validity of 2DH formulation of the model requires support from more laboratory and field data.

REFERENCES

Ahrens, J. P. (1987), "Characteristics of Reef Breakwaters", *Technical Report CERC-87-17*, Coastal Engineering Research Center, U.S. Army Engineer Waterways Experiment Station, Vicksburg, MS.

Apotsos, A., Raubenheimer, B., Elgar, S., Guza, R. T. and Smith, J. A. (2007), "Effects of wave rollers and bottom stress on wave setup", *J. Geophys. Res.*, 112, C02003, doi:10.1029/2006JC003549.

Atkinson, M. J. and Bilger R. W. (1992), "Effects of water velocity on phosphate uptake in coral reef-flat communities", *Limnol. Oceanogr.*, 37(2), 273–79.

Beji, S. and Battjes, J. A. (1993), "Experimental investigation of wave propagation over a bar", *Coast. Eng.*, 19, 151–162.

Battjes, J. A. (1974), "Surf-similarity", *Proc. 14th Int. Conf. Coastal Eng.*, ASCE, Copenhagen, Denmark, pp. 466-480.

Bellotti, G. (2004), "A simplified model of rip currents systems around discontinuous submerged barriers", *Coast. Eng.*, 51(4), 323–335.

Blenkinsopp, C. E. and Chaplin, J. R. (2008), "The effect of relative crest submergence on wave breaking over submerged slopes", *Coast. Eng.*, 55(12), 967–974.

Booij, N. (1983), "A note on the accuracy of the mild-slope equation", *Coast. Eng.*, 7(3), 191–203.

Bonneton, P., Lefebvre, J-P., Bretel, P., Ouillon, S. and Douillet, P. (2007), "Tidal modulation of wave-setup and wave-induced currents on the Aboré coral reef, New Caledonia", *J. Coast. Res.*, SI 50, 662–766.

Brander, R. W., Kench, P. S. and Hart D. E. (2004), "Spatial and temporal variations in wave characteristics across a reef platform, Warraber Island, Torres Strait, Australia", *Marine Geology*, 207(1-4), 169–184.

Brossard, J., Perret, G., Blonce, L. and Diedhiou A. (2009), "Higher harmonics induced by a submerged horizontal plate and a submerged rectangular step in a wave flume", *Coast. Eng.*, 56(1), 11–22.

Cáceres, I., Stive, M. J. F., Sanchez-Arcilla, A. and Trung, L. (2008), "Quantification of change in current intensities induced by wave overtopping around low-crested structures", *Coast. Eng.*, 55(2), 113–124.

Calabrese, M., Vicinanza, D. and Buccino, M. (2008), "2D wave setup behind submerged breakwaters", *Ocean Eng.*, 35(10), 1015–1028.

Callaghan, D. P., Nielsen, P., Cartwright, N., Gourlay, M. R. and Baldock,T. E. (2006), "Atoll lagoon flushing forced by waves", *Coast. Eng.*, 53(8), 691–704.

Camenen, B. and Larson, M. (2007), "Predictive formulas for breaker depth index and breaker type", *J. Coast. Res.*, 23(4), 1028–1041.

Carmo, J. A., Neves, G. M. and Voorde, M. T. (2011), "Designing a multifunctional artificial reef: studies on the influence of parameters with most influence in the vertical plane", *J. Coast. Conserv.*, 15(1), 99–112.

Christensen, E. D., Walstra, D. J. and Emerat, N. (2002), "Vertical variation of the flow across the surf zone", *Coast. Eng.* 45(1), 165–198.

Christou, M., Swan, C. and Gudmestad O. T. (2008), "The interaction of surface water waves with submerged breakwaters", *Coast. Eng.*, 55(12), 945–958.

Collins, I. A. (1970), "Probability of breaking wave characteristics", *Proc. 12th Int. Conf. Coastal Eng.*, ASCE, Washington, D.C., USA, pp. 399–414.

Cowen, E. A., Sou, I. M., Liu, P. L. -F. and Raubenheimer, R. (2003), "Particle image velocimetry measurements within a laboratory-generated swash zone", *J. Eng. Mech.* ASCE 129 (10),1119–1129.

Darwin, C. H. (1842), *The Structure and Distribution of Coral Reefs*, London: Smith, Elder and Co. 207 pp.

Dean, R. G. and Bender, C. J. (2006), "Static wave setup with emphasis on damping effects by vegetation and bottom friction", *Coast. Eng.*, 53(2-3), 149–156.

Demirbilek, Z., Nwogu, O. G. and Ward D. L. (2007), "Laboratory Study of Wind Effect on Runup over Fringing Reefs", *Report 1: Data report*, *Coastal and Hydraulics Laboratory Technical Report ERDC/CHL-TR-07-4*, U.S. Army Engineer Research and Development Center, Vicksburg, MS.

Demirbilek, Z. and Nwogu, O. G. (2007). "Boussinesq Modeling of Wave Propagation and Runup over Fringing Coral Reefs, Model Evaluation Report", *Coastal and Hydraulics Laboratory Technical Report, Chapter 4, ERDC/CHL*

TR-07-12, U.S. Army Engineer Research and Development Center, Vicksburg, MS.

Douillet, P., Ouillon, S. and Cordier, E. (2001), "A numerical model for fine suspended sediment transport in the southwest lagoon of New Caledonia", *Coral Reefs*, 20(4), 361–372.

Drønen, N., Karunarathna, H., Fredsøe, J., Sumer, B. M. and Deigaard, R. (2002), "An experimental study of rip channel flow", *Coast. Eng.* 45 (3-4), 223–238.

Falter, J. L., Atkinson, M. J. and Merrifield, M. A. (2004), "Mass transfer limitation of nutrient uptake by a wave-dominated reef flat community", *Limnol. Oceanogr.*, 49(5), 1820–1831.

Galvin, C. J. (1968), "Breaker type classification on three laboratory beaches", *J. Geophys. Res.*, 73(12), 3651–3659.

Galvin, C. J. (1969), "Breaker travel and choice of design wave height", *J. Wtrwy. and Harb. Div.*, ASCE, 95(WW2), 175–200.

Gerritsen, F. (1980), "Wave attenuation and wave set-up on a coastal reef", *Proc. 17th Int. Conf. Coastal Eng.*, ASCE, Sydney, Australia, pp. 444–461.

Goda, Y. (1970), "A synthesis of breaker indices", *Trans. Japan Soc. Civil Engrs.* 2(2), 39–49.

Goda, Y. (1974), "New wave pressure formulae for composite breakwaters", *Proc. 14th Int. Conf. Coastal Eng.*, ASCE, Copenhagen, Denmark, pp. 1702–1720.

Goda, Y. (2000), *Random Seas and Design of Maritime Structures*. World Sci. Press, Singapore, 443 pp.

Goda, Y. (2009), "Derivation of unified wave overtopping formulas for seawalls with smooth, impermeable surfaces based on selected CLASH datasets", *Coast. Eng.*, 56(4), 385–399.

Goda, Y. (2010), "Reanalysis of regular and random breaking wave statistics", *Coast. Eng. J.*, 52 (1), 71–106.

Gourlay, M. R. (1994), "Wave transformation on a coral reef", *Coast. Eng.*, 23(1-2), 17–42.

Gourlay, M. R. (1996a), "Wave set-up on coral reefs. 1. Set-up and wave-generated flow on an idealised two dimensional reef", *Coast. Eng.*, 27(3-4), 161–193.

Gourlay, M. R. (1996b), "Wave set-up on coral reefs. 2. Wave set-up on reefs with various profiles", *Coast. Eng.*, 28(1-4), 17–55.

Gourlay, M. R. and Colleter, G. (2005), "Wave-generated flow on coral reefs: an analysis for two-dimensional horizontal reef-flats with steep faces", *Coast. Eng.*, 52(4), 353–387.

Govender, K., Mocker, G. P. and Alport, M. J. (2002), "Video-imaged surf zone wave and roller structures and flow fields", *J. Geophys. Res.*, 107 (C7), 3072, 10.1029/2000JC000755.

Govender, K., Michallet, H., Alport, M. J., Pillay, U., Mocke, G. P. and Mory, M. (2009), "Video DCIV measurements of mass and momentum fluxes and kinetic energies in laboratory waves breaking over a bar", *Coast. Eng.*, 56(8), 876–885.

Guza, R. T. and Thornton, E. B. (1981), "Wave set-up on a natural beach", *J. Geophys. Res.*, 86, 4133–4137.

Haas, K. and Svendsen, Ib. A. (2002), "Laboratory measurements of the vertical structure of rip currents", *J. Geophys. Res.*, 107(C5), 3047, 10.1029/2001 JC000911.

Hardy, T. A. and Young I. (1996), "Field study of wave attenuation on an offshore coral reef", *J. Geophys. Res.*, 101 (C6), 14311–14326.

Hearn, C. J. (1999), "Wave-breaking hydrodynamics within coral reef systems and the effect of changing sea level", *J. Geophys. Res.*, 104 (C12), 30007–30019.

Hearn, C. J., Atkinson, M. J. and Falter, J. L. (2001), "A physical derivation of nutrient-uptake rates in coral reefs: effects of roughness and waves", *Coral Reefs*, 20(4), 347–356.

Hearn, C. J. (2011), "Hydrodynamics of coral reefs", In: Hopley D (ed) *Encyclopedia of modern coral reefs*, Springer, Berlin, pp. 563–573.

Hench, J. L., Leichter, J. J., and Monismith, S. G. (2008), "Episodic circulation and exchange in a wave-driven coral reef and lagoon system", *Limnol. Oceanogr.*, 53(6) ,2681–2694.

Hsiao, S. C., Lynett, P., Hwung, H. H., and Liu, P. L. -F. (2005), "Numerical simulations of nonlinear short waves using the multi-Layer Model", *J. Eng. Mech.*, 131(3), 231–243.

Huang, Z. C., Hsiao, S. C., Hwung, H. H. and Chang, K. A. (2009), "Turbulence and energy dissipations of surf-zone spilling breakers", *Coast. Eng.* 56(7), 733–746.

Israeli, M. and Orsza, S. A. (1981), "Approximation of radiation boundary conditions", *J. Comp. Phys.*, 41, 113–115.

Iversen, H. W. (1952), "Laboratory study of breakers", *Gravity waves*, U.S. National Bureau of Standards, Washington, D. C., Circular 521, 9–32.

Jago, O. K., Kench, P. S. and Brander, R. W. (2007), "Field observations of wave-driven water-level gradients across a coral reef flat", *J. Geophys. Res.*, 112, C06027, doi:10.1029/2006JC003740.

Johnson, B. D. and Smith J. M. (2005), "Longshore current forcing by irregular waves", *J. Geophys. Res.*, 110, C06006, doi:10.1029/2004JC002336.

Johnson, H. K. (2006), "Wave modeling in the vicinity of submerged breakwaters", *Coast. Eng.*, 53(1), 39–48.

Karambas, Th. V. and Koutitas, C. (1992), "A breaking wave propagation model based on the Boussinesq equations", *Coast. Eng.*, 18(1-2), 1–19.

Kench, P. S. and Brander R. W. (2006), "Wave processes on coral reef flats: Implications for reef geomorphology using Australian case studies", *J. Coast. Res.*, 22(1), 209–223.

Kennedy, A. B., Chen, Q., Kirby, J. T. and Dalrymple, R. A. (2000), "Boussinesq modeling of wave transformation, breaking, and runup. I: 1D", *J. Wtrwy., Port, Coast. and Ocean Eng.*, ASCE, 126 (1), 43–50.

Kim, D. H., Lynett, P. and Socolofsky, S. A. (2009), "A depth-integrated model for weakly dispersive, turbulent, and rotational fluid flows", *Ocean Modeling*, 27(3-4), 198–214.

Kirby, J. T., Wei, G., Chen, Q., Kennedy, A. B. and Dalrymple, R. A. (1998), *FUNWAVE 1.0: Fully Nonlinear Boussinesq Wave Model Documentation and User's Manual*, Center for Applied Coastal Research, University of Delaware.

Komar, P. D. and Gaughan, M. K. (1973), "Airy wave theory and breaker height prediction", *Proc. 13th Int. Conf. Coastal Eng.*, ASCE, Vancouver, Canada, pp. 405–418.

Komar, P. D. (1998), *Beach Processes and Sedimentation*, 2nd Ed., Prentice Hall, Upper Saddle River, N. J. 544 pp.

Kraines S. B., Yanagi, T., Isobe, M. and Komiyama, H. (1998) "Wind-wave-driven circulation on the coral reef at Bora Bay, Miyako Island", *Coral Reefs*, 17(2), 133–143.

Kraines, S. B., Suzuki, A., Yanagi, T., Isobe, M., Guo, X. and Komiyama, H. (1999) "Rapid water exchange between the lagoon and the open ocean at Majuro Atoll due to wind, waves, and tide", *J. Geophys. Res.*, 104 (C7), 15635–15653.

Lara, J. L., Losada, I. J. and Guanche, R. (2008), "Wave interaction with low-mound breakwaters using a RANS model", *Ocean Eng.*, 35(13), 1388–1400.

Lin, P. and Liu, P. L. -F. (1998), "A numerical study of breaking waves in the surf zone", *J. Fluid Mech.*, 359, 239–264.

Lin, P. and Liu, P. L. -F. (1999), "An internal wave-maker for Navier-Stokes equations models", *J. Wtrwy., Port, Coast. and Ocean Eng.*, ASCE, 125(4), 207–215.

Longuet-Higgins, M. S. and Stewart, R. W. (1962), "Radiation stress and mass transport in gravity waves, with application to surf beats", *J. Fluid Mech.*, 13, 481–504.

Longuet-Higgins, M. S. and Stewart, R. W. (1964). "Radiation stresses in water waves; a physical discussion, with applications", *Deep-Sea Res.*, 11, 529–562.

Longuet-Higgins, M. S. (2005), "On wave set-up in shoaling water with a rough sea bed", *J. Fluid Mech.*, 527, 217–234.

Losada, I. J., Lara, J. L., Christensen, E. D. and Garcia, N. (2005), "Modelling of velocity and turbulence fields around and within low-crested rubble-mound breakwaters", *Coast. Eng.*, 52 (10-11), 887–913.

Lowe, R. J., Falter, J. L., Bandet, M. D., Pawlak, G. and Atkinson M. J. (2005), "Spectral wave dissipation over a barrier reef", *J. Geophys. Res.*, 110, C04001, doi:10.1029./2004.JC002711.

Lowe, R. J., Falter, J. L., Monismith, S. G. and Atkinson M. J. (2009a), "Wave-driven circulation of a coastal reef-lagoon system", *J. Phys. Oceanog.*, 39(4), 873–893.

Lowe, R. J., Falter, J. L., Monismith, S. G. and Atkinson M. J. (2009b), "A numerical study of circulation in a coastal reef-lagoon system", *J. Geophys. Res.*, 114, C06022, doi: 10.1029/2008JC005081.

Lugo-Fernandez, A., Roberts, H. H. and Wiseman W. J. (1998a), "Tide effects on wave attenuation and wave set-up on a Caribbean coral reef", *Est. Coast. Shelf. Sci.*, 47(4), 385–393.

Lugo-Fernandez, A., Roberts, H. H. and Suhayda, J. N. (1998b), "Wave transformations across a Caribbean fringing-barrier Coral Reef", *Cont. Shelf Res.*, 18(10), 1099–1124.

Lugo-Fernandez, A., Roberts H. H. and Wiseman, W. J. (2004), "Currents, water levels, and mass transport over a modern Caribbean coral reef: Tague Reef, St. Croix, USVI", *Cont. Shelf Res.*, 24(17), 1989–2009.

Luick, J. L., Mason, L., Hardy, T. and Furnas, M. J. (2007), "Circulation in the Great Barrier Reef Lagoon using numerical tracers and in situ data", *Cont. Shelf Res.*, 27(6), 757–778.

Lynett, P, Wu, T. R. and Liu, P. L. -F. (2002), "Modeling wave runup with depth-integrated equations", *Coast. Eng.*, 46(2), 89–107.

Lynett, P. and Liu, P. L. -F. (2004), "A two-layer approach to water wave modeling", *Proc. R. Soc. London, Ser. A*, 460, 2637–2669.

Lynett, P. (2006), "Nearshore wave modeling with high-order Boussinesq-type equations", *J. Wtrwy., Port, Coast. and Ocean Eng.*, ASCE, 132(5), 348–357.

Lynett, P. and Liu, P. L. -F. (2008), *Modeling Wave Generation, Evolution, and Interaction with Depth-Integrated, Dispersive Wave Equations, Coulwave Code Manual v.2.0*, Cornell Univ., Ithaca, N.Y.

Lynett, P., Melby, J. A. and Kim, D. H. (2010), "An application of Boussinesq modeling to Hurricane wave overtopping and inundation", *Ocean Eng.*, 37, 135–153.

Madin, J. S., Black, K. P. and Connolly S. R. (2006), "Scaling water motion on coral reefs: from regional to organismal scales", *Coral Reefs*, 25, 635–644.

Madsen, P. A. and Sørensen, O. R. (1992), "A new form of the Boussinesq equations with improved linear dispersion characteristics. Part 2: A slowly varying bathymetry", *Coast. Eng.*, 18(3-4), 183–204.

Madsen, P. A., Sørensen, O. R. and Schaffer, H. A. (1997), "Surf zone dynamics simulated by a Boussinesq-type model. Part I. Model description and cross-shore motion of regular waves", *Coast. Eng.*, 32(4), 255–287.

Madsen, P. A., Fuhrman, D. R. and Wang, B. (2006), "A Boussinesq-type method for fully nonlinear waves interacting with a rapidly varying bathymetry", *Coast. Eng.*, 53(5-6), 487–504.

McCowan, J. (1894), "On the highest wave of permanent type", *Philosophical Magazine*, 38, 351–358.

Mei, C. C., Stiassnie, M. and Yue, D. K. P. (2005), *Theory and Applications of Ocean Surface Waves*, World Sci. Press, Singapore, 1071 pp.

Miche, R. (1944), "Mouvements ondulatoires de lamer en profondeur ou décroissante", *Annles de Ponts et Chaussées*, 19, 370–406.

Monismith, S. G. (2007), "Hydrodynamics of coral reefs", *Annu. Rev. Fluid Mech.*, 39, 37–55.

Mory, M. and Hamm, L. (1997), "Wave height, setup and currents around a detached breakwater submitted to regular or random wave forcing", *Coast. Eng.*, 31(1-4), 77–96.

Munk, W. H. and Sargent, M. C. (1948), "Adjustment of Bikini atoll to ocean waves", *Trans. Am. Geophys. Union*, 29, 855–860.

Munson, B. R., Young, D. F. and Okiishi, T. H. (2002), *Fundamentals of Fluid Mechanics*, John Wiley & Sons. Inc., USA., 840 pp.

Nelson, R. C. (1987), "Design wave heights on very mild slopes: an experimental study", *Civil. Eng. Trans.*, *Inst. Eng. Aust.*, 29, 157–161.

Nelson, R. C. (1994), "Depth limited design wave heights in very flat regions", *Coast. Eng.*, 23(1-2), 43–59.

Nelson, R. C. (1996), "Hydraulic roughness of coral reef platforms", *Applied Ocean Research*, 18(5), 265–274.

Nwogu, O. (1993), "Alternative form of Boussinesq equations for nearshore wave propagation", *J. Wtrwy., Port, Coast. and Ocean Eng.*, ASCE, 119(6), 618–638.

Owen, M. W. (1980), "Design of Seawalls Allowing for Wave Overtopping", *Technical Report EX-924*, HR-Wallingford, UK.

Péquignet, A. C. N., Becker, J. M., Merrifield, M. A. and Aucan, J. (2009), "Forcing of resonant modes on a fringing reef during tropical storm Man-Yi", *Geophys. Res. Lett.*, 36, L03607, doi:10.1029/2008GL036259.

Péquignet A. -C., Becker, J. M., Merrifield, M. A. and Boc S. J. (2011), "The dissipation of wind wave energy across a fringing reef at Ipan, Guam", *Coral Reefs*, 30, 71–82.

Peregrine, D. H. (1967), "Long waves on a beach", *J. Fluid Mech.*, 27, 815–827.

Pullen, T., Allsop, N. W. H., Bruce, T., Kortenhaus, A., Schuttrumpf, H. and van der Meer, J. W. (2007), "EurOtop: Wave Overtopping of Sea Defenses and Related Structures: Assessment Manual", *Science Report: SC050059*, Environment Agency, UK.

Ranasinghe, R. S., Sato, S. and Tajima, Y. (2009), "Boussinesq modeling of waves and currents over submerged breakwaters", *Proc. 5th Int. Conf. Asian and Pacific Coasts.*, APAC, Singapore. Vol. 3, pp. 58–64.

Raubenheimer, B., Guza R. T. and Elgar S. (1996), "Wave transformation across the inner surf zone", *J. Geophys. Res.*, 101(C10), 25589–25597.

Roeber, V., Cheung, K. F. and Kobayashi, M. H. (2010). "Shock-capturing Boussinesq-type model for nearshore wave processes", *Coast. Eng.*, 57(4), 407–423.

Sakai, T. and Battjes, J. A. (1980), "Wave shoaling calculated from Cokelet's theory", *Coast. Eng.*, 4, 65–84.

Schäffer, H. A., Madsen, P. A. and Deigaard, R. (1993), "A Boussinesq model for waves breaking in shallow water", *Coast. Eng.*, 20(3-4), 185–202.

Seelig, W. N. (1980), "Two-dimensional Tests of Wave Transmission and Reflection Characteristics of Laboratory Breakwaters", *Technical Report 80-1*, Coastal Engineering Research Center, U.S. Army Engineer Waterways Experiment Station, Vicksburg, MS.

Seelig, W. N. and Ahrens, J. P. (1981), "Estimation of Wave Reflection and Energy Dissipation Coefficients for Beaches, Revetments and Breakwaters", *Technical Paper 81-1*, Coastal Engineering Research Center, U.S. Army Engineer Waterways Experiment Station, Vicksburg, MS

Seelig, W. N. (1983), "Laboratory study of reef-lagoon system hydraulics", *J. Wtrwy. Port, Coast. and Ocean Eng.*, ASCE, 109(4), 380–391.

She, K., Greated, C. A. and Easson, W. J. (1994), "Experimental study of three-dimensional wave breaking", *J. Wtrwy., Port, Coast. and Ocean Eng.*, ASCE, 120(1), 20–36.

She, K., and Canning, P. (2007), "Geometric Study of Monochromatic Wave Breaking on Beaches", *J. Wtrwy., Port, Coast. and Ocean Eng.*, ASCE, 133(5), 334–342.

Shirlal, K. G., Rao, S. and Manu (2007), "Ocean wave transmission by submerged reef–A physical model study", *Ocean Eng.*, 34 (14-15), 2093–2099.

Skotner, C. and Apelt, C. J. (1999), "Application of a Boussinesq model for the computation of breaking waves. Part 2: wave- induced setdown and set-up on a submerged coral reef", *Ocean Eng.*, 26(10), 927–947.

Smith, E. R. and Kraus, N. C. (1991), "Laboratory study of wave breaking over bars and artificial reefs", *J. Wtrwy., Port, Coast. and Ocean Eng.*, ASCE, 117(4), 307–325.

Storlazzi, C. D., Elias, E., Field, M. E. and Presto, M. K. (2011), "Numerical modeling of the impact of sea-level rise on fringing coral reef hydrodynamics and sediment transport", *Coral Reefs*, 30, 83–96.

Suh, K. D., Lee, C. and Park, W. S. (1997), "Time-dependent equations for wave propagation on rapidly varying topography", *Coast. Eng.*, 32(2-3), 91–117.

Sunamura, T. (1980), "A laboratory study of offshore transport of sediment and a model for eroding beaches", Proc. *17th Int. Conf. Coastal Eng.*, ASCE, Sydney, Australia, pp. 1051–1070.

Svendsen, Ib. A., Madsen, P. A. and Hansen, J. B. (1978), "Wave characteristics in the surf zone", *Proc. 16th Int. Conf. Coastal Eng.*, ASCE, Hamburg, Germany, Vol. 1, pp. 520–539.

Svendsen, Ib. A. and Putrevu, U. (1993), "Surf zone wave parameters from experimental data", *Coast. Eng.*, 19(3-4), 283–310.

Svendsen, Ib. A. (1984a), "Wave heights and setup in a surf zone", *Coast. Eng.*, 8(4), 303–329.

Svendsen, Ib. A. (1984b), "Mass flux and undertow in a surf zone", *Coast. Eng.*, 8(4), 347–364.

Svendsen, Ib. A. (1987), "Analysis of surf zone turbulence", *J. Geophys. Res.*, 92, 5115–5124.

Svendsen, Ib. A. (2006), *Introduction to Nearshore Hydrodynamics*, World Sci. Press, Singapore, 722 pp.

Symonds, G., Black, K. P. and Young I. R. (1995), "Wave-driven flow over shallow reefs", *J. Geophys. Res.*,100 (C2), 2639–2648.

Tait, R. J. (1972), "Wave set-up on coral reefs", *J. Geophys. Res.*, 77, 2207–2211.

Tao, J. (1983), "Computation of Wave Run-up and Wave Breaking", *Internal Report*, Danish Hydraulics Institute, Horsholm, Denmark.

Thornton, E. B. and Guza, R. T. (1983), "Transformation of wave height distribution", *J. Geophys. Res.*, 88 (C10), 5925–5938.

Ting, F. C. K. and Kirby, J. T. (1994), "Observation of undertow and turbulence in a laboratory surf zone", *Coast. Eng.*, 24(1-2), 51–80.

Torres-Freyermuth, A., Losada, I. J. and Lara, J. L. (2007), "Modeling of surf zone processes on a natural beach using Reynolds-Averaged Navier-Stokes equations", *J. Geophys. Res.*, 112, C09014, doi: 10.1029/2006JC004050.

Torres-Freyermuth, A., Lara, J. L. and Losada, I. J. (2010), "Numerical modeling of short- and long-wave transformation on a barred beach", *Coast. Eng.*, 57(3), 317–330.

Tsai, C. P., Chen, H. B., Hwung, H. H. and Huang, M. J. (2005), "Examination of empirical formulas for wave shoaling and breaking on steep slopes", *Ocean Eng.*, 32(3-4), 469–483.

U.S. Army Corps of Engineers (USACE) (2003), *Coastal Engineering Manual*, *Chap. II-4 and II-7*, U.S. Army Engineer Research and Development Center, Coastal and Hydraulics Laboratory, Vicksburg, MS.

Van der Meer, J. W. and d'Angremond, K. (1991), "Wave transmission at low-crested structures", *Proc. ICE Conference Coastal Structures and Breakwaters*, Institution of Civil Engineers, Thomas Telford, London, U.K. pp. 25–41.

Van der Meer, J. W. and Daemen, I. F. R. (1994), "Stability and wave transmission at low crested rubble mound structures", *J. Wtrwy., Port, Coast. and Ocean Eng.*, ASCE, 120 (1), 1–19.

Van der Meer, J. W. and Janssen, J. P. F. M. (1995), "Wave run-up and wave overtopping at dikes", In: Kobayashi, N., Demirbilek, Z. (Eds.), *Wave Forces on Inclined and Vertical Structures*, Ch. 1, pp. 1–27.

Van der Meer, J. W., Briganti, R., Zanuttigh, B. and Wang, B. (2005), "Wave transmission and reflection at low crested structures: design formulae, oblique wave attack and spectral change", *Coast. Eng.* 52 (10-11), 915–929.

Veeramony, J. and Svendsen, Ib. A. (2000), "The flow in surf-zone waves", *Coast. Eng.*, 39(2-4), 93–122.

Vetter, O., Becker, J. M., Merrifield, M. A., Pequignet, A.-C., Aucan, J., Boc, S. J. and Pollock, C. E. (2010), "Wave setup over a Pacific Island fringing reef", *J. Geophys. Res.*, 115, C12066, doi:10.1029/2010JC006455.

Vicinanza, D., Cáceres, I., Buccino, M., Gironella, X. and Calabrese, M. (2009), "Wave disturbance behind low-crested structures: diffraction and overtopping", *Coast. Eng.*, 56(11-12), 1173–1185.

Weggel, J. R. (1972), "Maximum breaker height", *J. Wtrwy., Harb. and Coast. Eng. Div.* ASCE, 98(WW4), 529–548.

Wei, G., Kirby, J. T., Grilli, S. T. and Subramanya, R. (1995), "A fully nonlinear Boussinesq model for surface waves. Part 1. Highly nonlinear unsteady waves", *J. Fluid Mech.*, 294, 71–92.

Wei, G., Kirby, J. T. and Sinha, A. (1999), "Generation of waves in Boussinesq models using a source function method", *Coast. Eng.*, 36(4), 271–299.

Wilmott, C. J. (1981), "On the validation of models", *Phys. Geogr.*, 2, 184–194.

Yao, Y., Lo, E. Y. M., Huang, Z. H. and Monismith S. G. (2009), "An Experimental Study of wave-induced set-up over a horizontal reef with an idealized ridge", *Proc. 28th Int. Conf. Offshore Mech. and Artic Eng.*, ASME, Honolulu, Hawaii, USA., Vol. 6, pp. 383–389.

Young, I. R. (1989), "Wave transformations on coral reefs", *J. Geophys. Res.*, 94 (C7), 9979–9989.

Zanuttigh, B., Martinelli, L. and Lamberti, A. (2008), "Wave overtopping and piling-up at permeable low crested structures", *Coast. Eng.*, 55 (6), 484–498.

Zelt, J. A. (1991), "The run-up of nonbreaking and breaking solitary waves", *Coast. Eng.*, 15(3), 205–246.

APPENDIX A: EXPERIMENTAL DATA IN CHAPTER 2

The experimental data for different combinations of reef-flat submergences (h_r) and fore-reef slopes (s) are shown in Tables A.1 - A.7. Tables A1, A2, A3 and A4 are the sources of dataset 1 (shown in Fig. 2.5) while Tables A2, A5, A6, A7 are the sources of dataset 2 (shown in Fig. 2.6).

Table A.1 Measured data with $h_r = 0.03\,m$ and $s = 1/6$

H_0 (m)	T (s)	Breaker type	Breaker location	H_b (m)	h_b (m)	L_s (m)	$\overline{\eta}_r$ (m)	K_t	K_r
0.094	1.001	plunging	fore-reef	0.100	0.088	2.030	0.012	0.111	0.099
0.078	0.999	plunging	fore-reef	0.090	0.075	1.900	0.010	0.119	0.106
0.063	1.001	plunging	fore-reef	0.070	0.058	1.650	0.008	0.146	0.088
0.042	1.000	plunging	fore-reef	0.055	0.050	1.600	0.004	0.128	0.031
0.032	0.999	plunging	fore-reef	0.045	0.038	1.280	0.003	0.215	0.066
0.027	1.000	plunging	reef edge	0.035	0.030	1.130	0.002	0.223	0.056
0.024	1.000	plunging	reef flat	0.032	0.030	1.100	0.001	0.232	0.048
0.021	1.000	plunging	reef flat	0.030	0.030	1.000	0.001	0.228	0.028
0.019	1.000	plunging	reef flat	0.024	0.030	1.050	0.001	0.267	0.041
0.016	1.000	spilling	reef flat	0.024	0.030	0.950	0.000	0.294	0.073
0.011	1.000	spilling	reef flat	0.018	0.030	0.900	0.000	0.475	0.140
0.091	1.251	plunging	fore-reef	0.110	0.103	2.670	0.015	0.116	0.089
0.072	1.251	plunging	fore-reef	0.090	0.075	2.300	0.012	0.109	0.090
0.055	1.250	plunging	fore-reef	0.075	0.067	2.150	0.009	0.125	0.073
0.039	1.250	plunging	fore-reef	0.055	0.047	1.880	0.005	0.233	0.088
0.032	1.250	plunging	fore-reef	0.048	0.038	1.630	0.004	0.152	0.038
0.023	1.250	plunging	reef edge	0.030	0.030	1.380	0.002	0.245	0.046
0.018	1.250	plunging	reef flat	0.025	0.030	1.130	0.001	0.292	0.095
0.015	1.250	spilling	reef flat	0.020	0.030	1.050	0.001	0.345	0.090
0.011	1.250	spilling	reef flat	0.015	0.030	0.970	0.000	0.422	0.034
0.088	1.667	plunging	fore-reef	0.115	0.108	3.000	0.018	0.115	0.135
0.069	1.666	plunging	fore-reef	0.090	0.088	2.700	0.014	0.105	0.171
0.053	1.666	plunging	fore-reef	0.075	0.075	2.550	0.010	0.219	0.136
0.037	1.667	plunging	fore-reef	0.050	0.055	2.280	0.006	0.194	0.129
0.021	1.667	plunging	fore-reef	0.030	0.038	1.880	0.002	0.207	0.067
0.017	1.667	plunging	reef edge	0.024	0.030	1.780	0.001	0.283	0.060
0.014	1.667	spilling	reef flat	0.022	0.030	1.590	0.001	0.309	0.090
0.011	1.667	spilling	reef flat	0.020	0.030	1.550	0.000	0.359	0.098

Table A.2 Measured data with $h_r = 0.05\,m$ and $s = 1/6$

H_0 (m)	T (s)	Breaker type	Breaker location	H_b (m)	h_b (m)	L_s (m)	$\overline{\eta}_r$ (m)	K_t	K_r
0.127	1.006	plunging	fore-reef	0.130	0.120	2.380	0.015	0.144	0.052
0.107	1.002	plunging	fore-reef	0.115	0.103	2.180	0.012	0.163	0.076
0.098	0.999	plunging	fore-reef	0.100	0.087	1.950	0.010	0.183	0.053
0.081	1.000	plunging	fore-reef	0.085	0.075	1.780	0.007	0.183	0.086
0.071	1.001	plunging	fore-reef	0.078	0.065	1.700	0.006	0.236	0.052
0.061	1.000	plunging	fore-reef	0.070	0.057	1.720	0.004	0.273	0.012
0.051	0.999	plunging	reef edge	0.060	0.050	1.680	0.003	0.228	0.075
0.043	1.000	plunging	reef flat	0.043	0.050	1.480	0.002	0.296	0.077
0.034	1.001	plunging	reef flat	0.035	0.050	1.150	0.001	0.399	0.056
0.026	1.001	spilling	reef flat	0.030	0.050	1.100	0.001	0.464	0.102
0.022	1.002	spilling	reef flat	0.028	0.050	1.050	0.000	0.584	0.054
0.019	1.002	spilling	reef flat	0.027	0.050	0.950	0.000	0.713	0.122
0.016	1.001	non	..	..	..	..	..	..	..
0.015	1.001	non	..	..	..	..	..	..	..
0.008	1.000	non	..	..	..	..	..	..	..
0.132	1.248	plunging	fore-reef	0.140	0.153	3.000	0.018	0.151	0.049
0.118	1.252	plunging	fore-reef	0.130	0.112	2.500	0.016	0.158	0.089
0.092	1.249	plunging	fore-reef	0.110	0.103	2.300	0.013	0.196	0.126
0.074	1.250	plunging	fore-reef	0.095	0.087	1.950	0.009	0.177	0.056
0.059	1.250	plunging	fore-reef	0.078	0.066	2.030	0.005	0.219	0.045
0.049	1.250	plunging	fore-reef	0.060	0.055	1.910	0.004	0.263	0.069
0.045	1.250	plunging	reef edge	0.055	0.050	1.780	0.003	0.280	0.094
0.040	1.250	plunging	reef flat	0.050	0.050	1.680	0.002	0.286	0.080
0.031	1.250	plunging	reef flat	0.035	0.050	1.550	0.001	0.358	0.047
0.027	1.250	plunging	reef flat	0.033	0.050	1.450	0.001	0.513	0.022
0.025	1.250	spilling	reef flat	0.035	0.050	1.370	0.001	0.577	0.018
0.022	1.250	spilling	reef flat	0.030	0.050	1.250	0.001	0.660	0.012
0.019	1.250	spilling	reef flat	0.027	0.050	1.200	0.000	0.623	0.006
0.017	1.250	non	..	..	..	..	..	..	..
0.012	1.250	non	..	..	..	..	..	..	..
0.112	1.666	plunging	fore-reef	0.150	0.128	3.500	0.020	0.127	0.135
0.095	1.665	plunging	fore-reef	0.125	0.112	3.300	0.016	0.148	0.117
0.075	1.666	plunging	fore-reef	0.105	0.087	3.000	0.012	0.169	0.112
0.057	1.667	plunging	fore-reef	0.085	0.073	2.720	0.008	0.205	0.057
0.039	1.666	plunging	fore-reef	0.055	0.058	2.280	0.004	0.294	0.021
0.035	1.667	plunging	fore-reef	0.045	0.055	2.310	0.003	0.311	0.007
0.030	1.667	plunging	reef edge	0.042	0.050	2.130	0.002	0.379	0.021
0.026	1.667	plunging	reef flat	0.035	0.050	2.030	0.001	0.495	0.058
0.023	1.667	spilling	reef flat	0.035	0.050	1.950	0.001	0.535	0.068
0.021	1.667	spilling	reef flat	0.030	0.050	1.930	0.001	0.578	0.077
0.019	1.667	spilling	reef flat	0.030	0.050	1.850	0.000	0.568	0.067
0.016	1.667	spilling	reef flat	0.025	0.050	1.850	0.000	0.617	0.123

0.010	1.666	non	..	..	..	..	..	..	..

Table A.3 Measured data with $h_r = 0.07\,m$ and $s = 1/6$

H_0 (m)	T (s)	*Breaker type*	*Breaker location*	H_b (m)	h_b (m)	L_s (m)	$\overline{\eta}_r$ (m)	K_t	K_r
0.105	1.000	plunging	fore-reef	0.105	0.118	2.320	0.008	0.205	0.063
0.092	1.000	plunging	fore-reef	0.100	0.098	2.250	0.007	0.207	0.088
0.081	1.000	plunging	fore-reef	0.082	0.078	2.080	0.005	0.270	0.095
0.076	1.000	plunging	reef edge	0.075	0.070	2.030	0.004	0.299	0.077
0.073	1.000	plunging	reef flat	0.070	0.070	1.900	0.004	0.290	0.046
0.063	1.001	plunging	reef flat	0.060	0.070	2.000	0.003	0.322	0.038
0.049	1.001	plunging	reef flat	0.055	0.070	1.700	0.001	0.327	0.083
0.043	1.000	plunging	reef flat	0.050	0.070	1.650	0.001	0.378	0.108
0.041	1.001	plunging	reef flat	0.052	0.070	1.550	0.001	0.404	0.067
0.035	1.000	spilling	reef flat	0.043	0.070	1.450	0.000	0.454	0.137
0.032	1.000	spilling	reef flat	0.040	0.070	1.350	0.000	0.488	0.161
0.031	1.000	spilling	reef flat	0.040	0.070	1.350	0.000	0.562	0.188
0.028	1.000	non	..	..	..	..	..	..	..
0.026	1.000	non	..	..	..	..	..	..	..
0.022	1.000	non	..	..	..	..	..	..	..
0.104	1.250	plunging	fore-reef	0.120	0.107	2.550	0.010	0.235	0.037
0.087	1.249	plunging	fore-reef	0.110	0.098	2.570	0.008	0.283	0.089
0.075	1.249	plunging	fore-reef	0.085	0.078	2.480	0.005	0.300	0.082
0.070	1.249	plunging	reef edge	0.080	0.070	2.380	0.004	0.325	0.103
0.064	1.250	plunging	reef flat	0.070	0.070	2.250	0.004	0.355	0.103
0.059	1.250	plunging	reef flat	0.065	0.070	2.180	0.003	0.367	0.103
0.048	1.250	plunging	reef flat	0.055	0.070	1.950	0.002	0.376	0.075
0.039	1.250	plunging	reef flat	0.050	0.070	1.890	0.001	0.362	0.058
0.036	1.250	plunging	reef flat	0.045	0.070	1.900	0.001	0.399	0.055
0.034	1.250	spilling	reef flat	0.045	0.070	1.800	0.001	0.419	0.058
0.031	1.250	spilling	reef flat	0.043	0.070	1.850	0.000	0.457	0.060
0.028	1.250	spilling	reef flat	0.042	0.070	1.880	0.000	0.522	0.068
0.026	1.250	spilling	reef flat	0.035	0.070	2.050	0.000	0.659	0.113
0.023	1.250	non	..	..	..	..	..	..	..
0.019	1.250	non	..	..	..	..	..	..	..
0.103	1.667	plunging	fore-reef	0.125	0.132	3.450	0.015	0.173	0.106
0.086	1.666	plunging	fore-reef	0.118	0.115	3.300	0.010	0.210	0.036
0.068	1.667	plunging	fore-reef	0.098	0.090	2.950	0.007	0.282	0.029
0.062	1.666	plunging	fore-reef	0.090	0.082	2.800	0.006	0.290	0.037
0.056	1.667	plunging	fore-reef	0.068	0.077	2.720	0.005	0.303	0.027
0.049	1.667	plunging	reef edge	0.065	0.070	2.680	0.003	0.352	0.015
0.044	1.667	plunging	reef flat	0.060	0.070	2.580	0.003	0.425	0.020
0.039	1.667	plunging	reef flat	0.050	0.070	2.450	0.002	0.476	0.019

0.034	1.666	spilling	reef flat	0.045	0.070	2.320	0.001	0.546	0.016
0.031	1.666	spilling	reef flat	0.043	0.070	2.150	0.001	0.555	0.013
0.028	1.667	spilling	reef flat	0.040	0.070	2.100	0.001	0.618	0.009
0.025	1.667	spilling	reef flat	0.035	0.070	2.000	0.001	0.669	0.020
0.022	1.667	spilling	reef flat	0.035	0.070	1.950	0.000	0.709	0.063
0.020	1.667	non	..	..	..	..	..	..	..
0.013	1.667	non	..	..	..	..	..	..	..

Table A.4 Measured data with $h_r = 0.10\,m$ and $s = 1/6$

H_0 *(m)*	T *(s)*	*Breaker type*	*Breaker location*	H_b *(m)*	h_b *(m)*	L_s *(m)*	$\bar{\eta}_r$ *(m)*	K_t	K_r
0.138	1.000	plunging	fore-reef	0.130	0.150	2.580	0.008	0.222	0.067
0.125	0.999	plunging	fore-reef	0.120	0.112	2.550	0.007	0.280	0.086
0.117	1.000	plunging	reef edge	0.110	0.100	2.480	0.005	0.281	0.059
0.102	1.000	plunging	reef flat	0.097	0.100	2.580	0.004	0.309	0.054
0.092	1.000	plunging	reef flat	0.085	0.100	2.450	0.003	0.325	0.048
0.083	1.000	plunging	reef flat	0.080	0.100	2.450	0.003	0.337	0.062
0.075	1.000	plunging	reef flat	0.075	0.100	2.320	0.002	0.346	0.049
0.067	1.000	plunging	reef flat	0.070	0.100	2.200	0.001	0.354	0.080
0.063	1.000	spilling	reef flat	0.068	0.100	2.170	0.001	0.400	0.087
0.059	1.000	spilling	reef flat	0.060	0.100	2.280	0.001	0.437	0.112
0.054	1.000	spilling	reef flat	0.058	0.100	2.300	0.000	0.471	0.128
0.050	1.001	spilling	reef flat	0.055	0.100	2.100	0.000	0.503	0.165
0.045	1.000	non	..	..	..	..	..	..	..
0.041	1.001	non	..	..	..	..	..	..	..
0.143	1.250	plunging	fore-reef	0.145	0.137	3.050	0.011	0.227	0.122
0.128	1.248	plunging	fore-reef	0.130	0.125	3.030	0.008	0.246	0.059
0.108	1.247	plunging	fore-reef	0.120	0.117	2.980	0.006	0.268	0.027
0.102	1.250	plunging	reef edge	0.110	0.100	2.830	0.005	0.285	0.016
0.095	1.248	plunging	reef flat	0.095	0.100	2.750	0.004	0.339	0.060
0.083	1.249	plunging	reef flat	0.085	0.100	2.550	0.003	0.357	0.038
0.071	1.250	plunging	reef flat	0.078	0.100	2.450	0.002	0.409	0.028
0.066	1.250	plunging	reef flat	0.072	0.100	2.200	0.002	0.411	0.043
0.061	1.250	plunging	reef flat	0.070	0.100	2.160	0.001	0.422	0.050
0.056	1.250	spilling	reef flat	0.065	0.100	2.070	0.001	0.427	0.059
0.050	1.250	spilling	reef flat	0.060	0.100	2.080	0.000	0.485	0.095
0.045	1.250	spilling	reef flat	0.050	0.100	1.900	0.000	0.604	0.110
0.038	1.250	non	..	..	..	..	..	..	..
0.033	1.250	non	..	..	..	..	..	..	..
0.127	1.667	plunging	fore-reef	0.150	0.153	3.700	0.014	0.234	0.067
0.114	1.667	plunging	fore-reef	0.142	0.140	3.550	0.011	0.230	0.092
0.101	1.667	plunging	fore-reef	0.130	0.125	3.380	0.008	0.262	0.070

0.092	1.667	plunging	fore-reef	0.115	0.108	3.230	0.006	0.280	0.069
0.083	1.667	plunging	reef edge	0.105	0.100	3.130	0.005	0.312	0.058
0.073	1.667	plunging	reef flat	0.095	0.100	3.020	0.004	0.340	0.056
0.063	1.667	plunging	reef flat	0.083	0.100	2.900	0.003	0.403	0.051
0.058	1.667	plunging	reef flat	0.075	0.100	2.880	0.002	0.438	0.053
0.054	1.667	plunging	reef flat	0.072	0.100	2.800	0.002	0.461	0.062
0.050	1.667	spilling	reef flat	0.068	0.100	2.730	0.001	0.491	0.063
0.045	1.667	spilling	reef flat	0.065	0.100	2.730	0.001	0.531	0.067
0.040	1.667	non	reef flat	0.060	0.100	2.880	0.001	0.635	0.085
0.037	1.668	non	..	..	..	..	..	..	..
0.029	1.667	non	..	..	..	..	..	..	..

Table A.5 Measured data with $h_r = 0.05\,m$ and $s = 1/3$

H_0 *(m)*	T *(s)*	*Breaker type*	*Breaker location*	H_b *(m)*	h_b *(m)*	L_s *(m)*	$\overline{\eta}_r$ *(m)*	K_t	K_r
0.100	0.999	plunging	fore-reef	0.100	0.107	2.150	0.013	0.215	0.063
0.082	1.001	plunging	fore-reef	0.087	0.090	2.050	0.010	0.228	0.119
0.070	0.999	plunging	fore-reef	0.075	0.070	1.890	0.008	0.269	0.058
0.063	1.001	plunging	fore-reef	0.062	0.063	1.920	0.006	0.236	0.015
0.058	1.001	plunging	fore-reef	0.057	0.057	1.800	0.005	0.256	0.052
0.046	1.001	plunging	reef edge	0.048	0.050	1.580	0.003	0.298	0.089
0.038	0.999	plunging	reef flat	0.040	0.050	1.500	0.002	0.329	0.111
0.033	0.999	plunging	reef flat	0.035	0.050	1.470	0.001	0.345	0.138
0.029	1.000	plunging	reef flat	0.032	0.050	1.400	0.001	0.391	0.111
0.026	1.000	spilling	reef flat	0.030	0.050	1.300	0.000	0.408	0.114
0.021	1.000	spilling	reef flat	0.028	0.050	1.300	0.000	0.413	0.065
0.019	1.000	spilling	reef flat	0.023	0.050	1.300	0.000	0.523	0.100
0.016	1.000	non	..	..	..	..	..	..	..
0.012	1.000	non	..	..	..	..	..	..	..
0.103	1.249	plunging	fore-reef	0.105	0.123	3.000	0.016	0.158	0.159
0.088	1.250	plunging	fore-reef	0.095	0.107	2.800	0.013	0.159	0.084
0.068	1.250	plunging	fore-reef	0.075	0.090	2.450	0.009	0.226	0.095
0.056	1.251	plunging	fore-reef	0.062	0.067	2.280	0.007	0.323	0.016
0.041	1.251	plunging	fore-reef	0.050	0.057	1.950	0.003	0.334	0.127
0.036	1.250	plunging	reef edge	0.040	0.050	1.930	0.002	0.414	0.130
0.032	1.250	plunging	reef flat	0.036	0.050	1.830	0.002	0.444	0.069
0.027	1.250	plunging	reef flat	0.031	0.050	1.700	0.001	0.505	0.054
0.025	1.250	spilling	reef flat	0.030	0.050	1.540	0.001	0.493	0.065
0.023	1.250	spilling	reef flat	0.027	0.050	1.490	0.000	0.488	0.089
0.017	1.250	non	..	..	..	..	..	..	..
0.012	1.250	non	..	..	..	..	..	..	..
0.111	1.666	plunging	fore-reef	0.135	0.157	3.800	0.025	0.138	0.162

0.098	1.667	plunging	fore-reef	0.120	0.140	3.500	0.020	0.148	0.176
0.079	1.667	plunging	fore-reef	0.100	0.107	3.000	0.015	0.173	0.142
0.055	1.667	plunging	fore-reef	0.080	0.090	2.850	0.009	0.191	0.155
0.038	1.667	plunging	fore-reef	0.060	0.073	2.650	0.004	0.286	0.088
0.033	1.666	plunging	fore-reef	0.050	0.060	2.660	0.003	0.352	0.045
0.028	1.667	plunging	reef edge	0.042	0.050	2.580	0.002	0.367	0.094
0.023	1.667	spilling	reef flat	0.030	0.050	2.350	0.001	0.424	0.101
0.021	1.667	spilling	reef flat	0.028	0.050	2.220	0.001	0.438	0.110
0.018	1.667	spilling	reef flat	0.025	0.050	2.050	0.000	0.491	0.142
0.014	1.667	spilling	reef flat	0.023	0.050	1.900	0.000	0.667	0.116
0.009	1.667	non	..	..	..	..	..	..	..

Table A.6 Measured data with $h_r = 0.05\,m$ and $s = 1/9$

H_0 *(m)*	T *(s)*	*Breaker type*	*Breaker location*	H_b *(m)*	h_b *(m)*	L_s *(m)*	$\bar{\eta}_r$ *(m)*	K_t	K_r
0.111	1.001	plunging	fore-reef	0.105	0.108	2.450	0.009	0.165	0.049
0.096	1.001	plunging	fore-reef	0.095	0.097	2.350	0.008	0.191	0.055
0.080	1.000	plunging	fore-reef	0.075	0.080	2.100	0.006	0.206	0.059
0.067	1.001	plunging	fore-reef	0.065	0.066	1.850	0.004	0.216	0.032
0.052	1.001	plunging	reef edge	0.055	0.050	1.680	0.003	0.300	0.082
0.043	1.000	plunging	reef flat	0.045	0.050	1.630	0.002	0.337	0.050
0.040	1.000	plunging	reef flat	0.041	0.050	1.400	0.002	0.358	0.043
0.032	1.000	plunging	reef flat	0.035	0.050	1.350	0.001	0.410	0.045
0.028	1.000	spilling	reef flat	0.032	0.050	1.270	0.001	0.448	0.044
0.021	1.000	spilling	reef flat	0.030	0.050	1.300	0.000	0.630	0.076
0.017	1.000	non	..	..	..	..	..	..	..
0.098	1.250	plunging	fore-reef	0.098	0.091	2.600	0.010	0.145	0.037
0.081	1.250	plunging	fore-reef	0.086	0.078	2.330	0.008	0.236	0.076
0.061	1.250	plunging	fore-reef	0.075	0.072	2.130	0.005	0.277	0.091
0.051	1.250	plunging	fore-reef	0.065	0.067	2.030	0.003	0.266	0.071
0.051	1.250	plunging	fore-reef	0.060	0.058	1.900	0.003	0.265	0.043
0.038	1.250	plunging	reef edge	0.048	0.050	1.760	0.002	0.303	0.021
0.033	1.250	plunging	reef flat	0.038	0.050	1.670	0.001	0.353	0.042
0.031	1.250	plunging	reef flat	0.037	0.050	1.600	0.001	0.355	0.037
0.025	1.250	spilling	reef flat	0.035	0.050	1.450	0.001	0.492	0.050
0.019	1.250	spilling	reef flat	0.030	0.050	1.500	0.000	0.633	0.063
0.013	1.250	non	..	..	..	..	..	..	..
0.086	1.667	plunging	fore-reef	0.100	0.102	3.500	0.010	0.132	0.060
0.070	1.666	plunging	fore-reef	0.090	0.080	3.200	0.007	0.164	0.038
0.059	1.666	plunging	fore-reef	0.078	0.071	2.970	0.006	0.201	0.034
0.043	1.667	plunging	fore-reef	0.060	0.063	2.700	0.004	0.290	0.027
0.038	1.667	plunging	fore-reef	0.052	0.054	2.370	0.003	0.355	0.047

0.035	1.667	plunging	reef edge	0.045	0.050	2.230	0.002	0.382	0.058
0.031	1.667	plunging	reef flat	0.040	0.050	2.130	0.002	0.407	0.047
0.023	1.667	spilling	reef flat	0.032	0.050	2.000	0.001	0.489	0.042
0.020	1.667	spilling	reef flat	0.030	0.050	2.000	0.001	0.538	0.054
0.016	1.666	spilling	reef flat	0.028	0.050	2.000	0.000	0.691	0.065
0.012	1.666	non	..	..	..	..	..	..	..

Table A.7 Measured data with $h_r = 0.05\,m$ and $s = 1/12$

H_0 *(m)*	T *(s)*	*Breaker type*	*Breaker location*	H_b *(m)*	h_b *(m)*	L_s *(m)*	$\overline{\eta}_r$ *(m)*	K_t	K_r
0.098	1.000	plunging	fore-reef	0.088	0.105	2.470	0.008	0.141	0.008
0.080	1.000	plunging	fore-reef	0.078	0.083	2.230	0.006	0.164	0.047
0.067	1.000	plunging	fore-reef	0.070	0.068	2.050	0.004	0.192	0.061
0.051	1.000	plunging	fore-reef	0.060	0.060	1.850	0.003	0.218	0.055
0.046	1.000	plunging	reef edge	0.051	0.050	1.710	0.002	0.234	0.050
0.041	1.000	plunging	reef flat	0.048	0.050	1.580	0.002	0.235	0.059
0.036	1.000	plunging	reef flat	0.045	0.050	1.460	0.001	0.290	0.066
0.031	1.000	plunging	reef flat	0.040	0.050	1.380	0.001	0.323	0.068
0.026	1.000	spilling	reef flat	0.035	0.050	1.300	0.000	0.396	0.073
0.021	1.000	spilling	reef flat	0.028	0.050	1.350	0.000	0.488	0.115
0.016	1.000	non	..	..	..	..	..	..	..
0.096	1.250	plunging	fore-reef	0.100	0.114	2.800	0.009	0.150	0.053
0.078	1.250	plunging	fore-reef	0.095	0.081	2.600	0.007	0.233	0.028
0.061	1.250	plunging	fore-reef	0.070	0.073	2.450	0.005	0.215	0.032
0.049	1.251	plunging	fore-reef	0.058	0.056	2.050	0.003	0.315	0.070
0.042	1.250	plunging	reef edge	0.052	0.050	1.910	0.002	0.352	0.042
0.036	1.250	plunging	reef flat	0.048	0.050	1.840	0.002	0.352	0.031
0.030	1.250	plunging	reef flat	0.045	0.050	1.720	0.001	0.391	0.040
0.024	1.250	plunging	reef flat	0.040	0.050	1.750	0.001	0.483	0.048
0.021	1.250	spilling	reef flat	0.035	0.050	1.720	0.000	0.541	0.066
0.018	1.250	spilling	reef flat	0.030	0.050	1.730	0.000	0.730	0.078
0.012	1.250	non	..	..	..	..	..	..	..
0.085	1.667	plunging	fore-reef	0.110	0.118	3.740	0.009	0.136	0.008
0.068	1.667	plunging	fore-reef	0.088	0.085	3.250	0.007	0.153	0.031
0.056	1.667	plunging	fore-reef	0.080	0.071	2.930	0.005	0.186	0.042
0.042	1.667	plunging	fore-reef	0.068	0.060	2.700	0.003	0.284	0.050
0.035	1.667	plunging	reef edge	0.055	0.052	2.530	0.002	0.325	0.052
0.027	1.666	plunging	reef flat	0.043	0.050	2.230	0.001	0.371	0.026
0.020	1.666	spilling	reef flat	0.035	0.050	1.900	0.001	0.445	0.030
0.016	1.667	spilling	reef flat	0.028	0.050	2.000	0.000	0.561	0.058
0.013	1.667	non	..	..	..	..	..	..	..

APPENDIX B: EXPERIMENTAL DATA IN CHAPTER 3

The experimental data for different combinations of wave conditions (monochromatic and spectral) and reef profiles (with/without the ridge) are shown in Tables B.1 - B.4.

Table B.1 Measured data with monochromatic waves in the absence of the ridge

$h_0 = 0.35\,m$				$h_0 = 0.40\,m$				$h_0 = 0.45\,m$			
H_0 (m)	T (s)	$\bar{\eta}_r$ (m)	K_r	H_0 (m)	T (s)	$\bar{\eta}_r$ (m)	K_r	H_0 (m)	T (s)	$\bar{\eta}_r$ (m)	K_r
0.059	1.667	0.023	0.245	0.057	1.667	0.011	0.076	0.054	1.667	0.004	0.029
0.077	1.667	0.028	0.218	0.070	1.667	0.014	0.109	0.066	1.667	0.006	0.044
0.095	1.667	0.032	0.126	0.083	1.667	0.018	0.093	0.078	1.667	0.008	0.062
0.111	1.667	0.035	0.079	0.095	1.667	0.023	0.147	0.092	1.667	0.010	0.092
0.131	1.665	0.039	0.034	0.107	1.667	0.026	0.147	0.103	1.667	0.013	0.119
0.061	1.250	0.021	0.148	0.053	1.250	0.007	0.029	0.051	1.250	0.002	0.052
0.080	1.251	0.025	0.154	0.063	1.250	0.010	0.046	0.065	1.250	0.003	0.048
0.096	1.251	0.028	0.127	0.075	1.250	0.014	0.058	0.076	1.250	0.005	0.057
0.103	1.249	0.031	0.141	0.090	1.250	0.018	0.059	0.094	1.249	0.007	0.046
0.130	1.251	0.036	0.040	0.119	1.251	0.022	0.077	0.108	1.251	0.010	0.082
0.061	1.001	0.019	0.116	0.054	1.000	0.007	0.050	0.049	1.001	0.002	0.126
0.075	1.001	0.021	0.094	0.066	1.000	0.008	0.043	0.059	1.000	0.003	0.076
0.089	0.996	0.025	0.093	0.076	1.000	0.011	0.074	0.069	1.001	0.004	0.056
0.102	1.000	0.026	0.039	0.092	0.999	0.014	0.032	0.083	1.001	0.005	0.041
0.063	0.834	0.016	0.104	0.104	1.003	0.017	0.080	0.100	1.001	0.007	0.026
0.074	0.833	0.017	0.068	0.047	0.833	0.004	0.042	0.051	0.833	0.003	0.088
0.087	0.833	0.019	0.027	0.067	0.834	0.008	0.046	0.064	0.833	0.004	0.081
				0.083	0.832	0.010	0.061	0.075	0.833	0.004	0.079

Table B.2 Measured data with monochromatic waves in the presence of the ridge

$h_0 = 0.40\,m$				$h_0 = 0.41\,m$			
H_0 (m)	T (s)	$\overline{\eta}_r$ (m)	K_r	H_0 (m)	T (s)	$\overline{\eta}_r$ (m)	K_r
0.053	1.667	0.017	0.374	0.052	1.667	0.009	0.276
0.074	1.667	0.024	0.350	0.066	1.667	0.013	0.296
0.099	1.667	0.029	0.293	0.080	1.667	0.017	0.237
0.120	1.667	0.035	0.359	0.093	1.667	0.021	0.167
0.133	1.667	0.041	0.340	0.050	1.251	0.006	0.177
0.039	1.249	0.011	0.463	0.067	1.249	0.011	0.212
0.051	1.250	0.016	0.429	0.083	1.250	0.015	0.237
0.073	1.250	0.022	0.242	0.095	1.250	0.018	0.215
0.095	1.250	0.028	0.187	0.102	1.250	0.020	0.163
0.116	1.251	0.030	0.099	0.105	1.250	0.023	0.131
0.135	1.250	0.033	0.077	0.049	1.000	0.004	0.254
0.067	1.000	0.019	0.318	0.060	1.000	0.006	0.269
0.082	0.999	0.022	0.250	0.067	1.000	0.008	0.275
0.089	1.000	0.025	0.204	0.086	1.000	0.014	0.165
0.098	1.000	0.027	0.149	0.116	1.000	0.021	0.176
0.110	1.000	0.028	0.122	0.051	0.833	0.005	0.205
0.048	0.833	0.009	0.222	0.069	0.833	0.007	0.155
0.071	0.834	0.018	0.126	0.082	0.833	0.011	0.065
0.076	0.835	0.019	0.099				
$h_0 = 0.42\,m$				$h_0 = 0.45\,m$			
H_0 (m)	T (s)	$\overline{\eta}_r$ (m)	K_r	H_0 (m)	T (s)	$\overline{\eta}_r$ (m)	K_r
0.042	1.667	0.017	0.505	0.053	1.667	0.013	0.348
0.067	1.667	0.025	0.411	0.066	1.667	0.016	0.352
0.095	1.667	0.031	0.411	0.081	1.667	0.020	0.293
0.111	1.667	0.036	0.340	0.101	1.667	0.027	0.260
0.036	1.249	0.014	0.397	0.056	1.250	0.010	0.264
0.062	1.250	0.022	0.292	0.068	1.250	0.013	0.247
0.080	1.251	0.027	0.335	0.082	1.250	0.016	0.202
0.105	1.250	0.031	0.271	0.086	1.243	0.020	0.238
0.130	1.250	0.033	0.202	0.075	1.000	0.011	0.287
0.063	1.000	0.020	0.346	0.082	1.001	0.015	0.194
0.072	1.001	0.023	0.269	0.093	1.000	0.015	0.159
0.081	1.000	0.025	0.208				
0.093	1.001	0.027	0.177				
0.100	1.000	0.027	0.171				
0.044	0.833	0.014	0.325				
0.060	0.834	0.016	0.209				
0.071	0.834	0.021	0.124				

Table B.3 Measured data with spectral waves in the absence of the ridge

$h_0 = 0.35\ m$				$h_0 = 0.40\ m$				$h_0 = 0.45\ m$			
H_{s0} (m)	T_p (s)	$\bar{\eta}_r$ (m)	K_r	H_{s0} (m)	T_p (s)	$\bar{\eta}_r$ (m)	K_r	H_{s0} (m)	T_p (s)	$\bar{\eta}_r$ (m)	K_r
0.040	1.628	0.014	0.313	0.049	1.628	0.004	0.086	0.049	1.628	0.002	0.133
0.057	1.628	0.017	0.263	0.068	1.628	0.006	0.105	0.066	1.628	0.002	0.111
0.074	1.628	0.021	0.240	0.085	1.628	0.008	0.123	0.084	1.628	0.003	0.106
0.091	1.628	0.024	0.224	0.032	1.628	0.002	0.096	0.050	1.246	0.001	0.128
0.041	1.246	0.012	0.232	0.044	1.246	0.002	0.087	0.068	1.246	0.002	0.109
0.058	1.244	0.015	0.197	0.059	1.246	0.004	0.094				
0.074	1.244	0.018	0.184	0.074	1.246	0.006	0.108				
0.039	0.994	0.009	0.178	0.041	1.001	0.002	0.088				
0.056	0.984	0.013	0.154	0.054	1.001	0.003	0.094				

Table B.4 Measured data with spectral waves in the presence of the ridge

$h_0 = 0.40\ m$				$h_0 = 0.42\ m$				$h_0 = 0.45\ m$			
H_{s0} (m)	T_p (s)	$\bar{\eta}_r$ (m)	K_r	H_{s0} (m)	T_p (s)	$\bar{\eta}_r$ (m)	K_r	H_{s0} (m)	T_p (s)	$\bar{\eta}_r$ (m)	K_r
0.055	1.628	0.013	0.533	0.050	1.628	0.008	0.446	0.049	1.628	0.003	0.247
0.072	1.628	0.017	0.444	0.068	1.628	0.011	0.390	0.073	1.628	0.006	0.249
0.086	1.628	0.021	0.396	0.083	1.628	0.014	0.355	0.031	1.628	0.001	0.211
0.037	1.631	0.009	0.661	0.032	1.628	0.004	0.474	0.044	1.246	0.002	0.224
0.048	1.279	0.011	0.562	0.045	1.268	0.006	0.432	0.059	1.246	0.003	0.216
0.062	1.279	0.014	0.470	0.060	1.264	0.008	0.402	0.073	1.246	0.005	0.218
0.075	1.266	0.017	0.403	0.073	1.268	0.011	0.364	0.042	0.965	0.002	0.205
0.043	1.000	0.009	0.556	0.047	0.986	0.005	0.368	0.055	0.973	0.003	0.209
0.056	1.000	0.012	0.474	0.058	1.001	0.007	0.360				

APPENDIX C: LABORATORY STUDY ON EFFECTS OF ROUGHNESS ON WAVE-INDUCED SETUP[3]

Introduction

In section 3.5, an offshore-directed flow is identified under the trough of the surf zone waves propagating over the idealized platform reef model (i.e., the reef profile without the ridge). The bottom friction may dissipate the energy associated with the undertow, and affect the wave setup (see section 7.5 for a theoretical description). Previous experimental investigations (i.e., Gouraly, 1996a; Demirbilek et al., 2007) as well as the experiments in Chapter 3 focused mainly on the wave setup variations with the offshore wave conditions for relatively smooth reef flats. However, field measurements of reef flat surface roughness showed that coral reef has a very high drag coefficient being some orders of magnitude higher than that associated with normal shelves (Falter et al., 2004; Lowe et al., 2005; Hench et al., 2008). To understand the effects of reef surface roughness on wave-breaking and wave-induced setup, additional laboratory experiments were conducted under a series of monochromatic wave conditions. It has been found in Chapter 2 that most of the surf zone area was located on the reef flat, thus only the variation of the roughness on reef flat was studied. Two reef-flat models were examined: one with a smooth reef flat and another with a porous reef flat. Water surface elevations at different locations were measured to obtain the variations of wave-induced setup along the reef flat. Experimental results are reported here for one water depth and eighteen wave conditions. The wave-induced setups over a smooth reef flat are compared with those over porous reef flat.

Experimental Setup

Wave flume and reef models

The experimental settings are identical to that reported in section 3.2 (also see Fig. C.1), except for the arrangement of the reef flat. For the smooth reef flat model,

[3] This part of work has been presented at the 5th International Conference on Asian and Pacific Coasts, Singapore, 2009.

both the slope and the horizontal platform were made of PVC plates to simulate a smooth surface as shown in Figs. C.2(a) and C.2(b). Porous mats with 3 cm in height and 95.5% in porosity were paved uniformly on the reef flat to simulate the porous bottom. The top elevation of the porous mats is the same as that of the smooth reef flat (see Figs. C.2(c) and C.2(d)) so that the wave setups over these two models can be compared.

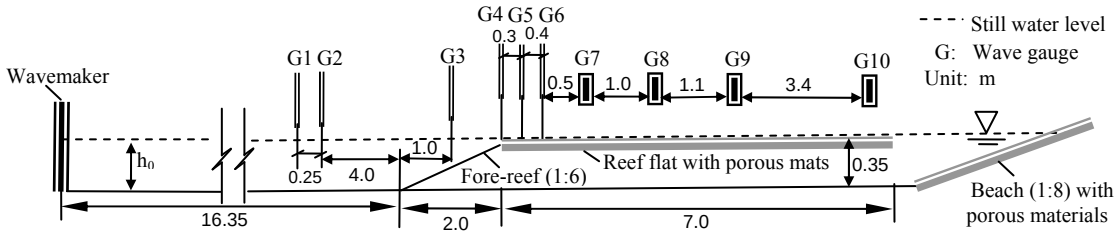

Fig. C.1 Sketch of the experimental setup.

Arrangement of instruments and experimental procedures

In very shallow water over the reef flat, four Ultralab® sensors (G7 - G10, General Acoustics Ltd.) were used to measure the free surface elevation. The distances between the adjacent wave gauges were optimized by some pilot tests to capture the location where the maximum setup may occur. G7 was 1.2 m away from the reef edge to ensure that this sensor was used outside the surf zone. Three resistance-type wave probes (G4 - G6, HR Wallingford Ltd.) were used to measure the setup in the surface zone on the reef flat. Before the reef model, two probes (G1 and G2) were used to separate the incident waves from the reflected waves. One more probe (G3) was placed on the fore-reef slope to estimate wave shoaling.

The target incident wave conditions were selected from a combination of five incident wave heights (ranging from 0.05 m to 0.13 m) and four wave frequencies (ranging from 0.6 Hz to 1.2 Hz). To compare the wave setups over the smooth reef flat and over the porous reef flat, similar wave conditions were used in the experiments.

To guarantee that the reef-flat was shallow enough and frictional dissipation might be dominant when waves came, the water depth (h_0) was fixed at 0.35 m in this study, i.e., the still water level coincides with the reef-flat elevation. The tests were first carried out for the smooth reef flat model under total 18 wave conditions, and then the same wave conditions were repeated for the porous reef flat model.

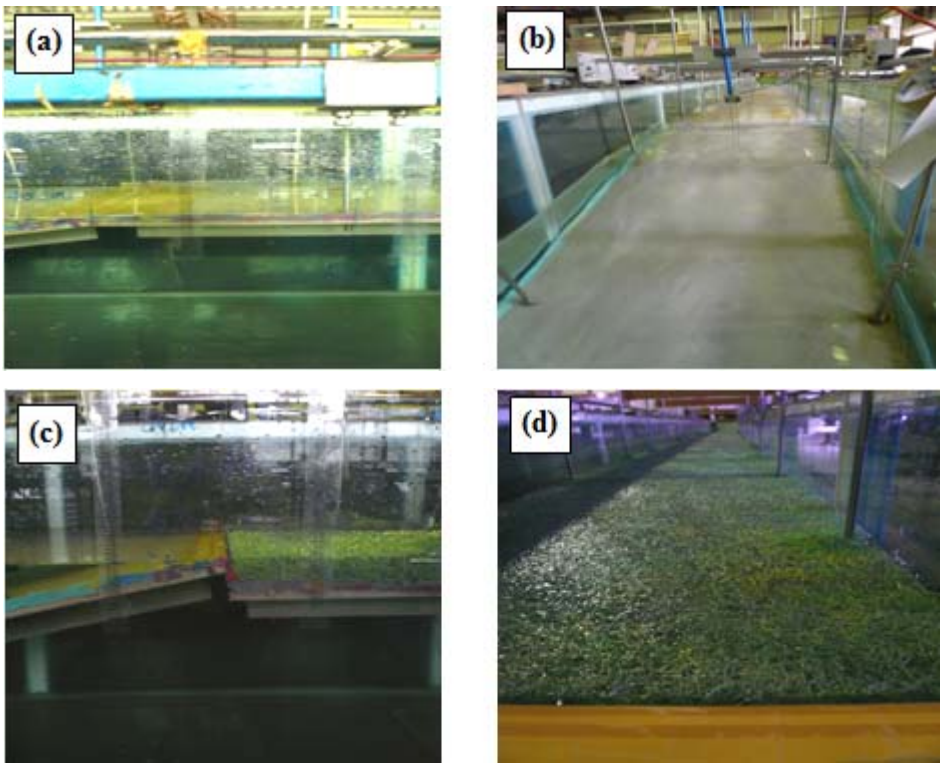

Fig. C.2 Reef flat models: (a) smooth reef flat (Side view); (b) smooth reef flat (Front view); (c) porous reef flat (Side view); (d) porous reef flat (Front view).

Results and Discussion

Wave transformation over the reef flat

Wave breaking commonly occurred on the slope or on the reef flat closed to the reef edge as a plunging breaker for all cases (e.g., Fig. C.3). Both the breaking point and breaker type were almost the same for these two reef models under the same incident wave condition. For the smooth reef flat, the surf zone might extend to one or two meters into the reef flat before wave breaking ceased and the oscillatory waves reformed. The reformed waves could propagate over the reef flat and reach

the beach at the end of the flume. However, for the porous reef flat, the surf zone became narrower and waves reformed earlier, the bore disappeared very fast due to the increased bottom friction. The reformed waves after wave breaking attenuated quickly due to the energy loss caused by the flows inside the porous mat. Consequently, the magnitude of wave-induced setup should be reduced according to the radiation stress theory in the surf zone described by Eq. (1.3). This conjecture will be verified in the following section. It could also be observed that for the porous reef flat, the reformed wave only propagated over a short distance before it damped away at the rear of the reef flat by frictional dissipation, hence waves could not reach the beach at the end of the flume. The reflection coefficient is small for most cases (less than 20%) and should have little effect on the results.

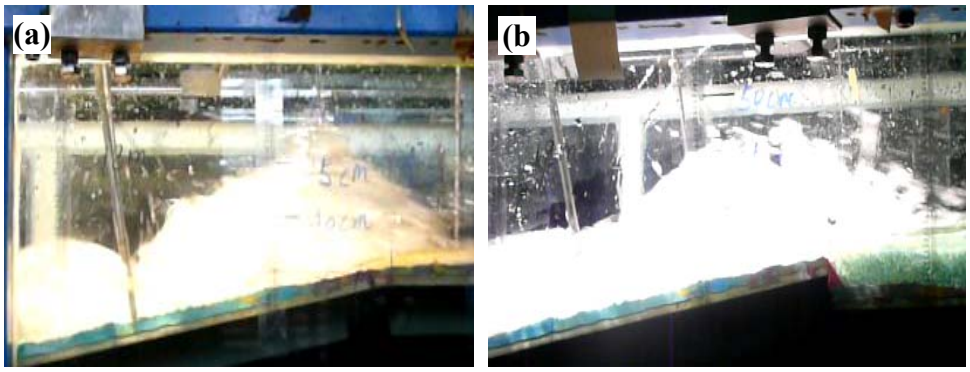

Fig. C.3 Wave breaking: (a) smooth reef flat; (b) porous reef flat ($H_0 = 0.10\,m$, $T = 1.25\,s$, $h_0 = 0.35\,m$).

Wave-induced setup with different reef flat models

The maximum wave-induced setup as a function of the deep-water wave height and the wave period is shown in Fig. C.4(a) for the two reef flat models. For the smooth reef flat, the maximum setup was obtained from G7; for the porous reef flat, the wave data from G2 were used to obtain the maximum wave setup. The wave setup averaged over the width of the reef flat was calculated by averaging the measurements from the 4 sensors (G7 - G10) and 3 probes (G4 - G6) on the reef flat. The variation of the averaged wave setup with the deep-water wave height and the wave period are shown in Fig. C.4(b) for the two reef-flat models.

As shown in Fig. C.4(a), for both models, the maximum wave setup on the reef flat almost linearly increases with increasing deep-water wave height, except for waves with smaller period. Meanwhile, by comparing the wave setups for similar deep-water wave heights, it could also be found that wave setup generally increases with increasing wave period. Moreover, the porous reef flat causes a decrease in the maximum wave setup for all wave conditions examined in the experiments, and a 4mm decrease in the wave setup had been observed for some wave conditions.

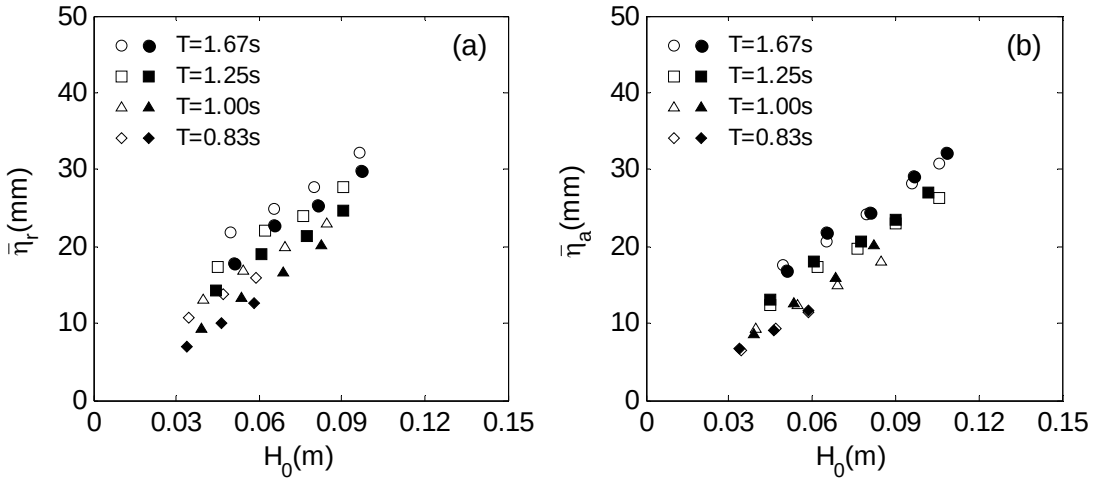

Fig. C.4 Maximum (a) and average (b) wave setup as a function of deep-water wave height (H_0) for different reef flats ($\bar{\eta}_r$ - maximum wave setup; $\bar{\eta}_a$ - average wave setup; Open markers - smooth reef flat; solid markers - porous reef flat; $h_0 = 0.35\ m$).

As observed in Fig. C.4(b), the trend of the averaged wave setup is similar to that of the maximum wave setup. However, under similar wave conditions, the discrepancies of the wave setups between smooth reef flat and porous reef flat were significantly reduced. For almost all the cases, the differences between averaged wave setups for the smooth and porous reef flat are less than *O*(1mm), which is in the range of measurements and errors from wave separation.

Two possible explanations for the effects of the porous reef flat are given as follows: (1) since the wave breaking point was on the fore-reef close to the reef edge and the location of the breaking point was not noticeably affected by the roughness of the reef flat, the roughness of the reef flat may affect the pattern of the mean flow in the water above the reef flat, and result in a redistribution of the wave setup over the reef flat. However, the energy and momentum losses for the smooth reef flat are similar to those for the porous reef flat. It is reasonable to anticipate that the wave setups averaged over the width of the reef flat are similar for the two reef flat models; (2) For porous reef flats, the bore attenuates rapidly, resulting in a much narrower surf zone, thus the contribution of the radiation stress and strong turbulent fluctuations to the wave setup is confined in a much narrower region close to the reef edge, resulting in a much longer region of nearly-constant wave setup. More systematic investigations are needed to quantify the reef surface roughness subjected to the surface waves.

Concluding Remarks

A series of laboratory tests has been carried out to study the effects of reef-flat roughness on the wave-induced setup. It is found that the behaviors of the wave transformation and wave setup for porous reef flat are different from those for the smooth reef flat. The present experiments show that the maximum setup over the reef flat increases with increasing deep-water wave height and wave period. The maximum wave-induced setup is larger for the smooth reef flat than for the porous reef flat. However, the characteristics of the reef flat tend to have immaterial effects on the wave setup averaged over the width of the reef flat.

APPENDIX D: SPONGE LAYERS FOR NUMERICAL SIMULATION

The sponge layers implemented in CoulWave is summarized here for completeness. Artificial damping terms f_1 and f_2 are added to the right hand sides of continuity equation and momentum equation, respectively. The inclusion of the damping layer in continuity equation is mainly for problems involving nonlinear long waves (e.g., solitary waves). The expressions for f_1 and f_2 are expressed as

$$f_1 = -w_1(x)\eta \tag{D.1}$$

$$f_2 = -w_1(x)u + w_2(x)u_{xx} \tag{D.2}$$

where w_1 and w_2 represent two kinds of damping mechanisms: Newtonian cooling and viscous damping (Israeli and Orszag, 1981). The expressions for w_1 and w_2 are given by

$$w_i\big|_{i=1,2} = \begin{cases} 0 & x \notin (X_s, X_e) \\ c_i \omega f(x) & x \in (X_s, X_e) \end{cases} \tag{D.3}$$

where X_s marks the start of sponge layer, X_e marks the end of the sponge layer, ω is the angular frequency of the waves to be damped and c_i is the coefficient. $f(x)$ is a smoothing function and expressed as

$$f(x) = \frac{\exp[(x - X_s)/W]^2 - 1}{\exp(1) - 1} \qquad x \in (X_s, X_e) \tag{D.4}$$

where $W = X_e - X_s$ is the sponge layer width. In this study, $c_1 = 10$, $c_2 = 0.01$ and $W = 1.25L$ are adopted as suggested by Lynett and Liu (2008).

APPENDIX E: DERIVATION OF SOME EQUATIONS IN CHAPTER 5

Derivation of h_b

The 1D energy balance between an offshore point and the breaking point for a steady wave train using normal incidence gives

$$(Ec_g)_0(1-K_r^2)-E_{fb}=(Ec_g)_b \tag{E.1}$$

where E is the wave energy density, c_g is the group velocity, K_r is the reflection coefficient, E_{fb} is loss of the energy flux dissipated by the bottom friction before the breaking point. We assume that E_{fb} can be parameterized as being proportional to the offshore energy flux, $E_{fb}=\alpha^2(Ec_g)_0$, by introducing a scaling parameter α. The subscripts 0 and b represent elevations offshore and the breaking point, respectively. Frequently, c_g on both sides of Eq. (E.1) can be computed by deep and shallow water wave approximation using linear wave theory, so that

$$\frac{gT}{4\pi}\frac{\rho g H_0^2}{8}(1-\alpha^2-K_r^2)=\sqrt{gh_b}\,\frac{\rho g H_b^2}{8} \tag{E.2}$$

where H_b is the breaker wave height, h_b is the breaker water depth. Eq. (E.2) can be reduced to

$$H_b^2=\frac{H_0^2 g^{1/2}T(1-\alpha^2-K_r^2)}{4\pi h_b^{1/2}} \tag{E.3}$$

The depth-limited breaking condition, i.e., $H_b=\gamma h_b$, is imposed on the above equation for H_b by assuming that the shoaling-induced setdown seaward of the surf zone can be neglected (i.e., $\overline{\eta}_b / h_b \ll 1$). Subsequent rearrangement yields

$$h_b=\frac{H_0(1-\alpha^2-K_r^2)^{0.4}}{(4\pi\gamma^2)^{0.4}S^{0.2}} \tag{E.4}$$

where S is offshore wave steepness given by Eq. (5.6).

Derivation of Eq. (5.7)

In the surf zone, the radiation stress can cause the mean water surface to change. Assuming that the depth variation in the surf zone is mild and the mean current is weak, the simplified 1D momentum balance (i.e., Eq. (5.2)) in the surf zone (ignoring friction term) is

$$g(h+\overline{\eta})\frac{d\overline{\eta}}{dx} = -\frac{1}{\rho}\frac{dS_{xx}}{dx} \tag{E.5}$$

where S_{xx} is the cross-shore radiation stress, which can be calculated using a wave theory. Using both the linear wave theory (i.e., Eq. (5.4)) and the depth-limited breaking condition (i.e., Eq. (5.5)) for S_{xx} gives

$$S_{xx} = \frac{3}{16}\rho g\gamma^2(h+\overline{\eta})^2 \tag{E.6}$$

Substituting Eq. (E.6) into Eq. (E.5) and rearranging the resultant equation arrives

$$(1+\frac{3}{8}\gamma^2)\frac{d\overline{\eta}}{dx} = -\frac{3}{8}\gamma^2\frac{dh}{dx} \tag{E.7}$$

Referring to Fig. 5.1 by ignoring the ridge, after integrating the equation above from the breaking point (x_b) to the reef edge (x_e) which is also assumed to be the end of the surf zone, one obtains

$$(8+3\gamma^2)(\overline{\eta}_r - \overline{\eta}_b) = -3\gamma^2(h_r - h_b) \tag{E.8}$$

where $\overline{\eta}_b$ is the wave-induced setdown at breaking point, $\overline{\eta}_r$ is the maximum wave setup on the reef flat and h_r is the reef-flat submergence. It then follows that

$$\overline{\eta}_r = \overline{\eta}_b + \frac{1}{1+8/3\gamma^2}(h_b - h_r) \tag{E.9}$$

$\overline{\eta}_b$ can be estimated by (Longuet-Higgins and Stewart, 1964)

$$\overline{\eta}_b = -\frac{H_b^2}{16h_b} = -\frac{\gamma^2 h_b}{16} \tag{E.10}$$

Substituting Eq. (E.10) into Eq. (E.9) yields Eq. (5.7).

Derivation of Eq. (5.9)

Gourlay (1996b) estimated the effects of the fore-reef slope and reef-crest submergence on the magnitude of the wave setup in the surf zone analytically based on conservation of energy. Subsequently, Gourlay and Colleter (2005) extended Gourlay (1996b)'s theoretical analysis to include the interaction between a unidirectional flow and the wave setup on the reef flat.

Applying the cross-shore conservation of wave energy

$$P_0 = P_r + P_d + P_t + P_v \tag{E.11}$$

where P_0 is the deep-water wave energy flux approaching the reef; P_r is the wave energy flux reflected from the fore-reef; P_d is the wave energy flux dissipated by breaking; P_t is the wave energy flux transmitted across the reef flat; P_v is the energy flux of the reef-flat current.

Assuming deep-water waves, the following two expressions for P_0 and P_r can be derived

$$P_0 = \frac{\rho g^2}{32\pi} H_o^2 T \tag{E.12}$$

$$P_r = K_r^2 \frac{\rho g^2}{32\pi} H_o^2 T \tag{E.13}$$

where K_r is the reflection coefficient.

For P_t, one can use the reef-flat shallow-water condition

$$P_t = \frac{\rho g}{8} K_t^2 H_o^2 \sqrt{g(\overline{\eta}_r + h_r)} \tag{E.14}$$

where K_t is the transmission coefficient.

For P_d, Eq. (E.5) is used and integrated over the surf zone (ignoring wave setdown)

$$P_d = \frac{2}{3}\frac{\rho\overline{\eta}_r}{K_p} g(\overline{\eta}_r + h_r)^{3/2} \tag{E.15}$$

where K_p is a reef profile shape factor, see Gourlay (1996b) for a detailed derivation of Eq. (E.15).

P_v can be determined by

$$P_v = \rho g q \Delta E = \rho g q[\overline{\eta}_r + q^2 / 2g(\overline{\eta}_r + h_r)^2] \tag{E.16}$$

where q is the mean flow per unit width; ΔE is the increase in specific energy relative to the reef flat.

Substituting Eqs. (E.12) - (E.16) into Eq. (E.11) with subsequent rearrangement and simplification gives

$$\overline{\eta}_r = \frac{g^2 H_0^2 T\left[1 - K_r^2 - 4\pi\gamma^2 \dfrac{\left(\overline{\eta}_r + h_r\right)^{5/2}}{H_0^2 g^{1/2} T} - \dfrac{16\pi q^3}{g^2 H_0^2 T\left(\overline{\eta}_r + h_r\right)^2}\right]}{32\pi\left[\dfrac{2}{3K_p} g^{3/2}\left(\overline{\eta}_r + h_r\right)^{3/2} + gq\right]} \tag{E.17}$$

For fringing reefs without the net flow on the reef flat, i.e., $q = 0$, Eq. (E.17) reduces to Eq. (5.9).

Derivation of Eq. (5.10)

Starting with the momentum balance with the radiation stress concept, i.e., Eq. (E.5), the assumption $h + \overline{\eta} \ll h$ in the surf zone leads to

$$gh(x)\frac{d\overline{\eta}}{dx} = -\frac{1}{\rho}\frac{dS_{xx}}{dx} \tag{E.18}$$

It is also assumed that the setup takes place at a representative depth (h_p) in the surf zone as Gourlay and Colleter (2005) did

$$h_p = \frac{(h_c + \overline{\eta}_r)}{K_p} \tag{E.19}$$

where K_p is reef-crest shape factor as discussed in section 5.2, In this case, integrating Eq. (E.18) gives

$$gh_p\overline{\eta}_r = g\overline{\eta}_r \frac{(h_c + \overline{\eta}_r)}{K_p} = -\frac{1}{\rho}(S_{xx}^s - S_{xx}^b) \tag{E.20}$$

where S_{xx}^b and S_{xx}^s are the cross-shore radiation stresses at the breaking point and the end of surf zone (which is assumed to coincide with the reef/ridge edge, See Fig. 5.1), respectively. The right-hand side of the above equation can also be estimated by linear wave theory and assuming that wave field is depth-limited at both breaking point and the end of surf zone

$$-\frac{1}{\rho}(S_{xx}^s - S_{xx}^b) = -\frac{1}{\rho}\left(\frac{3}{16}\rho g\gamma^2 h_c^2 - \frac{3}{16}\rho g\gamma^2 h_b^2\right) = \frac{3}{16}\gamma^2 g(h_b^2 - h_c^2) \tag{E.21}$$

Combining Eqs. (E.20) with (E.21) arrives

$$K_p = \frac{16}{3\gamma^2}\frac{\overline{\eta}_r(h_c + \overline{\eta}_r)}{(h_b^2 - h_c^2)} \tag{E.22}$$

Substituting Eq. (E.4) into the equation above gives Eq. (5.10) thus K_p. Note that Eq. (E.22) explicitly includes the dependent variable $\overline{\eta}_r$. This could be simplified if Eq. (5.8) is used to link $\overline{\eta}_r$ to the dependent variables, although the result will look a little complicated.

APPENDIX F: EVALUATION OF BOTTOM REACTION TERM ΔΠ IN CHAPTER 7 FOR AN IDEALIZED REEF PROFILE WITHOUT A RIDGE

Referring to Fig. F.1, for an idealized fringing reef profile without a ridge (a seaward planar fore-reef followed by a horizontal reef flat), the surfzone process always occurs near the reef edge (starting from x_b on the fore-reef to x_s on the reef flat, where $h_r = h_s$), the surfzone seabed slope on the fore-reef is

$$\frac{dh}{dx} = -s = \frac{h_r - h_b}{x_e - x_b} \tag{F.1}$$

where s is fore-reef slope. On the horizontal bottom, one has

$$\frac{dh}{dx} = 0 \tag{F.2}$$

To further simplify $\Delta\Pi$ in Eq. (7.3), a variation of wave-induced setup ($\overline{\eta}$) in the surf zone from x_b to x_s needs to be assumed. Both polynomials and power laws will be examined here.

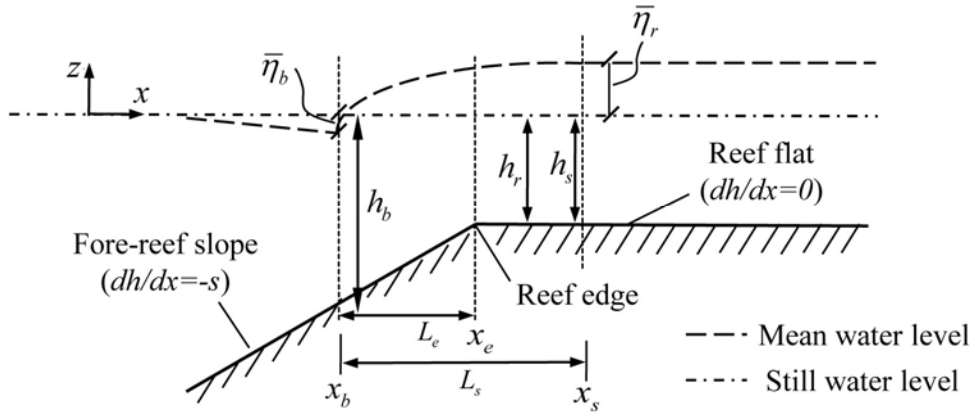

Fig. F.1 Surfzone seabed profile for an idealized reef and some notations adopted in this appendix.

Polynomial

Linear polynomial

A linear polynomial variation of $\overline{\eta}$ between x_b and x_s gives

$$\eta = \overline{\eta}_b + \left(\overline{\eta}_r - \overline{\eta}_b\right)\frac{x - x_b}{x_s - x_b} \tag{F.3}$$

for which the following boundary conditions are satisfied

$$\overline{\eta}(x_b) = \overline{\eta}_b; \qquad \overline{\eta}(x_s) = \overline{\eta}_r \tag{F.4}$$

where $\overline{\eta}_b$ is the wave-induced setdown at the breaking point and $\overline{\eta}_r$ is the maximum wave-induced setup on the reef flat. Substituting Eq. (F.3) into the expression of $\Delta\Pi$ in Eq. (7.3), one can carry out the following manipulations with the help of Eqs. (F.1) and (F.2)

$$\begin{aligned}
\Delta\Pi &= \int_{x_b}^{x_s} g\left(h + \overline{\eta}\right)\frac{dh}{dx}dx \\
&= g\int_{x_b}^{x_e}\left\{h\frac{dh}{dx} + \left[\overline{\eta}_b + \left(\overline{\eta}_r - \overline{\eta}_b\right)\frac{x - x_b}{x_s - x_b}\right]\frac{dh}{dx}\right\}dx \\
&= g\delta_1 + g\overline{\eta}_b\delta_2 + g\left(\overline{\eta}_r - \overline{\eta}_b\right)\delta_3 \\
&= \frac{g}{2}\left(h_r^2 - h_b^2\right) + g\overline{\eta}_b\left(h_r - h_b\right)\left(1 - \frac{\beta_0}{2}\right) + g\overline{\eta}_r\left(h_r - h_b\right)\frac{\beta_0}{2}
\end{aligned} \tag{F.5}$$

where

$$\delta_1 = \int_{x_b}^{x_e} h\frac{dh}{dx}dx = \frac{\left(h_r^2 - h_b^2\right)}{2} \tag{F.6}$$

$$\delta_2 = \int_{x_b}^{x_e}\frac{dh}{dx}dx = \left(x_e - x_b\right)\frac{h_r - h_b}{x_e - x_b} = h_r - h_b \tag{F.7}$$

$$\delta_3 = \int_{x_b}^{x_e}\frac{x - x_b}{x_s - x_b}\frac{dh}{dx}dx = \frac{1}{2}\frac{\left(x_e - x_b\right)^2}{\left(x_s - x_b\right)}\frac{h_r - h_b}{x_e - x_b} = \frac{\left(h_r - h_b\right)}{2}\beta_0 \tag{F.8}$$

$$\beta_0 = \frac{x_e - x_b}{x_s - x_b} = \frac{L_e}{L_s} \qquad (F.9)$$

Quadratic polynomial

A quadratic polynomial variation of $\overline{\eta}$ between x_b and x_s gives

$$\overline{\eta} - \overline{\eta}_b = 2\left(\overline{\eta}_r - \overline{\eta}_b\right)\frac{\left(x - x_b\right)}{x_s - x_b} - \left(\overline{\eta}_r - \overline{\eta}_b\right)\frac{\left(x - x_b\right)^2}{\left(x_s - x_b\right)^2} \qquad (F.10)$$

for which the following boundary conditions are satisfied

$$\overline{\eta}(x_b) = \overline{\eta}_b;\ \ \overline{\eta}(x_s) = \overline{\eta}_r;\ \left.\frac{d\overline{\eta}}{dx}\right|_{x=x_s} = 0 \qquad (F.11)$$

The third boundary condition in Eq. (F.11) ensures a smooth transition of $\overline{\eta}$ at the end of the surf zone.

Substituting Eq. (F.10) into the expression of $\Delta\Pi$ in Eq. (7.3), one can carry out the following manipulations with the help of Eqs. (F.1) and (F.2)

$$\begin{aligned}
\Delta\Pi &= \int_{x_b}^{x_s} g\left(h + \overline{\eta}\right)\frac{dh}{dx}dx = \int_{x_b}^{x_e} g\left(h + \overline{\eta}\right)\frac{dh}{dx}dx \\
&= g\int_{x_b}^{x_e}\left\{h\frac{dh}{dx} + \left[\overline{\eta}_b + 2\left(\overline{\eta}_r - \overline{\eta}_b\right)\frac{x - x_b}{x_s - x_b} - \left(\overline{\eta}_r - \overline{\eta}_b\right)\frac{\left(x - x_b\right)^2}{\left(x_s - x_b\right)^2}\right]\frac{dh}{dx}\right\}dx \\
&= g\delta_1 + g\overline{\eta}_b\delta_2 + 2g\left(\overline{\eta}_r - \overline{\eta}_b\right)\delta_3 - g\left(\overline{\eta}_r - \overline{\eta}_b\right)\delta_4 \\
&= \frac{g}{2}\left(h_r^2 - h_b^2\right) + g\overline{\eta}_b\left(h_r - h_b\right)\left(\frac{1}{3}\beta_0^2 - \beta_0 + 1\right) + g\overline{\eta}_r\left(h_r - h_b\right)\left(-\frac{1}{3}\beta_0^2 + \beta_0\right)
\end{aligned} \qquad (F.12)$$

where $\delta_1, \delta_2, \delta_3$ and β_0 are obtained by Eqs. (F.6) to (F.9) and

$$\delta_4 = \int_{x_b}^{x_e}\frac{\left(x - x_b\right)^2}{\left(x_s - x_b\right)^2}\frac{dh}{dx}dx = \frac{1}{3}\frac{\left(x_e - x_b\right)^3}{\left(x_s - x_b\right)^2}\frac{h_r - h_b}{x_e - x_b} = \frac{\left(h_r - h_b\right)}{3}\beta_0^2 \qquad (F.13)$$

Cubic polynomial

A cubic polynomial variation of $\overline{\eta}$ between x_b and x_s gives

$$\overline{\eta}-\overline{\eta}_b = 3\left(\overline{\eta}_r-\overline{\eta}_b\right)\frac{\left(x-x_b\right)^2}{\left(x_s-x_b\right)^2}-2\left(\overline{\eta}_r-\overline{\eta}_b\right)\frac{\left(x-x_b\right)^3}{\left(x_s-x_b\right)^3} \tag{F.14}$$

In addition to Eq. (F.11), the following boundary condition is imposed on Eq. (F.14)

$$\left.\frac{d\overline{\eta}}{dx}\right|_{x=x_b} = 0 \tag{F.15}$$

which ensures a smooth transition of $\overline{\eta}$ at the beginning of the surf zone. Following the same procedures above, we have

$$\Delta\Pi = \frac{g}{2}\left(h_r^2-h_b^2\right)+g\overline{\eta}_b\left(h_r-h_b\right)\left(\frac{1}{2}\beta_0^3-\beta_0^2+1\right)+g\overline{\eta}_r\left(h_r-h_b\right)\left(\beta_0^2-\frac{1}{2}\beta_0^3\right) \tag{F.16}$$

Quartic polynomial

A quartic polynomial variation of $\overline{\eta}$ between x_b and x_s gives

$$\overline{\eta}-\overline{\eta}_b = 6\left(\overline{\eta}_r-\overline{\eta}_b\right)\frac{\left(x-x_b\right)^2}{\left(x_s-x_b\right)^2}-8\left(\overline{\eta}_r-\overline{\eta}_b\right)\frac{\left(x-x_b\right)^3}{\left(x_s-x_b\right)^3}+3\left(\overline{\eta}_r-\overline{\eta}_b\right)\frac{\left(x-x_b\right)^4}{\left(x_s-x_b\right)^4} \tag{F.17}$$

Comparing with the cubic profile above, an additional boundary condition is imposed on Eq. (F.17) by noting that $\overline{\eta}$ shoreward of x_s is constant

$$\left.\frac{d^2\overline{\eta}}{dx^2}\right|_{x=x_s} = 0 \tag{F.18}$$

Following the same procedures above, we have

$$\begin{aligned}\Delta\Pi = {} & \frac{g}{2}\left(h_s^2-h_b^2\right)+g\overline{\eta}_b\left(h_r-h_b\right)\left(-\frac{3}{5}\beta_0^4+2\beta_0^3-2\beta_0^2+1\right)\\ & +g\overline{\eta}_r\left(h_r-h_b\right)\left(\frac{3}{5}\beta_0^4-2\beta_0^3+2\beta_0^2\right)\end{aligned} \tag{F.19}$$

Power law

A simple power law relationship between $\overline{\eta}$ and x in the surf zone gives

$$\eta = \overline{\eta}_b + \left(\overline{\eta}_r - \overline{\eta}_b\right)\left(\frac{x - x_b}{x_s - x_b}\right)^{\frac{1}{C}} \qquad C = 1, 2 \cdots N \tag{F.20}$$

for which the following boundary conditions are satisfied

$$\overline{\eta}(x_b) = \overline{\eta}_b; \qquad \overline{\eta}(x_s) = \overline{\eta}_r \tag{F.21}$$

Substituting Eq. (F.20) into the expression of $\Delta\Pi$ in Eq. (7.3), one can carry out the following manipulations with the help of Eqs. (F.1) and (F.2)

$$\begin{aligned}
\Delta\Pi &= \int_{x_b}^{x_s} g\left(h + \overline{\eta}\right)\frac{dh}{dx}dx \\
&= g\int_{x_b}^{x_e}\left\{h\frac{dh}{dx} + \left[\overline{\eta}_b + \left(\overline{\eta}_r - \overline{\eta}_b\right)\left(\frac{x - x_b}{x_s - x_b}\right)^{\frac{1}{C}}\right]\frac{dh}{dx}\right\}dx \\
&= g\delta_1 + g\overline{\eta}_b\delta_2 + g\left(\overline{\eta}_r - \overline{\eta}_b\right)\delta_0 \\
&= \frac{g}{2}\left(h_r^2 - h_b^2\right) + g\overline{\eta}_b\left(h_r - h_b\right)\left(1 - \frac{C}{1+C}\beta_0^{\frac{1}{C}}\right) + g\overline{\eta}_r\left(h_r - h_b\right)\frac{C}{1+C}\beta_0^{\frac{1}{C}}
\end{aligned} \tag{F.22}$$

where δ_1, δ_2 and β_0 are obtained by Eqs. (F.6), (F.7), (F.9) and

$$\delta_0 = \int_{x_b}^{x_e}\left(\frac{x - x_b}{x_s - x_b}\right)^{\frac{1}{C}}\frac{dh}{dx}dx = \frac{1}{\frac{1}{C}+1}\frac{\left(x_e - x_b\right)^{\frac{1}{C}+1}}{\left(x_s - x_b\right)^{\frac{1}{C}}}\frac{h_r - h_b}{x_e - x_b} = \frac{C}{1+C}\left(h_r - h_b\right)\beta_0^{\frac{1}{C}} \tag{F.23}$$

Synthesis

One can combine Eqs. (F.5), (F.12), (F.16), (F.19) and (F.22) in a compact form:

$$\Delta\Pi = \frac{g}{2}\left(h_r^2 - h_b^2\right) + g\overline{\eta}_b\left(h_r - h_b\right)\left(1 - \lambda\right) + g\overline{\eta}_r\left(h_r - h_b\right)\lambda \tag{F.24}$$

where

$$\lambda = \begin{cases} \dfrac{\beta_0}{2} & \textit{linear polynomial} \\ -\dfrac{1}{3}\beta_0^2 + \beta_0 & \textit{quadratic polynomial} \\ -\dfrac{1}{2}\beta_0^3 + \beta_0^2 & \textit{cubic polynomial} \\ \dfrac{3}{5}\beta_0^4 - 2\beta_0^3 + 2\beta_0^2 & \textit{quartic polynomial} \\ \dfrac{C}{1+C}\beta_0^{\frac{1}{C}} \quad C = 2,3,\cdots N & \textit{power law} \end{cases} \tag{F.25}$$

APPENDIX G: EVALUATION OF BOTTOM REACTION TERM ΔΠ IN CHAPTER 7 FOR AN IDEALIZED REEF PROFILE WITH A RECTANGULAR RIDGE

Referring to Fig. G.1, for an idealized fringing reef profile with a rectangle ridge (a seaward planar fore-reef followed by a horizontal reef flat, where the rectangle ridge is located on the reef edge), wave breaking always occurs near the reef edge, but the location where surfzone process ceases may be on the ridge top or on the reef flat behind the ridge, depending on both the cross-shore reef-crest (ridge) width (B) and incident wave conditions.

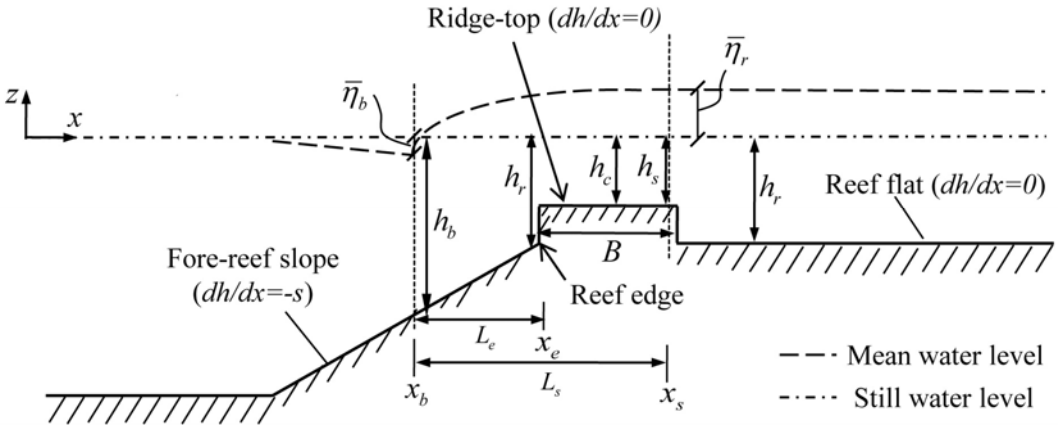

Fig. G.1 Surfzone seabed profile for an idealized reef with a rectangle ridge and some notations adopted in this appendix.

Considering the two singular points for the bottom slope at both seaside and leeside vertical slopes of the ridge, we have the integral in $\Delta\Pi$

$$\begin{aligned}&\int_{x_b}^{x_s} h\frac{dh}{dx}dx = \int_{x_b}^{x_e^-} h\frac{dh}{dx}dx + \int_{x_e^-}^{x_e^+} h\frac{dh}{dx}dx + 0 + \phi\int_{x_r^-}^{x_r^+} h\frac{dh}{dx}dx + 0 \\ &= \frac{1}{2}\left(h_r^2 - h_b^2\right) + \frac{1}{2}\left(h_c^2 - h_r^2\right) + \frac{\phi}{2}\left(h_r^2 - h_c^2\right) = \frac{1}{2}\left(h_c^2 - h_b^2\right) + \frac{\phi}{2}\left(h_r^2 - h_c^2\right)\end{aligned} \tag{G.1}$$

where x_e^- and x_e^+ represent immediately before and after the seaside edge of the ridge (x_e), respectively; similarly, x_r^- and x_r^+ represent immediately before and after the leeside edge of the ridge (x_r); and

$$\phi = \begin{cases} 0 & \textit{breaking ceases on the ridge} - \textit{top} \\ 1 & \textit{breaking ceases on the reef flat behind the ridge} \end{cases} \tag{G.2}$$

Another integral in $\Delta\Pi$ is

$$\begin{aligned} &\int_{x_b}^{x_s} \overline{\eta} \frac{dh}{dx} dx = \int_{x_b}^{x_e^-} \overline{\eta} \frac{dh}{dx} dx + \int_{x_e^-}^{x_e^+} \overline{\eta} \frac{dh}{dx} dx + 0 + \phi \int_{x_r^-}^{x_r^+} \overline{\eta} \frac{dh}{dx} dx + 0 \\ &= \int_{x_b}^{x_e^-} \overline{\eta} \frac{dh}{dx} dx + \left[\overline{\eta}_b + \left(\overline{\eta}_r - \overline{\eta}_b \right) \left(\beta_0 \right)^{\frac{1}{m}} \right] \left(h_c - h_r \right) \\ &+ \phi \left[\overline{\eta}_b + \left(\overline{\eta}_r - \overline{\eta}_b \right) \left(\beta_0 + \frac{B}{L_s} \right)^{\frac{1}{C}} \right] \left(h_r - h_c \right) \end{aligned} \tag{G.3}$$

where β_0 is defined in Eq. (F.9) and only the power law approximation to $\overline{\eta}$ in the surf zone, i.e., Eq. (F.20), is considered here (the polynomial approximations can be derived in a similar way although the expressions are more complicated), and

$$\int_{x_b}^{x_e^-} \overline{\eta} \frac{dh}{dx} dx = \overline{\eta}_b \left(h_r - h_b \right) \left(1 - \frac{C}{C+1} \beta_0^{\frac{1}{C}} \right) + \overline{\eta}_r \left(h_r - h_b \right) \left(\frac{C}{C+1} \beta_0^{\frac{1}{C}} \right) \tag{G.4}$$

which is derived in the same way as the last two terms in Eq. (F.22).

Combining Eqs. (G.1), (G.3) and (G.4) gives

$$\begin{aligned} &\Delta\Pi = \int_{x_b}^{x_s} g \left(h + \overline{\eta} \right) \frac{dh}{dx} dx = \frac{g}{2} \left(h_c^2 - h_b^2 \right) + \phi \frac{g}{2} \left(h_r^2 - h_c^2 \right) + g \overline{\eta}_b \left(h_r - h_b \right) \left(1 - \lambda \right) \\ &+ g \overline{\eta}_r \left(h_r - h_b \right) \lambda + g \left[\left(1 - \frac{C+1}{C} \lambda \right) \overline{\eta}_b + \frac{C+1}{C} \lambda \overline{\eta}_r \right] \left(h_c - h_r \right) \\ &+ \phi g \left[\overline{\eta}_b + \left(\overline{\eta}_r - \overline{\eta}_b \right) \left(\beta_0 + \frac{B}{L_s} \right)^{\frac{1}{C}} \right] \left(h_r - h_c \right) \end{aligned} \tag{G.5}$$

where

$$\lambda = \frac{C}{C+1}\beta_0^{\frac{1}{C}} \tag{G.6}$$

In the following derivations, we only consider the case that breaking creases on the ridge-top as shown in Fig. G.1, (i.e., $\phi = 0$ and $h_c = h_s$), which is consistent with our laboratory observations for the experimental data in Chapter 3 in the presence of a rectangle ridge. In this condition, Eq. (G.5) reduces to

$$\begin{aligned}\Delta\Pi = \int_{x_b}^{x_s} g(h+\bar{\eta})\frac{dh}{dx}dx = \frac{g}{2}\left(h_c^2 - h_b^2\right) + g\bar{\eta}_b\left(h_r - h_b\right)\left(1-\lambda\right) \\ + g\bar{\eta}_r\left(h_r - h_b\right)\lambda + g\left[\left(1-\frac{C+1}{C}\lambda\right)\bar{\eta}_b + \frac{C+1}{C}\lambda\bar{\eta}_r\right](h_c - h_r)\end{aligned} \tag{G.7}$$

Substituting Eqs. (7.5), (7.7) and (G.7) into Eq. (7.4) leads to a simple second order algebraic equation similar to Eq. (7.12), it has a unique positive solution in the form of Eq. (7.13) with

$$b = 2h_c + \frac{16(h_b - h_r)\lambda + 16\frac{C+1}{C}(h_r - h_c)\lambda}{(8+3\gamma_2^2)} \tag{G.8}$$

$$c = \frac{3\gamma_2^2 h_c{}^2 - 3\gamma_1^2 h_b^2\left(1+K_r^2\right) + 16\bar{\eta}_b\left(h_b - h_r\right)\left(1-\lambda\right) + 16\bar{\eta}_b\left(1-\frac{C+1}{C}\lambda\right)\left(h_r - h_c\right)}{8+3\gamma_2^2} \tag{G.9}$$

It can be found that if C is large enough so that $(C+1)/C \approx 1$, h_r in both Eqs. (G.8) and (G.9) would be cancelled out, and Eqs. (G.8) and (G.9) would reduce to Eqs. (7.14) and (7.15), respectively, with h_c being equivalent to the h_r in Eq. (7.9). However, as shown in section 7.3.3, $C = 4$ has been found to be appropriate for the reef profile with the ridge in Chapter 3. Therefore, if one uses the power law with $C = 4$, a best fit between predictions and the experimental data with the ridge in Chapter 3 gives $\beta_0 = 0.093$ for the exact expression Eq. (G.7) and $\beta_0 = 0.17$ for Eq.

(7.9) (in which h_c was used for h_r), respectively, with the same $R^2 = 0.94$, thus the increase of β_0 is substantial if Eq. (7.9) is extended to accommodate for the reef with a rectangle ridge. Meanwhile, for those reefs with relatively narrow reef crests (ridges), wave breaking may cease shoreward of the ridge ($\phi = 1$), the modification to β_0 due to the use of Eq. (7.9) may be more significant, depending on the ratio of the cross-shore reef-crest width to the surfzone width, i.e., B / L_s as indicated in Eq. (G.5). Consequently, the physical meaning of β_0 would become less obvious in those conditions.

APPENDIX H: APPLICATION OF SELECTED EXISTING ANALYTICAL MODELS TO SOME FIELD DATA

In this Appendix, the performance of Tait (1972)'s model (i.e., Eq. (5.8)) and Gourlay and Colleter (2005)'s model (i.e., Eq. (5.9)) in Chapter 5 is evaluated by the four field datasets in section 7.5. The predicted setups are plotted against the observed setups in Figs. H.1 and H.2 for the two models, respectively. In the model of Tait (1972), the empirical parameter γ is obtained by a best fit between the predictions and observations. In the model of Gourlay and Colleter (2005), $\gamma = 0.4$ on the reef flat was again used, and the empirical parameter K_p was obtained from a best agreement between the predictions and observations. Wave reflection was ignored in both models.

Comparing with Fig. 7.8, Fig. H.1 shows that overall the model of Tait (1972) performed as good as the proposed model in Chapter 7: Good predictions were found for Vetter et al. (2010)'s data, and reasonable predictions were found for Bonneton et al. (2007)'s data, but it failed to reproduce the Lowe et al. (2009a)'s results. Tait (1972)'s model seems to give a better prediction for Hench et al. (2008)'a data, but the author found that reproducing Hench et al. (2008)'s results with the proposed model in Chapter 7 can indeed be improved if the parameter C in the model is reduced from 7 to 4. Fig. H.1 also shows that the values of γ in the model of Tait (1972) for the four reefs generally fall into the (relatively wide) range previously observed in field (e.g., Camenen and Larson, 2007; Goda, 2010).

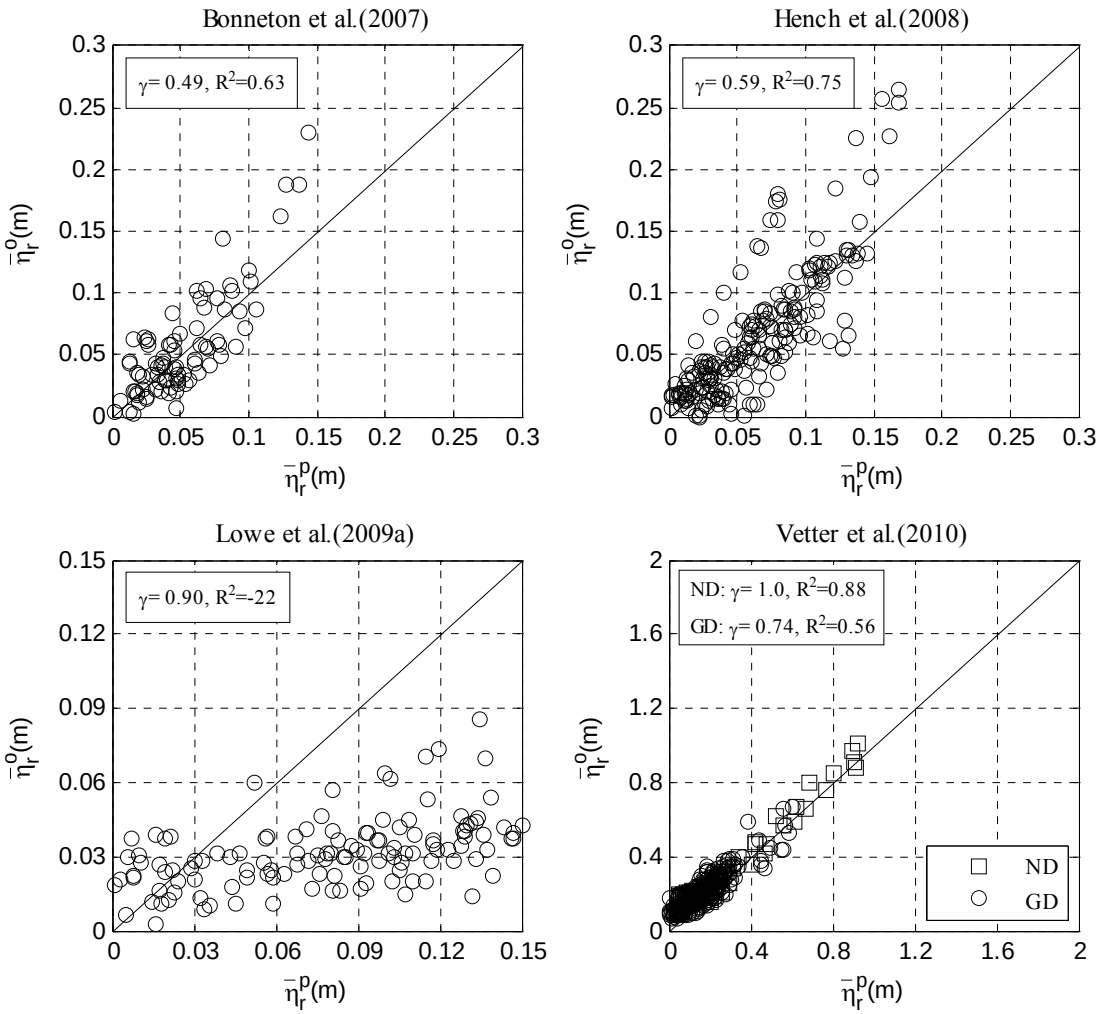

Fig. H.1 Predicted wave setup ($\bar{\eta}_r^p$) vs. observed wave setup ($\bar{\eta}_r^o$) for different field studies using the model of Tait (1972) (γ - parameter in the proposed model; R^2 - R-square; Solid line - $\bar{\eta}_r^p = \bar{\eta}_r^o$; ND - N-deployment; GD - G-deployment).

Fig. H.2 shows that the predictions for both data of Bonneton et al. (2007) and Hench et al. (2008) by the model of Gourlay and Colleter (2005) are similar to those by Tait (1972) shown in Fig. H.1. Notably, Gourlay and Colleter (2005)'s model significantly improved the predictions of Lowe et al. (2009a)'s data. This is because Eq. (5.9) is in agreement with Lowe et al. (2009a)'s observation that the wave setup was correlated with the offshore wave power. However, Gourlay and Colleter (2005)'s model gave poorer reproduction for Vetter et al. (2010)'s data than Tait

(1972)'s model. Vetter et al. (2010) has reported that surfzone process mostly completed on the fore-reef during their measurements, which violate some assumptions introduced in Gourlay and Colleter (2005)'s model. Generally, the values of K_p in the model of Gourlay and Colleter (2005) fall between 0.2 and 0.8 for the four reef profiles, in agreement with the values suggested by Gourlay (1996b).

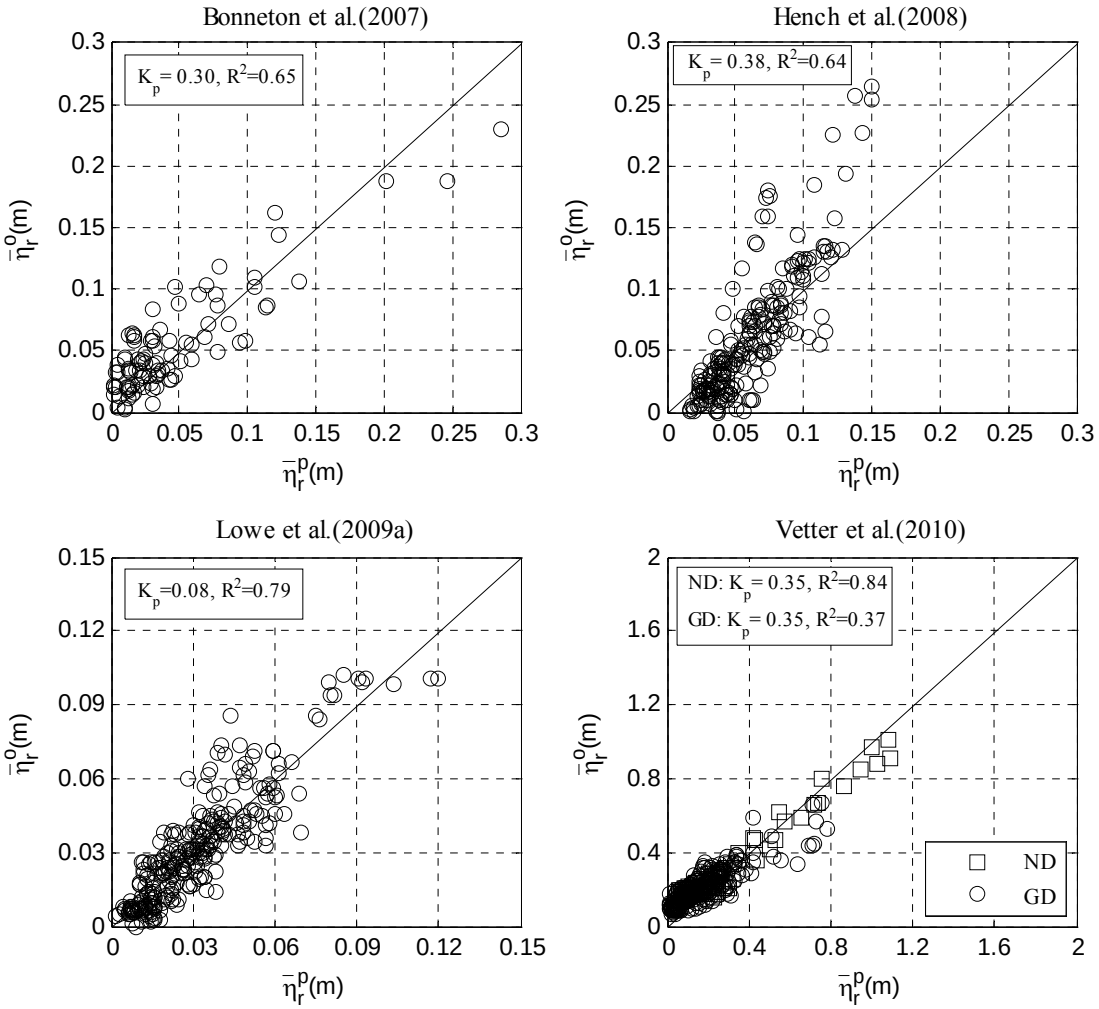

Fig. H.2 Predicted wave setup ($\overline{\eta}_r^p$) vs. observed wave setup ($\overline{\eta}_r^o$) for different field studies using the model of Gourlay and Colleter (2005) (γ - parameter in the proposed model; R^2 - R-square; Solid line - $\overline{\eta}_r^p = \overline{\eta}_r^o$; ND - N-deployment; GD - G-deployment).